Advances in the Modeling of Time-Resolved Laser-Induced Incandescence

by
Timothy Andrew Sipkens

A thesis
presented to the University of Waterloo
in fulfillment of the
thesis requirement for the degree of
Doctor of Philosophy
in
Mechanical and Mechatronics Engineering

Waterloo, Ontario, Canada, 2018

Examination committee membership

The following served on the Examining Committee for this thesis. The decision of the Examining Committee is by majority vote.

External examiner	Ömer Gülder Professor
Supervisor	Kyle J. Daun Associate Professor
Internal member	Sean Peterson Associate Professor
Internal member	Jean-Pierre Hickey Assistant Professor
Internal-external member	Peter Levine Associate Professor

Author's declaration

I hereby declare that I am the sole author of this thesis. This will be a true copy of the thesis, including any required final revisions, as accepted by my examiners.

I understand that my thesis may be made electronically available to the public.

Abstract

Aerosolized nanoparticles represent both great potential for the development of emerging technologies and one of the biggest challenges currently facing our planet. In the former case, aerosol-based synthesis techniques represent one of the most cost-effective approaches to generating engineered nanoparticles having applications that range from medicine to energy. In the latter case, aerosolized soot is the second largest forcing factor after carbon dioxide in climate change models and contributes significantly to asthma, bronchitis, and various other respiratory illnesses. The increased predominance of engineered nanoparticles also presents significant environmental and health risks due to various toxicological effects. In any of these cases, robust characterization is critical to the function and regulation of these nanoaerosols.

Time-resolved laser-induced incandescence (TiRe-LII) is well-suited to meeting this challenge. Since its inception in the 1980s, TiRe-LII has matured into a standard diagnostic for characterizing soot in combustion applications and, increasingly, engineered nanoparticles synthesized as an aerosol. The in situ nature of the technique makes it well-suited to probe in-flame soot formation and the fundamentals of nanoparticle formation. Moreover, its cost-effectiveness and real-time capabilities make TiRe-LII particularly well-suited as an avenue for online control of nanoparticle synthesis.

TiRe-LII involves heating nanoparticles within a sample volume of aerosol to incandescent temperatures using a short laser-pulse. Following the laser pulse, the nanoparticles return to the ambient gas temperature via conductive and evaporative cooling. The magnitude of the peak spectral incandescence signal can be used to derive the particle volume fraction, while the temperature decay of the nanoparticles can be used to infer thermophysical properties, including the nanoparticle size, thermal accommodation coefficient (TAC), and latent heat of vaporization. Data analysis requires the use of spectroscopic models, used to convert the observed incandescence to a volume fraction or nanoparticle temperature, and heat transfer models, used to model the changes in the nanoparticle temperature over the duration of a signal. These models have evolved considerably over the past two decades, increasing the interpretive power of TiRe-LII.

Nevertheless, there are several factors that impede further improvements to the reliability of TiRe-LII derived quantities. Several anomalies have been observed in measured signals collected from both engineered nanoparticle and soot, ranging from faster-than-expected temperature decays to inconsistencies in measurements between laboratories and experimental conditions. Resolving these differences is crucial to improving the robustness of TiRe-LII both as a combustion and engineered nanoparticle diagnostic. However, this first requires the development of advanced analysis tools that allow for a better understanding of nanoscale physics and the uncertainties associated with model development.

This thesis presents several advances in the modeling and interpretation of TiRe-LII signals. The current state-of-the-art in TiRe-LII models is first established and the process of model inversion is discussed, with particular reference to uncertainty quantification within the Bayesian perspective. This lays the foundation for analysis of the measurement errors associated with TiRe-LII signals, providing practitioners with another source of information to characterize measurement devices and fluctuations in observed processes. Next, a novel approach to describe the relationship between the peak nanoparticle temperature and the laser fluence is derived. This allows the first comparison of fluence curves obtained using different instrumentation and under different measurement conditions. This dissertation proceeds by examining inversion of the spectroscopic model to determine both the nanoparticle temperature decay and the factor that scales emission from the nanoparticles to the observed signal. Unexpected temporal effects in the latter quantity are examined as an additional source of information that TiRe-LII practitioners can use for nanoparticle characterization and for diagnosing problems with measurement devices. Molecular dynamics simulations are employed to calculate the thermal accommodation coefficient, a parameter fundamental to the heat transfer model used in interpreting the inferred nanoparticle temperature decay, using the results are used in an analysis of TiRe-LII collected from iron, silver, and molybdenum nanoparticles. The cross-comparison of these materials highlights the utility of the developed analysis tools and provides fundamental insights into both nanoscale physics and bulk thermophysical properties. This dissertation concludes with a critical discussion of model development, emphasizing the importance of complexity and uncertainty in model selection. This is particularly important in the context of the context of the increasingly divergent set of TiRe-LII models available in the literature, indicative of model tuning. In summary, this dissertation not only presents direct improvements to the spectroscopic and heat transfer models used in traditional TiRe-LII analysis but also presents a set of new approaches by which the remaining challenges in TiRe-LII analysis can be resolved.

Acknowledgements

The work contained in this thesis has been supported by many individuals, contributing everything from the background knowledge required for me to progress in my studies to the lending of experimental data that made the presented analysis possible.

First, thanks to my supervisor and mentor Kyle Daun, who has supported me in more ways than I can count over the duration of my tenure at the University of Waterloo. It is he who introduced me to the inner workings of the academic realm and whose anecdotes, while not always understood, made my tenure at the University of Waterloo considerably more stimulating. This is felt all the more due to the many happenings of these shared years.

I would also like to thank my fellow researchers and colleagues without whom completion of this degree would have been considerably less pleasant. To name just a few: Samuel Grauer, Nigel Singh, Paul Hadwin, Natalie Field, Roger Tsang, Jeff Labahn, Sina Talebi Moghaddam, Rodrigo Miguel, Mohit Verma, Kaihsiang Lin, Cory Yan, Kamalpreet Jhajj, Josh Rasera, Cangji Shi, and Jeff Hou.

Of special note, I would like to acknowledge the work of Nigel Singh whose many late nights performing experiments provided data critical to the analyses presented in this thesis. Your hard work was and still is appreciated. Additional thanks also go to Paul Hadwin whose statistical expertise was fundamental to many aspects of this work. Thank you for enduring my lack of understanding time and time again. I also owe much to Samuel Grauer: for the countless hours of discussion, for providing packets of creativity when it was required, and for being such a delightful flat mate. Your multi-faceted generosity has been greatly appreciated and remains an inspiration. Without your intellectual insights, I would not be the scholar I am today. I look forward to and hope for many more years of continued collaboration.

To the many others with whom I have shared time during the course of this degree (including Kathleen Laird, Carita Smith, Matt Thielke, Phi Hoang, Adam and Michelle Knowles, Steve VanDyk, and Karen Choi, among so many others such that a list of those individuals would be near impossible to compose), I thank you for

keeping me sane. Far from the least of which, I would like to thank my partner Solita Hoogendam for her continued support. Your joy and kindness have been both inspiring and encouraging, and I look forward to our continued adventures.

Thanks to Prof. Christof Schulz and many others at the Center for Nanointegration Duisburg-Essen (CENIDE) for the many fruitful discussions and guidance, particularly during my stay in Germany. I extend special thanks to Raphael Mansmann and Jan Menser for the many fruitful discussion that laid the foundation for ideas presented in this document. I further thank them for their continued friendship and support, without which my travels abroad, whether for research or conference attendance, would have been significantly less enjoyable. I owe much to you.

I would also like to thank Klaus Peter Geigle for useful discussions during my very short time spent there, for lending turbulent TiRe-LII data for analysis against the content of Chapter 4, and for your continued support of my academic ambitions.

I would also like extend thanks to the members of my examination committee, including Prof. Kyle Daun, Prof. Sean Peterson, Prof. Jean-Pierre Hickey, Prof. Cecile Devaud, Prof. Peter Levine, and Prof. Ömer Gülder. Your willingness to review and comment on this thesis is greatly appreciated.

I would also like to thank the Natural Science and Engineering Research Council (NSERC) of Canada and the University of Waterloo for granting me this opportunity by generously funding my research.

Finally, I would like to thank my family. I cherish your continued support and stability immensely.

To my parents,

Paul and Karen Sipkens

Table of contents

List of figures

List of tables

List of abbreviations

This section lists common abbreviations used in this work. It should be noted that the summarized abbreviations do not include those of the complementary diagnostics noted in Appendix A unless they receive explicit mention in the main text.

Abbreviation	Definition
BCC	Body-centered cubic
CARS	Coherent anti-Stokes Raman spectroscopy
CMC	Carboxymethylcellulose
DDA	Discrete dipole approximation
DLS	Dynamic light scattering
EAM	Embedded atom model
EDIP	Environment-dependent interatomic potential
FCC	Face-centered cubic
FS	Finnis-Sinclair potential
HRTEM	High-resolution transmission electron microscopy
ISF	Intensity scaling factor
LIF	Laser-induced flourescence
LII	Laser-induced incandescence
LCBOP	Long-range carbon bond-order potential
LJ	Lennard-Jones
LOSA	Line-of-sight attenuation
MAP	Maximum a posteriori estimate
MB	Maxwell-Boltzmann
MD	Molecular dynamics
MEAM	Modified embedded atom model

MLE	Maximum likelihood estimate
Nd:YAG	Neodymium-doped yttrium aluminum garnet
NVE	Number-volume-energy
NVT	Number-volume-temperature
PCA	Principle component analysis
PMT	Photomultiplier tube
pdf	Probability density function
QoI	Quantities-of-interest
RDG	Rayleigh-Debye-Gans, relating to the theory
RDG-FA	Rayleigh-Debye-Gans fractal-aggregate
SEM	Scanning electron microscope
SNR	Signal-to-noise ratio
SW	Stillinger-Weber
TAC	Thermal accommodation coefficient
TEM	Transmission electron microscopy
T2	Tersoff 2, referring to a specific parameterization of the Tersoff potential
T3	Tersoff 3, referring to a specific parameterization of the Tersoff potential
TiRe-LII	Time-resolved laser-induced incandescence
QoI	Quantities-of-interest

List of symbols

This section reviews the nomenclature used throughout this thesis. As this thesis draws from multiple bodies of literature, there are occasionally conflicts in the symbols used. In these cases, the "Section Restrictions" column indicates the scope of any given definition. In cases where a section is not given, the prescribed definition either applies to the entire thesis or all sections to which another definition does not apply. For cases of commonly used superscripts and subscripts, the general symbol is presented and an indication of the meaning of the subscript and superscript is supplied separately. Functions and operators are also listed in separate sections.

Latin characters

Symbol	Section Restrictions	Definition
a	7	Interatomic potential parameter, Morse potential, SW potential
A	-	Clausius-Clapeyron equation coefficient
A	7	Interatomic potential parameter, SW potential, Tersoff potential
$\mathbf{A}$	-	Linear operator
A_{ap}	-	Area of the aperture
A_g	-	Area of gas molecule
A_{lens}	-	Area of the lens
A_0	6	Pre-exponential factor, Arrhenius equation
b	7	Interatomic potential parameter, Tersoff potential
b_{ijk}	7	Interatomic potential parameter, bond strength modifier, bond-order potential
$\mathbf{b}$	-	Data vector, used for Bayes equation
B	7	Interatomic potential parameter, SW potential, Tersoff potential
B	9	Bayes factor
B_1, B_2, B_3	-	Fitting constants, fluence curve analysis
c	7	Interatomic potential parameter, Tersoff potential

c_g	-	Mean thermal speed of the gas
c_p	-	Specific heat capacity
$c_{p,0}$	9	Intercept for linear change in specific heat capacity
c_v	-	Mean thermal speed of the vapor
c_v	4	Coefficient of variation
C	-	Summary scaling factor for incandescence
C	9	Measurement credence
ΔC	9	Relative measurement credence
$C_{abs,\lambda}$	-	Spectral absorption cross section
C_1, C_2	-	Summary material constants, fluence curve analysis
d	7	Interatomic potential parameter, Tersoff potential
d_g	2.1	Diameter of gas molecule
d_p	-	Nanoparticle diameter
$d_{p,g}$	-	Geometric mean diameter
$d_{p,ut}$	6	Untransformed fraction
$d_{p,32}$	-	Sauter mean diameter
D	7	Interatomic potential parameter, potential well depth for Morse potential, Tersoff potential
D_n	-	Material constant, used in latent heat of vaporization expressions
e	-	Elementary charge
E	3, 8, 9	Evidence
E	7, 10, C	Energy
E_A	6	Activation energy, Arrhenius equation
E_i	7, C	Incident gas molecule energy
E_o	7, C	Scattered gas molecule energy
$E(\mathbf{m}_\lambda)$	-	Absorption function
$E(\mathbf{m})_r$	-	Absorption function ratio, across two wavelengths
f	-	Euken factor
f_V	-	Volume fraction
f_0	-	Temporal laser fluence profile
F	9	Fit

ΔF	9	Relative fit
F_0	-	Laser fluence
F_{ref}	-	Reference fluence, fluence curve analysis
$\mathbf{g}$	-	Gaussian random vector
G	-	Detector gain
h	-	Planck's constant
Δh_v	-	Specific latent heat of vaporization
ΔH_v	-	Molar latent heat of vaporization
$\mathbf{I}$	-	Identity matrix
$I_{b,\lambda}$	-	Spectral blackbody intensity
$\mathbf{J}$	-	Detector irradiation
$\bar{\mathbf{J}}$	-	Average detector irradiance (over multiple laser shots)
$\mathbb{J}$	-	Jacobian
k_B	-	Boltzmann's constant
k_g	-	Thermal conductivity of the gas
k_λ	-	Index of refraction, imaginary component
K		Watson's equation coefficient
Kn	-	Knudsen number
$\mathbf{L}$	-	Cholesky factorization of the inverse covariance, $\mathbf{L} = \text{chol}(\mathbf{\Sigma}^{-1})$
L_c	2	Characteristic length for mean free path calculations
m	-	Mass
m	7	Interatomic potential parameter, Tersoff potential
m_{FL}	9	Constant, Fish and Lielmezs equation
$\mathbf{m}_\lambda$	-	Complex index of refraction
M	2.1	Magnification
M	-	Molar mass
M_i, M_j	9	Model
n	-	Number density, can be molecular or electron
n	7	Interatomic potential parameter, Tersoff potential
n	9	Universal critical exponent, latent heat of vaporization
$\mathbf{n}$	4	Standard normal random vector

n_λ	-	Index of refraction, real component
N	-	Number of primary particles in an aggregate
N	7, C	Number of samples in Monte Carlo calculation of TAC
N''	-	Molecular number flux
p	-	Pressure
p	7	Interatomic potential parameter, SW potential
$\mathbf{p}$	-	Poisson random vector
p_{ref}	-	Reference pressure
q	7	Interatomic potential parameter, SW potential
q	9	Constant, Fish and Lielmezs equation
q_{abs}	-	Rate of laser absorption
q_{cond}	-	Rate of conductive heat transfer
q_{oth}	-	Rate of heat transfer due to other modes
q_{vap}	-	Rate of vaporization heat transfer
$Q_{abs,\lambda}$	-	Spectral absorption efficiency
r, r_{ij}	7	Interatomic distance
R	-	Universal gas constant
R	7	Interatomic potential parameter, Morse potential, SW potential, Tersoff potential
$\mathbf{R}$	9	Pearson correlation coefficient matrix
R_s	-	Specific gas constant, $R_s = R/M$
$\mathbf{s}$	-	Signal
$\tilde{\mathbf{s}}$	-	Single-shot signal
$\bar{\mathbf{s}}$	-	Average signal (over multiple laser shots)
Sk	-	Skew
t	-	Time
t_{lp}	-	Characteristic temporal width of the laser pulse
T	-	Temperature
T_{cr}	-	Critical temperature
T_m	-	Melting temperature
T_{peak}	-	Peak temperature

T_{ref}	-	Reference temperature, used independently in the Clausius-Clapeyron equation, latent heat of vaporization, and fluence curve analysis
$\tilde{T}$	-	Dimensionless temperature, in reference to the latent heat and renormalization group theory
u	-	Distance between the lens and probe volume
u	7	x-component of gas velocity
U_{ij}	7	Interatomic potential
U_R	7	Interatomic potential, attractive component
U_R	7	Interatomic potential, repulsive component
U_2	7	Pair interaction potential
U_3	7	Three-body contribution to interatomic potential
v	7	y-component of gas velocity
$\mathbf{v}$	-	Gas velocity
V	-	Volume of aerosol
w	7	Normal or z-component of gas velocity
x	-	Size parameter
$\mathbf{x}$	-	Quantities-of-interest (QoI)
X	-	Annealed fraction
Z	2	Measuring device impedance
Z	7	Coordination number
Z_c	9	Universal critical ratio, Meyra equation

Greek characters

Symbol	Section Restrictions	Definition
α	-	Thermal accommodation coefficient (TAC)
α_n	-	Normal TAC
α_t	-	Tangential TAC
β	-	Sticking coefficient, in regards to evaporation
β	7	Interatomic potential parameter, Tersoff potential
β_R	-	Román equation parameter
β_T	7	Inverse most probable speed of a gas molecule

χ	-	Used in describing the chi-squared distribution
δ	-	Tolman length
$\boldsymbol{\delta}$	4	Shot-to-shot error term
ε	7	Interatomic potential parameter, LJ potential well depth, SW potential
$\boldsymbol{\varepsilon}$	-	Electric permittivity
$\boldsymbol{\varepsilon}^{s}$	-	Signal error
$\boldsymbol{\varepsilon}^{x}$	-	Quantities-of-interest error
$\boldsymbol{\varepsilon}^{\theta}$	-	Nuisance parameters error
$\boldsymbol{\varepsilon}^{T}$	-	Temperature error
ε_0	-	Vacuum permittivity
ε_1	-	Component of dielectric function
ε_2	-	Component of dielectric function
$\boldsymbol{\phi}$	-	Combined quantities-of-interest and nuisance parameters
γ	-	Specific heat ratio, $\gamma = c_p/(c_p - R)$
γ	4	Standard deviation of Gaussian noise
γ	7	Interatomic potential parameter, SW potential
γ	7, C	Thermal accommodation coefficient, single scattering event
γ_s	-	Surface tension
η_λ	-	Calibration constant
φ	-	Equivalence ratio, pertaining to flames
ϕ	C	Angle between normal and tangential velocity components
Φ	-	Dimensionless fluence
Φ	7, C	Surface state
κ	9	Slope for linear change in specific heat capacity
λ	-	Wavelength
λ_g	-	Mean free path of the gas
λ_l	-	Laser wavelength
$\lambda_1, \lambda_2, \lambda_3$	7	Interatomic potential parameters, Tersoff potential
Λ	-	Intensity scaling factor (ISF)
μ	-	Mean, often of normal distribution
μ	-	Mass ratio, $\mu = m/m_s$

μ_g	-	Geometric mean
ν_g	-	Frequency of gas-nanoparticle collisions
π	-	Constant, 3.1415...
θ	2, 4	Amplification or scaling factor
θ	C	Angle between initial and scattered velocity in the tangential plane
$\boldsymbol{\theta}$	-	Nuisance parameters
θ_{ijk}	7	Three-body angle, interatomic potentials
θ_0	7	Interatomic potential parameter, SW equilibrium angle
Θ	-	Dimensionless temperature
Θ_λ	-	Spectral response of the detector
ρ	-	Density
ρ_j	7	Electron charge density, EAM potential
ρ_0, ρ_1	9	Linear density coefficients
σ	-	Standard deviation
σ	7	Interatomic potential parameter, LJ potential, SW potential
σ_{DC}	-	Direct current conductivity, Drude theory
σ_g	-	Geometric standard deviation, $\sigma_g = \ln(\sigma)$
σ_m	-	Maximum standard deviation
σ_t	-	Standard deviation of Gaussian temporal laser profile
$\boldsymbol{\Sigma}$	-	Covariance
τ	2	Plasma relaxation time, Drude theory
τ	4	Standard deviation of shot-to-shot error
τ	7	Temperature ratio, $\tau = T_g/T_s$
τ_λ	-	Spectral transmissivity of the optics
ω	-	Angular frequency of the electromagnetic field, Drude theory
ω_p	-	Plasma frequency
ω_b	-	Equivalent laser sheet thickness
ζ	2.1, 4	Photoelectric efficiency
ζ	-	Thermodynamic degrees of freedom
ζ	7	Interatomic potential parameter, Tersoff potential
ζ_{rot}	-	Rotational thermodynamic degrees of freedom

Operators and functions

Subscript	Definition
argmax(·)	Maximum
argmin(·)	Minimum
erf(·)	Error function
chol(·)	Cholesky factorization
cov(·)	Covariance
$\mathbb{E}(\cdot)$	Expected value
$f(\cdot)$	Velocity distribution
$f_c(\cdot)$	Cutoff function, for interatomic potentials
$F(\cdot)$	Embedding function, EAM potential
$g(\cdot)$	Miscellaneous functions used in fluence curve analysis, used in Chapter 5
$g(\theta)$	Interatomic potential function, angular dependence of potentials, exclusive to Chapter 7
$h(\cdot)$	Interatomic potential function for Tersoff potential, exclusive to SW potential in Chapter 7
$H(\cdot)$	Heaviside function
Im(·)	Imaginary component
$K(\cdot)$	Kernel
$L(\cdot)$	Loss function
$\ln\mathcal{N}(\cdot)$	Lognormal distribution
mean(·), $\langle\cdot\rangle$, $\bar{\cdot}$	Mean, average
$\mathcal{N}(\cdot)$	Normal distribution
$p(\cdot)$	Probability density function
var(·)	Variance
Weibull(·)	Weibull distribution
$W_{-1}(\cdot)$	Lower branch of the Lambert W function
$(\cdot)^{-1}$	Inverse
$\lvert\cdot\rvert$	Determinant

Common subscripts and superscripts

Subscript or superscript	Pertaining to
b (superscript)	Data
b (subscript)	Boiling point
bg	Background
c	Conduction subset of parameters
e	Electron
e	Evaporation subset of parameters, exclusive to Chapter 9
eff	Effective
flame	Flame
g	Gas
i	Incident, for scattering
LII,0	Nanoparticle contribution from the probe volume prior to the laser pulse
LSQ	Least-squares
MAP	Maximum a posteriori estimator
max	Maximum
MB	Maxwell-Boltzmann
meas	Measured
MLE	Maximum likelihood estimator
mod	Modeled
o	Scattered or outgoing, for scattering
p	Nanoparticle
po	Posterior
pr	Prior
r	Ratio
s	Surface
sim	Simulation
tr	Time response of detector
v	Vapor
x	Quantities of interest

λ	Spectral
0	Nominal or initial
2C	Two-color, related to ratio pyrometry

Chapter 1
Introduction

Aerosolized nanoparticles, which exist as the product of both industrial and natural processes, are an increasingly important area of science and technology with broad reaching implications. Iron nanoparticles exhibit unique magnetic properties that enable applications in magnetic storage devices and transformer cores [1]. They also have potential applications in water remediation, catalysis, and medicine, with specific functions including MRI contrast enhancement and hypothermia treatment. Silicon nanoparticles have potential medical applications, including in diagnostics, targeted drug delivery, cancer therapy, cell tracking and labelling, and tissue engineering [2]. Additionally, silicon nanoparticles have been shown to enhance the performance of electronic devices, including lithium-ion batteries [3], solid-state devices, light emitting diodes, printable electronics [4], and photovoltaics [5]. Silver nanoparticles are used extensively in creating antimicrobial surfaces, whether it be for medical devices or home appliances [6,7]. They have also seen use as biosensors, in catalysis, and have potential applications in optical data storage [8]. Other nanoparticles have found applications in cosmetics [9,10], optics [10–12], surface coatings [7,10], water purification [13–15], and medicine [16], among numerous other fields.

In many of these cases, gas-phase synthesis is one of the most economically feasible ways of scaling up engineered nanoparticle production to enable widespread advances in nanotechnology. Various techniques for gas-phase synthesis exist [17–20]. Iron nanoparticles, for example, have been synthesized using hot wall reactors [21,22], shock tubes [23], UV-laser photosynthesis [24], and chemical vapor condensation [25]. Aerosolized germanium and silicon nanoparticles have likewise been synthesized in the gas-phase by the thermal decomposition of germane and silane in plasma reactors [26,27]. Similar approaches have also been used to synthesize aerosolized silver and molybdenum nanoparticles. To improve the robustness of these techniques, it is important to develop diagnostics that can be used in the online control of synthesis conditions, thereby ensuring the desired properties of the nanoparticles over longer periods of time.

At the same time, nanoparticles can also have undesirable properties. The increased global production of engineered nanoparticles has brought to light several environmental concerns regarding how widespread use will impact the environment, with several studies examining the toxicological effects of inorganic nanoparticles (see [9,28–30] and references therein) and their effect on the environment [31–35]. Moreover, soot, which encompasses a broad spectrum of carbonaceous nanoparticles produced by combustion processes, is known to have significant implications on human health and the environment. Soot is the leading contributor to air pollution related health problems [36], with several studies noting that soot toxicity depends significantly on the primary nanoparticle size [37] and aggregate morphology [38]. Furthermore, it is established that the size of soot has a profound impact on combustion processes themselves [39,40], motivating diagnostics that can size in-flame soot. Poorly characterized optical properties [41,42] also make soot one of the largest uncertainties in climate change models. As such, proper control and regulation of nanoparticle emission is essential to managing environmental risks while making larger-scale nanoparticle production viable. This can only be accomplished if there first exists a suite of robust, economically-feasible diagnostics capable of characterizing these aerosols.

This thesis focuses on one such characterization technique for aerosolized nanoparticles that can be used in these applications: laser-induced incandescence (LII). LII is an optical nanoparticle diagnostic in which thermal radiation (or incandescence, for thermal radiation in the visible spectrum) is incited from aerosolized nanoparticles using a laser pulse. The current work focuses on pulsed LII, as opposed to continuous-wave LII as is discussed in Section A.1.6. The pulsed variant was originally developed as a combustion diagnostic and represents a mainstay for characterizing soot in flames. Within this context, the technique is most often used to determine soot volume fraction (SVF), or in the case of time-resolved laser-induced incandescence (TiRe-LII), soot primary particle size. While the temperature required to detect incandescence limits the range of materials that can be considered (e.g. polymers will vaporize at incandescent temperatures), LII has more recently been expanded to a wider set of materials, including metals [43–45], metal oxides [46,47], and elemental semiconductors [48,49]. Thus, although one would be remiss not to discuss LII within the context of combustion, specific note is made of those studies that extend LII beyond its combustion origins to characterize engineered nanoparticles. Moreover, this securely places LII at the intersection of nanotechnology, aerosol science, and combustion science, establishing its inherent interdisciplinary nature.

1.1 A note on complementary aerosol diagnostics

Laser-induced incandescence is only one of numerous diagnostics that exist for nanoparticle characterization. Accordingly, a thorough overview of the competing aerosol and combustion diagnostics is provided in Appendix A. Focus is placed on those studies that are often used to complement LII measurements, with particular note made of those studies in Table A.1 and Table A.2. The techniques are broadly categorized into *ex situ* and *in situ* techniques, where, here, this distinction indicates whether or not the technique can be used on the aerosol in place (in situ) or must be placed downstream or following a sampling procedure (ex situ). Such a definition is less common in aerosol science (where in situ is often made to include online or real time devices that are placed downstream of the process generating the aerosol) but is very useful in combustion where in situ techniques have the ability to probe the reaction field directly. The appendix also makes note of several diagnostics for characterizing the gas-phase of the aerosol which are used to complement LII measurements in this thesis, including coherent anti-Stokes Raman spectroscopy (CARS) and heated line-of-sight (HLOSA).

LII offers several unique benefits over the alternative diagnostics discussed in Appendix A. The technique has the advantage of being an in situ diagnostic and can be used to characterize nanoparticles during synthesis or reactions. This fact is often exploited by LII practitioners to derive two-dimensional spatial distributions of soot characteristics during combustion (e.g. [50–56]). Further, like many other in situ diagnostics, LII can often be applied in real time, facilitating a route towards cost-effective online control of nanoparticle synthesis. Furthermore, this approach can provide critical information regarding nanoparticle formation that is not possible through ex situ techniques. Other in situ diagnostics, such as extinction measurements described in Section A.2.1 or the two-color method described in Section A.2.3, are also often limited in that they are line-of-sight (LOS) techniques. Such techniques thus include contributions from everything along a path through the aerosol, making it challenging to localize effects. As LII itself uses a laser pulse to heat nanoparticles in the flame to elevated temperatures, emission is localized to the laser-affected region of the process. The increased amount of thermal radiation emitted by the nanoparticles also provides an improved signal-to-noise ratio against the traditional two-color method.

1.2 A brief history of pulsed laser-induced incandescence (LII)

LII itself was first established as a potential particle sizing technique, mostly within the context of interference with Raman scattering signals. In 1974, Weeks and Duley [57] first presented time-resolved signals of light emission following laser-irradiation of carbon black and alumina powders. They presented a simple energy

balance that they used to obtain an analytical expression of nanoparticle cooling, noting qualitative agreement between this expressions and experimental signals. In 1977, Eckbreth [58] noted incandescence signals in pulsed Raman scattering experiments, which was called laser-modulated incandescence (LMI) at the time. Eckbreth advanced upon the previous heat transfer analysis, particularly expanding upon the vaporization model. This work also laid the basis for the fluence curves that are now superfluous in the literature and the focus of Chapter 5. Melton [59] later developed the first established spectroscopic and heat transfer models used more widely to determine nanoparticle size. Although the model was simplistic, it showed the feasibility of the TiRe-LII technique for quantifying nanoparticle properties. Dasch [60] continued to develop the vaporization model for soot, albeit within the context of CW-LII. Nevertheless, the study still proved useful within the context of developing heat transfer models for pulsed LII. Dasch also noted a *threshold* fluence at which cooling switches from being dominated by conduction to vaporization, which remains important to fluence curve modeling today. The observations of Eckbreth and Melton were later used by Rohlfing [61], who measured thermal radiation from laser-excited carbon clusters.

1.2.1 Developments in the 1990s

Development of the technique progressed rapidly through the 1990s. A vast majority of the developments in this decade were focused on the spatial distributions of soot in a variety of combustion environments and the cross-contamination of LII, LIF, and elastic scattering signals. A summary of these studies is provided in Table 1.1. The earliest works examined the two-dimensional spatial distribution of soot in diesel engines, using a laser sheet at 532 nm to incite LII from soot and placing a camera perpendicular to the laser sheer [62–64]. Other studies expanded the technique to consider laminar (e.g. [51,65,66]) and turbulent flames (e.g. [67,68]).

Many of the early studies also featured spectral measurements, aimed to determine if and when LII signals are corrupted by or are corrupting other signals. Cignoli et al. [66], for example, examined the emission spectrum from a flame following excitation with a 266 nm Nd:YAG laser. During the laser pulse, fluorescence and scattering lines were clearly visible in the emission spectra. However, they also noted that these phenomena stopped corrupting the signal as soon as 20 ns after the laser pulse. Accordingly, the authors proposed LII as a robust 2D imaging tool for cases where multiple emission phenomenon may be convolved simply by examining a signal delayed sufficiently after the laser pulse. Vander Wal and Weiland [51] also examined the spectral emission from laser-excited soot, this time at excitation wavelengths of 532 nm and 1064 nm. The spectral results revealed many of the same characteristics noted by Cignoli and coworkers, namely LIF from the C_2 swan bands

Table 1.1 Summary of LII studies in the literature from the 1990s that focus on determining the soot volume fraction. Occasionally the papers were difficult to access resulting in some omissions. In some cases, studies with a similar experimental setup or line of investigation are grouped. Note that λ_l is the laser wavelength used for excitation.

Study	Year	Process investigated	Fuels	λ_l [nm]
zur Loye et al. [62]	1990	Engine cylinder	Diesel	532
Dec et al. [63]	1991	Engine cylinder	Diesel	532
Pinson et al. [64]	1993	Engine cylinder	Diesel	-
Tait and Greenhalgh [67][2]	1993	Turbulent jet flame	Propane	308, 1064
Quay et al. [65][2]	1994	Co-flow laminar diffusion flame	Ethylene	532, 1064
Cignoli et al. [70][1]	1994	Co-flow laminar diffusion flame	Propane	266
Vander Wal and Weiland [51][1,2]	1994	Co-flow laminar diffusion flame, Flat laminar premixed flame	Ethylene	532, 1064
Shaddix et al. [71], Shaddix and Smyth [72][2]	1994, 1996	Flickering co-flow laminar flame	Methane, Ethylene	560
Ni et al. [50][2]	1995	Co-flow laminar diffusion flame	Ethene	532
Bengtsson and Alden [73][1]	1995	Flat laminar premixed flame	Ethene	532
Vander Wal and Dietrich [74]	1995	Droplet flame	Decane	1064
Vander Wal [43]	1996	Co-flow laminar diffusion flame	Ethylene	1064
Vander Wal et al. [68,75]	1996	Turbulent jet diffusion flame	Ethylene	266, 1064
Appel et al. [69] [1]	1996	Flat laminar premixed flame	Acetylene	532
Case and Hofeldt [76][2]	1996	Engine exhaust	Diesel	532
Vander Wal [77,78], Vander Wal et al. [79] [1]	1996-1998	Transitory droplet diffusion flame, Inverse diffusion flame	Ethylene	266, 1064
Mewes and Seitzman [80]	1997	-	-	532, 1064
Snelling et al. [56,81]	1997, 1999	Co-flow laminar diffusion flame	Ethylene	1064
Choi and Jensen[82]	1998	-	-	-
McManus et al. [83][2]	1998	Co-flow laminar diffusion flame	Ethylene	532
Vander Wal et al. [84,85][2]	1998, 1999	Jet diffusion flame, Flat laminar premixed flame	Ethylene, Acetylene	532, 1064
Snelling et al. [86]	1999	Engine exhaust	Diesel	1064

[1] Studies include spectral measurements.
[2] Studies include fluence curves.

and scattering lines on top of the incandescence. For the 532 nm excitement, the elastic scattering signal from soot in the flame was also clearly visible. Appel et al. [69] also made spectral measurements at various heights-above-burner (HAB) over a flat flame burner and at times sufficiently delayed after the pulse to avoid other forms of emission.

Other studies expanded on Eckbreth's [58] analysis by considering the effects of increasing the laser fluence on the LII signal. Tait and Greenhalgh [67] noted that they expected the LII signal should decrease beyond some fluence, a consequence of mass loss reducing the volume fraction of soot in the flame. However, with a limited number of experimental measurements, they observed no such decline. They attributed this to the increasing spatial width of the laser sheet with increasing fluence that excites a progressively larger amount of soot in the flame. Subsequent studies are divided on whether there exists a slow increase [65,72] or a decline [50,51,76,83,84] in the LII signal in this *saturation* or *plateau* regime. Notably, Shaddix and Smyth [72] collected large amounts of data in attempts to create a robust fluence curve for a flickering methane flame, using gate widths of both 19 and 85 ns. They also extending the range of fluences well above those used in the other studies, specifically 10 J/cm^2. They noted a nearly identical trend in the data for both gate times and fuels. Also notable, McManus et al. [83] presented an analysis of the change in the temporal decay of the LII signals over a range of laser fluences that is comparable to those observations made in Chapter 5.

This decade also saw the first significant advances in measuring nanoparticle size from TiRe-LII signals. Will et al. [87] extended the 2D approach of soot characterization to determine the spatial distribution of nanoparticle sizes in a laminar ethene–air diffusion. Will and coworkers later expanded their analysis to further examine the 2D distribution of nanoparticle sizes, including adding simultaneous inference of SVF [88], an early uncertainty analysis [89], and measurements inside a diesel engine [90]. Roth and Filippov [91] presented the first analysis of TiRe-LII signals to derive a nanoparticle size distribution. They note how this inversion problem takes on the form of a Fredholm integral equation of the first kind (IFK) and attempted to solve the problem using an iterative algorithm using both simulated and experimental data. Geitlinger and coworkers [92,93] combined elastic scattering and LII in the RAYLIX system (discussed in Appendix A) to calculate SVF and mean nanoparticle size in both laminar and turbulent flames. The latter study [93] includes a statistical analysis of the temporal variation in quantities for turbulent flames.

The end of the 1990s also saw the use of LII on non-carbonaceous, engineered nanoparticles. Vander Wal [94] made some of the first LII measurements of this kind, examining tungsten, iron, molybdenum, and titanium nanoparticles. While they did not infer nanoparticle sizes from the LII data, the observed laser emission that decayed after the pulse and suggested that sizing would be possible if nanoparticle cooling could be modeled accurately. Around the same time, Filippov et al. [44] extended their previous analysis on soot [91] to investigate

laser-induced emission from carbon, silver, and titanium nitride powders, further widening the range of materials considered.

Oher notable advancement in the field during this decade include the introduction of new heat transfer models, such as those by Hofeldt [76,95], Will et al. [87–89], Roth and Filippov [91], and McManus et al. [83] (who included a thermionic term); the application of Abel inversion to LII [81]; the transmission electron microscopy (TEM) studies by Vander Wal and co-workers [68,77–79,84,85]; the combined two-pulse and high-resolution TEM (HRTEM) experiments by Vander Wal et al. [84]; and the complementary coherent anti-Stoke Raman spectroscopy (CARS) work for thermometry by Snelling et al. [56].

1.2.2 Developments in recent years

By the 2000s, LII had become a mainstream diagnostic for SVF measurement and saw an expansion into a wider area of application beyond what can be reviewed here. A review of the advancements up until 2007 is provided by Schulz et al. [96] and up until 2015 is provided by Michelsen et al. [97]. The 2000s marked a distinct shift in application of the diagnostic as it moved from being prominently an approach for SVF measurement to also being a time-resolved nanoparticle sizing technique. Accordingly, a significant amount of the progress in this time period was made in developing and applying improved heat transfer models to be used for nanoparticle sizing and thermophysical property determination. Many of the models developed in the early 2000s are summarized in comparative studies by Schulz et al. [96] and Michelsen et al. [98]. Significant new models include those of Bladh and Bengtsson [99], Smallwood et al. [100], Lehre et al. [101], Starke et al. [23,44,91], Schittkowski et al. [102], Kock et al. [21,103], and Michelsen et al. [104,105]. Notable advances include the development of annealing and oxidation submodels by Michelsen [104]; several analyses of the thermal accommodation coefficient, which is the focus of Chapter 7 [106–112]; investigation of the effect of aggregation [111,113–120]; and consideration of the influence of the soot absorption function [110,111,121,122]. Such models were also shown to be able to infer the vaporization parameters for soot [123]. Some discussion of the available models in LII literature is provided in Chapter 2.

The first decade of the 2000s also saw the application of LII to an extended range of engineered nanoparticles, a summary table of which is included in Appendix B. These studies include examination of Fe [21,23,24], Mo [124], Si [125,126], MnO [127], TiO_2 [70,128], and SiO_2 [46] nanoparticles. The prominence of metal oxide studies stems from interest in flame synthesis techniques and its relation to combustion. Beyond the metal oxides, work is dominated by studies investigating iron nanoparticles, which has, in some regard, become a reference system

for engineered nanoparticles. In general, observations made on these engineered nanoparticles provide both new challenges and advantages over soot measurements. Although requiring the development of new and occasionally more advanced models, often the uncertainties in the properties of these alternative materials are lower than soot, making inference more robust. Through the 2010s, LII analyses have been further applied to Ag [45], Fe [45,129,130], Mo [45,131,132], Ni [133], Fe_2O_3 [134], Si [48,49], Ge [135], and Cu [136]. Studies are trending away from the metal oxides, with only one study so far in the current decade. This is likely a consequence of complexities in modeling the heat transfer from these particles. Iron remains a prominent material of study, resulting in it forming a significant basis for the work in Chapter 8 and Chapter 9. Moreover, the comparative analysis of multiple metals in Chapter 8 represents the first comparative analysis since the study on carbon, silver, and titanium nitride by Filippov et al. [44] in 1999. With advancements in the field, such a comparative study is quite advantageous, providing additional information on the limitations and anomalies that exist in TiRe-LII analyses.

During this time, there have also been several other unique instances of LII analyses. Comparative studies featuring cross-examination of LII against broader range of emissions measuring techniques, like scanning mobility particle sizers (SMPS) [137–139], became more prevalent. Several groups advanced the understanding of LII analyses in high pressure environments, including work by Hofmann et al. [140] and Geigle and coworkers [141–143], and under high vacuum conditions [144]. Hult et al. [53] used a sweeping laser sheet to report 3D distributions of SVF in both laminar and turbulent flames. Snelling et al. [145,146] developed a calibration free LII measurement technique for determining SVF using incandescence measured at two wavelengths, the use of which has become common in the literature. Michelsen [147] also investigated LII induced using a picosecond laser pulse.

1.3 Overview of contents

This document outlines advances upon this narrative, presenting tools that can be applied to answer remaining questions in TiRe-LII modeling and data analysis. This incorporates new methods stretching from the analysis of measurement errors in TiRe-LII signals to determining fundamental nanoparticle properties using established or novel heat transfer models. The structure of the document steps through a novel approach of analyzing TiRe-LII signals that aims to extract the most information possible from TiRe-LII signals. In this regard, the goal of the thesis is to provide tools that facilitate interlaboratory comparison, to develop TiRe-LII as

a tool for fundamental scientific inquiry, and to establish methods that can be used to answer remaining questions in the field.

The thesis begins in Chapter 2 by providing an overview of the basic form of TiRe-LII models that have been developed over the years and serves as the basis for the analyses presented in the remainder of the work. This includes a discussion of the spectroscopic and heat transfer models of nanoparticle absorption, emission, heating, and cooling. Chapter 3 builds on this foundation by providing the necessary background for inverting these models to acquire quantities-of-interest (QoI) from the data. This includes an introduction to the Bayesian framework, which forms the basis for several of the statistical analyses used throughout this work. As such, Chapter 3 continues with an overview of random variables and Bayes equation.

The remaining chapters proceed with the analysis of TiRe-LII signals, progressing in each chapter forward through what could be considered a novel approach to analysis. In this way, Chapter 4 starts by discussing the information that can be extracted from measurement noise in the raw incandescence signals, improving upon the current measurement error model and demonstrating how measurement errors can be used to diagnose the experimental apparatus and the observed process.

Chapter 5 progresses with a discussion of fluence curves, a tool often used by practitioners as an initial gauge of their apparatus. Fluence curves follow the increase in the peak temperature of the nanoparticles or emitted incandescence with increasing laser fluence. Here, a simple, novel method of defining fluence regimes is presented. This provides practitioners with a tool to create non-dimensional curves that allow for the first ever interlaboratory comparison of fluence curves. The method simplifies the heat transfer model to only consider absorption and evaporation, the balance of which creates the expected fluence curve characteristics.

Chapter 6 examines inversion of the spectroscopic model, which is used to define the nanoparticle temperature and intensity scaling factor (ISF) from the data. In this chapter, the ISF is formally defined, and a method of interpreting the temporal changes in this parameter is presented. The chapter concludes by briefly noting how this information can be used to reduce uncertainties in the pyrometrically-inferred temperature decay that is traditionally used for nanoparticle sizing and identify anomalies in the measured TiRe-LII.

Chapter 7 moves towards an analysis of the nanoparticle temperature decay, focusing on quantifying the thermal accommodation coefficient (TAC), which is one of the leading sources of uncertainty in the heat transfer model. The chapter aims to decrease uncertainties in TiRe-LII analyses by quantifying this parameter independent of TiRe-LII measurements using molecular dynamics (MD). The chapter specifically presents new

MD simulations that examine the uncertainties introduced into the TAC by varying the surface potential parameterization used to simulate the nanoparticle surface. The results indicate that significant changes occur in the TAC about phase changes, with particularly large changes about the melting point that correspond to increases in tangential accommodation. Moreover, within a specific phase, the TAC is observed to change very little with surface temperature, a fact that is both useful to TiRe-LII inference and informative to the underlying physics.

Chapter 8 moves to a more traditional inference in which nanoparticle characteristics are determined from the decay in nanoparticle temperature. The chapter describes the application of the experimental technique developed by Sipkens et al. [112] to do a comparative study of engineered metal nanoparticles, including analysis of laser-induced emission from iron, silver, and molybdenum nanoparticles. The results demonstrate the abilities and limitations of TiRe-LII analyses on engineered nanoparticles, all while incorporating a Bayesian perspective for robust uncertainty quantification. Moreover, several of the novel approaches identified in the previous chapters, including calculation of the ISF, are used in the analysis. The work has several implications, including identifying cases in which the TAC and nanoparticle diameter cannot be independently estimated from TiRe-LII data and notes regarding how the observed laser-induced emission from silver may not be incandescence.

Chapter 9 finally presents Bayesian model selection as a method for characterizing the optimal model to be used in interpreting TiRe-LII data. Such a method has the potential to perform two significant tasks in the context of TiRe-LII. First, it demonstrates how TiRe-LII can be used not only to identify the optimal quantities-of-interest for a given model, but also to identify the most practical model for predicting the thermophysical properties of a material. This establishes TiRe-LII as a method not only for determining the nanoparticle size but also the fundamental characteristics of materials. Second, it serves the important role of moderator in settling disputes between the increasingly diverse set of models being developed by TiRe-LII practitioners. While not applied to soot in the present work, the demonstration of the technique here could have particularly large impact in the context of soot where the models are become increasing complex and are often tuned to data sets from specific laboratories.

Chapter 10 concludes this work, summarizing the findings of this thesis and identifying areas of future work. The most prominent future directions include: a push towards interlaboratory comparison using the developed suite of LII-based tools; investigation of laser-induced emission from silver as an avenue for future

nanoparticle characterization; the application of the presented MD technique to characterize the TAC for amorphous and graphitic soot; and finally the application of the Bayesian model selection technique to address dissention in the literature regarding the model to interpret TiRe-LII from soot [98].

Chapter 2
The basic TiRe-LII model

The basic TiRe-LII model is composed of two primary components: (i) a spectroscopic model, which relates the irradiation of the detector to incandescence from the nanoparticles, and (ii) a heat transfer model, governing the heating and cooling of the nanoparticle. The current chapter discusses the basic form of these submodels that is ubiquitous in the literature and provides the necessary background to understand the variants of these submodels that are employed throughout the remainder of this thesis.

2.1 Spectroscopic model and aerosol emission

The spectroscopic model simulates incandescent emission from the aerosol, which is here built up from emission from a single nanoparticle to the overall emission by the aerosol.

2.1.1 The interaction of light with a single nanoparticle

The light emitted from a single nanoparticle at some temperature, $T_{\mathrm{p,i}}$ and wavelength λ is given by [148]

$$J_{\lambda,\mathrm{i}}^{\mathrm{sp}} = C_{\mathrm{abs},\lambda}\left(d_{\mathrm{p}}\right) I_{\mathrm{b},\lambda}\left[T_{\mathrm{p,i}}\left(d_{\mathrm{p}}\right)\right] = \frac{\pi d_{\mathrm{p}}^2}{4} Q_{\mathrm{abs},\lambda}\left(d_{\mathrm{p}}\right) I_{\mathrm{b},\lambda}\left[T_{\mathrm{p,i}}\left(d_{\mathrm{p}}\right)\right], \tag{2.1}$$

where $C_{\mathrm{abs},\lambda}$ is the wavelength and size-dependent absorption cross section of the nanoparticle; $Q_{\mathrm{abs},\lambda}$ is the absorption efficiency, defined as the ratio of the optical to the geometric cross section,

$$Q_{\mathrm{abs},\lambda} = \frac{C_{\mathrm{abs},\lambda}\left(d_{\mathrm{p}}\right)}{\pi d_{\mathrm{p}}^2 / 4}; \tag{2.2}$$

and $I_{\mathrm{b},\lambda}$ is Planck's law for blackbody intensity. The blackbody intensity is given by Planck's Law

$$I_{\mathrm{b},\lambda}\left[T_{\mathrm{p,i}}\left(d_{\mathrm{p}}\right)\right] = \frac{2hc^2}{\lambda^5}\left[\exp\left(\frac{hc}{\lambda k_{\mathrm{B}} T_{\mathrm{p,i}}\left(d_{\mathrm{p}}\right)}\right) - 1\right]^{-1}, \tag{2.3}$$

where $I_{\mathrm{b},\lambda}$ is in units of W/(m^3·sr), h is Planck's constant, c is the speed of light in a vacuum, k_{B} is Boltzmann's constant, $T_{\mathrm{p,i}}$ is the nanoparticle temperature at the i^{th} time, and d_{p} is the nanoparticle diameter. It is worth noting

that $I_{b,\lambda}$ is an implicit function of both the nanoparticle diameter and time through the nanoparticle temperature, which forms the basis for the embedded heat transfer model discussed in Section 2.2. It is important that this expression not be defined with respect to an emissivity (which is often done erroneously in the literature, e.g. [97,104]), as the emissivity loses its physical meaning for nanoparticles where the quantity can take on values greater than unity.

The interaction of light with small spherical nanoparticles is most generally described by Mie's solution to the Maxwell equations [148,149], the details of which lie beyond the scope of this thesis. For the sake of this work it is simply noted that the analytical solution is phrased in terms of an infinite sum of Bessel functions. Accordingly, evaluating the scattering, extinction, and absorption cross sections of the nanoparticle using Mie theory is performed numerically by truncating the higher order terms in the infinite sum. Figure 2.1a shows the trends in $Q_{abs,\lambda}$ predicted by Mie theory for iron and soot with nanoparticle size, using the code from Ref. [150]. It is noted that regimes for absorption can be specified based on the common characteristics observed in these curves, which are defined based on the dimensionless quantity $x \cdot |\mathbf{m}_\lambda|$, where $x = \pi d_p/\lambda$ is the size parameter and $\mathbf{m}_\lambda = n_\lambda + k_\lambda \cdot i$ is the complex index of refraction with $i = (-1)^{1/2}$. For cases where $x \cdot |\mathbf{m}_\lambda| \gg 1$, absorption is said to occur in the geometric regime. In this regime, the interaction of light with the nanoparticle can be calculated by tracing rays that refract and reflect at the nanoparticle surface (cf. [151,152]). This case is not of interest in this work as the nanoparticles are never large enough that such an approach is reasonable.

In the lower limit, where the nanoparticle size is sufficiently smaller than the wavelength of light, that is satisfying the phase shift parameter criterion, $x \cdot |\mathbf{m}_\lambda| \ll 1$, and the size parameter criterion, $x \ll 1$ [151,153], Mie theory can be approximated using the Rayleigh approximation. In this simplified case, the absorption efficiency and cross section are shown to asymptotically approach [151]

$$Q_{abs,\lambda} = 4x \cdot E(\mathbf{m}_\lambda) \text{ and } C_{abs,\lambda}(d_p) = \frac{\pi^2 d_p^3}{\lambda} E(\mathbf{m}_\lambda), \tag{2.4}$$

where

$$E(\mathbf{m}_\lambda) = \mathrm{Im}\left(\frac{\mathbf{m}_\lambda^2 + 2}{\mathbf{m}_\lambda^2 + 2}\right) \tag{2.5}$$

is the absorption function. This expression is also included in Figure 2.1a, corresponding to a linear increase with x or d_p. Figure 2.1b also shows the absorption efficiency predicted by Mie theory normalized by the Rayleigh approximation. Visualizing the trends with nanoparticle size in this way reinforces the regimes and identifies

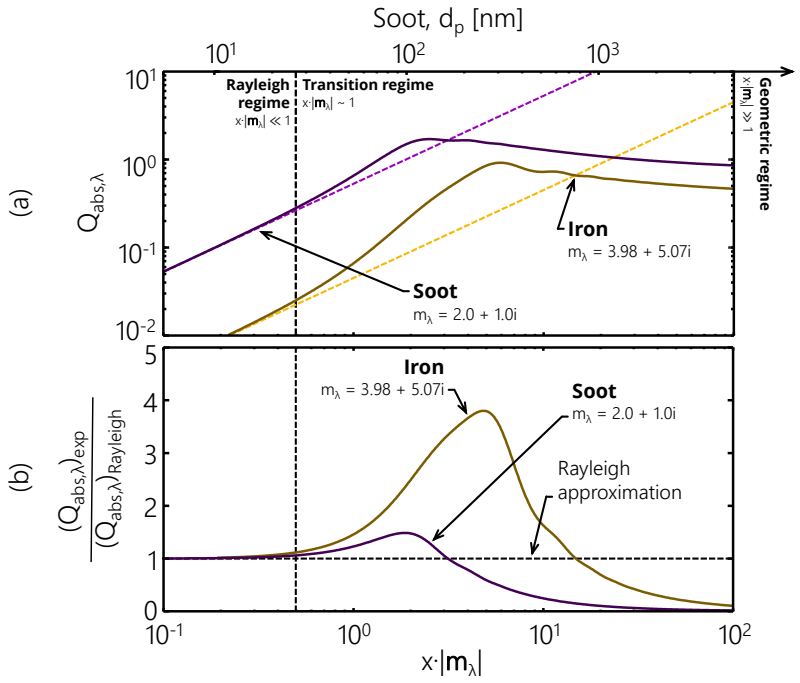

Figure 2.1 Trends in the (a) absorption efficiency and (b) absorption efficiency normalized by the Rayleigh approximation with nanoparticle size for iron and soot for a wavelength of 1064 nm. Solid lines correspond to the Mie solution calculated from the code associated with Ref. [150], and dashed lines correspond to the Rayleigh apprxoimation. The complex index of refraction corresponds to Jenzen [154] in Bond and Bergstrom [41], which corresponds to $E(\mathbf{m}_\lambda) = 0.29$. The complex index of refraction for iron corresponds to Krishnan et al. [155].

that the relative error induced by using the Rayleigh approximation is more significant for iron than for soot. Such a plot also shows similar trends as those observed Figure 8.6, which has consequences noted there. The Rayleigh assumption is valid in many instances of TiRe-LII analysis, in particular for the cases of soot primary particles where its validity extends up to ~50 nm. For this reason, the Rayleigh approximation is adopted nearly universally throughout this work under the premise that $x\cdot|\mathbf{m}_\lambda|$ is small. It is noted in Chapter 8, however, that this approach is often not valid for emission from metal nanoparticles, resulting in anomalies that are reported in that chapter.

Having selected a method of calculating the absorption cross section, the task of determining the absorption by the nanoparticle reduces to that of determining the complex index of refraction. In the case of soot, large discrepancies exist in the literature [41,42,156]. This thesis does not seek to resolve these differences but notes that practitioners are continually seeking to improve our understanding of these properties and how their uncertainties propagate through TiRe-LII models [156,157]. In select cases, dispersion theory can be employed to

predict the spectral dependence of the optical properties. Drude theory is one such theory, which is predicated on the idea that electrons move ballistically between positive ions or neutrals in the material, shown schematically in Figure 2.2. When an external electromagnetic field is applied, the motion of the electrons becomes coupled with the field. Electron scattering from ions or neutrals in the material then results in an increase in the thermal excitation of the material. Mathematically, the theory amounts to defining the dielectric functions of a material, ε_1 and ε_2, as

$$\varepsilon_1 = n_\lambda^2 - k_\lambda^2 = 1 - \frac{\omega_p^2 \tau}{1+\omega^2\tau^2} \tag{2.6}$$

and

$$\varepsilon_2 = 2 n_\lambda k_\lambda = \frac{\omega_p^2 \tau}{\omega\left(1+\omega^2\tau^2\right)}, \tag{2.7}$$

where $\omega = 2\pi c_0/\lambda$ is the angular frequency of the electromagnetic field and ω_p and τ are the plasma frequency and relaxation time, which are characteristic of the material. The plasma frequency and relaxation time can be further written in terms of the effective number density of electrons per unit volume and the direct current conductivity. More information on this theory is provided in Bohren and Huffman [151]. The principles underlying this theory are well suited to some liquid metals and metalloids, including silver, silicon, and germanium, which have large quantities of valence electrons. As such, Drude theory has been used in TiRe-LII analyses by Menser et al. for silicon [49] and germanium [135] nanoparticles and the silver nanoparticles examined in Chapter 8.

The problem of determining the optical properties can be complicated by nanoparticle annealing or temperature-dependencies. For instance, it is generally accepted that soot undergoes an annealing process during laser-heating where soot transforms from an amorphous carbon to an onion-layered graphitic structure (which is shown in high-resolution TEM images reproduced from Ref. [85] in Figure A.1d in Appendix A). This is expected to have consequences on the optical properties of the soot [104], a principle further affirmed by heated LOSA measurements by Saffaripour et al. [158]. Unfortunately, the current models predicting changes to the optical properties are imprecise or do not match experimental results and represent an important uncertainty in TiRe-LII analyses. It is possible that the intensity scaling factor analysis presented in Chapter 6 could aid in reducing these uncertainties, though further work is required to refine the technique for use as such.

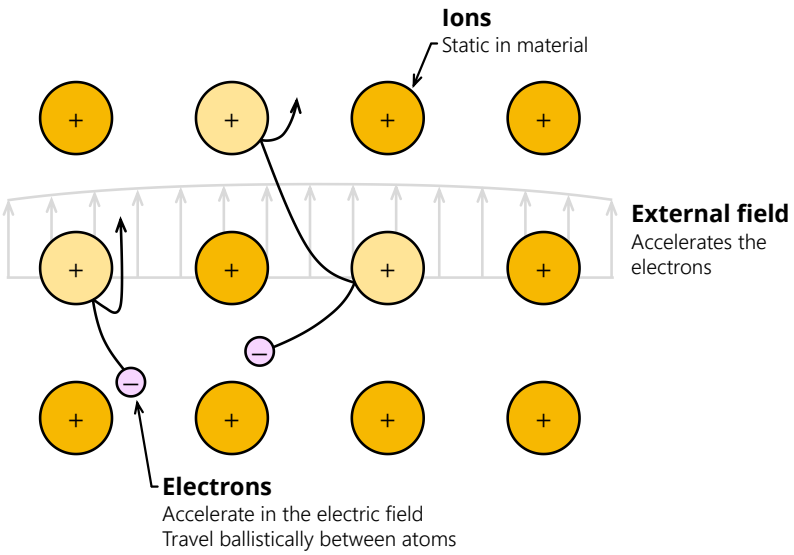

Figure 2.2 Schematic of the Drude model and the effect of an external electromagnetic field, which accelerates the electrons which scattering from ions in the material according to the frequency of the applied field.

2.1.2 The interaction of light with an aggregate

Soot and other nanoparticles often occur in aggregates rather than as single particles, such as those shown in SEM and TEM images in Figure A.1 in Appendix A. Aggregates require generalized methods for solving Maxwell's equations for non-spherical objects, numerous methods for which exist [153,159,160]. The T-matrix method [161,162], for example, is a surface-based method that provides a solution for an arbitrarily shaped particle. However, the technique requires an integral over the particle surface which can be computationally intensive within the context of most LII modeling. Alternatively, the discrete dipole approximation (DDA) [163,164] calculates the absorption or scattering properties of an arbitrarily shaped particle by segregating the domain into a series of dipoles that interact with one another and the incident wave. Calculations proceed numerically. Unfortunately, DDA suffers from many of the same limitations as the T-matrix method, particularly in that it can be computationally demanding.

In LII analyses, it is common to adopt the Rayleigh-Debye-Gans (RDG) approximation [165]. This approximation applies when two conditions are met:

$$\left|\mathbf{m}_\lambda - 1\right| \ll 1 \text{ and } 2x\left|\mathbf{m}_\lambda - 1\right| \ll 1 . \tag{2.8}$$

The former of condition can be said to imply that the electromagnetic field inside a spherical particle is identical to the incident field or, identically, that the incident light does not reflect at the nanoparticle surface. The latter condition amounts to no significant change in the phase and amplitude of the light inside the arbitrarily shaped particle. It is notable that the conditions under which the RDG approximation is valid differ from those under which the Rayleigh approximation is valid, which indicates that RDG is valid for a different range of nanoparticle sizes. For RDG theory, a particle of arbitrary shape can be represented by a series of infinitesimal spheres, which are, by definition, Rayleigh scatterers. The total scattering or absorption by the object can then be calculated by integrating over all of these infinitesimal spheres in an arbitrary geometry (occasionally even allowing an analytical solution [165]). The theory has seen various applications, first for solid spheres [153,166], followed by non-spherical particles [167,168], fractal aggregates [169–172], and biological particles [173,174]. The variant for fractal aggregates, denoted RDG-FA, adopts the natural interpretation of using the primary particles in a fractal aggregate as the Rayleigh scatterers in RDG. The approximation is sufficient to state that the primary particles in the aggregate absorb independently [153] (although this does not equally hold for the scattering cross section of the aggregate, for which other expressions are available [42,153,169,171]). In this case, the absorption cross section of the aggregate can be stated rather simply as

$$C_{\mathrm{abs},\lambda}^{\mathrm{agg}}\left(d_{\mathrm{p}}\right)=N\frac{\pi^2 d_{\mathrm{p}}^3}{\lambda}E\left(\mathbf{m}_{\lambda}\right)=NC_{\mathrm{abs},\lambda}\left(d_{\mathrm{p}}\right), \tag{2.9}$$

where N is the number of primary particles in the aggregate. The expression for the incandescence from the aggregate then becomes

$$J_{\lambda,\mathrm{i}}^{\mathrm{agg}}=N\frac{\pi^2 d_{\mathrm{p}}^3}{\lambda}E\left(\mathbf{m}_{\lambda}\right)I_{\mathrm{b},\lambda}\left[T_{\mathrm{p,i}}\left(d_{\mathrm{p}}\right)\right]=NC_{\mathrm{abs},\lambda}\left(d_{\mathrm{p}}\right)I_{\mathrm{b},\lambda}\left[T_{\mathrm{p,i}}\left(d_{\mathrm{p}}\right)\right]. \tag{2.10}$$

Such a treatment is ideal in that the emission from the aggregate is proportional to the number of primary particles.

Finally, if it is assumed that the aerosol is otherwise optically thin, the light emitted from the aggregate (or isolated nanoparticles for the unaggregated case) then travels uninterrupted to the detector, without being scattered or reabsorbed. The total irradiance on the detector can then be stated as the sum of $J_{\lambda,\mathrm{i}}^{\mathrm{agg}}$ over all of the aggregates in the aerosol. This is often phrased per unit volume of aerosol, V, and in terms of the volume fraction of nanoparticles in the aerosol, f_{V},

$$\frac{J_{\lambda,\mathrm{i}}}{V} = 6 f_{\mathrm{V}} \frac{\pi}{\lambda} E\left(\mathbf{m}_{\lambda}\right) I_{\mathrm{b},\lambda}\left[T_{\mathrm{p,i}}\left(d_{\mathrm{p}}\right)\right]. \tag{2.11}$$

Alternatively, if one is not interested in the volume fraction, the various wavelength and size independent constants including the number of particles can be grouped into a parameter single C, so that

$$J_{\lambda,\mathrm{i}} = C \cdot C_{\mathrm{abs},\lambda}\left(d_{\mathrm{p}}\right) \cdot I_{\mathrm{b},\lambda}\left[T_{\mathrm{p,i}}\left(d_{\mathrm{p}}\right)\right]. \tag{2.12}$$

This is the procedure is adopted in a wide range of works, including Refs. [45,49,91,112], and in the current work where the volume fraction is not of primary interest.

In many instances, emission from the aerosol is complicated by polydispersity in the nanoparticle size distribution, if not within single aggregates then between different aggregates. Having applied RDG-FA theory, polydispersity can be incorporated by integrating the blackbody function over the nanoparticle size distribution, $p(d_{\mathrm{p}})$. When combined with Eq. (2.12), this gives

$$J_{\lambda,\mathrm{i}} = C \int_{d_{\mathrm{p}}} C_{\mathrm{abs},\lambda}\left(d_{\mathrm{p}}\right) \cdot I_{\mathrm{b},\lambda}\left[T_{\mathrm{p,i}}\left(d_{\mathrm{p}}\right)\right] \cdot p\left(d_{\mathrm{p}}\right) \cdot \mathrm{d}d_{\mathrm{p}} \,. \tag{2.13}$$

This form is used in Refs. [45,48,131] and in close variants in several other works (e.g. [49,91,175]). Polydispersity also has consequences on the pyrometric temperature as discussed in Chapter 3.

2.1.3 Detector signal

The incandescence from the aerosol acts as the irradiance on the detector, where the photons are converted to an electrical signal. This thesis does not seek to review the various kinds of detectors that are used in TiRe-LII, which can include streak cameras and photomultiplier tubes (PMTs). It is noted, however, that Snelling et al. [145] expressed the hypothetical noise-free, single-shot signal registered by the j^{th} channel of the detector, denoted as $\tilde{s}_{\mathrm{j,i}}$, as

$$\tilde{s}_{\mathrm{j,i}} = Z G M^2 A_{\mathrm{ap}} \frac{A_{\mathrm{lens}}}{4\pi u^2} \omega_{\mathrm{b}} \int_0^{\infty} \frac{J_{\lambda,\mathrm{i}}}{V} \tau_{\lambda} \Theta_{\lambda} \mathrm{d}\lambda \,, \tag{2.14}$$

where Z is the impedance of the measuring device, G is the detector gain, M is the magnification, A_{ap} is the area of the aperture, A_{lens} is the area of the lens in the collection optics, u is the distance between the lens and probe volume, ω_{b} is the laser sheet thickness, τ_{λ} is the transmissivity of the optics (particularly the transmissivity of the bandpass filters used to distinguish between the emission at different wavelengths), and Θ_{λ} is spectral response of the detector. The ratio of the area of the lens to $4\pi u^2$ is sufficient to define the solid angle over which the emission is collected. These parameters are identified in the schematic of a typical LII setup provided in

Figure 2.3. Many of these parameters are determined by calibrating the detector against a known, continuous light source. Accordingly, for simplicity, the signal for a single-shot is often rather written in terms of summary parameters, which can envelope the constants from Eq. (2.12), so that

$$\tilde{s}_{\mathrm{j,i}} = \frac{\Lambda \cdot \eta_{\mathrm{j}}}{C} J_{\lambda_{\mathrm{j}},\mathrm{i}} = \Lambda \cdot \eta_{\mathrm{j}} \int_{d_{\mathrm{p}}} C_{\mathrm{abs},\lambda_{\mathrm{j}}}\left(d_{\mathrm{p}}\right) \cdot I_{\mathrm{b},\lambda_{\mathrm{j}}}\left[T_{\mathrm{p,i}}\left(d_{\mathrm{p}}\right)\right] \cdot p\left(d_{\mathrm{p}}\right) \cdot \mathrm{d}d_{\mathrm{p}} \,, \tag{2.15}$$

where Λ is the intensity scaling factor (ISF), defined in Chapter 6, and η_λ is a channel-dependent calibration factor, determined using a known, continuous light source. This form, or the equivalent for a monodisperse aerosol,

$$\tilde{s}_{\mathrm{j,i}} = \Lambda \cdot \eta_{\mathrm{j}} \cdot C_{\mathrm{abs},\lambda_{\mathrm{j}}}\left(d_{\mathrm{p}}\right) \cdot I_{\mathrm{b},\lambda}\left[T_{\mathrm{p,i}}\left(d_{\mathrm{p}}\right)\right], \tag{2.16}$$

are used nearly exclusively throughout this work. When the ISF is inferred from the data, it often envelopes varies unmodeled effects beyond those considered in the approach of Snelling et al. [145]. Such variations in the ISF have resulted in various anomalies noted in the literature, such as those observed in Refs. [80,145,176].

It is also noted that an alternate phrasing is useful within the context of signal noise (see Chapter 4), namely that the signal is

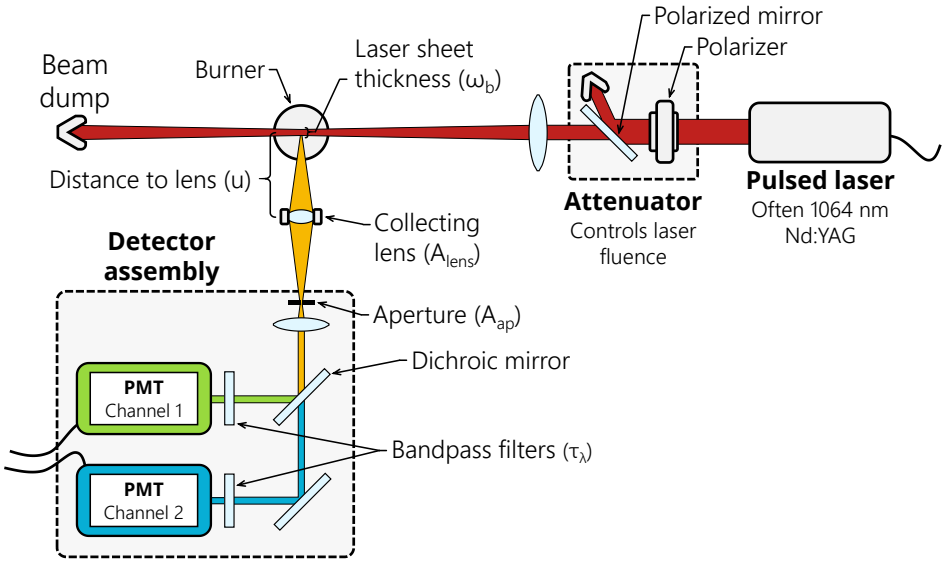

Figure 2.3 Schematic of a typical two-colour LII setup. Parameters defining the optical geometry, including u, ω_b, A_{lens}, and A_{ap}, are also indicated.

$$\tilde{s}_{\mathrm{j,i}} = \theta\zeta J_{\lambda_\mathrm{j},\mathrm{i}} = \theta\zeta C \int_{d_\mathrm{p}} C_{\mathrm{abs},\lambda_\mathrm{j}}\left(d_\mathrm{p}\right)\cdot I_{\mathrm{b},\lambda_\mathrm{j}}\left[T_{\mathrm{p,i}}\left(d_\mathrm{p}\right)\right]\cdot p\left(d_\mathrm{p}\right)\cdot \mathrm{d}d_\mathrm{p}\,, \tag{2.17}$$

or, for a monodisperse aerosol,

$$\tilde{s}_{\mathrm{j,i}} = \theta\zeta J_{\lambda_\mathrm{j},\mathrm{i}} = \theta\zeta C\cdot C_{\mathrm{abs},\lambda_\mathrm{j}}\left(d_\mathrm{p}\right)\cdot I_{\mathrm{b},\lambda_\mathrm{j}}\left[T_{\mathrm{p,i}}\left(d_\mathrm{p}\right)\right] \tag{2.18}$$

where ζ is the photoelectric efficiency of the detector, describing the number of photoelectrons produced when a single photon is imaged onto the detector, and θ is the amplification or scaling due to calibration or other signal processing steps, which transforms the raw voltage of the photoelectrons to a usable signal.

2.2 Heat transfer model

Attention now shifts to the temperature that is embedded in the spectroscopic model. This temperature varies over time, increasing during laser heating and decreasing due to various cooling mechanisms following the laser pulse. This provides a source of information about thermophysical characteristics and nanoparticle size. This section describes the heat transfer model governing nanoparticle heating during the laser pulse and cooling following the laser pulse. This part of the model can vary greatly between laboratories and materials [45,98] and, as such, only the basics relevant to the subsequent chapters are introduced.

2.2.1 The energy balance on the nanoparticle

The temperature profile in TiRe-LII can be modeled using an energy balance at the nanoparticle surface, shown schematically in Figure 2.4. This can be expressed mathematically as

$$\frac{d}{dt}\left(m_\mathrm{p} c_\mathrm{p} T_\mathrm{p}\right) = q_\mathrm{abs} + q_\mathrm{cond} + q_\mathrm{vap} + q_\mathrm{oth}\,, \tag{2.19}$$

where t is time, m_p is the mass of the nanoparticle, c_p is the specific heat capacity, q_abs is the rate of laser absorption by the nanoparticle, q_cond is the rate energy transfer due to conduction to the surrounding gas, q_vap is the rate energy transfer due to vaporization from the nanoparticle, and q_oth is the rate of energy transfer due to other modes, such as radiation [59,91,104], annealing [104], oxidation [104,177,178], and thermionic emission [83,96,179,180]. Generally, the terms in q_oth result in energy transfer rates that are orders of magnitude less than the remaining terms and are often omitted in analyses. The sign of each of the terms, considering whether energy is gained or lost, is considered in the discussion of each term below. The rates of change in the mass and specific heat capacity are considered small relative to the rate of change in the temperature, such that only one term remains after expanding the left-hand side of the equation using the product rule. TiRe-LII is also normally only

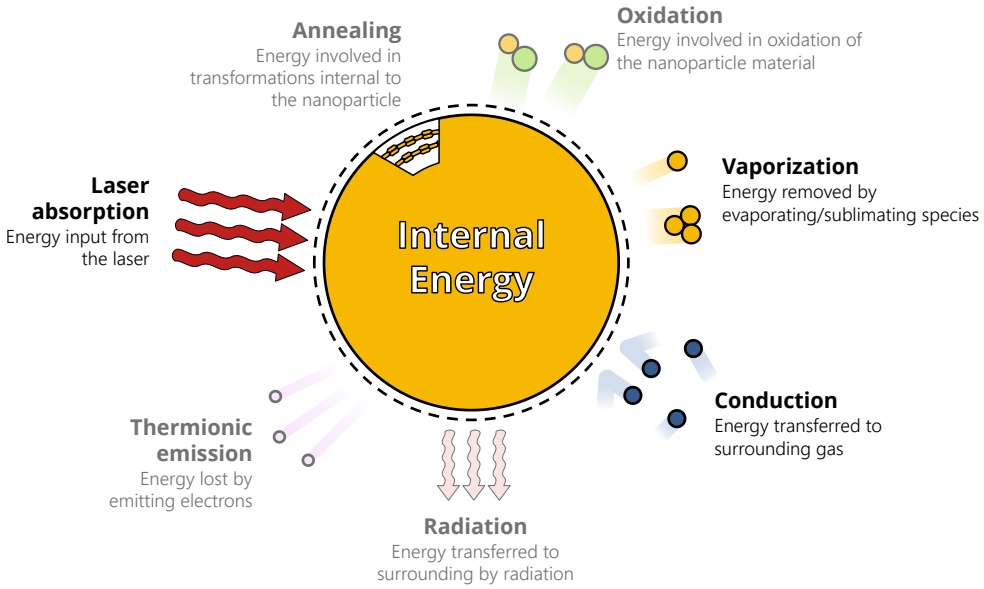

Figure 2.4 Schematic demonstrating the energy balance on the nanoparticle. The commonly neglected cooling or heating terms are faded.

applied to approximately spherical nanoparticles, an assumption adopted throughout this work. Combining these simplifications, Eq. (2.19) is widely written as

$$c_{\mathrm{p}}\rho\frac{\pi d_p^3}{6}\frac{\mathrm{d}T_{\mathrm{p}}}{\mathrm{d}t}=q_{\mathrm{abs}}-q_{\mathrm{cond}}-q_{\mathrm{vap}}\,, \tag{2.20}$$

where ρ is the density of the nanoparticle material. In this equation, the nanoparticle diameter and density will also change over time due to the thermal swelling and mass loss. The latter phenomenon creates a system of coupled ordinary differential equations (ODEs) that is discussed further in Section 2.2.4. The nanoparticle diameter is normally given in terms of the instantaneous nanoparticle mass and density [98]

$$d_{\mathrm{p}}=\left(\frac{6m_{\mathrm{p}}}{\pi\rho}\right)^{1/3}. \tag{2.21}$$

While this expression correctly accounts for thermal expansion, it should be noted that changes in ρ offset changes to the nanoparticle diameter so that $\rho\pi d_{\mathrm{p}}^3/6$ is still equal to the nanoparticle mass in Eq. (2.20). It is also notable that increasing the diameter of the nanoparticle will result in an increase in the rate of laser absorption,

discussed below in Section 2.2.2, which may be non-physical. Regardless, Eq. (2.21) is adopted throughout this work to calculate the nanoparticle diameter, under the assumption that this effect is small.

2.2.2 Laser absorption

The laser absorption term acts as the primary energy source in Eq. (2.19). Most generally, the absorption is given as the product of the absorption cross section of the nanoparticle at the laser wavelength, as discussed in Section 2.1, and the temporal laser fluence (energy per unit area) profile

$$q_{\text{abs}} = C_{\text{abs},\lambda_1}\left(d_{\text{p}}\right) f_0\left(t\right), \tag{2.22}$$

where λ_1 is the laser wavelength and $f_0(t)$ is the temporal profile of the laser energy. The laser energy is often phrased in terms of the laser fluence over the duration of the pulse

$$F_0 = \int_t f_0\left(t\right)\mathrm{d}t\,. \tag{2.23}$$

Temporal laser profiles in numerical studies are generally modeled as Gaussian with heavy tails [98,113,115,181]. Koechner [182] suggested that Q-switching an Nd:YAG laser can produce these kind of temporal laser profiles. This was later confirmed in a study by Bladh et al. [183]. The laser profiles are also often spatially non-uniform, resulting a spatial distribution of nanoparticle temperatures within the probe volume at any instant (e.g. [99,115,157,176,184]). Further, changing the laser fluence will cause a different temperature response from the nanoparticle. For spherical nanoparticles in the Rayleigh limit, Eq. (2.22) can be written as

$$q_{\text{abs}} = \frac{\pi^2 d_{\text{p}}^3}{\lambda_1} E\left(\mathbf{m}_{\lambda_1}\right) f_0\left(t\right). \tag{2.24}$$

It is noted that, unlike in the geometric scattering regime, this expression predicts a volumetric uptake of the laser energy into the nanoparticle. This expression is adopted almost universally in TiRe-LII studies, with the exception of some works by Michelsen and coworkers [98,178], which account for saturation of linear, single photon absorption and C_2 photodesorption. When Eq. (2.24) is used in conjunction with Eq. (2.20) and in the absence of significant cooling over the duration of the laser pulse, the d_{p}^3 terms on both sides of the equation will cancel out. This results in nanoparticles of all sizes, up to the breakdown of the Rayleigh approximation, heating up at the same rate and reaching the same peak temperature. However, when the Rayleigh approximation is not valid, the nanoparticles in a polydisperse aerosol will reach different peak temperatures, increasing the effect of polydispersity.

The presence of the nanoparticle diameter in Eq. (2.24) signifies that nanoparticle swelling will result in an increase in laser absorption by the nanoparticle. There has been some discussion in the TiRe-LII community regarding the validity of such an approach, as the number of atoms available to interact with the laser light does not change as the nanoparticle swells. This phenomenon is only noted here as it requires additional study that lies outside of the scope of this thesis.

2.2.3 Conduction

For high boiling point materials and low laser fluences, conduction is the dominant form of nanoparticle cooling. An overview of the state of conduction modeling within the context of LII is provided by Liu et al. [185], Kuhlmann et al. [117], and Filippov and Rosner [186]. The size regime for conduction is determined by the dimensionless Knudsen number

$$\mathrm{Kn} = \frac{\lambda_g}{L_c}, \tag{2.25}$$

where λ_g is the mean free path of the gas and L_c is a characteristic length, set to the radius of the nanoparticle [185]. The mean free path for the gas can be calculated in different ways. Liu et al. [185] noted that there are restrictions to which expression for the mean free path can be used in the various continuum regime expressions. This thesis defers this discussion to that work and the references cited therein, rather only presenting two of the expressions used in the LII literature. Liu et al. [185] adopted the expression for collisions in an ideal gas, where the mean free path is [187]

$$\lambda_g = \frac{1}{2^{1/2} A_g n_g} = \frac{k_B T_g}{2^{1/2} A_g p_g}, \tag{2.26}$$

where $A_g = \pi d_g^2$ is the cross-sectional collision area of the gas, $n_g = p_g/(k_B T_g)$ is the molecular number density of the gas, T_g is the gas temperature, and p_g is the gas pressure. The expression adopted by Kuhlmann et al. [117] from McCoy and Cha [188] alternatively phrases the mean free path in terms of the thermal conductivity of the gas

$$\lambda_g = \frac{k_g(\gamma - 1)}{f p_g}\left(\frac{\pi m_g T_g}{2k_B}\right)^{1/2}, \tag{2.27}$$

where k_g is the thermal conductivity of the gas, $\gamma = c_p/(c_p - R)$, R is the universal gas constant, and $f \approx (9\gamma\text{-}5)/4$ is the Eucken factor. In general, both the thermal conductivity of the gas and γ in this expression can be temperature dependent.

2.2.3.1 Continuum regime conduction

For Kn $\gg$ 1, conduction occurs in the continuum regime, where heat transfer is limited by the thermal conductivity of the gas. This yields the common expression

$$q_{\text{cond}} = -\bar{k}_{\text{g}} \pi d_{\text{p}} \left(T_{\text{p}} - T_{\text{g}} \right), \tag{2.28}$$

where

$$\bar{k}_{\text{g}} \equiv \frac{1}{\left(T_{\text{p}} - T_{\text{g}} \right)} \int_{T_{\text{g}}}^{T_{\text{p}}} k_{\text{g}} \, \mathrm{d}T \tag{2.29}$$

is an average thermal conductivity of the gas over the range of temperatures that are experience by the nanoparticle. Solving this expression yields a temperature gradient in the gas. It is noted that these expressions are not used directly in LII analyses where satisfying Kn $\gg$ 1 is never practically achieved. The expressions are, however, useful in the context of transition regime conduction, discussed in Section 2.2.3.3 below.

2.2.3.2 Free molecular conduction

For cases where Kn $\ll$ 1, conduction occurs in the free molecular regime. Here the frequency of gas-nanoparticle collisions declines considerably. When a collision does occur, gas molecules will travel ballistically away from the nanoparticle, moving long distances into the bulk gas without losing their gained energy. As a result, there is effectively no temperature gradient in the gas. Rather, the energy transfers freely through to the bulk gas, and the limiting factor in heat transfer becomes the dynamics and frequency of the gas-nanoparticle collisions themselves. As such, free molecular conduction is written as the product of the frequency of gas-nanoparticle collisions and the average energy transferred during a collision, that is

$$q_{\text{cond}} = -\nu_{g} \left\langle E_{\text{o}} - E_{\text{i}} \right\rangle, \tag{2.30}$$

where ν_{g} is the frequency of gas-nanoparticle collisions, $\langle \cdot \rangle$ denotes an average, and E_{i} and E_{o} are the incident and scattered energies of the gas atoms. The gas-nanoparticle collision frequency can be determined through the application of collision theory, assuming a single nanoparticle with a mass and diameter much greater than that of the gas molecules,

$$\nu_{\text{g}} = \frac{\pi d_{\text{p}}^2}{4} n_{\text{g}} c_{\text{g}} = \frac{\pi d_{\text{p}}^2 c_{\text{g}} p_{g}}{4 k_{\text{B}} T_{\text{g}}}, \tag{2.31}$$

where $c_{\text{g}} = [8 k_{\text{B}} T_{\text{g}}/(\pi m_{\text{g}})]^{1/2}$ is the mean thermal speed of the gas and $\pi d_{\text{p}}^2/4$ corresponds to the cross-sectional area of the nanoparticle. This expression can be equivalently derived as the product of a number flux away from the

nanoparticle, $N_g'' = n_g c_g/4$, and the surface area of the nanoparticle. In this case, the factor of ¼ moves from the cross-sectional area of the nanoparticle to modifying c_v so that is corresponds to the mean velocity normal to the surface. This latter convention is used in deriving the vaporization expression in Section 2.2.4.

Determining the average energy transfer during a gas-nanoparticle collision is more involved. The energy transfer is normally rewritten in terms of the thermal accommodation coefficient (TAC), α, defined as the ratio of the actual average energy transfer to the maximum energy transfer allowed by the second law, $\langle E_o - E_i \rangle_{max}$, so that

$$\left\langle E_o - E_i \right\rangle = \alpha \left\langle E_o - E_i \right\rangle_{max}. \tag{2.32}$$

The TAC itself is the leading source of uncertainty in free molecular conduction calculations and is often used as a fitting parameter in the interpretation of TiRe-LII data [21,24,45,111,112] (including in parts of Chapter 8). More recently, however, researchers have introduced dynamics-based models to highlight the physics underlying the TAC [48,107,108,189], most notably by using molecular dynamics (MD).

The remaining quantity in Eq. (2.32), the maximum energy transfer, will occur when the gas molecule equilibrates with the nanoparticle surface and scatters, on average, at the nanoparticle temperature. The amount of energy required for the gas molecule to reach equilibrium depends on the thermodynamic degrees-of-freedom (DOF) of the gas molecule, ζ, including its translational, rotational (ζ_{rot}), and vibrational components. In the classical limit of statistical mechanics, each DOF contains an energy of $k_B T/2$. It is notable that, in this case, the flux of nanoparticles onto the surface preferentially selects those gas molecules with large velocity components normal to the surface. This increases the maximum energy transfer available to be transferred by an additional $k_B T/2$. Further discussion of this phenomenon is deferred to Appendix C. The maximum allowable energy transfer is thus given by

$$\left\langle E_o - E_i \right\rangle_{max} = \frac{1}{2} k_B \left(\zeta + 1\right)\left(T_p - T_g\right). \tag{2.33}$$

In practice, the number of DOF available can depend on both the gas molecule and temperature. All gas molecules, regardless of temperature, have three translational degrees of freedom corresponding to the three spatial dimensions. For most cases, even up to the temperatures featured in TiRe-LII, the vibrational modes are inaccessible, reducing the total available DOF to

$$\zeta = 3 + \zeta_{rot}. \tag{2.34}$$

The main differentiating feature between gas molecules is thus the number of rotational degrees of freedom, ζ_{rot}. For monatomic gases, there are no rotational degrees of freedom and $\zeta = 3$. For linear polyatomic gas molecules, including carbon dioxide and nitrogen, there are two rotational degrees of freedom (rotation about the bonds is non-physical) so that $\zeta = 5$. Finally, for non-linear polyatomic gas molecules, like methane, three rotational degrees of freedom are available so that $\zeta = 6$. In any of these cases, the overall conduction rate is finally given by

$$q_{cond} = -\alpha \frac{\pi d_p^2}{4} n_g c_g \frac{k_B(\zeta+1)}{2}\left(T_p - T_g\right) = -\alpha \frac{\pi d_p^2}{4} n_g c_g k_B \left(2 + \frac{\zeta_{rot}}{2}\right)\left(T_p - T_g\right), \tag{2.35}$$

which is the form adopted in Refs. [45,112] and through this thesis.

Alternatively, practitioners can rephrase the problem in terms of the specific heat capacity or $\gamma = c_p/(c_p - R)$. In this case, Filippov and Rosner [185,186] state the free molecular conduction rate as

$$q_{cond} = -\alpha \frac{\pi d_p^2}{4} n_g c_g \frac{k_B}{2}\left(\frac{\gamma+1}{\gamma-1}\right)\left(T_p - T_g\right). \tag{2.36}$$

This expression is equivalent to Eq. (2.35) when $\zeta+1 = (\gamma+1)/(\gamma-1)$. Conveniently, for monatomic gases, where $\zeta = 3$, this corresponds to $\gamma = 5/3$, which is the value of γ most often adopted for those gases. For linear polyatomic gas molecules, where $\zeta = 5$, this corresponds to $\gamma = 7/5$, with similar implications. A main advantage to employing this latter expression is including experimental estimates of the variation of γ with temperature. Further, for cases where γ would vary considerably over a range of temperatures, the value of γ can be replaced with an average defined as

$$\frac{1}{\overline{\gamma}-1} \equiv \frac{1}{T_p - T_g}\int_{T_g}^{T_p} \frac{1}{\gamma-1} \mathrm{d}T. \tag{2.37}$$

For the sake of the current work, it is assumed that this temperature dependence is negligible and Eq. (2.35) is employed for the free molecular conduction rate. An alternative derivation of these expressions is provided by Liu et al. [185], starting from the Maxwell-Boltzmann equations.

2.2.3.3 Transition regime conduction

More generally, conduction from isolated nanoparticles of any size can be calculated based on transition regime techniques (for which no analytical solution exists [185]). Bird [187] reports several methods, including approximate analytical and interpolation techniques, which are briefly reviewed by Liu et al. [185]. Interpolation methods are defined based on

$$q_{\text{cond}} = \left(\frac{1}{q_{\text{cont}}} + \frac{1}{q_{\text{fm}}} \right)^{-1}. \tag{2.38}$$

where q_{cont} and q_{fm} denote the conductive cooling rates calculated by the continuum and free molecular approaches, respectively. Theoretically, these terms could take on any of the forms given in the preceding sections. Originally, Melton [59] adopted the interpolation method of McCoy and Cha [188], where the heat conduction rate is given by

$$q_{\text{cond}} = -\frac{2\pi d_{\text{p}}^2 k_{\text{g}} \left(T_{\text{p}} - T_{\text{g}} \right)}{d_{\text{p}} + \frac{8 f \lambda_g}{\alpha \left(\gamma + 1 \right)}}, \tag{2.39}$$

which represents the heat transfer rate as a mixture of nanoparticle-gas and gas-gas collision frequencies. Such an expression was subsequently used in several other modeling papers [95,104,111,117].

Alternatively, the most successful and recommended approach to calculate transition regime conduction is Fuch's method [190,191]. This approach separates the region surrounding the nanoparticle into a collisionless boundary (or Langmuir) layer of thickness δ and the remaining space. At the interface between these regions, one defines an intermediate temperature, T_δ. Then, inside the boundary layer, conduction is considered to be free molecular and is driven by a temperature difference of (T_{p}–T_δ). Outside of the boundary layer, conduction occurs continuously away from an effective sphere encompassing the boundary layer and being driven by a temperature difference of (T_δ–T_{g}). Equating these conduction rates at the boundary, one can solve for T_δ, the value of which can be inserted into either the continuum or free molecular expression to determine the overall conduction rate. This approach has been implemented in the TiRe-LII literature on several occasions [192–195]. It is notable that either of these methods of evaluating transition regime conduction are particularly powerful in that they can be applied to the full range of Knudsen numbers, replicating both free molecular and continuum regime conduction rates.

Figure 2.5 shows sample calculations of the rate of conductive heat transfer as a function of Knudsen number for iron nanoparticle in argon gas. The upper axis identifies the gas pressure corresponding to any given Knudsen number and a nanoparticle diameter of 100 nm. As the continuum conduction rate is not a function of pressure, no Knudsen number dependence is observed. By contrast, it can be noted that in the free molecular regime, the rate of conduction declines with decreasing gas pressure (that is with increasing Knudsen number), a consequence of there being fewer collisions between the nanoparticle and the gas molecules. Figure 2.5 also

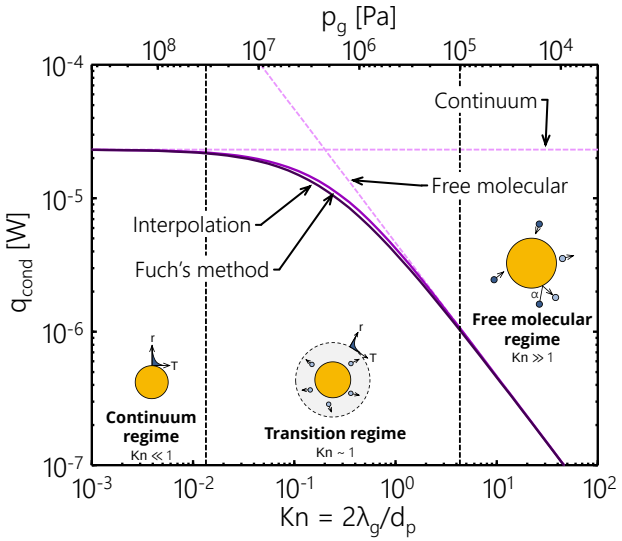

Figure 2.5 Transition from free molecular conduction to continuum regime conduction for iron nanoparticles in argon gas as a function Knudesen number, Kn, and gas pressure for a nanoparticle of diameter d_p = 100 nm. For the calculations, the average thermal conductivity of argon is taken as k_g = 0.035 W·m^{-1}·K^{-1} [196] and the cross section is taken as the variable soft sphere value in Bird [187], d_g = 0.411 nm. Transition regime methods are indicated in purple (interpolation) and yellow (Fuch's method).

identifies the two transition regime schemes noted in the preceding parameter. The transition regime methods are generally consistent with one another. In either case, it can be noted that the transition regime methods asymptotically approach the continuum regime expression for low Knudsen numbers and the free molecular expression for high Knudsen numbers.

2.2.3.4 Aggregation effects

Some works have also examined a so-called *shielding* wherein the outer nanoparticles in an aggregate shield the inner nanoparticles from interacting with the surrounding gas resulting in a reduction in the conductive cooling rate. Such an effect would also result in a temperature distribution in the primary particles in as aggregate during cooling. Filippov et al. [114] made a sizeable contribution to understanding these processes by applying a Monte Carlo approach in which the trajectories of the gas molecules around the aggregate are tracked over time. Scattering kernels (discussed briefly in Appendix C) are used to model the interactions between the gas molecules and the nanoparticles. The effect of nanoparticle shielding can then be quantified into a shielding parameter. A schematic demonstrating the simulated amount of shielding for the primary particles in an aggregate is reproduced in Figure 2.6 from the work of Filippov et al. [114]. Liu et al. [113,197] further simulated the effect that shielding has on the nanoparticle temperature decay and later extended this treatment using Monte Carlo

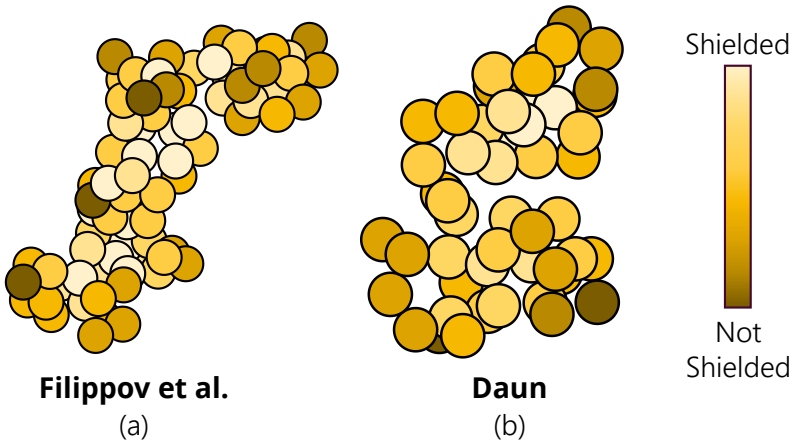

Figure 2.6 Monte Carlo estimates of the shielding effect for an aggregate reproduced from Filippov et al. [114] and Daun [118]. Here, the darker nanoparticles are those that are less shielded and will cool more quickly. Generally, those nanoparticles near the center of the aggregate are more shielded from interacting with the gas.

simulations. The authors generally concluded that, while there was some influence of aggregate structure on the cooling rate, this effect is small for the free molecular case. Later, Daun [118] improved on the Monte Carlo approach by applying a more physically realistic Cercignani-Lampis-Lord (CLL) kernel to model gas-nanoparticle interactions. The distribution of the shielding parameter for that case is also reproduced in Figure 2.6. Johnsson et al. [120] extended these approaches by considering bridging between the primary particles in the aggregate and reapplying the Monte Carlo approach of Daun [118]. Bladh et al. [119] performed an experimental study considering soot-laden aerosols with three different levels of aggregation, interpreting the data using the model of Liu et al. [113]. The influence of the phenomenon is still expected to be small for the cases observed in this work and is generally neglected in this thesis. It is noted, however, that the MD simulations in Chapter 7 could provide improved estimates of the scattering kernel, which could be used to improve estimates of the shielding parameter using the Monte Carlo approach. This is, however, a topic of future work and is out of the scope of this thesis.

2.2.3.5 Local gas heating

Another source of uncertainty in conductive cooling models is local gas heating. Several studies [198–200] have noted that, particularly for high fluences and soot concentrations, the gas temperature surrounding the nanoparticle increases over the duration of nanoparticle cooling. The magnitude of this change has been

suggested to be up to several hundred Kelvin. More often, however, the soot loading and fluences are such that this effect is small (~30 K [200]) and is neglected accordingly in this work.

2.2.4 Vaporization

Evaporation submodels can vary greatly between laboratories. The evaporation term is normally stated as the product of the energy lost per unit mass and the rate of nanoparticle mass loss, that is

$$q_{\mathrm{vap}} = \Delta h_{\mathrm{v}} \frac{\mathrm{d}m_{\mathrm{p}}}{\mathrm{d}t} = \frac{\Delta H_{\mathrm{v}}}{M_{\mathrm{v}}} \frac{\mathrm{d}m_{\mathrm{p}}}{\mathrm{d}t}, \tag{2.40}$$

where Δh_{v} and ΔH_{v} are the specific or molar heat of vaporization in units of energy per unit mass and mole respectively. This expression reveals the coupled nature of this problem, wherein $\mathrm{d}m_{\mathrm{p}}/\mathrm{d}t$ must be solved simultaneous to Eq. (2.19) or (2.20). It is generally accepted that evaporation from the nanoparticles will occur in the free molecular regime for TiRe-LII. This corresponds to the release of individual atoms, or clusters of atoms, from the surface that travel ballistically away from the surface. In this case, the rate of mass loss can be derived by applying continuity at the nanoparticle surface

$$\frac{\mathrm{d}m_{\mathrm{p}}}{\mathrm{d}t} = -\beta m_{\mathrm{v}} \pi d_{\mathrm{p}}^2 N_v'' = -\beta m_{\mathrm{v}} \pi d_{\mathrm{p}}^2 \frac{p_{\mathrm{v}} c_{\mathrm{v}}}{4 k_{\mathrm{B}} T_{\mathrm{p}}}, \tag{2.41}$$

where β is the sticking coefficient that describes the probability that vapor atoms or molecules will return to the surface, m_{v} is the mass of the vapor species, $c_{\mathrm{v}} = [8 k_{\mathrm{B}} T_{\mathrm{p}}/(\pi m_{\mathrm{v}})]^{1/2}$ is the mean thermal speed of the vapor assuming that the vapor is at the nanoparticle temperature, $N_{\mathrm{v}}'' = n_{\mathrm{v}} c_{\mathrm{v}}/4$ is the vapor number flux, $n_{\mathrm{v}} = p_{\mathrm{v}}/k_{\mathrm{B}} T_{\mathrm{p}}$ is the vapor number density, p_{v} is the vapor pressure, and πd_{p}^2 corresponds to the surface area of the nanoparticle. This equation can be equivalently stated in terms of the density of the vapor and nanoparticle material, as per Refs. [58–60], by applying the ideal gas law. Expanding Eq. (2.40) thus gives

$$q_{\mathrm{vap}} = -\Delta h_{\mathrm{v}} \beta m_{\mathrm{v}} \pi d_{\mathrm{p}}^2 \frac{p_{\mathrm{v}} c_{\mathrm{v}}}{4 k_{\mathrm{B}} T_{\mathrm{p}}} = -\Delta H_{\mathrm{v}} \beta \pi d_{\mathrm{p}}^2 \frac{p_{\mathrm{v}} c_{\mathrm{v}}}{4 R T_{\mathrm{p}}}, \tag{2.42}$$

which is the expression adopted in the current work. This expression in the literature is also occasionally written in terms of a different thermal velocity $\bar{w} = [k_{\mathrm{B}} T_{\mathrm{p}}/(2 m_{\mathrm{v}})]^{1/2}$, yielding the expression given in the review by Michelsen et al. [98] and several of the studies cited therein. The Hofmann model in Michelsen et al. [104] further modifies this expression to account for transition regime effects at higher pressures, adopting the interpolation approach similar to that described in Section 2.2.3.3. Other more complex variants on the vaporization model

exist in the literature, including those of Hofeldt [95], Michelsen [104,178], and Michelsen et al. [177], but will not be discussed significantly in this thesis.

The remaining models in the literature differ primarily in how they treat m_v, p_v, ΔH_v, and β. A summary of these differences for soot is provided by Michelsen et al. [98]. The sticking coefficient has varied, generally ranging from 0.5 to unity [98]. The value of the parameter is taken as unity in the current work, noting that this value has been applied rather universally for engineered nanoparticles (e.g. [45,49,201]). The mass of the vapor, often phrased rather in terms of the molar mass of the vapor, is often taken as the atomic mass for engineered nanoparticles (e.g. [45,49]) and often includes temperature-dependent expressions for soot [98]. Of the remaining terms, only the most general expressions are reviewed here, leaving additional details to the realization of the model in the various chapters of this document.

The heat of vaporization of soot is most often taken as either constant or a polynomial with temperature [98]. For engineered nanoparticles, several more recent studies [45,48,112] have employed Watson's equation [202]

$$\Delta h_v = K\left(1-T_r\right)^{0.38}, \tag{2.43}$$

where K is a material constant, $T_r = T_p/T_{cr}$ is a reduced temperature, and T_{cr} is the critical temperature. The Watson equation was also used in the work of Leider et al. [203] for carbon, whose work forms the basis for many of the available TiRe-LII heat transfer submodels for soot. However, in that work, the equation is only applied at temperatures well in excess of the boiling point of carbon, that is temperatures which are very rarely observed in TiRe-LII applications. Chapter 9 discusses other expressions available in the literature in more detail, particularly in regards to iron. These include the expressions of Román et al. [204] and Meyra et al. [205].

The vapor pressure can be predicted via several temperature dependent expressions. The most commonly used expression in TiRe-LII analysis is the Clausius-Clapeyron equation, which assumes thermal equilibrium between the nanoparticle and the gas. In that case, the vapor pressure is given by

$$p_v = p_{ref}\cdot\exp\left[-\frac{\Delta H_{v,ref}}{R}\left(\frac{1}{T_p}-\frac{1}{T_{ref}}\right)\right] = A\cdot\exp\left(-\frac{\Delta h_{v,ref}}{R_s T_p}\right) = \exp\left(C_0-\frac{C_1}{T_p}\right), \tag{2.44}$$

where p_{ref}, $\Delta h_{v,ref}$, and T_{ref} are the pressure, latent heat of vaporization, and temperature at some reference point and A, C_0, and C_1 are material constants that can be related to the aforementioned reference point. Use of this expression is predicated on the assumption that heat of vaporization is constant with temperature. Other expressions have been proposed to account for the temperature variations in the heat of vaporization [206], but

will not be used in this work. The Will and Liu models for soot described in Michelsen et al. [98] opt rather to employ a high dimensional polynomial fit to the data from Leider et al. [203] for the vapor pressure. This work adopts the common assumption that the Clausius-Clapeyron equation is sufficient to describe the vapor pressure curve, both for soot and engineered nanoparticles.

The vapor pressure curve can be further modified to account for nanoparticle size effects using the Kelvin equation

$$p_{\mathrm{v}} = p_{\mathrm{v,o}} \cdot \exp\left(\frac{4\gamma_{\mathrm{s}}}{d_{\mathrm{p}} \rho R_{\mathrm{s}} T_{\mathrm{p}}} \right), \tag{2.45}$$

where $p_{\mathrm{v,o}}$ is the bulk pressure as can be calculated by the Clausius-Clapeyron equation, γ_{s} is the surface tension, and $R_{\mathrm{s}} = R/M$ is the specific gas constant. The Kelvin equation has not been used to date within the context of TiRe-LII analyses on soot, only receiving a brief mention by Kuhlmann et al. [117] where the expression was not used. The expression has, however, seen use within the context of TiRe-LII from engineered nanoparticles [45,48,49,112,130,207]. In those works, there is also discussion regarding the size-dependence of the surface tension itself. Eremin et al. [130] make mention of Nanda et al. [208] who determined that the surface tension of nanoparticles is higher than that observed in bulk. More recently, Sipkens et al. [112] made broader statements regarding the surface tension, instead suggesting use of the Tolman equation to predict the surface tension

$$\gamma_{\mathrm{s}} = \frac{\gamma_{\mathrm{s,o}}}{1 + 4\delta / d_{\mathrm{p}}}, \tag{2.46}$$

where $\gamma_{\mathrm{s,o}}$ is the surface tension of the bulk material and δ is the so-called Tolman length. The authors gave a brief review of the values of δ that have been considered in the literature, most of which are given in reference to the equilibrium distance between atoms, σ_{LJ}. Unfortunately, there is little consensus on what value to use, with different studies suggesting both positive and negative values for δ. Figure 2.7 demonstrates the combined effect of the Kelvin equation and the Tolman equation for two proposed values of δ for iron nanoparticles. The effect of the Tolman equation is generally negligible until ~4 nm, below which the vapor pressure can deviate above or below that predicted by the Kelvin equation depending on the value of δ. Within the context of this work, these uncertainties are sufficiently small for the nanoparticles considered that any deviations are sufficiently predicted by the Kelvin equation.

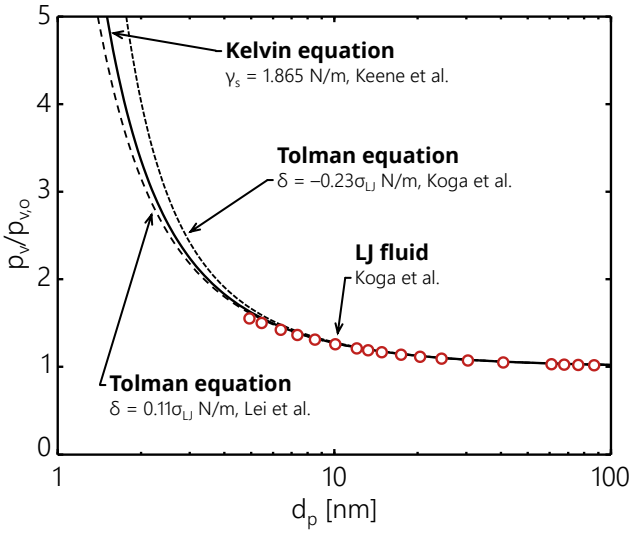

Figure 2.7 Effect of the Kelvin and Tolman equations on the vapor pressure of a nanoparticle for iron at T_p = 3500 K. Two cases of the Tolman equation are shown, including $\delta = 0.11\sigma_{LJ}$ [209] and $\delta = -0.23\sigma_{LJ}$ [210], where σ_{LJ} = 0.2517 [211]. Also shown is the results from a Lennard-Jones (LJ) fluid from Koga et al. [210].

2.2.5 A short word on other terms

The additional terms that are occasionally included in the energy balance, Eq. (2.19), have been reviewed by Michelsen et al. [97] and are often neglected. Accordingly, the present discussion of these terms is limited. The most commonly included term is radiation. The total energy lost due to radiation can be calculated by integrating the thermal emission defined by Eq. (2.1) over all wavelengths,

$$q_{\text{rad}} = \int_0^\infty C_{\text{abs},\lambda}\left(d_p\right) I_{b,\lambda}\left[T_p\left(t, d_p\right)\right] \mathrm{d}\lambda \,, \tag{2.47}$$

which is typically done numerically. Unlike absorption and emission calculations, the radiative energy transfer term requires an estimate of the broadband value of $E(\mathbf{m}_\lambda)$ and may require the incorporation of Mie theory for shorter wavelengths. While this term is often included in energy balances, most practitioners note that, in spite of this being the phenomenon responsible for measurement, its effect on the energy balance is negligible.

Oxidation at the nanoparticle surface has the potential to influence the temperature decay, the mass loss rate, and the optical properties of the nanoparticle. The oxidation model most often used in TiRe-LII for soot can be attributed to Michelsen [104] and has been adopted in several other studies [177,178,199]. In these studies, oxidation results in a mass loss which must be incorporated into Eq. (2.41) when solving the coupled ODEs

$$\left(\frac{dm_p}{dt}\right)_{ox} = -\pi d_p^2 2 m_C k_{ox}, \tag{2.48}$$

where m_C is the mass of a carbon atom and k_{ox} is the oxidation rate constant for the reaction $2C + O_2 \rightarrow 2CO$. A heating term can also to be added to the energy balance of the form

$$q_{ox} = -\left(\frac{\Delta H_{ox} + 2\alpha c_p^{CO} T_p}{2M_C}\right)\left(\frac{dm_p}{dt}\right)_{ox}, \tag{2.49}$$

where ΔH_{ox} is the enthalpy of the oxidation reaction, M_C is the molar mass of carbon, and c_p^{CO} is the specific heat capacity of carbon monoxide. The existence of a TAC, α, in this expression represents only partial accommodation of the carbon monoxide as it leaves the nanoparticle. The effect on the optical properties has seen little discussion in the literature. Here, it is simply noted that oxidation of engineered nanoparticles, such as iron, may result in an oxide layer that forms on the outside of the nanoparticle, resulting in a core-shell nanoparticle with enhanced optical properties. Further study outside of the scope of this thesis is required to quantify these effects.

Annealing, which has only been considered in the context of soot, has been observed in HRTEM analyses of Vander Wal and Choi [85] and de Iuliis et al. [212], among others external to the TiRe-LII field [213,214]. It has been observed that soot anneals from an amorphous carbon phase to onion-like carbon, consisting of rings of graphite. Such changes, which can be observed in Figure A.1 in Appendix A, carry the possibility of changing the physical and optical properties of the nanoparticles and a release energy that introduces an additional heating term into the energy balance. Michelsen [104] developed the only model of soot annealing that has been used in TiRe-LII analyses to date, examining defect annihilation and creation in the nanoparticle. The technique involves simultaneously solving for the annealing fraction, X, over time, along with Eqs. (2.19) and (2.41). Unfortunately, the existing annealing model is known to overestimate the speed of annealing at flame temperatures [215]. A simplified annealing model is developed in Chapter 6 of this thesis in part to address this issue. While the new model is not as rigorous in its derivation, it has the advantage of improved qualitative agreement with experimental observations that is useful in the context of simulating TiRe-LII signals.

Several others have included thermionic emission as a cooling term. The inclusion of thermionic emission in the energy balance for TiRe-LII dates back to McManus et al. [83]. Since, the thermionic term has been included only rarely in LII analyses [96,98,179,180,216]. The effect is more likely to influence LII in terms of

bremsstrahlung emission from the aerosol or the effect that particle charging could have on aggregate morphology during laser heating [217].

2.3 Summarizing notes

This chapter establishes the basis for the variants of the TiRe-LII model used in subsequent chapters for analysis. The precise implementation of the model will depend on the material and experimental conditions considered. Accordingly, most chapters will give an overview of the variant of this model that is used in that chapter. Figure 2.8 demonstrates how the different modes of energy transfer vary with nanoparticle temperature for three gas-surface pairs: Soot-Ar, Fe-Ar, and Mo-Ar. One can note that vaporization becomes the dominant form of energy transfer much earlier for iron than it does for molybdenum and soot. This has consequences on the information that can be inferred from the data (as noted in Chapter 8). Figure 2.8 also shows the significance of the various modes, including laser absorption, over the duration of a TiRe-LII signal, considering laser-excitation of soot in an argon buffer gas at a fluence of $F_0 = 0.2$ J/cm^2. It is notable that vaporization is the dominant form of cooling for the first 100 ns following the laser pulse, after which conduction becomes dominant.

It is also noted here that these models occasionally still fail to describe time-resolved incandescence signals. The most prominent anomaly is the so-called *anomalous cooling* effect, a term used throughout the literature to

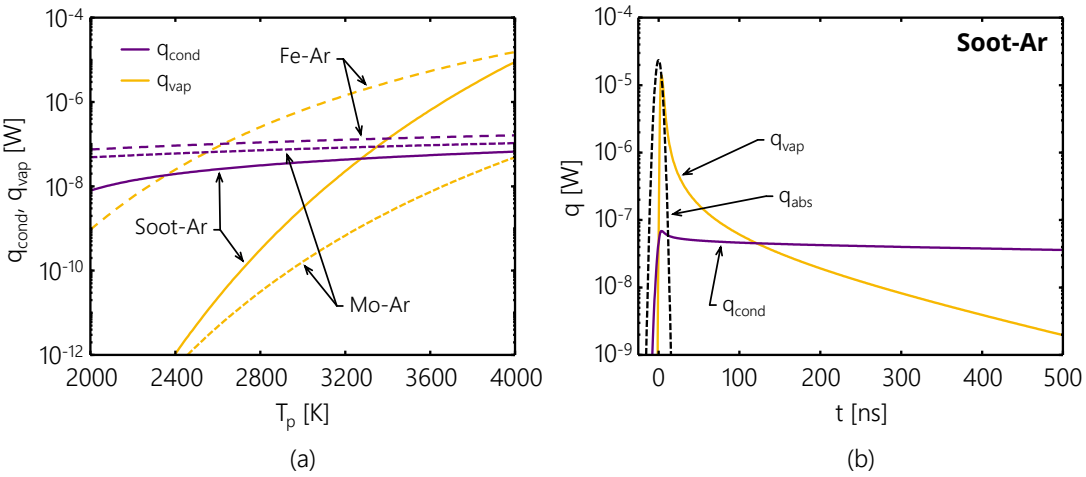

Figure 2.8 The significance of the absorption, conduction, and vaporization heat transfer modes (a) as a function of nanoparticle temperature and (b) as a function of time after the peak laser fluence. For (a), the case of Soot-Ar, Fe-Ar, and Mo-Ar are shown. The models used to generate the curves correspond to that proposed in Chapter 6 for soot and that used in Chapter 8 for Fe and Mo. Vaporization becomes the dominant form of heat transfer at approximately 2630 K, 3275 K, and 4050 K for Fe, soot, and Mo respectively. For (b), the trends in the different modes are shown over time for the case of C-Ar at a fluence of 0.2 J/cm^2 and using the model from Chapter 6.

describe the unexpectedly rapid decay in the pyrometrically-defined temperature in the period immediately following the laser pulse [106,110,194,198]. Although several studies have suggested potential phenomena that could be responsible, including other emission phenomena [136], local gas heating [200,218], and aggregate collapse (based on the ideas in Refs. [41,219,220]), there is no consensus on the underlying cause. Several other researchers [117,123,221] have also observed a *retarded cooling* phenomenon shortly after the laser pulse for moderate to high laser fluences. While the current work does not explicitly seek to resolve these known problems, it does provide tools that will allow more in-depth investigation of these phenomena that could answer remaining questions.

Chapter 3
Inference, model inversion, and the Bayesian framework

The previous chapter has established the forward model for nanoparticle emission and cooling, which is used to calculate the expected incandescent emission and particle temperature from a known set of thermophysical properties of the aerosol. In practice, however, practitioners want to do the inverse: measuring the incandescence to determine the temperature or the thermophysical properties of the aerosol. A schematic demonstrating the typical structure of the TiRe-LII inference problem is shown in Figure 3.1. Traditionally, the spectroscopic and heat transfer models are inverted separately to obtain quantities-of-interest. This chapter discusses this approach to model inversion, as well as the case of coupling the spectroscopic and heat transfer models. Further, this chapter also discusses how uncertainty quantification can be incorporated into these procedures, highlighting the Bayesian approach in Section 3.3.

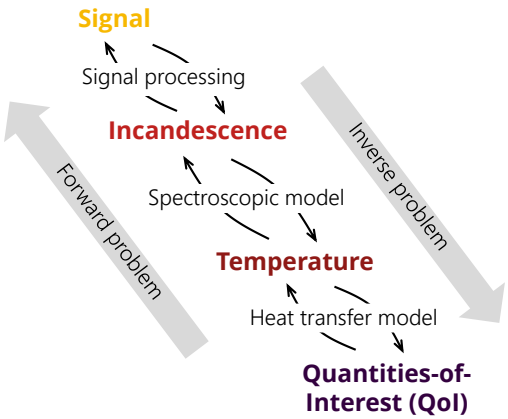

Figure 3.1 Schematic demonstrating the typical structure of inference from TiRe-LII data, often featuring three phases: (i) signal processing, (ii) spectrocopic modeling, and (iii) heat transfer modeling.

3.1 Model inversion

3.1.1 Inverting the spectroscopic model

The measured spectral signal in volts at any given time can be written in terms of the modeled signal, as defined in Section 2.1.3, and as a system of non-linear equations,

$$\tilde{\mathbf{s}}_{\mathrm{i}}^{\mathrm{meas}} = \tilde{\mathbf{s}}_{\mathrm{i}}^{\mathrm{mod}}\left(T_{\mathrm{p,i}}, \Lambda_{\mathrm{i}}\right) + \boldsymbol{\varepsilon}_{\mathrm{i}}^{\mathrm{s}} = \frac{\Lambda \cdot \eta_{\lambda}}{C}\mathbf{J}_{\mathrm{i}} + \boldsymbol{\varepsilon}_{\mathrm{i}}^{\mathrm{s}}, \tag{3.1}$$

where $\tilde{\mathbf{S}}_{\mathrm{i}}^{\mathrm{meas}} = [(\tilde{S}_{1,\mathrm{i}}^{\mathrm{meas}}), (\tilde{S}_{2,\mathrm{i}}^{\mathrm{meas}}), \ldots]^{\mathrm{T}}$ is a vector containing the measured signal at multiple wavelengths, $\tilde{\mathbf{S}}_{\mathrm{i}}^{\mathrm{mod}} = [(\tilde{S}_{1,\mathrm{i}}), (\tilde{S}_{2,\mathrm{i}}), \ldots]^{\mathrm{T}}$ is an analogous vector defined for the modeled signal, where each row corresponds to evaluating any of Eqs. (2.14)-(2.18) at a specific wavelength, and $\boldsymbol{\varepsilon}_{\mathrm{i}}^{\mathrm{s}}$ is some measurement error vector. The spectroscopic model can then be inverted by finding the value of $T_{\mathrm{p,i}}$ that best corresponds to the measured value. There are various ways to do this. Most generally, this inversion can be performed by defining some cost or objective function on the difference between the experimental and modeled signal,

$$\left[T_{\mathrm{p,i}}, \Lambda_{\mathrm{i}}\right]^{\mathrm{T}} = \underset{T_{\mathrm{p,i}}, \Omega_{\mathrm{i}}}{\arg\min}\left\{L\left[\tilde{\mathbf{s}}_{\mathrm{i}}^{\mathrm{meas}} - \tilde{\mathbf{s}}_{\mathrm{i}}^{\mathrm{mod}}\left(T_{\mathrm{p,i}}, \Lambda_{\mathrm{i}}\right)\right]\right\}, \tag{3.2}$$

where $L(\cdot)$ is the cost function that is to be minimized. Such treatments amount to spectral fitting and are the de facto methods for measurements considering more than two wavelengths (cf. [14,28]). Most often a quadratic loss is chosen for the cost function to return the least-squared estimate,

$$\left[T_{\mathrm{p,i}}^{\mathrm{LSQ}}, \Lambda_{\mathrm{i}}^{\mathrm{LSQ}}\right]^{\mathrm{T}} = \underset{T_{\mathrm{p}}, \Omega}{\arg\min}\left\{\left\|\tilde{\mathbf{s}}_{\mathrm{i}}^{\mathrm{meas}} - \tilde{\mathbf{s}}_{\mathrm{i}}^{\mathrm{mod}}\left(T_{\mathrm{p,i}}, \Lambda_{\mathrm{i}}\right)\right\|_2^2\right\}, \tag{3.3}$$

where $\|\cdot\|_2$ denotes the two-norm. This procedure can be statistically justified in the case of normally-distributed, homoscedastic measurement error (as will be shown in the context of the Bayesian framework in Section 3.3.3). This approach can be modified to account for *heteroskedasticity* (having uncertainties that vary across the data set) in the measurement error by weighting the signal at each wavelength differently, amounting to weighted least-squares. Theoretically and with proper calibration, Λ_{i} can be determined *a priori*, reducing the dimension of the problem and allowing for inference of the temperature using single wavelength measurements. However, there remain concerns regarding the accuracy with which Λ_{i} can be determined, which is the focus of Chapter 6.

In the case of *two-color* or *auto-compensating* LII (AC-LII) [145], the system formed by Eq. (3.1) is composed of two equations and, excluding the unknown error term, two unknowns. If one also invokes Wien's approximation to Planck's law,

$$I_{\mathrm{b},\lambda}\left(T_{\mathrm{p,i}},d_{\mathrm{p}}\right)\approx\frac{2hc^{2}}{\lambda^{5}}\left[\exp\left(\frac{hc}{\lambda k_{\mathrm{B}}T_{\mathrm{p,i}}\left(d_{\mathrm{p}}\right)}\right)\right]^{-1}, \tag{3.4}$$

which is valid for $\lambda k_{\mathrm{B}}T \ll hc$, and assumes a monodisperse aerosol, the solution for the temperature at any given time can be found analytically by taking the ratio of the signals (that is, by using *ratio pyrometry*),

$$T_{\mathrm{p,i}}^{2\mathrm{C}}\approx\frac{hc}{k_{\mathrm{B}}}\left(\frac{1}{\lambda_{2}}-\frac{1}{\lambda_{1}}\right)\left[\ln\left(\frac{\tilde{s}_{1,\mathrm{i}}^{\mathrm{meas}}\eta_{\lambda_{2}}E\left(\mathbf{m}_{\lambda_{2}}\right)\lambda_{1}^{6}}{\tilde{s}_{2,\mathrm{i}}^{\mathrm{meas}}\eta_{\lambda_{1}}E\left(\mathbf{m}_{\lambda_{1}}\right)\lambda_{2}^{6}}\right)\right]^{-1}=\frac{hc^{2}}{k_{\mathrm{B}}}\left(\frac{1}{\lambda_{2}}-\frac{1}{\lambda_{1}}\right)\left[\ln\left(\frac{\tilde{s}_{\mathrm{r}}^{\mathrm{meas}}\lambda_{r}^{6}}{\eta_{\mathrm{r}}E\left(\mathbf{m}\right)_{\mathrm{r}}}\right)\right]^{-1}, \tag{3.5}$$

where λ_1 and λ_2 are the detection wavelengths and $\lambda_{\mathrm{r}} = \lambda_1/\lambda_2$, $\tilde{s}_{\mathrm{r}}^{\mathrm{meas}}$, η_{r}, and $E(\mathbf{m})_{\mathrm{r}}$ are the ratios of the respective quantities at the two wavelengths. In this approach to calculating the temperature, the ISF and explicit nanoparticle size dependencies cancel out and are generally disregarded by researchers. Chapter 6 revisits this calculation and examines how explicit inference of the ISF and its temporal variation can be exploited to learn more about the measured signal.

These procedures are complicated by the inclusion of polydispersity, wherein the true signal is rather given by Eq. (2.15),

$$\tilde{s}_{\mathrm{j,i}}^{\mathrm{mod}}=\Lambda\cdot\eta_{\mathrm{j}}\int_{d_{\mathrm{p}}}C_{\mathrm{abs},\lambda_{\mathrm{j}}}\left(d_{\mathrm{p}}\right)I_{\mathrm{b},\lambda_{\mathrm{j}}}\left[T_{\mathrm{p,i}}\left(d_{\mathrm{p}}\right)\right]\cdot p\left(d_{\mathrm{p}}\right)\cdot\mathrm{d}d_{\mathrm{p}}\,. \tag{3.6}$$

In this case, the temperature derived from either spectral fitting or Eq. (3.5) is a so-called *effective temperature*, corresponding to a weighted average of the temperature of different sized nanoparticles in the aerosol. The weighting of any nanoparticle size class is highly non-linear, increasingly rapidly with nanoparticle size. For nanoparticles in the Rayleigh regime, Eq. (3.6) can be alternatively stated as

$$\tilde{s}_{\lambda,\mathrm{i}}^{\mathrm{mod}}=\Lambda\cdot\eta_{\mathrm{j}}\int_{d_{\mathrm{p}}}\frac{\pi^{2}d_{\mathrm{p}}^{3}}{\lambda_{\mathrm{j}}}E\left(\mathbf{m}_{\lambda_{\mathrm{j}}}\right)I_{\mathrm{b},\lambda_{\mathrm{j}}}\left[T_{\mathrm{p,i}}\left(d_{\mathrm{p}}\right)\right]\cdot p\left(d_{\mathrm{p}}\right)\cdot\mathrm{d}d_{\mathrm{p}}\,, \tag{3.7}$$

revealing a cubic increase in the significance of emission as the nanoparticle diameter increases. Convolved with this effect is the fact that larger nanoparticles stay at elevated temperatures for longer periods of time following the laser pulse and thus further dominate emission later in the signal. Including this effect in TiRe-LII analyses requires consideration of the coupling of the spectroscopic and heat transfer models, a topic discussed further in Section 3.1.3.

3.1.2 Inverting the heat transfer model

Inversion of the heat transfer model transforms the nanoparticle temperature inferred by inverting the spectroscopic model to nanoparticle characteristics or quantities-of-interest (QoI). Since the forward model requires the solution of a system of ODEs, the model is generally non-linear. Practitioners originally focused on measuring TiRe-LII signals at two instances in time and used those two points during model inversion [87–89]. More recently, however, least-squares minimization through non-linear programming has become the default method used to invert the heat transfer model. As with the general case of inverting the spectroscopic model, this involves defining some kind of cost or objective function,

$$\mathbf{x}^{\mathrm{LSQ}} = \arg\min_{\mathbf{x}} \left\{ L\left[\mathbf{T}_{\mathrm{p}}^{\mathrm{meas}} - \mathbf{T}_{\mathrm{p}}^{\mathrm{mod}}\left(\mathbf{x}\right) \right] \right\}, \tag{3.8}$$

where $\mathbf{x}$ is a vector of some QoI in which the practitioner is interested and $\mathbf{T}_{\mathrm{p,i}} = [\, T_{\mathrm{p},1},\ T_{\mathrm{p},2}, \ldots]^{\mathrm{T}}$ is a vector containing the temperature at multiple times. As with Eq. (3.2), the choice of a cost function composed of the sum of the squares of the residual would result in a least-squares procedure, where

$$\mathbf{x}^{\mathrm{LSQ}} = \arg\min_{\mathbf{x}} \left\{ \left\| \mathbf{T}_{\mathrm{p}}^{\mathrm{meas}} - \mathbf{T}_{\mathrm{p}}^{\mathrm{mod}}\left(\mathbf{x}\right) \right\|_2^2 \right\}. \tag{3.9}$$

Moreover, similar modifications can be made to account for heteroskedasticity by weighting the temperature data differently based on the amount of measurement error, which grows considerably over the duration of the signal.

As with the spectroscopic model, polydispersity is known to cause problems in the latter portion of the signal where emission is dominated by large nanoparticles. In these cases, the effective temperature decay inferred from the measured incandescence signal cannot be modeled using the heat transfer submodel alone, instead requiring consideration of the coupled heat transfer and spectroscopic submodels as discussed in the following section.

3.1.3 Inverting the coupled spectroscopic and heat transfer models

An alternative approach to this problem is to invert the spectroscopic and heat transfer submodels simultaneously, that is to infer the nanoparticle properties directly from the measured incandescence signal by embedding the heat transfer model into the spectroscopic model. As noted in both of the preceding sections, such an approach is necessary in the case of polydispersity. For an embedded heat transfer submodel, a least-squares approach can again be taken, so that

$$\mathbf{x} = \arg\min_{\mathbf{x}} \left\{ \left\| \mathbf{s}^{\text{meas}} - \mathbf{s}^{\text{mod}}\left(\mathbf{x}\right) \right\|_2^2 \right\}, \tag{3.10}$$

where **s** is a vector containing the measured or modeled signal, in this case composed of the signal at all times and wavelengths. Such an approach is often more computationally costly as it involves fitting to the signal at all times and wavelengths simultaneously. Also, unlike the approach described in Section 3.1.1, this procedure requires a simultaneous method for determining changes in T_{p} and Λ over time. While the heat transfer submodels available to predict the temperature decay are superfluous through the literature, models to account for temporal variations in Λ are effectively non-existent (motivating Chapter 6). Most practitioners consider that Λ does not change over the duration of the signal or only declines due to mass loss. This forms the basis for studies such as Roth and Filippov [91] and Hadwin et al. [222]. Unfortunately, several studies, including the interpretation of the data in Chapter 6, have indicated that there are temporal variations in Λ that cannot be captured by this treatment [49,80,131,145,222]. These observations make the embedded model approach challenging and unfavorable in the simple case of a monodisperse nanoparticle size distribution. Consequently, this approach is avoided in this work except when polydispersity is considered.

For the polydisperse cases, an approach to avoid having to calculate Λ is to first convert the observed incandescence to an effective temperature, following the procedure of Section 3.1.1 assuming that the aerosol is monodisperse. One then derives the equivalent modeled effective temperature by first solving the heat transfer submodel for a series of nanoparticle size classes and then using these as an input to numerically integrate Eq. (3.6),

$$\tilde{s}_{\text{j,i}}^{\text{mod}} \approx \Lambda \cdot \eta_{\text{j}} \sum_{k} C_{\text{abs},\lambda_{\text{j}}}\left(d_{\text{p,k}}\right) I_{\text{b},\lambda_{\text{j}}}\left[T_{\text{p,i}}\left(d_{\text{p,k}}\right)\right] \cdot p\left(d_{\text{p,k}}\right) \Delta d_{\text{p,k}}\,, \tag{3.11}$$

where $\Delta d_{\text{p,k}}$ corresponds to the discretization level at the k^{th} nanoparticle size class. Finally, the modeled effective temperature is derived by applying an analogous procedure as was performed on the experimental signal to the modeled signal. Fitting proceeds by comparing the modeled and observed effective temperature using non-linear optimization.

Even when using this procedure, complications can be encountered when inferring the nanoparticle size distribution. In this case, Eq. (3.6) forms a Volterra integral equation of the first kind (IFK) [223],

$$\tilde{s}_{\text{j,i}}^{\text{mod}} = \Lambda \cdot \eta_{\text{j}} \int_{d_{\text{p}}} K_{\text{j}}\left(d_{\text{p}}, t_{\text{i}}\right) \cdot p\left(d_{\text{p}}\right) \cdot \mathrm{d}d_{\text{p}}\,, \tag{3.12}$$

where

$$K_j\left(d_p,t_i\right)=C_{abs,\lambda_j}\left(d_p\right)I_{b,\lambda_j}\left[T_{p,i}\left(d_p\right)\right] \tag{3.13}$$

is called the *kernel* and contains the embedded heat transfer submodel. During inversion, the smoothing operation of Eq. (3.12) makes the problem of solving for an ambiguous nanoparticle size distribution from a measured signal mathematically ill-posed [224]. The approach taken to avoid this pitfall is to regularize the problem by adding information known beforehand, that is *a priori*. TiRe-LII practitioners most often do this by assuming that the nanoparticle size distribution is lognormal,

$$p\left(d_p\right)=\frac{1}{d_p\ln\left(\sigma_g\right)\left(2\pi\right)^{1/2}}\exp\left[-\left(\frac{\ln\left(d_p\right)-\ln\left(d_{p,g}\right)}{2^{1/2}\ln\left(\sigma_g\right)}\right)^2\right], \tag{3.14}$$

where $d_{p,g}$ and σ_g are the geometric mean and standard deviation. This reduces the dimension of the problem to that of inferring two parameters, $d_{p,g}$ and σ_g, thereby resolving much of the ill-posedness. Nevertheless, uncertainties remain due to collinearity between the inferred parameters. This has been noted by several practitioners who found a family of solutions for the distribution parameters that describe the effective temperature decay [45,48,113,225]. This effect is significantly amplified by model parameter uncertainties, a fact which motivates a discussion of robust uncertainty quantification.

3.2 Uncertainty quantification

When inverting these models, simply inferring point estimates of the nanoparticle characteristics is not sufficient; one must also ascertain the uncertainty attached to those quantities. This topic contributes considerably to the content of this document. Several approaches to uncertainty quantification exist in the TiRe-LII literature. Will et al. [89], for example, inferred nanoparticle sizes using statistical replication from ten groups of 50 signals. The range in the value of the repeatedly inferred quantities allowed for an estimate of uncertainties in the nanoparticle size resulting from signal noise.

Roth and Filippov [91] were the first to note that inference of the nanoparticle size distribution from TiRe-LII signals involves an IFK, as discussed in Section 3.1.3. This results in a series of solutions that can reproduce the data. This relationship has often been visualized using the chi-squared function [45,47–49,101,131,225,226], which can be defined generally in matrix form as

$$\chi^2\propto\left(\mathbf{b}^{meas}-\mathbf{b}^{mod}\right)^T\left(\mathbf{\Sigma}^b\right)^{-1}\left(\mathbf{b}^{meas}-\mathbf{b}^{mod}\right), \tag{3.15}$$

where $\mathbf{b}^{\text{meas}}$ is the measured data, which can correspond to the temperature when inverting the heat transfer submodel or the incandescence signal when inverting the spectroscopic submodel; $\mathbf{b}^{\text{mod}}$ is the modeled data; and $\mathbf{\Sigma}^{\text{b}}$ is the covariance of the data. In the case of independent noise, then the covariance matrix is diagonal, $\boldsymbol{\sigma}^{\text{b}} = \text{diag}(\mathbf{\Sigma}^{\text{b}})$, and the chi-squared function can be rewritten as

$$\chi^2 \propto \sum_i \left(\frac{b_i^{\text{meas}} - b_i^{\text{mod}}}{\sigma_i^{\text{b}}} \right)^2 = \left\| \frac{b_i^{\text{meas}} - b_i^{\text{mod}}}{\sigma_i^{\text{b}}} \right\|_2^2 . \tag{3.16}$$

It is worth noting that this corresponds to the weighted sum-of-squares with a weighting related to the measurement error in $\mathbf{b}$ and is also closely related to the log-likelihood function resulting from a Bayesian approach (cf. Section 3.3.3). Studies inferring the nanoparticle size distribution width and mean noted a characteristic shape of the chi-squared function, featuring a valley of solutions that produce similar values of the chi-squared function. The chi-squared function for the case of Si-Ar, based on the data of Sipkens et al. [48], is shown in Figure 3.2. Similar valleys have also been noted in Refs. [45,47,101,226] and to a lesser extent in Ref. [225]. It should be noted that while this valley represents structure in the model inversion, often uncertainties resulting from measurement errors are minimized by averaging over multiple shots, centralizing the uncertainty bounds to a local region in this valley (see the result of sampling methods in Ref. [48]). These bounds again expand, however, when model parameter uncertainties are incorporated into the analysis.

Liu et al. [113] noted that the family of solutions resulting from the above inversion can be approximated by a single Sauter mean diameter, $d_{\text{p,32}}$, defined as

$$d_{\text{p,32}} \equiv \frac{\int_0^\infty d_{\text{p}}^3 p\left(d_{\text{p}}\right) \text{d}d_{\text{p}}}{\int_0^\infty d_{\text{p}}^2 p\left(d_{\text{p}}\right) \text{d}d_{\text{p}}} . \tag{3.17}$$

This quantity can be inferred in the place of the geometric mean to reduce uncertainties. The preference for this quantity over the geometric mean results from the structure of the problem described in Chapter 2, wherein the heat transfer submodel contains a sensible energy term that is proportional to the volume of the nanoparticle (d_{p}^3) and cooling terms that are proportional to the surface area of the nanoparticle (d_{p}^2). For a lognormal size distribution, the Sauter mean diameter can be computed analytically,

$$d_{\text{p,32}} = d_{\text{p,g}} \cdot \exp\left[\frac{5}{2} \ln\left(\sigma_{\text{g}}\right)^2 \right]. \tag{3.18}$$

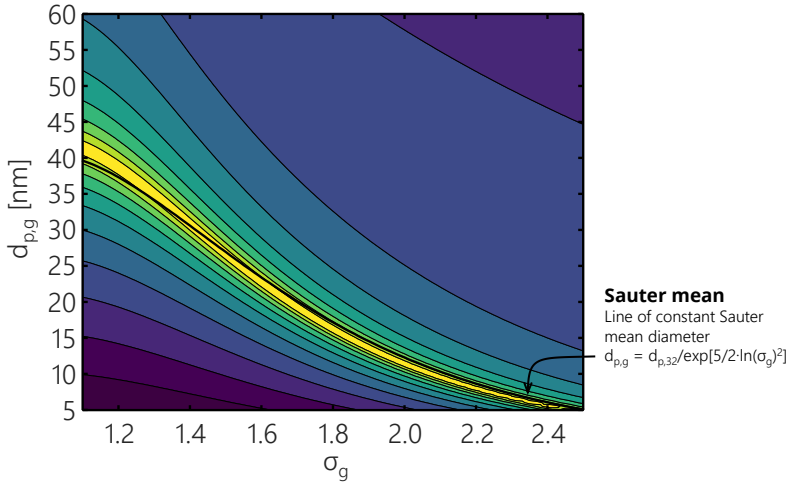

Figure 3.2 Logarithmic contours of the chi-squared function for simultaneous inference of the geometric mean and standard deviation of the nanoparticle size distribution for silicon, based on temperature data from Sipkens et al. [48]. The relationship indicates a valley of solutions that can model the data relatively well. Also indicated is a line of constant Sauter mean diameter.

Daun et al. [225] and Sipkens et al. [48] later showed that this curve runs along a path similar in shape to the valley noted in the chi-squared function, affirming the observation of Liu and coworkers. A sample line of constant Sauter mean diameter is included in Figure 3.2 to demonstrate this principle.

More recently, practitioners have increasingly inferred the nanoparticle size simultaneously with the thermal accommodation coefficient from TiRe-LII data. This presents its own challenges in terms of uncertainties. Kock et al. [21] noted how several combinations of the nanoparticle diameter and TAC could produce similar temperature decays for low laser fluences. Later, Sipkens et al. [131] visualized the chi-squared function for simultaneous inference of the nanoparticle diameter and TAC from TiRe-LII measurements on molybdenum nanoparticles. This analysis revealed that simultaneous inference of the nanoparticle size and TAC is not possible for molybdenum nanoparticles. This is a result of the parameters appearing in a fixed ratio, so that they cannot be distinguished in the case that cooling is restricted to conductive cooling. The cross-examination of multiple materials in Chapter 8 highlights and solidifies these observations, noting specifically when independent inference of the TAC and nanoparticle size is possible.

Alternative approaches are generally taken to consider how uncertainties in model parameters propagate through to inferred quantities, most commonly using perturbation or relative sensitivity analyses. These analyses consider how the uncertainties in some model parameter, θ_j, propagates through to an inferred quantity, x_i, by approximating the model as locally linear. In this case, the error is approximated by

$$\varepsilon_i^x = \varepsilon_j^\theta \cdot \left(\left. \frac{\partial x_i}{\partial \theta_j} \right|_{\theta_i^0} \right) \approx \varepsilon_j^\theta \cdot \left(\left. \frac{\Delta x_i}{\Delta \theta_j} \right|_{\theta_i^0} \right), \tag{3.19}$$

where ε_i^x is the uncertainty in the i^{th} inferred quantity, ε_j^θ is the uncertainty assigned to the j^{th} model parameter prior to measurement, and θ_j^0 is the nominal value of the j^{th} model parameter. The derivative is calculated by perturbing θ_j from its nominal value by $\Delta\theta_j$ and observing the change Δx_i in the i^{th} inferred quantity, amounting to a finite difference scheme. Will et al. [89] was the first to take such an approach in TiRe-LII, applying $\boldsymbol{\varepsilon}_\theta = \Delta\boldsymbol{\theta} = 0.1 \cdot \boldsymbol{\theta}^0$ to determine the sensitivity of the nanoparticle diameter to the optical properties, vaporization submodel parameters, and gas temperature. Similar approaches have been employed by various other authors [23,48,130,131,225,227].

Crosland et al. [228] took a more general approach to quantifying the uncertainties that propagate through the spectroscopic model, opting instead to use sampling methods. In this approach, the authors specified distributions for the various model parameters, such as the calibration constants, laser fluence, and soot optical properties. Proceeding with a Monte Carlo procedure, random values are sampled for each of these parameters from the prescribed distributions. The temperature and volume fraction are then determined repeatedly using the AC-LII procedure described above for each set of sampled model parameters. Upon sampling enough values, the results can be compiled to define distributions on the temperature and volume fraction, with the peak of the distribution representing a point estimate and the distribution width representing uncertainties propagated through the model. Such methods remove the assumption of a locally linear model and calculate the true distribution of uncertainty in inferred quantities, including the simultaneous incorporation of the measurement error. The authors also extended this analysis to include spatial information about uncertainties in the volume fraction throughout a flame. Analogous sampling methods were later adopted by Sipkens et al. [45,48,112] to propagate uncertainties due to heat transfer model parameters, such as the latent heat of vaporization and gas temperature, through to inferred nanoparticle diameters and TACs.

3.3 The Bayesian framework

In recent years, Bayesian treatments of the problem have become more prominent. Bayesian methods were originally developed in the early 19th century to incorporate incomplete and noisy data [229] and have since developed into a prominent approach to understanding problems in physics [230]. Bayesian inference was first used in the context of TiRe-LII by Sipkens et al. [1] on silicon data, where it was only used in the context of measurement error in the observed TiRe-LII signals. That work also used an uninformative prior and diagonal

data covariance, effectively reducing the problem to estimating the maximum likelihood estimate (MLE), discussed further in Section 3.3.3 below, by weighted least-squares regression. Analogous to the chi-squared plot introduced above, the authors plotted the value of the log-likelihood over an array of values for the QoI, $\mathbf{x}$, which revealed the relationship between $d_{p,g}$ and σ_g following inference (previously indicated in Figure 3.2). Sampling methods were used to probe the likelihood and evaluate credibility bounds. Follow-up work by Sipkens et al. [112] on iron adopted a very similar approach in quantifying uncertainties from measurement errors.

Subsequently, a series of works by Hadwin et al. [156,157,222] applied the Bayesian approach to the TiRe-LII spectroscopic model. The earlier works examined the role that uncertainties in the optical constants [156] and other model parameters [157], including the spatial laser fluence profile, have on inferred nanoparticle temperatures and volume fraction close to the peak TiRe-LII signal. The final work in that series [222] expanded on this treatment by considering the temperature, volume fraction, and nanoparticle size as non-stationary random variables, whose values are allowed to evolve over time. That work demonstrated how the Kalman filter can be used to improve TiRe-LII analyses by incorporating an evolution model to propagate uncertainties over the signal duration.

Menser et al. [49] incorporated the constants in the Clausius-Clapeyron as nuisance parameters using the Bayesian procedure during their inference of the nanoparticle mean and TAC. The authors applied appropriate priors to the nuisance parameters to improve the robustness of their estimates. The work proceeded to plot the posterior distribution over an array of values for the QoI. The contours revealed the expected shape, with the credibility bounds increasing when uncertainties in the Clausius-Clapeyron constants are incorporated.

3.3.1 Random variables

The Bayesian framework itself is based on random variables, that is parameters that, rather than having a single, deterministic value, are described stochastically by some distribution from which they take a random value. Such a treatment allows one to incorporate the uncertainties in the state-of-knowledge of quantities into models. As an example, consider that the measurement data, $\mathbf{b}$, whether it be temperature or incandescence, will contain some form of measurement error that can form the basis of a distribution. One could learn about this distribution by repeatedly exciting an aerosol with multiple laser shots. These processes are inherently random (that is, containing *aleatoric uncertainties*), so that a slightly different signal would be observed following each laser shot. A sample histogram for the signal at a given time, indicated in Figure 3.3, reveals how the signal could be distributed. This information can be encoded in a probability density function (pdf) that is said to describe the

random variable, in this case the signal. This pdf exhibits a higher value about values where the signal is more frequently observed. In this case, a normal distribution adequately describes the signal variation. Moreover, if the signal at each wavelength can be considered as normally distributed, the vector of signals over multiple wavelengths can be phrased in terms of a multivariate normal distribution. Mathematically, this is denoted as

$$\mathbf{s}_i^{\text{meas}} \sim \mathcal{N}\left(\mathbf{s}_i^{\text{mod}}, \mathbf{\Sigma}^s\right), \tag{3.20}$$

where $\mathbf{\Sigma}^s$ is a covariance matrix. Further consideration of the signal as a collection of random variables is the topic of Chapter 4.

The other model parameters, $\boldsymbol{\theta}$, including the optical properties or the boiling point of the material, also contain uncertainties. These can be understood as random variables, not because their true value is random, but because our state-of-knowledge of their true value can be encoded as a probability distribution (that is, *epistemic uncertainties*). Together, both these kinds of uncertainties can be propagated through to uncertainties in our QoI, which can themselves be understood as random variables having a distribution.

3.3.2 Bayes equation

In the context of data inference, knowledge about the QoI after performing a measurement is described by the posterior pdf, $p(\mathbf{x}|\mathbf{b})$. This quantity is calculated by Bayes' equation

$$p\left(\mathbf{x}|\mathbf{b}\right) = \frac{p\left(\mathbf{b}|\mathbf{x}\right) p_{\text{pr}}\left(\mathbf{x}\right)}{p\left(\mathbf{b}\right)}, \tag{3.21}$$

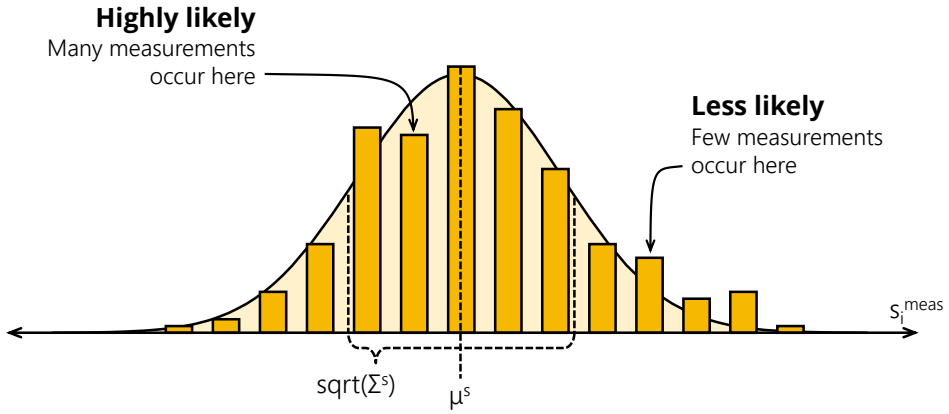

Figure 3.3 Schematic demonstrating the measurement of a TiRe-LII signal at a specific instant in time, $s_{j,i}^{\text{meas}}$, as a random variable. The histrogram represents binned samples of the signal over multiple shots. The distribution shown behind encodes this information into a normal distribution, where the signal measured during another laser shot can be understoof to take on a random value from that distribution.

where $p(\mathbf{b}|\mathbf{x})$ is the likelihood, $p_{\text{pr}}(\mathbf{x})$ is the prior, and $p(\mathbf{b})$ is the evidence, which is also denoted here as E. Model parameters not considered in the QoI are called nuisance parameters, $\boldsymbol{\theta}$, and can be included into this procedure by adding them to the inference

$$p\left(\mathbf{x},\boldsymbol{\theta}|\mathbf{b}\right)=\frac{p\left(\mathbf{b}|\mathbf{x},\boldsymbol{\theta}\right)p_{\text{pr}}\left(\mathbf{x},\boldsymbol{\theta}\right)}{E}. \tag{3.22}$$

Statistics on the QoI alone are then obtained by marginalizing the posterior over the nuisance parameters

$$p\left(\mathbf{x}|\mathbf{b}\right)=\int_{\boldsymbol{\theta}} p\left(\mathbf{x},\boldsymbol{\theta}|\mathbf{b}\right)\cdot\mathrm{d}\boldsymbol{\theta}=\frac{1}{E}\int_{\boldsymbol{\theta}} p\left(\mathbf{b}|\mathbf{x},\boldsymbol{\theta}\right)p_{\text{pr}}\left(\mathbf{x},\boldsymbol{\theta}\right)\cdot\mathrm{d}\boldsymbol{\theta}. \tag{3.23}$$

Such integrals can be challenging to compute if $\boldsymbol{\theta}$ is of a high dimension, often requiring sampling methods or simplifying assumptions to make the problem analytically tractable. For ease of notation, a parameter $\boldsymbol{\phi}=[\mathbf{x}^{\text{T}},\boldsymbol{\theta}^{\text{T}}]^{\text{T}}$ is defined so that Bayes equation can equivalently be written as

$$p\left(\boldsymbol{\phi}|\mathbf{b}\right)=\frac{p\left(\mathbf{b}|\boldsymbol{\phi}\right)p_{\text{pr}}\left(\boldsymbol{\phi}\right)}{E}, \tag{3.24}$$

which is the form used through the remainder of this chapter.

3.3.3 The likelihood

The likelihood, $p(\mathbf{b}|\boldsymbol{\phi})$, relates the measured data to the QoI and nuisance parameters, $\boldsymbol{\phi}$. For TiRe-LII, such a distribution is closely related to the one depicted in Figure 3.3 in that the measurement and model errors are encoded into a distribution. The distribution is phrased as a function of $\boldsymbol{\phi}$ however. In this respect, if evaluating a model at a given $\boldsymbol{\phi}$ does not give results that match the data, the probability associated with that value of $\boldsymbol{\phi}$ should be lower. Typically, though not always, the vector of observations is well-modeled as a multivariate normal distribution with respect to $\mathbf{b}$, in which case

$$\begin{aligned} p\left(\mathbf{b}|\boldsymbol{\phi}\right)&=\left|2\pi\boldsymbol{\Sigma}^{\text{b}}\right|^{-1/2}\exp\left\{-\frac{1}{2}\left(\mathbf{b}^{\text{meas}}-\mathbf{b}^{\text{mod}}\left(\boldsymbol{\phi}\right)\right)^{\text{T}}\left(\boldsymbol{\Sigma}^{\text{b}}\right)^{-1}\left(\mathbf{b}^{\text{meas}}-\mathbf{b}^{\text{mod}}\left(\boldsymbol{\phi}\right)\right)\right\} \\ &=\left|2\pi\boldsymbol{\Sigma}^{\text{b}}\right|^{-1/2}\exp\left\{-\frac{1}{2}\left\|\mathbf{L}^{\text{b}}\left[\mathbf{b}^{\text{meas}}-\mathbf{b}^{\text{mod}}\left(\boldsymbol{\phi}\right)\right]\right\|_2^2\right\} \end{aligned}, \tag{3.25}$$

where $|\cdot|$ denotes the determinant, $\mathbf{b}^{\text{meas}}$ is a vector of experimental data, $\mathbf{b}^{\text{mod}}(\boldsymbol{\phi})$ is modeled data, $\boldsymbol{\Sigma}^{\text{b}}$ is the covariance of model errors and measurement noise, and $\mathbf{L}$ = chol($\boldsymbol{\Sigma}^{-1}$) is the Cholesky factor of the inverse covariance matrix. In the special case of independent error, $\boldsymbol{\Sigma}^{\text{b}}$ is a diagonal matrix containing the variance of each observation, and $\mathbf{L}^{\text{b}}$ is a diagonal matrix containing the inverse of the standard deviation of each observation. Maximizing Eq. (3.25) gives the maximum likelihood estimate (MLE) of $\boldsymbol{\phi}$, which is expressed as

$$\boldsymbol{\phi}^{\text{MLE}} = \arg\min_{\boldsymbol{\phi}} \left\{ \left\| \mathbf{L}^{\text{b}} \left[\mathbf{b}^{\text{meas}} - \mathbf{b}^{\text{mod}}\left(\boldsymbol{\phi}\right) \right] \right\|_2^2 \right\}. \tag{3.26}$$

It is worth noting that this expression shares a form with that of a least-squares analysis (shown above in Section 3.1) and provides a way of understanding the assumptions that enter into the adoption of the latter procedure. For systems with independent errors, the MLE will be the weighted least-squares estimate where the weighting is the inverse of the standard deviation of the error for each data point in $\mathbf{b}$. Figure 3.4 demonstrates the principle of the likelihood with respect to a TiRe-LII signal. At each point in time, a distribution is defined about the signal measured at that point in time with model results farther from the signal being considered less probable. Also shown is the model evaluated at a hypothetical $\boldsymbol{\phi}^{\text{A}}$ and $\boldsymbol{\phi}^{\text{B}}$. The case of $\boldsymbol{\phi}^{\text{B}}$ gives a curve that does not match the measured signal and will thus be less probable than the case of $\boldsymbol{\phi}^{\text{A}}$, which can reproduce the data.

For large datasets (that is, for large $\mathbf{b}$), the exponential of the negative of the norm in the likelihood will be nearly zero, which can introduce numerical instabilities when evaluating the likelihood. For this reason, it is often more convenient to work in terms of the log-likelihood, defined as

$$\begin{aligned} \log\left[p\left(\mathbf{b}|\boldsymbol{\phi}\right) \right] &= \log\left(\left| 2\pi\boldsymbol{\Sigma}^{\text{b}} \right|^{-1/2} \right) - \frac{1}{2} \left(\mathbf{b}^{\text{meas}} - \mathbf{b}^{\text{mod}}\left(\boldsymbol{\phi}\right) \right)^{\text{T}} \left(\boldsymbol{\Sigma}^{\text{b}} \right)^{-1} \left(\mathbf{b}^{\text{meas}} - \mathbf{b}^{\text{mod}}\left(\boldsymbol{\phi}\right) \right) \\ &= \log\left(\left| 2\pi\boldsymbol{\Sigma}^{\text{b}} \right|^{-1/2} \right) - \frac{1}{2} \left\| \mathbf{L}^{\text{b}} \left[\mathbf{b}^{\text{meas}} - \mathbf{b}^{\text{mod}}\left(\boldsymbol{\phi}\right) \right] \right\|_2^2 \end{aligned}. \tag{3.27}$$

This increases the stability of the problem, with ramifications for sampling methods and Bayesian model selection as discussed in Chapter 9. Furthermore, examination of Eq. (3.27) reveals that the log-likelihood shares much the same form as the chi-squared function defined in Eq. (3.15). As such, plotting the log-likelihood can visualize the relationship between parameters in an analogous manner, producing the same contours identified in Figure 3.2. This is exploited throughout this thesis as a way of visualizing the relationship between the parameters in $\boldsymbol{\phi}$, in cases where the number of parameters is limited to two or less (e.g. the relationship between d_{p} and α in Chapter 8).

It is noted that while Eq. (3.25) is multivariate normal with respect to $\mathbf{b}$, it is not necessarily multivariate normal with respect to $\boldsymbol{\phi}$. The latter case only occurs for linear models, that is when

$$\mathbf{b}^{\text{mod}} = \mathbf{A}\boldsymbol{\phi}, \tag{3.28}$$

where $\mathbf{A}$ is the sensitivity matrix containing the linear coefficients, which are invariant of $\boldsymbol{\phi}$. In this case, the likelihood can be phrased as

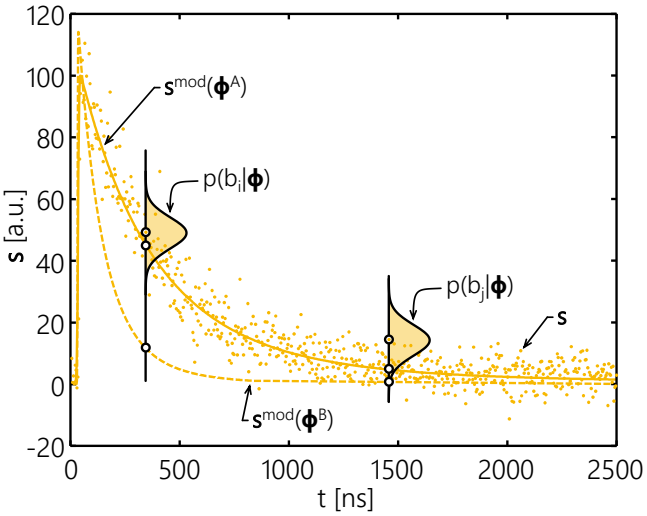

Figure 3.4 Demonstration of the likelihood. The pdf is defined about a measured data point, b_i, with a spread representative of the measurement noise and expected model errors. The likelihood will be lower for cases where there is a large discrepency between the modeled and measured signals. It is also notable that the likelihood will be the product of the value of this distribution over all time. In this respect, $\boldsymbol{\phi}^A$ is significantly preferred (having a higher likelihood) over $\boldsymbol{\phi}^B$.

$$\begin{aligned} p\left(\mathbf{b}|\boldsymbol{\phi}\right) &= \left|2\pi\boldsymbol{\Sigma}^{\mathrm{b}}\right|^{-1/2} \exp\left\{-\frac{1}{2}\left(\mathbf{b}^{\mathrm{meas}}-\mathbf{A}\boldsymbol{\phi}\right)^{\mathrm{T}}\left(\boldsymbol{\Sigma}^{\mathrm{b}}\right)^{-1}\left(\mathbf{b}^{\mathrm{meas}}-\mathbf{A}\boldsymbol{\phi}\right)\right\} \\ &= \left|2\pi\boldsymbol{\Sigma}^{\mathrm{b}}\right|^{-1/2} \exp\left\{-\frac{1}{2}\left\|\mathbf{L}^{\mathrm{b}}\left(\mathbf{b}^{\mathrm{meas}}-\mathbf{A}\boldsymbol{\phi}\right)\right\|_2^2\right\} \end{aligned}. \tag{3.29}$$

For non-linear models the likelihood can deviate significantly from multivariate normal with respect to $\boldsymbol{\phi}$ over a large domain (Figure 3.2 demonstrates one such case). In these cases, it is often useful to invoke Laplace's approximation [230,231], in which the log-likelihood is approximated by a Taylor series expansion about the MLE,

$$\log\left[p\left(\mathbf{b}|\boldsymbol{\phi}\right)\right] \approx \log\left[p\left(\mathbf{b}|\boldsymbol{\phi}^{\mathrm{MLE}}\right)\right] + \nabla\log\left[p\left(\mathbf{b}|\boldsymbol{\phi}\right)\right]\left(\boldsymbol{\phi}-\boldsymbol{\phi}^{\mathrm{MLE}}\right) \tag{3.30}$$

or

$$p\left(\mathbf{b}|\boldsymbol{\phi}\right) \approx C\exp\left[\left(\boldsymbol{\phi}-\boldsymbol{\phi}^{\mathrm{MLE}}\right)^{\mathrm{T}}\mathbb{J}^{\mathrm{T}}\left(\boldsymbol{\Sigma}^{\mathrm{b}}\right)^{-1}\mathbb{J}\left(\boldsymbol{\phi}-\boldsymbol{\phi}^{\mathrm{MLE}}\right)\right], \tag{3.31}$$

where

$$C = \left|2\pi\boldsymbol{\Sigma}^{\mathrm{b}}\right|^{-1/2}\exp\left[-\frac{1}{2}\left(\mathbf{b}^{\mathrm{meas}}-\mathbb{J}\boldsymbol{\phi}^{\mathrm{MLE}}\right)^{\mathrm{T}}\left(\boldsymbol{\Sigma}^{\mathrm{b}}\right)^{-1}\left(\mathbf{b}^{\mathrm{meas}}-\mathbb{J}\boldsymbol{\phi}^{\mathrm{MLE}}\right)\right] \tag{3.32}$$

and $\mathbb{J}$ is the *Jacobian*. The Jacobian is defined as the sensitivity of a modeled data point to an input parameter, that is

$$\mathbb{J}_{ij} = \frac{\partial\left(b_i^{meas} - b_i^{mod}\right)}{\partial\phi_j} = \frac{\partial b_i^{mod}}{\partial\phi_j}, \tag{3.33}$$

which is evaluated about the MLE in this case. This approach is convenient in that many optimization routines output the Jacobian for use in these calculations. By this definition, $\mathbb{J} = \mathbf{A}$ for a linear model. Laplace's approximation has been shown to be valid for TiRe-LII under specific conditions [156] and will be used alongside sampling techniques for rapid uncertainty quantification.

3.3.4 The prior

The prior, $p_{pr}(\boldsymbol{\phi})$, contains the state-of-knowledge of the QoI and nuisance parameters known a priori. There are multiple ways to encode information into priors. In this thesis, two types of priors are employed. The first is the uninformative prior, which states that the practitioner does not know anything about $\boldsymbol{\phi}$ a priori or, equivalently, that all of the information about $\boldsymbol{\phi}$ should be derived from the data through the likelihood. As a result, the posterior will be identical to the likelihood. The second is the maximum entropy prior. These priors minimize the information content of the priors, subject to the constraints derived from testable information available in the literature (cf. [232]). Most often, these are point estimates and uncertainties (e.g. experimental uncertainties or uncertainties derived from the range of values reported in the literature) which justifies a multivariate normal prior [233],

$$p_{pr}\left(\boldsymbol{\phi}\right) = \left|2\pi\boldsymbol{\Sigma}^{pr}\right|^{-1/2} \exp\left\{-\frac{1}{2}\left\|\mathbf{L}^{pr}\left(\boldsymbol{\phi} - \boldsymbol{\phi}^{0}\right)\right\|_2^2\right\}, \tag{3.34}$$

where $\boldsymbol{\Sigma}^{pr}$ and $\boldsymbol{\phi}^0$ are the expected covariance and value for the QoI and $\mathbf{L}^{pr}$ is the Cholesky factorization of $\boldsymbol{\Sigma}^{pr}$. Within the context of TiRe-LII, priors can be placed on any number of parameters, ranging from the nanoparticle diameter to the boiling temperature.

3.3.5 The evidence

The evidence, $p(\mathbf{b})$ or E, gives the probability density of the observation, $\mathbf{b}$. It can be equally understood as normalizing the product of the likelihood and prior to conserve total probability in the posterior. Accordingly, it can be defined as

$$E = p(\mathbf{b}) = \int_{\boldsymbol{\phi}} p(\mathbf{b}|\boldsymbol{\phi}) p_{\text{pr}}(\boldsymbol{\phi}) \cdot \mathrm{d}\boldsymbol{\phi} = \int_{\mathbf{x}} \int_{\boldsymbol{\theta}} p(\mathbf{b}|\boldsymbol{\phi}) p_{\text{pr}}(\boldsymbol{\phi}) \cdot \mathrm{d}\boldsymbol{\theta} \cdot \mathrm{d}\mathbf{x} \,. \tag{3.35}$$

Evaluating the evidence in this manner requires computing an integral over all dimensions of $\boldsymbol{\phi}$, which can be computationally-intensive. This is particularly true in non-linear systems that contain high dimensional $\boldsymbol{\phi}$ or highly correlated information about $\boldsymbol{\phi}$. In TiRe-LII, Eq. (25) has historically been approximated with sampling methods, like wild bootstrapping [131] and Markov-chain Monte Carlo (MCMC) [48,112], or by invoking Laplace's approximation for the likelihood. This latter approach is demonstrated in Chapter 9.

3.3.6 The posterior

The posterior pdf combines the likelihood and prior to form a comprehensive solution in Bayesian inversion. Point estimates for $\boldsymbol{\phi}$ are often taken from the peak of the distribution, called the maximum a posteriori (MAP) estimate. As the evidence is not a function of $\boldsymbol{\phi}$, the posterior is proportional to the likelihood and the prior. Accordingly, maximizing the product of the likelihood and prior is sufficient to find the MAP. For the case of a multivariate normal likelihood and prior, one can find the MAP estimate using optimization methods to evaluate,

$$\begin{aligned} \boldsymbol{\phi}^{\text{MAP}} &= \arg\max_{\boldsymbol{\phi}} \left\{ p(\boldsymbol{\phi}|\mathbf{b}) \right\} \\ &= \arg\min_{\boldsymbol{\phi}} \left\{ \left\| \mathbf{L}^{\text{b}} \left[\mathbf{b}^{\text{meas}} - \mathbf{b}^{\text{mod}}(\boldsymbol{\phi}) \right] \right\|_2^2 + \left\| \mathbf{L}^{\text{pr}} \left(\boldsymbol{\phi} - \boldsymbol{\phi}^0 \right) \right\|_2^2 \right\} . \end{aligned} \tag{3.36}$$

Credibility intervals on and correlation between the QoI and nuisance parameters are obtained from the posterior covariance. This requires computation of the evidence, which, as per Section 3.3.5, can be computationally-intensive to compute. However, when a linear model is combined with prior distributions of the multivariate normal form, one can exploit the useful quality that the prior is a conjugate prior. In this case, the pdfs in Eqs. (3.25) and (3.34) can be combined to produce a multivariate normal posterior (a convenient property exploited in Chapter 9),

$$p(\boldsymbol{\phi}|\mathbf{b}) = \left| 2\pi \boldsymbol{\Sigma}^{\text{po}} \right|^{-1/2} \exp\left\{ -\frac{1}{2} \left\| \mathbf{L}^{\text{po}} \left(\boldsymbol{\phi} - \boldsymbol{\phi}^{\text{MAP}} \right) \right\|_2^2 \right\}, \tag{3.37}$$

where the posterior covariance is

$$\boldsymbol{\Sigma}^{\text{po}} = \left[\mathbf{L}^{\text{po}} \left(\mathbf{L}^{\text{po}} \right)^{\text{T}} \right]^{-1} = \left[\mathbf{A}^{\text{T}} \left(\boldsymbol{\Sigma}^{\text{b}} \right)^{-1} \mathbf{A} + \left(\boldsymbol{\Sigma}^{\text{pr}} \right)^{-1} \right]^{-1} . \tag{3.38}$$

In the non-linear but Laplace-approximated case, the posterior is also multivariate normal, with a posterior covariance defined by Eq. (3.38) except that the matrix $\mathbf{A}$ is approximated using the Jacobian, $\mathbb{J}$, as discussed in Section 3.3.3.

As with the likelihood above, the relationship between the parameters in ϕ can be visualized by plotting the posterior, or log-posterior, as a function of ϕ. This is possible in the case that distribution has two or fewer parameters in ϕ or in the case of marginalizing over enough parameters that this becomes true.

3.3.7 Outlook

The current work presents several advances to this Bayesian perspective. Chapter 4 examines our understanding of measurement errors in collected signals as a random variable and investigates how one can understand and analyze these errors to critique an experimental apparatus. Chapter 8 performs a Bayesian inference on TiRe-LII data from three types of non-carbonaceous nanoparticles, using the framework to estimate uncertainties and improve our understanding of the underlying physics. Finally, Chapter 9 uses the Bayesian perspective to demonstrate a method for selecting between competing models in a statistically robust fashion. This is particularly important given the plethora of competing, and often discordant, models available in the literature.

Chapter 4
Generalized measurement error model[1]

When interpreting LII data, it is important to understand how measurement error and noise relate to experimental design, signal processing procedures, uncertainty quantification, and variability in the measured process. Case and Hofeldt [76] for example, discuss the role of shot noise in the context of experimental design for LII measurements on diesel engine exhaust. They justify their selection of photomultiplier tubes (PMTs) over other devices based on their superior detection at low light levels. They also suggest that PMT voltage traces from multiple shots should be averaged to improve the signal-to-noise (SNR) ratio, which is now a nearly universal practice for aerosols having time-invariant properties. Will et al. [89] made similar statements about experimental design for spatially-resolved measurements on an ethylene laminar diffusion flame, specifically suggesting that the SNR can be improved by increasing the number of averaged shots or the detection optics aperture diameter. More recently, Mansmann et al. [200] proposed a new method of improving the SNR at longer cooling times, using gated PMTs to increase the dynamic range of detector instrument. Other practitioners make more general comments about the role of noise and the SNR on the experimental design of LII systems [56,80,217,234]. As noted in Chapter 3, yet other practitioners have propagated the uncertainties due to measurement error or noise through to uncertainties in quantities inferred from TiRe-LII data (e.g. [48,131,226,235]).

None of these studies, however, address the interaction between shot-to-shot variation in the aerosol and the observed measurement errors. Moreover, practitioners generally focus solely on reducing the amount of noise that is observed in TiRe-LII signals. This chapter approaches measurement errors from a different perspective: as a source of information that practitioners can leverage to provide important information about the LII

[1] Information presented in this chapter has been disseminated as:
Sipkens, T. A., Hadwin, P. J., Grauer, S. J., and Daun, K. J., 2017, "General error model for analysis of laser-induced incandescence signals," Appl. Opt., **56**(30), pp. 8436–8445. doi: 10.1364/ao.56.008436

instrument (such as the steadiness of the laser light source) or the aerosol system being measured (such as fluctuations in the measured process). This is done by developing a new measurement error model that is first demonstrated on simulated signals. Accordingly, this chapter starts by reviewing the variant of the spectroscopic and heat transfer submodels used to generate the simulated TiRe-LII signals. The chapter continues by describing how signals generated from a single-shot irradiance on a detector can be modeled as a combination of Poisson and Gaussian random variables. This model is extended to accommodate fluctuations in the aerosol system, which becomes important in multishot analysis. Gaussian shot-to-shot variation in the measurement is shown to produce a quadratic relationship between the variance and the expected value of these of signals. The degree of nonlinearity in these curves thus indicates the significance of shot-to-shot fluctuations relative to other noise sources. Comparing the mean and variance of TiRe-LII data can thus provide valuable information about the measured process (e.g. gas-phase nanoparticle reactors and soot formed within turbulent flames). The generalized error model is finally used to analyze TiRe-LII data from four different experiments, including the data analyzed later in Chapter 8, to highlight the utility of the developed approach.

4.1 TiRe-LII model

Here, the monodisperse case of the spectroscopic model is considered. The hypothetical noise-free is thus given by Eq. (2.18),

$$\tilde{s}_{\mathrm{j,i}} = \theta\zeta J_{\lambda_\mathrm{j},\mathrm{i}} = \theta\zeta C \cdot C_{\mathrm{abs},\lambda_\mathrm{j}}\left(d_\mathrm{p}\right) I_{\mathrm{b},\lambda_\mathrm{j}}\left[T_\mathrm{p}\left(t_\mathrm{i}, d_\mathrm{p}\right)\right], \tag{4.1}$$

where, as per Chapter 2, ζ is the photoelectric efficiency of the detector and θ is the amplification or scaling due to calibration or other signal processing steps. Unlike the form of the expressions shown in Chapter 3 for model inversion (where the signal is arranged as a vector of wavelength for fitting), the present chapter considers the incandescence signal at a single wavelength, arranging the signal as a vector of increasing time, that is $\mathbf{J}_\lambda = [J_{\lambda,1}, J_{\lambda,2}, \ldots J_{\lambda,\mathrm{i}}, \ldots]^\mathrm{T}$, $\tilde{\mathbf{S}}_\mathrm{j} = [\tilde{S}_{\mathrm{j},1}, \tilde{S}_{\mathrm{j},2}, \ldots \tilde{S}_{\mathrm{j,i}}, \ldots]^\mathrm{T}$, and $\mathbf{t} = [t_1, t_2, \ldots t_\mathrm{i}, \ldots]$. For ease of notation and readability, the current chapter will consider the signal for each wavelength independently, so that the wavelength in the notation is excluded (i.e. $\tilde{\mathbf{S}} = \tilde{\mathbf{S}}_\lambda$ and $\mathbf{J} = \mathbf{J}_\lambda$). The time-resolved, noise-free, single-shot signal is thus written in vector form as

$$\tilde{\mathbf{S}} = \theta\zeta\mathbf{J}. \tag{4.2}$$

For this chapter, the nanoparticle temperature is simulated by solving Eq. (2.20),

$$m_\mathrm{p} c_\mathrm{p} \frac{\mathrm{d}dT_\mathrm{p}}{\mathrm{d}t} = q_\mathrm{abs} - q_\mathrm{cond} - q_\mathrm{evap}, \tag{4.3}$$

using the Runge-Kutta method. The conduction and evaporation cooling rates are modeled in the free molecular regime. Signals are generated for carbon nanoparticles in nitrogen, so that $\zeta_{rot} = 2$, using a gas temperature T_g = 1750 K and the Michelsen model described in Ref. [98]. The simulation deviates from Michelsen's original model in that only C_3 sublimation is considered, as opposed to a range of different-sized carbon clusters, and a thermal accommodation coefficient of $\alpha = 0.37$ [111] is used. A summary of these model parameters is provided in Table 4.1. The incandescence signal is simulated for a laser pulse having a top-hat spatial profile; Gaussian temporal profile with a full width half maximum of 8 ns; a laser fluence of $F_0 = 0.05$ J/cm^2; and a nanoparticle diameter of 30 nm. Measurements are sampled at 400 MHz, corresponding to time intervals of 2.5 ns. It is noted that the heat transfer model is not needed to analyze the measurement error in the experimental signals and is only used in this chapter to generate synthetic signals.

Table 4.1 Heat transfer model parameter values used in Chapter 4. Values are representative of the Michelsen's model in Ref. [98], except in that only the sublimation of C_3 is considered and the TAC is substituted for that of the Liu model [111] in Ref. [98].

Property	Value	Notes
Density, ρ	$2303–7.3106\times10^{-2}\cdot T$ kg/m^3	-
Specific heat capacity, c_p	T-depedent[a]	In units of J/(kg·K)
Absorption function at laser wavelength, $E(\mathbf{m}_{\lambda l})$	0.34	Taken as constant with wavelength
Thermal accommodation coefficient, α	0.37	Taken from Liu model [111] in Ref. [98]
Specific latent heat of vaporization, Δh_v	$(8.443\times10^5–26.921\cdot T)/M_v$ J/kg	-
Molar mass of vapor, M_v	0.03603 kg/mol	Taken as molecular mass of C_3
Sticking coefficient, β	0.1	Taken as that for C_3 in Michelsen model in Ref. [98]
Vapor pressure, p_v	Clausius-Clapeyron equation, Eq. (2.44)	Using p_{ref}, $\Delta h_{v,ref}$, T_{ref}, and below and in units of Pa
Referene pressure, p_{ref}	101,325 Pa	Taken as atmospheric pressure
Reference, latent heat of vaporization, $\Delta h_{v,ref}$	2.034×10^7 J/kg	Taken by evaluating Δh_v above at T_{ref}
Refrence temperature, T_{ref}	4136.78 K	Taken as that for C_3 in Michelsen model in Ref. [98]

[a] Given as $c_p = \frac{R}{0.01201}\left\{1.115\left(\frac{597}{T}\right)^2 \exp\left(\frac{597}{T}\right)\left[\exp\left(\frac{597}{T}\right)-1\right]^{-2} + 1.789\left(\frac{1739}{T}\right)^2 \exp\left(\frac{1739}{T}\right)\left[\exp\left(\frac{1739}{T}\right)-1\right]^{-2} + \frac{T}{8620}\right\}$, where T is in K and c_p is in J/(kg·K).

4.2 Signal noise or error model

4.2.1 Poisson-Gaussian noise model

This chapter represents the signal generated by the spectral irradiance on the detector from a single laser shot as a random vector as described in reference to the Bayesian framework in Section 3.3.1. The pdf is derived by analyzing the physical processes that generate the measurement. Specifically, for a single laser shot, the signal noise is well-approximated by the Poisson-Gaussian process (e.g., [236]) where the measured signal, $\mathbf{s}^{\text{meas}}$, is

$$\mathbf{s}^{\text{meas}} = \tilde{\mathbf{s}} + \boldsymbol{\varepsilon}^{\text{s}} = \tilde{\mathbf{s}} + \mathbf{p}\left(\tilde{\mathbf{s}}\right) + \mathbf{g}. \tag{4.4}$$

Here, $\tilde{\mathbf{s}}$ is the expected signal for a single laser shot, which will correspond to the modeled value; $\boldsymbol{\varepsilon}^{\text{s}}$ is the noise in the signal at the specified wavelength; and $\mathbf{p}$ and $\mathbf{g}$ are random vectors describing the Poisson and Gaussian measurement noise, respectively. A detailed description of $\mathbf{p}$ and $\mathbf{g}$ and their distributions is given in the appendix of Ref. [237].

Poisson noise arises from the discrete nature of the photon counting process and the inherent variability and randomness of photonic emission, prior to any amplification or signal processing. Counting processes are ubiquitous in nature and can generally be described by a Poisson distribution [236]. For shot noise, the Poisson distribution has a variance of $\zeta\mathbf{J}$, where ζ is the quantum efficiency of the detector. Provided a sufficient number of photons, the noise can be approximated by an independent normal random vector, having a standard deviation given by the square root of the single-shot signal, i.e. $\tilde{\mathbf{s}}^{1/2}$ [236], where the exponent indicates the elementwise square root of the vector $\tilde{\mathbf{s}}$. This noise is subsequently amplified and scaled by processing steps, such that the standard deviation of the noise becomes $(\theta\tilde{\mathbf{s}})^{1/2}$. This can be expressed in vector form by elementwise multiplication with a standard normal random vector, $\mathbf{n}^{\text{p}}$, to make the role of the noise parameters explicit. Given the assumption of independence, the random vector has entries distributed as $n_{\text{i}}^{\text{p}} \sim \mathcal{N}(0, 1)$, where $\mathcal{N}(\mu, \sigma^2)$ denotes a normal distribution with mean μ and variance σ^2. The Hadamard or elementwise product, "$\circ$", is used to state this in vector form as

$$\mathbf{p}\left(\tilde{\mathbf{s}}\right) = \left(\theta\tilde{\mathbf{s}}\right)^{1/2} \circ \mathbf{n}^{\text{p}}. \tag{4.5}$$

The Gaussian noise term accounts for electrical and thermal noise. On TiRe-LII timescales, it is reasonable to consider this noise as independent and well-modeled as Gaussian white noise [238]. For thermal noise, this is easily justified [239]. For the remaining sources of electronic noise, the assumption of white noise becomes less reasonable, but can then be incorporated by introducing a structured covariance matrix for the noise. For the

sake of present discussions, the assumption is carried that the noise is reasonably white or independent. As before, the Gaussian noise scaled by θ can be phrased as the product of a standard normal random vector and a scalar factor, γ, so that

$$\mathbf{g} = \gamma \mathbf{n}^{\mathrm{G}}, \tag{4.6}$$

where $\mathbf{n}^{\mathrm{G}}$ is a standard normal random vector where each entry is distributed according to $n_i^{\mathrm{G}} \sim \mathcal{N}(0,1)$. The larger the value of γ, the larger the effect that Gaussian noise has on the signal. As this parameterization considers the case where the Gaussian noise has been scaled by θ, the units are the same as the signal.

Combining these expressions results in a final form describing a signal from a single laser shot in terms of standard normal vectors and a set of noise parameters

$$\mathbf{s}^{\mathrm{meas}} = \tilde{\mathbf{s}} + \underbrace{\left(\theta \tilde{\mathbf{s}}\right)^{1/2} \circ \mathbf{n}^{\mathrm{P}}}_{\text{Poisson error, } \mathbf{p}} + \underbrace{\gamma \mathbf{n}^{\mathrm{G}}}_{\substack{\text{Gaussian} \\ \text{error, } \mathbf{g}}} . \tag{4.7}$$

This corresponds to Eq. A9 in Ref. [237].

4.2.2 Generalized shot-to-shot error model

TiRe-LII analyses typically employ the shot-averaged signal, calculated over multiple realizations of $\mathbf{J}$, to stabilize the inference. In reality, this average approximates the true mean $\bar{\mathbf{J}}$, and, conceptually, variation in $\mathbf{J}$ is a source of posterior uncertainty in LII. The duration of a typical single-shot measurement is on the order of 1 μs, lasting from the start of the laser pulse until the nanoparticles cool to an extent that noise overwhelms the incandescence signal. By contrast, the shot frequency is on the order of 5 Hz or 0.2 s between shots. As such, variation in $\mathbf{J}$ between shots may be influenced by large-timescale fluctuations in the flow, such as turbulent variation in the nanoparticle volume fraction. To account for this variation, this chapter introduces the expected mean irradiance on the detector, $\bar{\mathbf{J}}$. The expected signal for a single shot, $\tilde{\mathbf{s}}$, can thus be approximated by the expected mean signal, $\bar{\mathbf{s}}$ (which is related to $\bar{\mathbf{J}}$) plus an error due to shot-to-shot variation

$$\tilde{\mathbf{s}} = \bar{\mathbf{s}} + \boldsymbol{\delta}, \tag{4.8}$$

where $\boldsymbol{\delta}$ is a random vector accounting for the change in the irradiance over multiple shots. As this term extends beyond what is traditionally considered noise, the term *measurement error* is used in this thesis to describe the combination of traditional signal noise and shot-to-shot-induced errors. In practice, the expected value of the signal over multiple shots, $\bar{\mathbf{s}}$, can be approximated by the average of the observed signals, which is denoted as $\langle \mathbf{s} \rangle$. Incorporating Eq. (4.8) into Eq. (4.4) gives

$$\mathbf{s}^{\text{meas}} = \bar{\mathbf{s}} + \boldsymbol{\delta} + \mathbf{p}\left(\tilde{\mathbf{s}}\right) + \mathbf{g}\,. \tag{4.9}$$

Note that the single-shot signal, $\tilde{\mathbf{s}}$, still features in $\mathbf{p}$ and thus requires a second substitution in realizing Eq. (4.9). The problem is then reduced to determining an appropriate distribution for the shot-to-shot variation, $\boldsymbol{\delta}$. Theoretically, multiple physical effects can be included into this term by altering one's choice for the distribution of $\boldsymbol{\delta}$.

In this analysis, fluctuations in the measured volume fraction are considered as the primary source of variation in $\boldsymbol{\delta}$. Consider a dimensionless volume fraction that is normalized by the true mean volume fraction, $f_\text{V}/\bar{f}_\text{V}$. In many flow scenarios, this quantity is roughly normally-distributed (in reality there is some skew in the distribution of most properties [240,241]) with a mean of unity and a dimensionless standard deviation that is denoted here as τ. This can be expressed mathematically as

$$f_\text{V}/\bar{f}_\text{V} \sim \mathcal{N}\left(1, \tau^2\right) \tag{4.10}$$

or, equivalently,

$$f_\text{V}/\bar{f}_\text{V} \sim \tau n + 1\,, \tag{4.11}$$

where n is a standard normal random variable, $n \sim \mathcal{N}(0, 1)$. The value of τ indicates the amount of temporal variation in the measurement process, which could include key timescales in turbulent and unsteady flames. Any new value of the volume fraction sampled from this expression will apply to the entire signal from a single laser shot, over which the volume fraction is relatively constant. Using Eq. (4.1), the single-shot irradiance can thus be stated as

$$\mathbf{J} = \left(\tau n + 1\right)\bar{\mathbf{J}}\,. \tag{4.12}$$

Using Eq. (4.2), the single-shot signal is then expressed as

$$\tilde{\mathbf{s}} = \theta\zeta\mathbf{J} = \theta\zeta\left[\left(\tau n + 1\right)\bar{\mathbf{J}}\right] = \underbrace{\theta\zeta\bar{\mathbf{J}}}_{\substack{\text{True average} \\ \text{signal, } \bar{\mathbf{s}}}} + \underbrace{\theta\zeta\tau n\bar{\mathbf{J}}}_{\substack{\text{Shot-to-shot} \\ \text{error, } \boldsymbol{\delta}}}\,. \tag{4.13}$$

This can be broken into its random component,

$$\boldsymbol{\delta} = \theta\zeta\tau n\bar{\mathbf{J}}\,, \tag{4.14}$$

and constant component, $\bar{\mathbf{s}} = \theta\zeta\bar{\mathbf{J}}$, to match the form of Eq. (4.8). This can then be restated in terms of $\bar{\mathbf{s}}$,

$$\tilde{\mathbf{s}} = \bar{\mathbf{s}} + \underbrace{\tau n \bar{\mathbf{s}}}_{\substack{\text{Shot-to-shot} \\ \text{error, } \boldsymbol{\delta}}} . \tag{4.15}$$

As per Section 4.2.1, Poisson noise corrupts the single-shot signals so that by combining Eq. (4.5) and (4.15), a new expression for the Poisson noise can be derived:

$$\mathbf{p}\left(\bar{\mathbf{s}}\right) = \left[\theta\left(\bar{\mathbf{s}} + \tau n \bar{\mathbf{s}}\right)\right]^{1/2} \circ \mathbf{n}^{\mathrm{P}} = \left[\theta\left(1 + \tau n\right)\bar{\mathbf{s}}\right]^{1/2} \circ \mathbf{n}^{\mathrm{P}} . \tag{4.16}$$

This expression now also accounts for the shot-to-shot variation in aerosol volume fraction. These definitions are substituted into Eq. (4.9) to obtain a final expression for the signal in terms of $\bar{\mathbf{s}}$

$$\mathbf{s}^{\mathrm{meas}} = \bar{\mathbf{s}} + \underbrace{\tau n \bar{\mathbf{s}}}_{\substack{\text{Shot-to-shot} \\ \text{error, } \boldsymbol{\delta}}} + \underbrace{\left[\theta\left(1 + \tau n\right)\bar{\mathbf{s}}\right]^{1/2} \circ \mathbf{n}^{\mathrm{P}}}_{\text{Poisson error, } \mathbf{p}} + \underbrace{\gamma \mathbf{n}^{\mathrm{G}}}_{\substack{\text{Gaussian} \\ \text{error, } \mathbf{g}}} , \tag{4.17}$$

which corresponds to Eq. A18 in Ref. [237]. It is notable that this error model is useful in Monte Carlo-based TiRe-LII simulations, wherein a set of signals is generated from $\bar{\mathbf{s}}$ by repeatedly sampling n, $\mathbf{n}^{\mathrm{P}}$, and $\mathbf{n}^{\mathrm{G}}$ and evaluating Eq. (4.17). A sample of this procedure is provided in source code in Ref. [242] included as supplemental material to Ref. [237].

To illustrate, consider signals simulated by evaluation of the spectroscopic and heat transfer models described in Section 4.1, and corrupted with varying degrees of noise characterized by τ, θ, and γ. Figure 4.1 shows two sample signals from single shots evaluated using different values of τ and γ. The plots show the expected trends. In the case of lower magnitudes of Gaussian noise, indicated by the lower value of γ in Figure 4.1, the noise in the signal is visibly diminished. This effect is particularly notable at low signal levels, where Gaussian noise is expected to be dominant. Also note that when $\tau \neq 0$, the true signal from a single laser shot, $\tilde{\mathbf{s}}$, is biased from the expected average signal, $\bar{\mathbf{s}}$, due to a random fluctuation in $\boldsymbol{\delta}$. Thus, even after the addition of Poisson-Gaussian noise, nearly all of the measured signal remains below $\bar{\mathbf{s}}$.

It is noted here that this error model is not limited only to TiRe-LII analyses but could also be useful for other laser-based diagnostics where the same physical mechanisms are present, specifically those of Poisson-Gaussian noise and Gaussian variations in a phenomenon between laser shots. In LIF characterization of turbulent plumes (e.g. [243,244]), for example, this model could potentially be used to efficiently quantify the temporal fluctuations in species concentrations (such as OH).

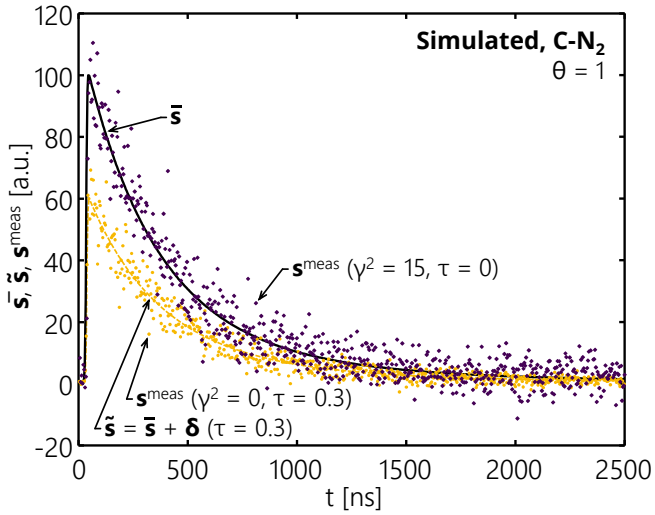

Figure 4.1 Two realizations of noisy signals, $\mathbf{s}^{meas}$, from a single-shot at different error model parameter values. Also shown is a true single-shot signal before corruption with Poisson-Gaussian noise, $\tilde{\mathbf{s}} = \bar{\mathbf{s}} + \boldsymbol{\delta}$, and the true average signal, $\bar{\mathbf{s}}$. The signal for $\tau = 0.3$ is biased due to a fluctuation in the probe volume fraction.

4.3 Extracting information from signal variance

This error model can now be used to analyze the variance of measured TiRe-LII signals. To do so, it is proposed that one examine the relationship between the expected mean, approximated by $\langle \mathbf{s} \rangle$, and the variance of the signals. This section derives an analytical expression describing this relationship and demonstrates how TiRe-LII practitioners can use experimental data to infer the noise parameters for their detection system, evaluate a theoretical signal-to-noise ratio that defines a signal cutoff, and quantify fluctuations in the measured process.

4.3.1 Describing signal covariance

Consider the covariance of signals governed by the measurement error model described in Section 4.2,

$$\mathrm{cov}\left(\mathbf{s}^{meas}\right) = \mathrm{cov}\left(\bar{\mathbf{s}} + \boldsymbol{\delta} + \mathbf{p} + \mathbf{g}\right), \tag{4.18}$$

where $\mathrm{cov}(\cdot)$ denotes covariance. This expression can be evaluated by using the definition of the covariance

$$\mathrm{cov}\left(\mathbf{s}\right) = \mathbb{E}\left(\mathbf{s}\mathbf{s}^{\mathrm{T}}\right) - \mathbb{E}\left(\mathbf{s}\right)\mathbb{E}\left(\mathbf{s}\right)^{\mathrm{T}}, \tag{4.19}$$

where $\mathbb{E}(\cdot)$ denotes the expected value. Implementing this definition for Eq. (4.18),

$$\mathrm{cov}\left(\mathbf{s}^{meas}\right) = \mathbb{E}\left[\left(\bar{\mathbf{s}} + \boldsymbol{\delta} + \mathbf{p} + \mathbf{g}\right)\left(\bar{\mathbf{s}} + \boldsymbol{\delta} + \mathbf{p} + \mathbf{g}\right)^{\mathrm{T}}\right] - \mathbb{E}\left(\bar{\mathbf{s}} + \boldsymbol{\delta} + \mathbf{p} + \mathbf{g}\right)\mathbb{E}\left(\bar{\mathbf{s}} + \boldsymbol{\delta} + \mathbf{p} + \mathbf{g}\right)^{\mathrm{T}}. \tag{4.20}$$

One can proceed in simplifying this expression by making several observations:

1. The expected value of $\boldsymbol{\delta}$, $\mathbf{p}$, and $\mathbf{g}$, as exist in the second term, will be zero, as each of these quantities only has randomness originating from either a single normal random vector (for $\boldsymbol{\delta}$ and $\mathbf{g}$) or multiple independent standard normal random variables (for $\mathbf{p}$). After exploiting the distributive property of the expected value, the second term in Eq. (4.20) then reduces to $\mathbb{E}(\bar{\mathbf{s}})\mathbb{E}(\bar{\mathbf{s}})^{\mathrm{T}} = \bar{\mathbf{s}}\bar{\mathbf{s}}^{\mathrm{T}}$.
2. The expected value of the products between the $\boldsymbol{\delta}$, $\mathbf{p}$, and $\mathbf{g}$ terms (e.g. $\boldsymbol{\delta}\mathbf{p}^{\mathrm{T}}$, $\mathbf{p}\mathbf{g}^{\mathrm{T}}$) will also be zero. This is a consequence of all of the standard normal random variables making up each of these products being independent. It should be noted that the same is not true of the product of each term with itself (e.g. $\mathbf{p}\mathbf{p}^{\mathrm{T}}$), where some of the standard normal random variables will be perfectly correlated by definition. This observation reduces the first term in Eq. (4.20) to

$$\mathbb{E}\left[\left(\bar{\mathbf{s}}+\boldsymbol{\delta}+\mathbf{p}+\mathbf{g}\right)\left(\bar{\mathbf{s}}+\boldsymbol{\delta}+\mathbf{p}+\mathbf{g}\right)^{\mathrm{T}}\right] = \mathbb{E}\left(\bar{\mathbf{s}}\bar{\mathbf{s}}^{\mathrm{T}}+\bar{\mathbf{s}}\boldsymbol{\delta}^{\mathrm{T}}+\bar{\mathbf{s}}\mathbf{p}^{\mathrm{T}}+\bar{\mathbf{s}}\mathbf{g}^{\mathrm{T}}+\boldsymbol{\delta}\boldsymbol{\delta}^{\mathrm{T}}+\mathbf{p}\mathbf{p}^{\mathrm{T}}+\mathbf{g}\mathbf{g}^{\mathrm{T}}\right). \tag{4.21}$$

3. The expected value of the product of $\bar{\mathbf{s}}$ with the $\boldsymbol{\delta}$, $\mathbf{p}$, and $\mathbf{g}$ terms will also be zero, a consequence of the only randomness being contained in the independent standard normal random variables that make up each of $\boldsymbol{\delta}$, $\mathbf{p}$, and $\mathbf{g}$. After invoking the distributive property of the expected value, the first term in Eq. (4.20) now reduces to

$$\mathbb{E}\left[\left(\bar{\mathbf{s}}+\boldsymbol{\delta}+\mathbf{p}+\mathbf{g}\right)\left(\bar{\mathbf{s}}+\boldsymbol{\delta}+\mathbf{p}+\mathbf{g}\right)^{\mathrm{T}}\right] = \mathbb{E}\left(\bar{\mathbf{s}}\bar{\mathbf{s}}^{\mathrm{T}}\right)+\mathbb{E}\left(\boldsymbol{\delta}\boldsymbol{\delta}^{\mathrm{T}}\right)+\mathbb{E}\left(\mathbf{p}\mathbf{p}^{\mathrm{T}}\right)+\mathbb{E}\left(\mathbf{g}\mathbf{g}^{\mathrm{T}}\right). \tag{4.22}$$

4. It is finally noted that $\mathbb{E}(\bar{\mathbf{s}}\bar{\mathbf{s}}^{\mathrm{T}}) = \bar{\mathbf{s}}\bar{\mathbf{s}}^{\mathrm{T}}$. This cancels out with what remains of the second term in Eq. (4.20), so that

$$\mathrm{cov}\left(\mathbf{s}^{\mathrm{meas}}\right) = \mathbb{E}\left(\boldsymbol{\delta}\boldsymbol{\delta}^{\mathrm{T}}\right)+\mathbb{E}\left(\mathbf{p}\mathbf{p}^{\mathrm{T}}\right)+\mathbb{E}\left(\mathbf{g}\mathbf{g}^{\mathrm{T}}\right). \tag{4.23}$$

The remaining terms in Eq. (4.23) will be non-zero. The first and last term result from the expected value of the product of a standard normal random vector with itself, which can be shown to be the identity matrix, $\mathbf{I}$. With this knowledge, the first and last term in Eq. (4.23) are straightforward substitutions of Eqs. (4.14) and (4.6), that is

$$\mathbb{E}\left(\boldsymbol{\delta}\boldsymbol{\delta}^{\mathrm{T}}\right) = \left(\theta\zeta\tau\right)^{2}\mathbf{J}\mathbf{J}^{\mathrm{T}} \tag{4.24}$$

and

$$\mathbb{E}\left(\mathbf{g}\mathbf{g}^{\mathrm{T}}\right) = \gamma^{2}\mathbf{I}. \tag{4.25}$$

Finally, from Eq. (4.16), the remaining term can be written as

$$\mathbb{E}\left(\mathbf{p}\mathbf{p}^{\mathrm{T}}\right)=\mathbb{E}\left[\theta\left(1+\tau n\right)\left(\bar{\mathbf{s}}^{1/2}\circ\mathbf{n}^{\mathrm{P}}\right)\left(\bar{\mathbf{s}}^{1/2}\circ\mathbf{n}^{\mathrm{P}}\right)^{\mathrm{T}}\right]. \tag{4.26}$$

The components remaining in the expected value can be expanded and, after noting that the expected value of the product of n with any of remaining random variables is zero, gives

$$\mathbb{E}\left(\mathbf{p}\mathbf{p}^{\mathrm{T}}\right)=\theta\cdot\mathbb{E}\left[\left(\bar{\mathbf{s}}^{1/2}\circ\mathbf{n}^{\mathrm{P}}\right)\left(\bar{\mathbf{s}}^{1/2}\circ\mathbf{n}^{\mathrm{P}}\right)^{\mathrm{T}}\right]. \tag{4.27}$$

This can be further evaluated to give

$$\mathbb{E}\left(\mathbf{p}\mathbf{p}^{\mathrm{T}}\right)=\theta\cdot\mathrm{diag}\left(\bar{\mathbf{s}}\right), \tag{4.28}$$

where diag(**v**) denotes a diagonal matrix with vector **v** on the diagonal. Therefore, the covariance, written in terms of $\bar{\mathbf{s}}=\theta\zeta\bar{\mathbf{J}}$, is

$$\mathrm{cov}\left(\mathbf{s}^{\mathrm{meas}}\right)=\underbrace{\tau^2\bar{\mathbf{s}}\bar{\mathbf{s}}^{\mathrm{T}}}_{\substack{\text{Shot-to-shot}\\\text{contribution}}}+\underbrace{\theta\cdot\mathrm{diag}\left(\bar{\mathbf{s}}\right)}_{\substack{\text{Poisson}\\\text{contribution}}}+\underbrace{\gamma^2\mathbf{I}}_{\substack{\text{Gaussian}\\\text{contribution}}}. \tag{4.29}$$

The signal variance is defined as the diagonal of the covariance matrix, so that

$$\mathrm{var}\left(\mathbf{s}^{\mathrm{meas}}\right)=\underbrace{\tau^2\bar{\mathbf{s}}\circ\bar{\mathbf{s}}}_{\substack{\text{Shot-to-shot}\\\text{contribution}}}+\underbrace{\theta\bar{\mathbf{s}}}_{\substack{\text{Poisson}\\\text{contribution}}}+\underbrace{\gamma^2\mathbf{1}}_{\substack{\text{Gaussian}\\\text{contribution}}}, \tag{4.30}$$

where **1** denotes a vector of ones.

Equation (4.30) reveals a novel quadratic relationship between the variance and the true average signal, $\bar{\mathbf{s}}$. It is notable that, in the absence of shot-to-shot variation ($\tau = 0$),

$$\mathrm{var}\left(\mathbf{s}\right)=\theta\bar{\mathbf{s}}+\gamma^2\mathbf{1}, \tag{4.31}$$

which is a linear relationship corresponding to the Poisson-Gaussian model [236]. Thus, one can conclude that shot-to-shot fluctuations in the measured process will result in a non-linear relationship between the mean and variance of the signals. This feature can be used to diagnose the stability of an observed process using TiRe-LII data.

Figure 4.2 shows a plot of signal variance against signal mean for a set of 500 shots, generated by the model from Section 4.1 for a range of τ and γ. Hypothetical amplification parameters were selected such that the maximum expected value of the incandescence traces was 100. In the absence of shot-to-shot variation ($\tau = 0$), the variance scales linearly with the expected signal (which is approximated as the average over multiple shots) due to photonic shot-noise, as per Eq. (4.31). Increasing the Gaussian noise component introduces a vertical offset.

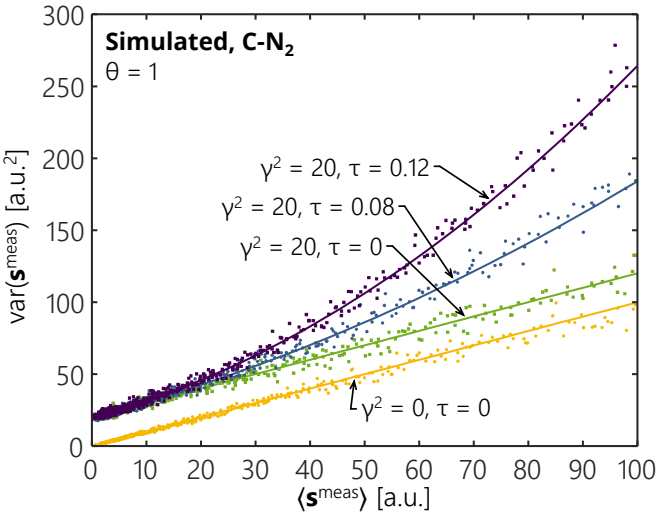

Figure 4.2 Average, $\langle \mathbf{s}^{meas} \rangle$, versus variance of simulated signals across 500 shots using the procedure described in the text. The parameters γ and τ indicate the degree of Gaussian noise and shot-to-shot variation respectively and θ is held constant at unity. Solid lines correspond to the modeled variance given by Eq. (4.30).

Adding variation in the volume fraction, $\tau > 0$, introduces a quadratic component to the curves, consistent with Eq. (4.30). It can be shown that the average for a set of 100+ shots is insensitive to the noise parameters and is a good estimate of the expected value $\bar{\mathbf{J}}$.

4.3.2 Signal-to-noise ratio

The SNR informs practitioners of the amount of noise relative to their measured signal. In applications where Poisson noise is present, the SNR can be defined as the ratio of the mean signal to the square root of its variance [245], yielding

$$\mathrm{SNR}_i^2 = \frac{m\bar{s}_i^2}{\tau^2\bar{s}_i^2 + \theta\bar{s}_i + \gamma^2}, \tag{4.32}$$

where i is an index indicating the signal at the i^{th} time and m is the number of shots in the average. In the design-of-experiment context, Eq. (4.32) indicates how the measurement error model parameters influence the SNR. For example, as τ is multiplied by $\bar{s}_i^2$, it has a more dramatic effect at times close to the laser pulse, when the signal is largest. As one would expect, the SNR is optimized when τ, θ, and γ are minimized and m is maximized.

The SNR can also be rearranged into a quadratic equation

$$0=\left(\tau^2-mc_{\mathrm{v,i}}^2\right)\bar{s}_{\mathrm{i}}^2+\theta\bar{s}_{\mathrm{i}}+\gamma^2, \tag{4.33}$$

where $c_{\mathrm{v,i}}$ is the coefficient of variation, that is, the reciprocal of the signal-to-noise ratio at the I^{th} timestep. The positive solution of the expression,

$$\bar{s}_{\mathrm{i}}^{*}=\arg\max\left\{\frac{-\theta\pm\left[\theta^2-4\gamma^2\left(\tau^2-c_{\mathrm{v}}^2\right)\right]^{1/2}}{2\left(\tau^2-c_{\mathrm{v}}^2\right)}\right\}, \tag{4.34}$$

gives the signal at which a specific SNR or coefficient of variation, c_{v}, is expected. This may prove useful in truncating signals, though a decision must still be made as to the suitable SNR at which this should occur. In this work, a SNR of unity is proposed, which denotes the point at which the measurement error contributes as much to the signal as the true detector irradiance. In any case, the point at which the signal, $\bar{s}_{\mathrm{i}}$, drops below the chosen $\bar{s}_{\mathrm{i}}^{*}$, should be chosen as a cutoff.

4.3.3 Inferring noise parameters from the data

In order to deploy the derived error model in an experimental setting, it is first necessary to relate the parameters in Eq. (4.30) to a set of measurement data. Eq. (4.30) can be presented as a linear system of equations, that is as an adaptation of Eq. (3.28),

$$\mathbf{b}^{\mathrm{meas}}=\mathbf{A}\mathbf{x}+\boldsymbol{\varepsilon}^{\mathrm{b}}. \tag{4.35}$$

In this case, $\mathbf{b}^{\mathrm{meas}}=\mathrm{var}(\mathbf{s}^{\mathrm{meas}})$ is the variance in the observed signal; $\mathbf{A}$ is defined from Eq. (4.30) as

$$\mathbf{A}=\left[\bar{\mathbf{s}}\circ\bar{\mathbf{s}}\quad\bar{\mathbf{s}}\quad\mathbf{1}\right]; \tag{4.36}$$

$\mathbf{x}=[\tau^2,\theta,\gamma^2]^{\mathrm{T}}$ is a vector containing the noise parameters; and $\boldsymbol{\varepsilon}^{\mathrm{b}}$ is a random vector that accounts for uncertainty in $\mathbf{b}^{\mathrm{meas}}$. For the sake of the current work it is assumed the uncertainties in $\mathbf{b}^{\mathrm{meas}}$ are normally distributed and homoscedastic with a value equal to the variance in the variance of the peak signal, that is, $\boldsymbol{\Sigma}^{\mathrm{b}}=\sigma_{\mathrm{m}}^2\cdot\mathbf{I}$ where $\sigma_{\mathrm{m}}^2=\max\{\mathrm{var}(\mathrm{var}(\mathbf{s}^{\mathrm{meas}}))\}$. Though the variance in the variance does not immediately appear homoscedastic (see Figure 4.3 and Figure 4.5), this alternative form accounts for the fact that modeling errors, such as the one caused by approximating the Poisson noise as Gaussian, are expected to be larger for weaker signals. Furthermore, selecting the maximum variance in the variance should serve as a conservative baseline for uncertainties in the error model parameters. The error model parameters are now determined using a least-squares approach. A supplemental code demonstrating this procedure was included with the original work [237,242]. Confidence

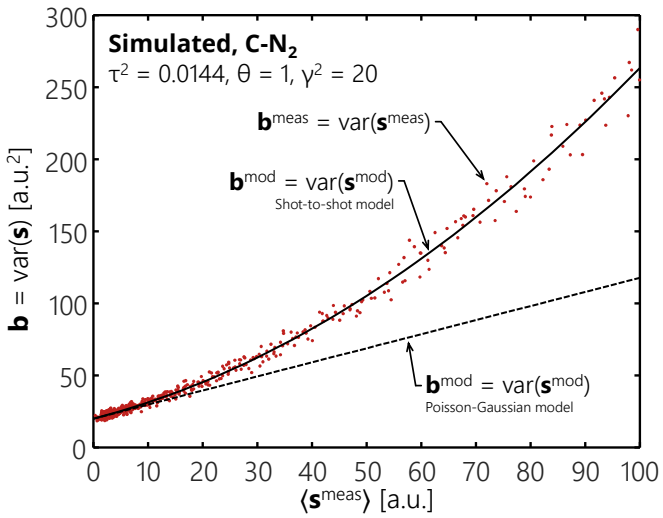

Figure 4.3 Average, $\langle \mathbf{s}^{meas} \rangle$, versus observed signal variance, $\mathbf{b}^{obs}$, and modeled signal variance, $\mathbf{b}^{mod}(\mathbf{x}^{MLE})$, evaluated at the least-squares estimate, for C-N_2. Also shown is the equivalent Poisson-Gaussian modeled variance, using the least-squares estimate of θ and γ.

intervals can be approximated with an uninformative prior and assuming $\boldsymbol{\varepsilon}^b$ is a normally-distributed random vector. From Eq. (3.38), this results in a posterior covariance matrix for $\mathbf{x}$ of

$$\boldsymbol{\Sigma}^{\mathbf{x}} = \sigma_m^2 \left(\mathbf{A}^T \mathbf{A} \right)^{-1}; \tag{4.37}$$

For the current chapter, reported credible intervals on the inferred parameters correspond to a single standard deviation (i.e. a 68% confidence interval), given by the square root of the diagonals of $\boldsymbol{\Sigma}^x$.

To demonstrate this principle, consider simulated signals generated by sampling standard random variables according to Section 4.1, using 500 shots and source noise parameters $\mathbf{x}^0 = [0.0144, 1, 20]^T$. Figure 4.3 shows the expected value versus observed variance derived for the simulated data and the corresponding least-squares fit. The observed and least-squares estimate of the signal variance both exhibit the expected non-linear behavior for $\tau > 0$. Inferring the noise parameters yields $\mathbf{x}^{LSQ} = [0.0146 \pm 0.0013, 0.98 \pm 0.10, 20.3 \pm 1.1]^T$, indicating that the source noise parameters are contained within the given 68% confidence intervals.

The value of τ derived by this procedure could be particularly useful as it indicates the percentage variation in the aerosol properties between shots. This requires a transformation of τ^2 to τ, which results in a posterior distribution that is no longer normal. Accordingly, a sample-based technique is used to estimate τ from a set of τ^2 samples. For the above inference problem, it is found that $\tau = 0.121 \pm 0.005$, where the confidence interval corresponds to one standard deviation of the samples. An analogous treatment can be applied to γ, yielding γ =

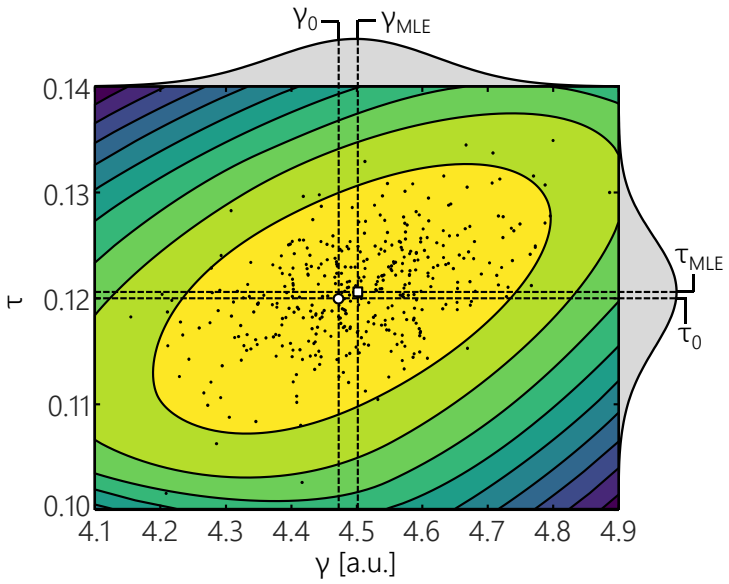

Figure 4.4 Contours of the log-likelihood marginalized over θ for C-N_2 simulated data as a function of τ and γ. The noise parameters used to generate the data, $\mathbf{x}^0$, are indicated by a white circle, and the least-squares estimate, $\mathbf{x}^{MLE}$, are indicated by a white square. The marginal distributions for τ and γ are shown on the right and upper axes respectively. Points indicate samples of τ and γ following sampling from the posterior distribution for τ^2, θ, and γ^2.

4.50 ±0.13 a.u. Figure 4.4 shows the chi-squared function or log-likelihood, marginalized over θ, having the components τ^2 and γ^2 transformed to τ and γ. A set of 400 samples is also shown, which conform to the log-likelihood contours. It is noted that a small amount of correlation exists between the variables, indicated by the angle of the ellipsoidal contours with respect to the primary axes.

4.3.4 Inferring noise parameters from experimental data

This process is now applied to experimental TiRe-LII signals, collected for iron nanoparticles in neon gas [45], germanium nanoparticles formed in a plasma reactor [135], and soot in an ethylene laminar diffusion flame [222,246]. Figure 4.5 shows the average signal versus variance for a selection of observed data. Table 4.2 gives the least-squares estimates of the measurement error model parameters.

The iron nanoaerosol [45] is produced by passing a nanocolloid through a pneumatic atomizer (see Chapter 8). This apparatus produced surges of aerosol that manifest as fluctuations in the nanoparticle volume fraction. This is reflected in the plot of the expected LII signal versus variance in Figure 4.5a, which indicates a nonlinear curve that resembles the simulated case shown in Figure 4.2. Least-squares estimates of the shot-to-shot variation, given by τ, indicate fluctuations around 25% of the average signal. This is considerably larger than the values of τ in the other studies reported in Table 4.2. As the shot-to-shot variations overwhelm other sources of

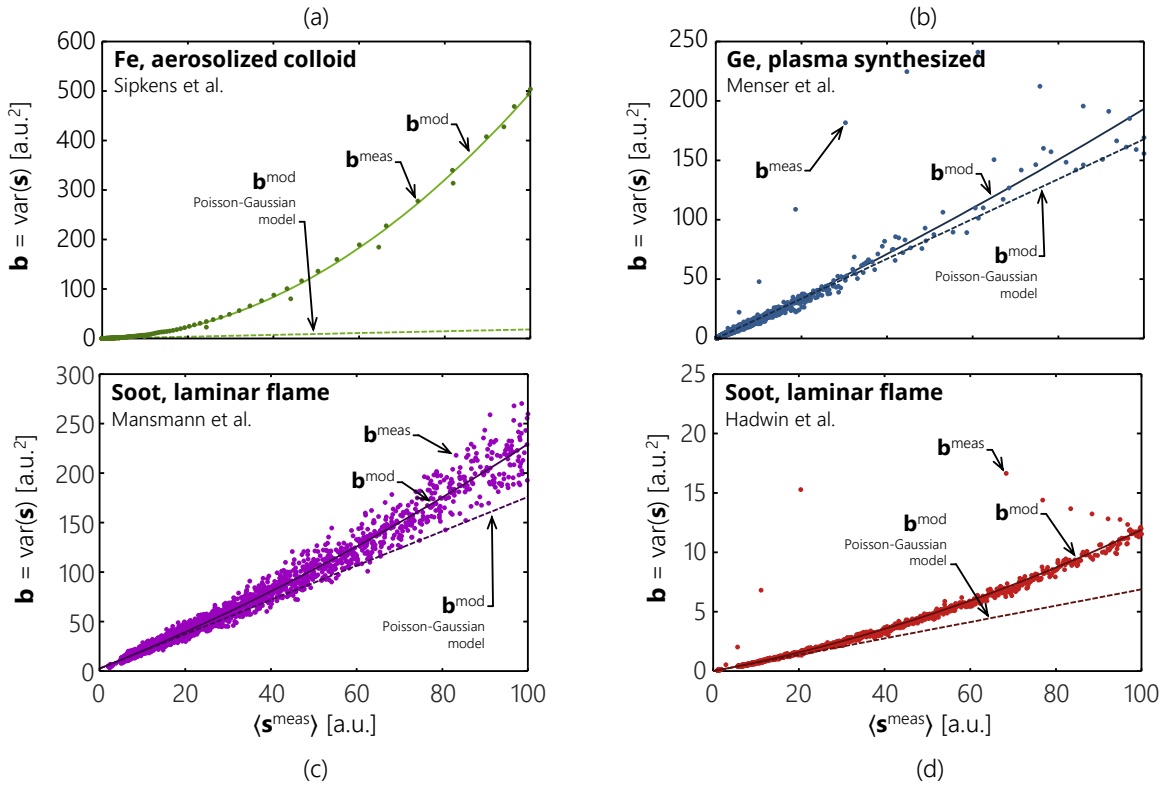

Figure 4.5 Mean versus variance of experimental signals for (a) aerosolized iron nanoparticle in an neon buffer gas measured at λ = 442 nm [45]; (b) plasma-synthesized germanium nanoparticles measured at λ = 684 nm [135]; (c) soot in an ethylene laminar diffusion flame measured at λ = 684 nm [246]; and (d) soot in an ethylene laminar diffusion flame at a wavelength of λ = 780 nm [222].

noise, the uncertainties in τ are relatively small compared to those in θ and γ. The Gaussian noise contribution to the signal is negligible compared to the other two components, so that the modeled variance nearly intersects the origin.

The plasma-synthesized germanium nanoparticles are produced using the reactor setup described in Ref. [135]. The nanoparticles are energized with a laser at a fluence of F_0 = 0.2 J/cm^2 (measured at ±2%) and using the TiRe-LII apparatus described in Ref. [246] and Chapter 6. Figure 4.5b indicates significantly less nonlinearity in the mean versus variance plot relative to the iron data. The shot-to-shot variation in the germanium study, indicated by the value of τ, is less than 8 percent of the expected signal. It is expected that the shot-to-shot variation is caused by small fluctuations in the particle loading over time, rather than fluctuations in the laser fluence, which were measured to be small. However, as the value of τ inferred from the data could encompass many possible sources of shot-to-shot error, it is difficult to conclude on the precise source of this shot-to-shot variation without additional experimentation. With the reduction in the shot-to-shot variation, uncertainties

Table 4.2 Maximum likelihood estimates ($\mathbf{x}^{MLE}$) and associated uncertainties for noise parameters inferred from experimental data on aerosolized iron nanoparticles [45], on germanium nanoparticles produced in a plasma reactor [135], on soot in an ethylene laminar diffusion flame [222,246]. Uncertainties correspond to the square root of the diagonal of $\mathbf{\Sigma}^x$. In cases that uncertainties in τ and γ are omitted, sampling is ineffective due to the large number of imaginary results. Estimates of $\bar{s}_i^*$ correspond to the expected signal at which the SNR is unity, expressed in percentage of peak.

Study	Channel or case	τ^2	τ	θ	γ^2 [a.u]	γ [a.u.]	$\bar{s}_i^*$ (% of peak)
Sipkens et al. [45] Iron, aerosolized colloid	Ch. 1, Ne, λ = 442 nm	0.0478 ±0.0054	0.219 ±0.012	0.18 ±0.43	0.1 ±1.6	-	0.39
	Ch. 2, Ne, λ = 716 nm	0.0640 ±0.0057	0.253 ±0.011	0.31 ±0.42	0.1 ±2.3	-	0.55
Menser et al. [135] Germanium, plasma synthesized	Ch. 1, λ = 500 nm	0.0005 ±0.0040	~ 0.023	4.17 ±0.30	0.00 ±0.56	-	4.18
	Ch. 2, λ = 500 nm	0.0017 ±0.0036	~ 0.042	4.08 ±0.27	0.12 ±0.51	-	4.12
	Ch. 3, λ = 684 nm	0.0025 ±0.0014	0.051 ±0.017	1.68 ±0.10	0.00 ±0.34	-	1.68
	Ch. 4, λ = 797 nm	0.0043 ±0.0023	0.066 ±0.021	3.55 ±0.15	0.00 ±0.75	-	3.56
Mansmann et al. [246] Soot, laminar flame	Ch. 1, λ = 500 nm	0.0062 ±0.0032	0.079 ±0.024	7.66 ±0.25	1.15 ±2.70	-	7.86
	Ch. 2, λ = 500 nm	0.0043 ±0.0031	~ 0.066	7.47 ±0.25	0.7 ±2.7	-	7.60
	Ch. 3, λ = 684 nm	0.00535 ±0.0008	0.0731 ±0.0057	1.731 ±0.072	2.7 ±1.1	1.63 ±0.34	2.73
	Ch. 4, λ = 797 nm	0.0001 ±0.0015	~ 0.012	3.41 ±0.13	0.0 ±2.1	-	3.42
Hadwin et al. [222] Soot, laminar flame	λ = 420 nm	0.000728 ±0.000087	0.0270 ±0.0016	0.174 ±0.006	0.030 ±0.060	-	0.29
	λ = 780 nm	0.000501 ±0.00003	0.0224 ±0.0008	0.0689 ±0.0031	0.000 ±0.043	-	0.07

in the other noise estimates derived from the germanium data are notably less than those derived from the iron data. As with the iron study, the Gaussian noise contribution is negligible compared to Poisson noise and fluctuations between shots. Figure 4.5b also reveals some outliers above the expected trend, which are a result of higher variances in the measurements during the signal rise (likely due to small amount of temporal laser jitter).

The soot particles produced using the laminar diffusion flame described in Ref. [246], are excited with a laser at a fluence of F_0 = 0.052 J/cm^2. Figure 4.5c suggests a low level of shot-to-shot variation. The inferred noise parameters are generally consistent with this observation, with values of τ around 7 percent. However, it is noted that uncertainties in τ are very large, likely due to the larger contribution of Poisson noise relative to the other forms of noise, which makes it challenging to resolve τ. Inspection of individual shots supports this conclusion. The low amount of shot-to-shot noise is consistent with the stability of the laminar diffusion flame. The majority of shot-to-shot variation is likely a result of fluctuations in the laser energy between shots [158]. Inferred values of τ are also consistent across the first three channels. The final channel deviates from the expected trend, indicating a problem with this channel. As the oscilloscope is optically-triggered, laser jitter is kept to a

minimum and one does not observe the outliers above the main trend that are observed in the measurements of iron and germanium emission. The Gaussian noise component is again negligible.

Soot particles in Ref. [222] are generated in the same flame as the previous study [246]. Inspection of Figure 4.5d shows significantly smaller variances than the other measurements considered here. The inferred shot-to-shot variation in this study is less than 1% of the average signal, indicative of a high-quality laser source and stable soot production in the laminar flame. A similar set of outliers appear above the trend, similar to those observed in the germanium study, Figure 4.5b. This may again be a result of a small degree of temporal laser jitter. Consistent with previous studies, the Gaussian noise in the signal remains negligible.

4.4 Conclusions

This chapter presents a generalized TiRe-LII measurement error model that can be used for experimental design and to characterize fluctuations in the aerosol properties or laser energy between shots. The original Poisson-Gaussian noise model for single-shot signal is expanded to include shot-to-shot variations. The improved model allows for accurate simulation of realistic, noisy signals for testing new analysis techniques and provides a better understanding of the noise structure for inference of quantities from TiRe-LII data. This is used in subsequent chapters, like Chapter 9, to produce simulated TiRe-LII signals corrupted with realistic noise.

Further, this chapter shows how one can exploit the relationship between the expected value or mean and the variance of a measured signal over multiple shots to derive information about the experimental apparatus and the stability of the aerosol. Specifically, a linear relationship indicates that the signal is corrupted by purely Poisson-Gaussian noise where the underlying process is stable. Quadratic relationships, in contrast, indicate Gaussian shot-to-shot variations that could arise from variations in aerosol volume fraction or fluctuations in laser energy. The measurement error parameters of a given setup, including the shot-to-shot variation, can be inferred by fitting a quadratic curve to an expected value versus variance curve.

Finally, this technique is applied to experimental data on aerosolized iron nanoparticles, plasma-synthesized germanium, and soot in a laminar diffusion flame. The recovered error model parameters contain information about the investigated processes that can aid in experimental design and provide unique information of the variability of the measured process. Although it remains difficult to determine the precise source of the variability in the observed process, with proper experimentation, this technique could prove useful in extending TiRe-LII to characterizing unstable aerosols such as turbulent flames [54].

Chapter 5
A novel approach to fluence curve modeling[2]

Fluence curves have various roles in TiRe-LII analyses, including for determining the start of the evaporative-cooling regime, for validating collected signals, and for troubleshooting measurement devices. In this regard, it is one of the first forms of analysis that TiRe-LII practitioners use to inform on their experiments. Fluence curves, in general, highlight the relationship between peak temperature, peak incandescence signal, or integrated incandescence signal and the laser energy. Figure 5.1 shows several such curves for peak nanoparticle temperature versus laser fluence taken the literature. Despite having similar characteristics, these curves exhibit a wide range of so-called *plateau temperatures* (though the curves generally continue to increase after plateauing) as well as a range of fluences at which the plateau temperature is reached. Such observations have led to fluence curves never being compared between studies. This chapter presents a method to formally define fluence regimes that facilitates a broader comparison between fluence curves in the literature. Specifically, a series of simple analytical expressions are presented that use non-dimensional parameters to collapse experimental fluence curves onto a single curve.

5.1 The fluence curve

LII-based fluence studies originate with the work of Eckbreth [58]. Eckbreth attributed trends in experimentally-determined peak temperatures, T_{peak}, with laser fluence to a balance between the laser energy input and nanoparticle evaporation. Subsequent experimental fluence studies [43,50,51,65,72,110,121,130,235,247–257] confirmed the existence of a *saturation* or *plateau* regime in integrated TiRe-LII signals. These observations have prompted various theoretical investigations. Snelling et al. [115] and Smallwood et al. [100], for example, showed

[2] Information presented in this chapter has been disseminated as:
Sipkens, T. A., and Daun, K. J., 2017, "Defining regimes and analytical expressions for fluence curves in pulsed laser heating of aerosolized nanoparticles," Opt. Express, **25**(5), pp. 5684-5696. doi: 10.1364/oe.25.005684

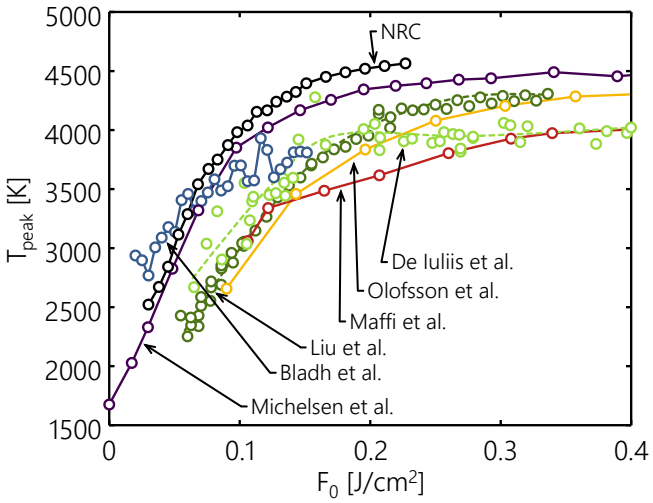

Figure 5.1 Experimental-based peak temperature fluence curves from a range of sources in the literature [97,110,176,253,258,260,261]. The curves demonstrate the range of values observed in the literature, which is rarely considered and never compared between studies.

how the temporal and spatial laser profiles, initial nanoparticle size, absorption efficiency, and detector gate width could influence the fluence curve characteristics. Schraml et al. [123] compared peak temperature versus laser irradiance curves to infer information about the evaporation properties of their soot samples. Bladh and Bengtsson [99] simulated the effect of polydispersity and the spatial laser profile on numerical fluence curves. De Iuliis et al. [258] used fluence curves to infer an absorption efficiency at the laser wavelength. Bladh et al. [259], Delhay et al. [249], and Olofsson et al. [260] performed numerical simulations to complement experiments, while Michelsen et al. [104,261], López-Yglesias et al. [262], Goulay et al. [122], and Lemaire and Mobtil [178] performed a similar analysis, with some additional discussion of the underlying physics. Even more recently attempts have been made to use experimental peak temperature fluence curves for gas thermometry [263,264].

Fluence curves have also been derived for LII measurements on non-carbonaceous nanoparticles, including iron [45,130], molybdenum [45,124,131,132], silver [45], silicon [49], and tungsten [94], and in the context of the laser-based nanoparticle synthesis of tungsten nanoparticles [265–267], (the curves from which share many of the same characteristics as those used in LII applications).

While some analytical models have also been derived for microparticles [268], the mechanisms governing laser absorption and evaporative cooling of nanoparticles are fundamentally different than the nanoparticles considered in this study, as noted in Section 2.2. The current work seeks to advance on the summarized

theoretical treatments by establishing the first closed-form analytical model for the high fluence regime and by using the derived expression to define non-dimensional parameters that can be used to establish the fluence regime. This first requires a description of the variant of the heat transfer model employed in the current chapter.

5.2 The heat transfer model

The current fluence curve expressions are derived from consideration of an energy balance on a spherical nanoparticle, Eq. (2.20),

$$c_{\mathrm{p}}\rho\frac{\pi d_p^3}{6}\frac{\mathrm{d}T_{\mathrm{p}}}{\mathrm{d}t}=q_{\mathrm{abs}}-q_{\mathrm{cond}}-q_{\mathrm{vap}}\,. \tag{5.1}$$

For measurements on the timescale of the laser pulse, conduction from the nanoparticles occurs at sufficiently slow rates that the total energy transferred due this mode is negligible. The absorption term is taken as Eq. (2.24)

$$q_{\mathrm{abs}}=\frac{\pi^2 d_p^3}{\lambda_1}E\left(\mathbf{m}_{\lambda_1}\right)f_0\left(t\right), \tag{5.2}$$

where, as per Eq. (2.23), the laser fluence is determined by integrating the temporal profile of the laser energy over the pulse. The fluence profile often modeled as Gaussian with a heavy tail [98,113,115,181]. The effect of the temporal fluence profile is revisited in Section 5.5.1. The vaporization term is taken as Eq. (2.42),

$$q_{\mathrm{vap}}=\Delta h_{\mathrm{v}}\frac{dm_{\mathrm{p}}}{dt}=-\Delta h_{\mathrm{v}}\beta m_{\mathrm{v}}\pi d_{\mathrm{p}}^2\frac{p_{\mathrm{v}}c_{\mathrm{v}}}{4k_{\mathrm{B}}T_{\mathrm{p}}}\,, \tag{5.3}$$

and the vapor pressure is calculated using the Clausius-Clapeyron equation, Eq. (2.44), using the form:

$$p_{\mathrm{v}}=A\cdot\exp\left(-\frac{\Delta h_{\mathrm{v}}}{R_{\mathrm{s}}T_{\mathrm{p}}}\right), \tag{5.4}$$

where R_{s} is the specific gas constant and $A = p_{\mathrm{ref}}\cdot\exp[\Delta h_{\mathrm{v}}/(R_{\mathrm{s}}T_{\mathrm{ref}})]$ is a material constant. Expanding, this gives

$$q_{\mathrm{vap}}=-\Delta h_{\mathrm{v}}\beta d_{\mathrm{p}}^2 A\left(\frac{\pi m_{\mathrm{v}}}{2k_{\mathrm{B}}T_{\mathrm{p}}}\right)^{1/2}\cdot\exp\left(-\frac{\Delta h_{\mathrm{v}}}{R_{\mathrm{s}}T_{\mathrm{p}}}\right). \tag{5.5}$$

The implied mass balance is solved simultaneously to the energy balance.

Although Eq. (5.1) can be solved numerically to obtain the fluence curve, additional insights can be made if several assumptions are imposed:

A1. The laser temporal profile is modeled as a step function, i.e. the laser energy rate is constant over the duration of the laser pulse, t_{lp}. This can be expressed mathematically as

$$f_0(t) = \frac{F_0}{t_{lp}}\left[H\left(-\frac{t_{lp}}{2} - t\right)H\left(\frac{t_{lp}}{2} - t\right)\right], \tag{5.6}$$

where $H(x)$ is the Heaviside delta.

A2. The specific heat capacity, density, latent heat of vaporization, and other intensive thermodynamic properties are assumed to be constant over the entire temperature range considered.

A3. Evaporation occurs in the free molecular regime and absorption occurs in the Rayleigh limit.

A4. Free-molecular evaporation is the only significant cooling mode and there is only one vaporized species. This means that the vapor pressure will be defined by a single Clausius-Clapeyron equation. In the case of carbon, the only sublimated species is assumed to be C_3, which has the lowest vaporization temperature [98]. Furthermore, there is no enhanced evaporation associated with interface curvature

A5. Nanoparticle sizes in the sample aerosol are monodisperse.

The effect of relaxing these assumptions is discussed further in Section 5.6 below, referring to the numbers assigned to each of the assumptions above.

5.3 Simulated fluence curves

To identify fluence regimes and inform the derivation of an analytical model, numerical solutions to the coupled ordinary differential equations, Eqs. (5.1) and (5.5), subject to the assumptions described above, are determined using a Runge-Kutta scheme for soot. Values of 8 ns, 1750 K, 30 nm, and 1064 nm are chosen for t_{lp}, T_g, d_p, and λ_1 respectively. Following A2 above, temperature-invariant material properties for soot are used, forming the *constant model*. The values of the constant model are summarized in Table 5.1. Most values are taken from the Kock model [226] in Ref. [98]. The resultant temperature curves, shown in Figure 5.2, reveal three distinct regimes. The low fluence regime is distinguished by a linear increase in temperature with respect to time, with the peak occurring at the end of the laser pulse. Without a significant heat loss mechanism, the temperature remains constant after the laser pulse. At moderate fluences, evaporation induces a nonlinear variation in temperature with respect to time and causes the temperature to decline significantly following the pulse. At high fluences, the peak temperature occurs during the laser pulse as the evaporative cooling rate exceeds the laser heating rate at longer times.

Table 5.1 Heat transfer model parameter values for the constant model implemented in this chapter.

Property	Value	Source and notes
Density, ρ	1860 kg/m^3	Taken from the Kock model [226] in Michelsen et al. [98]
Specific heat capacity, c_p	1900 J/(kg·K)	Taken from the Kock model [226] in Michelsen et al. [98]
Absorption function at laser wavelength, $E(\mathbf{m}_{\lambda l})$	0.4	Taken from the Liu model [111] in Michelsen et al. [98]
Specific latent heat of vaporization, Δh_v	2.195×10^7 J/kg	Corresponds to ΔH_v = 7.9078 J/mol from the Kock model [226] in Michelsen et al. [98]
Molar mass of vapor, m_v	5.983×10^{-26} kg	Corresponds to C_3, M_v = 0.3603 kg/mol
Sticking coefficient, β	1	Taken from the Kock model [226] in Michelsen et al. [98]
Vapor pressure, p_v	Clausius-Clapeyron equation	See Eq. (2.44)
Clausius-Clapeyron equation parameter, A	3.608×10^{15} Pa	Corresponds to p_{ref} = 60.5 Pa and T_{ref} = 3000 K form the Kock model [226] in Michelsen et al. [98]

Plotting the peak temperatures as a function of laser fluence, as shown in Figure 5.3, further highlights these three regimes. In this scenario, the low fluence regime occurs for $F_0 < 0.1$ J/cm^2, the transition or moderate fluence regime occurs for 0.1 J/cm^2 < F_0 < 0.2 J/cm^2, and the plateau or high fluence regime occurs for $F_0 > 0.2$ J/cm^2. This forms the basis for determining the physical mechanisms dominating each regime and facilitates the calculation of the analytical model in the subsequent section.

5.4 Fluence regimes and analytical model

5.4.1 Low fluence regime

Practitioners often aim to work at low fluences to avoid the large uncertainties associated with the vaporization models, which are especially large in the case of soot. At low fluences, two additional simplifications can be made.

First, vaporization is negligible over the laser pulse duration so that $q_{vap} \approx 0$ and the nanoparticle mass remains constant. Thus, Eq. (5.1) can be simplified and rearranged to define the differential equation

$$\frac{dT_p}{dt} = \frac{6\pi}{\lambda_1 c_p \rho} E\left(\mathbf{m}_{\lambda_1}\right) f_0(t). \tag{5.7}$$

This equation is separable and the nanoparticle temperature can be determined analytically for cases where the integral of $f_0(t)$ is tractable. For a square temporal laser pulse, for example, one can integrate both sides and, after noting that the nanoparticle will start at the gas temperature, can state

$$T_p - T_g = \frac{6\pi}{\lambda_1 c_p \rho} E\left(\mathbf{m}_{\lambda_1}\right) \frac{F_0}{t_{lp}} \left(t - \frac{t_{lp}}{2} \right). \tag{5.8}$$

The result indicates a linear increase in the nanoparticle temperature, which can theoretically be used for simple gas thermometry. Moreover, this matches the simulated rise in the nanoparticle temperature plotted in Figure 5.2. Equivalently, for a Gaussian temporal laser pulse with a standard deviation of σ_t, one can state

$$T_p - T_g = \frac{6\pi}{\lambda_1 c_p \rho} E\left(\mathbf{m}_{\lambda_1}\right) \frac{F_0}{2} \left[1 + \mathrm{erf}\left(\frac{t - \sigma_t}{\sigma_t 2^{1/2}} \right) \right], \tag{5.9}$$

where erf(·) denotes the error function. This could again be used for gas thermometry by fitting the temperature rise over the laser pulse to this expression. Of course, the reliability of such an approach would require a robust estimate of the nanoparticle temperature during heating, which is challenging given uncertainties in the spectroscopic model about the laser pulse.

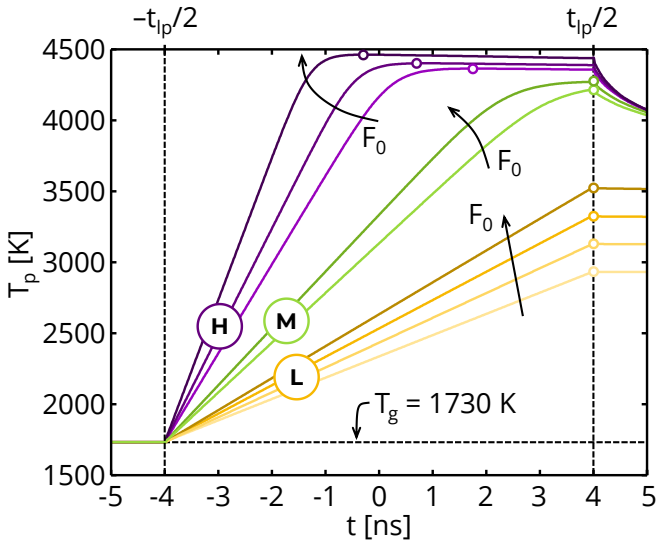

Figure 5.2 Simulated nanoparticle temperature versus time during and shortly following a step laser pulse for soot. The curves are grouped according to their physical characteristics or regimes with 'L', 'M', and 'H' denoting the low, moderate, and high regimes, respectively. Curves correspond to F_0 = [0.06, 0.07, 0.08, 0.09, 0.14, 0.16, 0.25, 0.3, 0.4] J/cm^2. The peak temperature is indicated by a circle.

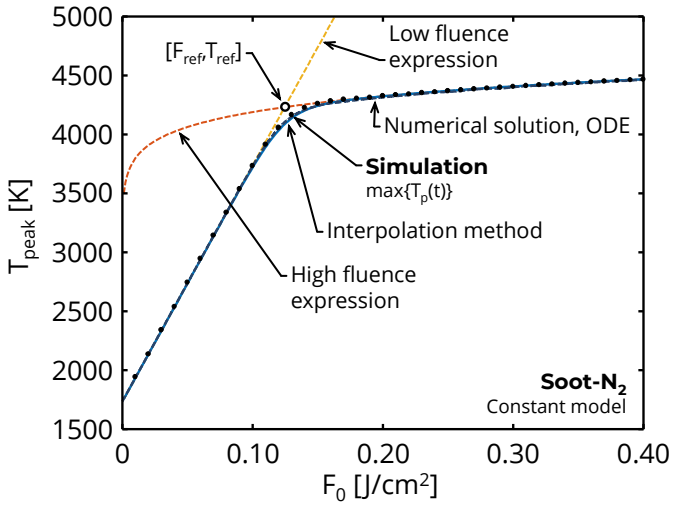

Figure 5.3 Simulated peak temperatures as a function of fluence, plotted alongside the proposed low fluence and high fluence expressions from Sections 5.4.1 and 5.4.2 respectively and the interpolation method from Section 5.4.3 (solid blue line). Also shown is the numerical solution to the ODE defined by Eq. (5.27) using the approximation for $g(T_{peak}, F_0)$ identified in Section 5.4.3 (dashed blue line).

Second, since laser heating far exceeds the magnitude of any evaporative cooling, the peak nanoparticle temperature must occur the end of the laser pulse. Thus, the peak nanoparticle temperature can be determined by integrating Eq. (5.7) over the duration of the laser pulse, which for the case of temperature-invariant thermophysical and optical properties (A2) gives

$$\int_{T_g}^{T_{peak}} \mathrm{d}T_p = \int_{t_{1p}} \frac{6\pi}{\lambda_1 c_p \rho} E\left(\mathbf{m}_{\lambda_1}\right) f_0(t) \cdot \mathrm{d}t\,, \tag{5.10}$$

Upon invoking the definition of the laser fluence, Eq. (2.23), one can then state

$$T_{peak} - T_g = \frac{6\pi}{\lambda_1 c_p \rho} E\left(\mathbf{m}_{\lambda_1}\right) F_0\,. \tag{5.11}$$

It is worth noting that this solution applies for any form of $f_0(t)$. Accordingly, it is found that the peak temperature is a linear function of the laser fluence, regardless of the temporal shape of the laser profile. This linear relationship has been observed in previous studies (e.g. [111,258]).

Equation (5.11) lends itself rather naturally to a non-dimensional analysis. Consider a dimensionless temperature, Θ, defined with respect to some reference peak temperature, T_{ref}, as

$$\Theta = \frac{T_{\text{peak}} - T_{\text{g}}}{T_{\text{ref}} - T_{\text{g}}}\,. \tag{5.12}$$

One can then define a reference fluence by incorporating this definition into Eq. (5.11) and solving for the fluence

$$F_{\text{ref}} = \frac{\lambda_1 c_{\text{p}} \rho \left(T_{\text{ref}} - T_{\text{g}} \right)}{6\pi E\left(\mathbf{m}_{\lambda_1} \right)}\,. \tag{5.13}$$

Thus, a natural non-dimensional laser fluence is defined as

$$\Phi = \frac{F_0}{F_{\text{ref}}} = \frac{6\pi E\left(\mathbf{m}_{\lambda_1} \right)}{\lambda_1 c_{\text{p}} \rho \left(T_{\text{ref}} - T_{\text{g}} \right)} F_0\,. \tag{5.14}$$

While the value of T_{ref} in these definitions is arbitrary, a convenient value of T_{ref} that is useful in defining the regimes is discussed in Section 5.4.2 below. The dimensionless curves should thus be independent of the nanoparticle material, the value of $E(\mathbf{m}_{\lambda\text{laser}})$, the temporal width and shape of the laser pulse, and the value of d_{p} (provided the assumptions regarding the Rayleigh regime). It also has the added advantage that a unit change in the dimensionless fluence will result in an equal change in the dimensionless temperature. This expression is plotted in Figure 5.3, along with the simulated curves found by solving Eqs. (5.1) and (5.5) numerically.

5.4.2 High fluence or plateau regime

Due to the relative insensitivity of the peak temperature to small variations in laser fluence, practitioners occasionally prefer to carry out LII experiments (particularly those used to find f_{V}) within the plateau regime. This is predicated on the assumption that all of the nanoparticles in the aerosol will reach similar peak temperatures, even when there may be spatial variations in the laser fluence profile. While this is useful in the context of volume fraction measurements, this imposes larger uncertainties on inferred nanoparticle sizes and thermophysical properties due to the necessary inclusion of vaporization submodels. Eckbreth [58] suggested that the relationship between the peak nanoparticle temperature and fluence in this regime could be determined by equating the laser input and vaporization from the nanoparticle. Figure 5.2 affirms this observation and suggests there exists some critical fluence at which the heating rate exactly balances evaporative cooling at the end of the laser pulse. Beyond this, the laser input and vaporization will balance before the end of the laser pulse, shifting the peak temperature back in time. This point is defined by equating q_{abs} and q_{vap},

$$q_{\text{abs}} = \frac{\pi^2 d_p^3}{\lambda_1} E\left(\mathbf{m}_{\lambda_1} \right) f_0\left(t \right) = \Delta h_{\text{v}} \beta d_{\text{p}}^2 A \left(\frac{\pi m_{\text{v}}}{2 k_{\text{B}} T_{\text{p}}} \right)^{1/2} \cdot \exp\left(-\frac{\Delta h_{\text{v}}}{R_{\text{s}} T_{\text{p}}} \right) = -q_{\text{vap}}\,. \tag{5.15}$$

Following assumption A2 and equating Eqn. (5.2) and (5.3), this can be used to give

$$\left(\frac{1}{T_{\text{peak}}}\right)^{0.5}\exp\left(-\frac{\Delta h_{\text{v}}}{R_{\text{s}}T_{\text{peak}}}\right)=\frac{d_{\text{p}}E\left(\mathbf{m}_{\lambda_1}\right)}{\Delta h_{\text{v}}\beta A\lambda_1}\left(\frac{2k_{\text{B}}}{m_{\text{v}}}\right)^{0.5}\pi^{1.5}\frac{F_0}{t_{\text{lp}}}. \tag{5.16}$$

Note that the right-hand side of Eq. (5.16) depends on d_{p} and therefore, by extension, also depends on the particle mass. Assuming that the nanoparticle size is approximately constant with temperature, this expression can be rearranged into the novel expression

$$T_{\text{peak}}=\frac{-2\Delta h_{\text{v}}}{R_{\text{s}}\cdot W_{-1}\left\{-\dfrac{4k_{\text{B}}}{R_{\text{s}}\Delta h_{\text{v}}m_{\text{v}}}\left[\dfrac{d_{\text{p}}E\left(\mathbf{m}_{\lambda_1}\right)}{\beta At_{\text{lp}}\lambda_1}\right]^2\pi^3F_0^{\,2}\right\}}, \tag{5.17}$$

where $W_{-1}(\cdot)$ is the lower branch of Lambert W (or product log) relation. This can equivalently be stated in terms of the dimensionless temperature and fluence defined in Section 5.4.1,

$$\Theta=\frac{-2\Delta h_{\text{v}}\left(T_{\text{ref}}-T_{\text{g}}\right)}{R_{\text{s}}\cdot W_{-1}\left\{-\dfrac{\pi k_{\text{B}}}{9R_{\text{s}}\Delta h_{\text{v}}m_{\text{v}}}\left[\dfrac{d_{\text{p}}\rho c_{\text{p}}\left(T_{\text{ref}}-T_{\text{g}}\right)}{\beta At_{\text{lp}}}\right]^2\Phi^2\right\}}+T_{\text{g}}. \tag{5.18}$$

Grouping the material properties and constants in the Lambert W function into a single material property, C_1, defined as

$$C_1=\frac{k_{\text{B}}\pi}{9R_{\text{s}}\Delta h_{\text{v}}m_{\text{v}}}\left(\frac{\rho c_{\text{p}}}{\beta A}\right)^2, \tag{5.19}$$

gives

$$\Theta=\frac{-2\Delta h_{\text{v}}\left(T_{\text{ref}}-T_{\text{g}}\right)}{R_{\text{s}}\cdot W_{-1}\left\{-C_1\left[\dfrac{d_{\text{p}}\left(T_{\text{ref}}-T_{\text{g}}\right)\Phi}{t_{\text{lp}}}\right]^2\right\}}+T_{\text{g}}. \tag{5.20}$$

This expression can be used to define a useful reference temperature, T_{ref}, corresponding to the point where Eqs. (5.14) and (5.20) intersect, which is then assigned the coordinate [1,1] on the dimensionless fluence curve. This gives

$$T_{\mathrm{ref}} \cdot W_{-1}\left\{-C_1\left[\frac{d_{\mathrm{p}}\left(T_{\mathrm{ref}}-T_{\mathrm{g}}\right)}{t_{\mathrm{lp}}}\right]^2\right\}=\frac{-2\Delta h_{\mathrm{v}}}{R_{\mathrm{s}}}, \tag{5.21}$$

which can be solved numerically. Along with the material properties, this reference temperature depends on the temporal laser profile, indicated by the presence of t_{lp}, the nanoparticle size, and the gas temperature. This indicates that the reference temperature inherently depends on the experimental conditions. The corresponding reference fluence can then be evaluated from

$$F_{\mathrm{ref}}=\frac{\lambda_{\mathrm{l}}\rho c_{\mathrm{p}}\left(T_{\mathrm{ref}}-T_{\mathrm{g}}\right)}{6\pi E\left(\mathbf{m}_{\lambda_{\mathrm{l}}}\right)}. \tag{5.22}$$

Comparing the laser fluence to the reference value indicates the fluence regime: $F_0 \ll F_{\mathrm{ref}}$ corresponds to the low fluence regime, while $F_0 \gg F_{\mathrm{ref}}$, corresponds to the high fluence regime. The derived expressions also indicate the different kinds of information that measurements carried out in the low and high fluence regimes contain about the unknown parameters. For instance, the high fluence regime curve contains information about the nanoparticle size, d_{p}, while the peak temperature in the low fluence regime curve is insensitive to this parameter. This analysis suggests that fluence curves could complement inference of nanoparticle sizes derived through traditional TiRe-LII analysis.

It is briefly noted that at sufficiently high fluences, the nanoparticle will begin to breakdown allowing for LIBS and plasma emission. No studies have methodically examined this transition, though Menser et al. [269] and Talebi Moghaddam et al. [270] have begun to make strides in this direction.

5.4.3 Moderate or transition fluence regime

At fluences around the reference fluence, the vaporization heat transfer rate influences the peak temperature reached by the nanoparticles but never equates the rate of laser uptake by the nanoparticle. In this scenario, the energy balance gives

$$\frac{\mathrm{d}T_{\mathrm{p}}}{\mathrm{d}t}=\frac{6\pi}{\lambda_{\mathrm{l}}c_{\mathrm{p}}\rho}E\left(\mathbf{m}_{\lambda_{\mathrm{l}}}\right)f_0\left(t\right)-\frac{6\Delta h_{\mathrm{v}}\beta A}{c_{\mathrm{p}}\rho d_{\mathrm{p}}}\left(\frac{m_{\mathrm{v}}}{2\pi k_{\mathrm{B}}T_{\mathrm{p}}}\right)^{1/2}\exp\left(-\frac{\Delta h_{\mathrm{v}}}{R_{\mathrm{s}}T_{\mathrm{p}}}\right). \tag{5.23}$$

A summary material property, C_2, is again defined to simplify the expressions presented below,

$$C_2=\frac{6\Delta h_{\mathrm{v}}\beta A}{c_{\mathrm{p}}\rho}\left(\frac{m_{\mathrm{v}}}{2\pi k_{\mathrm{B}}}\right)^{1/2}, \tag{5.24}$$

so that

$$\frac{\mathrm{d}T_\mathrm{p}}{\mathrm{d}t}=\frac{6\pi}{\lambda_1 c_\mathrm{p}\rho}E\left(\mathbf{m}_{\lambda_1}\right)f_0(t)-\frac{C_2}{d_\mathrm{p}}\left(\frac{1}{T_\mathrm{p}}\right)^{1/2}\exp\left(-\frac{\Delta h_\mathrm{v}}{R_\mathrm{s}T_\mathrm{p}}\right). \tag{5.25}$$

In general, this differential equation is intractable. It is useful to note however that, as with the low fluence regime, the peak nanoparticle temperature in this regime will still occur at the end of the laser pulse (as the energy lost by evaporation never equates the laser energy input). Thus, proceeding with an integration over the laser pulse, Eq. (5.23) becomes

$$T_\mathrm{peak}-T_\mathrm{g}=\frac{6\pi}{\lambda_1 c_\mathrm{p}\rho}E\left(\mathbf{m}_{\lambda_1}\right)F_0-\int_{t_\mathrm{lp}}\frac{C_2}{d_\mathrm{p}}\left(\frac{1}{T_\mathrm{p}}\right)^{1/2}\exp\left(-\frac{\Delta h_\mathrm{v}}{R_\mathrm{s}T_\mathrm{p}}\right)\mathrm{d}t\,. \tag{5.26}$$

While this does not make the equation tractable, it does give some physical insight. Specifically, it can be noted that the otherwise linear trend in the peak temperature with fluence will be reduced by the second term, that is the energy lost due to evaporation over the duration of the laser pulse.

An alternative phrasing of the problem can be derived by taking the derivative of Eq. (5.26) with respect to fluence,

$$\frac{\mathrm{d}T_\mathrm{peak}}{\mathrm{d}F_0}=\frac{6\pi}{\lambda_1 c_\mathrm{p}\rho}E\left(\mathbf{m}_{\lambda_1}\right)-g\left(T_\mathrm{peak},F_0\right), \tag{5.27}$$

where

$$g\left(T_\mathrm{peak},F_0\right)=\frac{\mathrm{d}}{\mathrm{d}F_0}\int_{t_\mathrm{lp}}\frac{C_2}{d_\mathrm{p}}\left(\frac{1}{T_\mathrm{p}}\right)^{1/2}\exp\left(-\frac{\Delta h_\mathrm{v}}{R_\mathrm{s}T_\mathrm{p}}\right)dt\,. \tag{5.28}$$

is a function accounting for the increase in the evaporation over the duration of the laser pulse for a differential increase in laser fluence. This term can be approximated by considering that a differential increase in fluence can be well-represented by a proportionally small increase in the laser pulse duration. For a square temporal laser profile, a differential increase in the laser fluence corresponds to a differential increase in the laser pulse duration of

$$\mathrm{d}t_\mathrm{lp}=\frac{t_\mathrm{lp}}{F_0}\mathrm{d}F_0\,. \tag{5.29}$$

If it is then also assumed that the nanoparticle temperature is constant at the peak temperature over this differential increase in the laser pulse duration, one can state

$$g\left(T_{\text{peak}}\right)\approx\frac{t_{\text{lp}}C_2}{F_0 d_{\text{p}}}\left(\frac{1}{T_{\text{p}}}\right)^{1/2}\exp\left(-\frac{\Delta h_{\text{v}}}{R_{\text{s}}T_{\text{peak}}}\right). \tag{5.30}$$

Unfortunately, to the best of the author's knowledge, this differential equation is also intractable. One can continue by solving the combination of Eq. (5.27) and Eq. (5.30) numerically. This solution is also shown in Figure 5.3, indicating that this form well-represents the peak temperature over the entire fluence curve, even well into the high fluence regime (a consequence of the nanoparticle temperature being similar at the peak and at the end of the pulse in the high fluence regime, cf. Figure 5.2). This method is not preferred for discussions in the current chapter as it does not yield a closed-form for the entire domain but could prove useful in other analyses. In particular, solutions to this ODE could be fit to experimental fluence curves to determine thermophysical properties.

More simply, one can introduce an interpolation function (similar to the treatment for transition regime conduction discussed in Section 2.2.3.3) to model a smooth transition between two intersecting functions, g_1 and g_2, with known asymptotic properties [271],

$$g\left(x\right)=\left[g_1^{\,n}\left(x\right)+g_2^{\,n}\left(x\right)\right]^{1/n}. \tag{5.31}$$

Increasing $|n|$ sharpens the transition between the two functions. Figure 5.3 indicates that $n = -20$ gives good agreement to the numerical simulations from Section 5.3.

It is noted that for very small fluences, $F_0 < 0.0015$ J/cm^2, the Lambert W function will decline to zero resulting in non-physical results from the interpolation function. However, such fluences never occur in experimental settings (where the LII is often too small to measure), rendering this effect insignificant. In general, this will result in expressions of the form

$$T_{\text{peak}}\left(F_0\right)=\left\{\left(B_1F_0+T_{\text{g}}\right)^n+\left[\frac{B_2}{W_{-1}\left(B_3F_0^2\right)}\right]^n\right\}^{1/n}, \tag{5.32}$$

where B_1, B_2, and B_3 are constants that depend on the material and experimental conditions. This is the form of the *analytical model* discussed throughout the remainder of this work.

5.4.4 A word on the integrated incandescence

Often, TiRe-LII practitioners examine fluence curves with respect to changes in an incandescence signal integrated over some gate rather than a peak temperature with fluence. Unlike the peak temperature, which shifts back in time with increasing fluence, integrated incandescence fluence curves are often evaluated about a fixed time period relative to the laser pulse. This presents unique challenges that are deemed out of the scope of this thesis. It is noted, however, that incandescence fluence curves can be simulated by evaluating Eq. (2.16),

$$\tilde{s}_{\mathrm{j,i}} = \Lambda \eta_{\mathrm{j}} C_{\mathrm{abs},\lambda_{\mathrm{j}}}\left(d_{\mathrm{p}}\right) I_{\mathrm{b},\lambda_{\mathrm{j}}}\left[T_{\mathrm{p,i}}\left(d_{\mathrm{p}}\right)\right], \tag{5.33}$$

and integrating over the temporal width of the gate. Such a calculation does require an estimate of the ISF and how it changes with laser fluence and with time. As noted in Chapter 6 below, this can cause inconsistencies in measurements depending on what gate time is chosen, specifically suffering from the vaporization, detector response function, and annealing effects. In all cases, the reduction in the ISF resulting from vaporization at high laser fluences will result in a drop in the integrated incandescence signal beyond the reference fluence, a feature occasionally observed in the literature (e.g. [51,96,254,255]).

5.5 Model errors induced by assumptions

Consider now the effect of relaxing the simplifying assumptions required to realize the analytical solution, Eq. (5.33). This will result in estimates of the *model errors* in the analytical expressions, that is deficiencies in the derived expression relative to the true physics. Estimates of the model errors are generated by first simulating fluence curves, corresponding to solving Eq. (5.1) at a range of fluences numerically, in this case using a Runge-Kutta scheme. One can then examine the difference between the simulated results and the analytical solution. Note that A3 is not considered, as the free molecular assumption for sublimation is considered a non-reducible component of the model. Furthermore, A4 is not considered independently and is incorporated into Section 5.5.2, a consequence of the fact that the effect of including multiple species sublimation is well-understood in terms of a discussion of temperature-dependent properties.

5.5.1 Effect of temporal laser profile (A1)

The largest departure from the true experimental conditions comes from modeling the temporal profile of the laser pulse with a step function (A1). The true time-averaged, temporal laser fluence profile is often Gaussian or skewed Gaussian [98,113,115,181]. To this end, this section simulates the peak nanoparticle temperature for Gaussian and lognormal fluence profiles using the Runge-Kutta scheme and compares this to the analytical expressions. The Gaussian case employs a full-width half maximum (FWHM) of 8 ns, which corresponds to the

t_{lp} used in the simulations from Section 5.3. Two lognormal fluence profiles are also considered by adding skew, defined for a lognormal distribution as

$$\mathrm{Sk} = \left(\sigma_g^{\ln(\sigma_g)} + 2\right)\left(\sigma_g^{\ln(\sigma_g)} - 1\right)^{1/2}. \tag{5.34}$$

By this definition, the case of no skew will correspond to a Gaussian profile. For the lognormal cases, the distribution is fit to the profile given in [98], giving μ_g = 10.8 ns and σ_g = 1.34 and a corresponding skew of Sk = 0.928. A moderate case with a skew of Sk = 0.5 is also considered. In either case, the profile is shifted back so that the mean of the distribution occurs at t = 0. In all of these cases, the value t_{lp} required to evaluate the analytical model is assigned to the full-width half maximum (FWHM) of the implemented laser fluence profile.

Figure 5.4 shows the model error induced by relaxing A1. The plot also includes the model error induced by using an interpolation function through the transition regime in the place of a simulation. It is noted that this latter curve is quite jagged, a result of numerical errors in the Runge-Kutta derived peak temperature for the case of considering the sharp edges associated with using an input step function for the laser profile. For the Gaussian and lognormal cases, changes to the low fluence regime are negligible. This is expected as the low-fluence expressions are integrated over the laser pulse and are thus insensitive to the choice of laser fluence profile. Near the transition fluence, the redistribution of the laser energy over time results in a lower nanoparticle temperature relative to the one obtained by assuming a step function. This can be somewhat corrected by

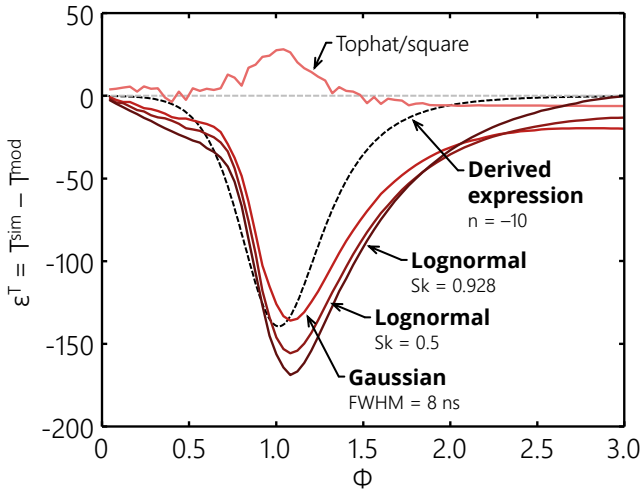

Figure 5.4 Model error in the peak temperature, ε^T, induced by relaxing the assumption of a tophat temporal laser fluence profile to Gaussian and lognormal profiles with various amounts of skew. Also included is the difference between using n = –20 and –10 in the interpolation function.

adopting $n = -10$ in the interpolation function. Even without correction, the model error in this region is limited to 5% of the total temperature rise. The discrepancy reduces again for $\Phi > 2.5$.

5.5.2 Effect of temperature-dependent properties (A2 and A4)

Relaxing A2 allows the material properties to change with nanoparticle temperature, here manifesting as temperature-dependent ρ, c_p, and Δh_v. Evaluating the fluence model of Section 5.4 requires a reference value for each of these properties, which are calculated at T_g, $(T_g + T_b)/2$, and T_b for ρ, c_p, and Δh_v when considering other models proposed in the literature. Simulations using the temperature-dependent properties and the fluence model of Section 5.4 can be compared for a range of heat transfer models available in the literature, including the Michelsen (only considering sublimation of C3), Liu, and Kock models, as defined in Michelsen et al. [98] and the Sipkens model, further described in Chapter 6. The error induced by this treatment is plotted with fluence in Figure 5.5.

The Michelsen model results in the largest model error, which is most significant in the low fluence regime (that is $\Phi < 1$). This is a result of enhanced absorption following thermal swelling of the nanoparticle. In the other models, this is countered by significant increases in the specific heat capacity, which requires more energy input to heat the material up by one degree of temperature. Consequently, these models exhibit a downward shift in the model error for $\Phi > 0.3$. This second effect is most significant for the Kock model, resulting in a model error

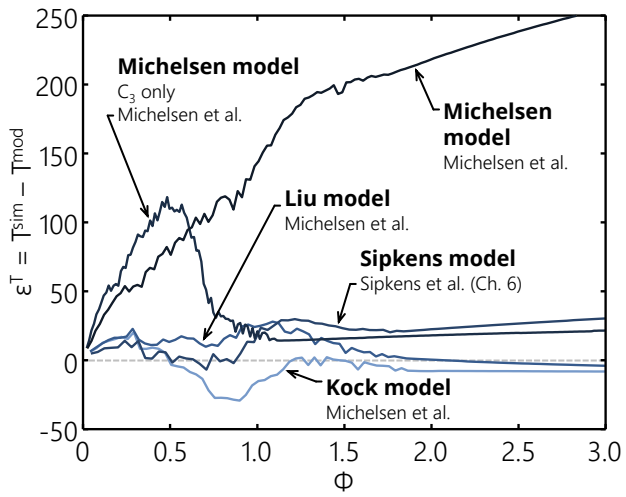

Figure 5.5 Model error in the analytical model induced in the peak temperature, ε^T, by relaxing the assumption of constant material properties. Four alternative material property models are considered: the Michelsen (only considering sublimation of C_3), Liu, and Kock models from Michelsen et al. [98] and the Sipkens model, further described in Chapter 6. Also indicated is the Michelsen model including the sublimation of multiple species.

of ~20 K around $\Phi \approx 0.8$. Model errors extending into the high fluence regime (that is $\Phi > 1$) are dominated by the temperature dependence of ΔH_v, and are limited to ~40 K. It is noted that, with the exception of the enhanced absorption due to thermal swelling in the Michelsen model, these model errors are of the same magnitude as the model error introduced by using an interpolation function through the transition regime and amount to only 1% of the peak temperature.

Figure 5.5 also includes the model errors induced by applying the Michelsen model from Ref. [98], which features sublimation of multiple species. The temperature-independent values are generally derived in an analogous manner described above. The exception are the sublimation model parameters, which are taken about a reference temperature corresponding to the boiling point of C_3 at atmospheric pressure, that is $T_{\text{ref}} = 4137$ K. The reference pressure for use in the interpolation function is then taken as atmospheric ($p_{\text{ref}} = 101{,}325$ Pa), and the molar mass and latent heat of vaporization is the vapor pressure-weighted values for each quantity at this reference temperature. The model errors in this case become quite large, a result of significant variations in the sublimation properties with temperature. As a result, it is worth noting that these results are sensitive to the choice of reference properties, which can shift the reference temperature and fluence considerably.

5.5.3 Effect of polydispersity (A5)

As discussed in previous chapters, polydispersity can have a significant impact on the temperature decay observed from a nanoparticle. Chapter 2 noted that the expected signal from a polydisperse aerosol can be represented by Eq. (2.15),

$$\tilde{s}_{\text{j,i}} = \Lambda \cdot \eta_{\text{j}} \int_{d_{\text{p}}} C_{\text{abs},\lambda_{\text{j}}}\left(d_{\text{p}}\right) I_{\text{b},\lambda_{\text{j}}}\left[T_{\text{p,i}}\left(d_{\text{p}}\right)\right] \cdot p\left(d_{\text{p}}\right) \cdot \text{d}d_{\text{p}} \,. \tag{5.35}$$

Furthermore, as noted in Chapter 3, this can be used to define an effective nanoparticle temperature that will deviate from the monodisperse case. This has ramifications on peak temperature fluence curves. Figure 5.6 examines the model error induced in the peak temperature fluence curve as the distribution width increases. The monodisperse case has a small model error, which, as noted above, is a consequence of remaining inadequacies in the interpolation function relative to the simulations around the reference fluence. Increasing polydispersity does not have an effect on the peak temperature in the low fluence regime, a consequence of all of the nanoparticle size classes reaching an identical peak temperature. At higher fluences, the vaporization term, which is size-dependent, induces model errors. At this point, the ratio of laser absorption to sublimation causes the larger nanoparticles to reach higher temperatures. Furthermore, as these large nanoparticles are also weighted more

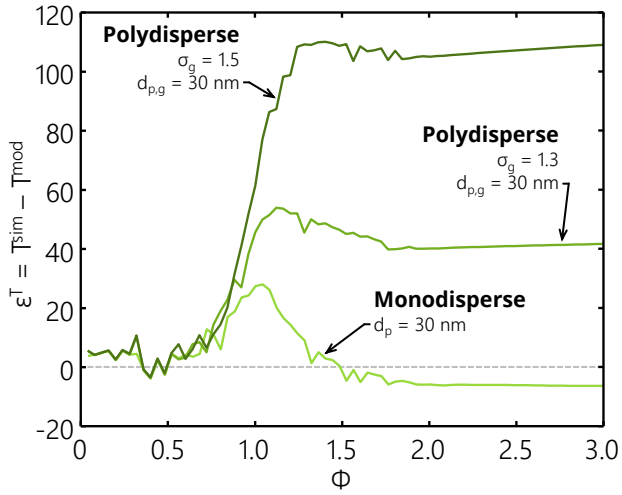

Figure 5.6 Model error in the analytical model induced in the peak temperature, ε^T, by relaxing the assumption of a monodisperse particle size distribution using a lognormal distribution with two geometric standard deviations.

heavily in the integral (cf. Eq. (5.35)), the peak nanoparticle temperature will shift upwards. This model error increases with increasing nanoparticle size distribution width up to +100 K for a distribution having a geometric standard deviation of $\sigma_g = 1.5$.

5.5.4 Combined assumption relaxation

Figure 5.7 examines the model errors induced by simultaneous relaxation of the various phenomena discussed in this chapter. The case shown uses the Michelsen model from Ref. [98], restricting sublimation to C_3 only; a lognormal temporal laser profile with a skew of Sk = 0.928; and a lognormal nanoparticle size distribution with a width of $\sigma_g = 1.5$. The curve exhibits a combination of the various features noted in previous sections, including (i) the positive model error at low fluences due to thermal swelling of the nanoparticle, (ii) the dip in the model error about a reference fluence of unity due to the temporal shape of the laser pulse, and (iii) a large positive model error in the high fluence regime due to a non-linear combination of the polydispersity and sublimation submodel parameter temperature dependencies. This represents a rather extreme case in which the physics underlying each of these assumptions is significantly inadequate. Despite this, the model errors presented in Figure 5.7 correspond to less than 10% of the predicted peak temperatures.

5.6 Experimental comparison

The theoretical dimensionless fluence curve treatment is now applied to experimental curves for soot reported in the literature, specifically those of Michelsen et al. [97,261], Bladh et al. [253], Maffi et al. [110], Olofsson et al.

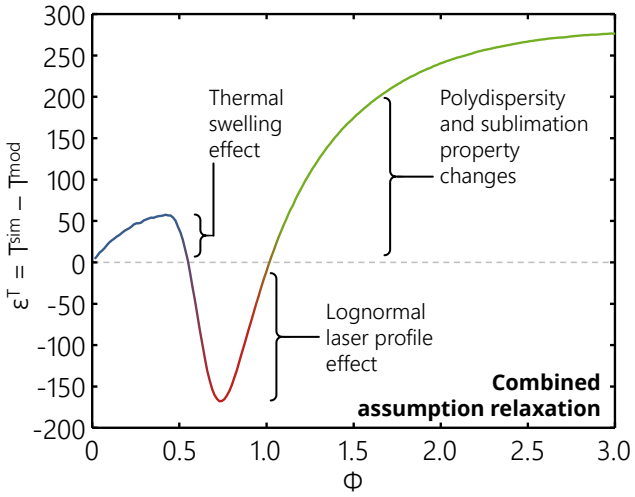

Figure 5.7 Combined model error in the analytical model induced in the peak temperature, ε^T, by relaxing the assumption of a monodisperse particle size distribution, using the temperature dependent properties from the Michelsen model (considering C_3 only), and employing a lognormal distribution for the temperoral variation of the laser pulse energy.

[260], De Iuliis et al. [258], and Liu et al. [176], as well as data from an LII experiment carried out at the National Research Council of Canada (matching the experimental conditions given in Snelling et al. [111] and used in the work of Hadwin et al. [222]). The laser fluences in these studies range from 0.083 to 0.189 J/cm^2.

As noted previously, there is some discord in the literature regarding the radiative properties of soot. Moreover these are known to vary between experiments based on factors that include fuel type, local combustion conditions, and the *age* of the soot [41,260,272]. This would make applying a single value for $E(\mathbf{m}_{\lambda 1})$ unreasonable. Rather, here a value for $E(\mathbf{m}_{\lambda 1})$ is estimated for each study based on the slope of the low fluence regime data. These values are provided in Table 5.2. The large range of estimated $E(\mathbf{m}_{\lambda 1})$ is characteristic of that found in the literature [156]. It can be noted that the estimated values of $E(\mathbf{m}_{\lambda 1})$ for Maffi et al. [110] and Olofsson et al. [260], who collected data under similar experimental conditions, are the same, as one would expect. It is also worth noting that several of these $E(\mathbf{m}_{\lambda 1})$ values are quite large, lying slightly above the range suggested in the literature [156] (particularly those values associated with the studies of Liu et al. [176] and the NRC data). The reason for this discrepancy remains unknown and should be addressed in future research.

Regarding the remaining properties required to evaluate the analytical model, the gas temperature is inferred by extrapolating the peak temperature data back to zero fluence, which generally results in temperatures consistent with the value provided in each study. As noted previously that such an approach

amounts to a novel form of thermometry, whereby the local gas temperature in the flame is determined from the LII fluence curve. The nanoparticle size and laser pulse width are taken from the respective works and summarized in Table 5.2. The remaining material properties are taken from the constant model as defined above. It is also noted that there is considerable uncertainty regarding the spectral dependence of $E(\mathbf{m}_\lambda)$ [41,156]. Hadwin et al. [156,157], for example, investigated some of the uncertainties introduced by this assumption, which has an impact both the temperature and intensity scaling factor (see Chapter 6) inferred from the data. For comparative purposes, however, the temperature data here is derived assuming a wavelength-independent $E(\mathbf{m}_\lambda)$, as is prominent in the literature [42,96,156]. This requires a correction to the original temperatures reported by Maffi et al. [110] and De Iuliis et al. [258], which were calculated assuming a wavelength-dependent $E(\mathbf{m}_\lambda)$ [273] that is distinct from other values reported in the literature.

Figure 5.8 shows that the analytical model reproduces experimentally-observed trends, and that the non-dimensionalization of the problem reduces much of the experimental scatter observed in Figure 5.1. Moreover, the predicted reference fluences for each study, given in Table 5.2, coincide with the transition points in the experimental fluence curves. Remaining discrepancies, such as an overestimation of the plateau temperature for various studies [110,176,253,258], suggest that the present model does not capture all of the physical processes that underlie the measurements or that there are remaining experimental uncertainties that have not been properly taken into account. These observations can be used to motivate further investigation. As a case and point: it is

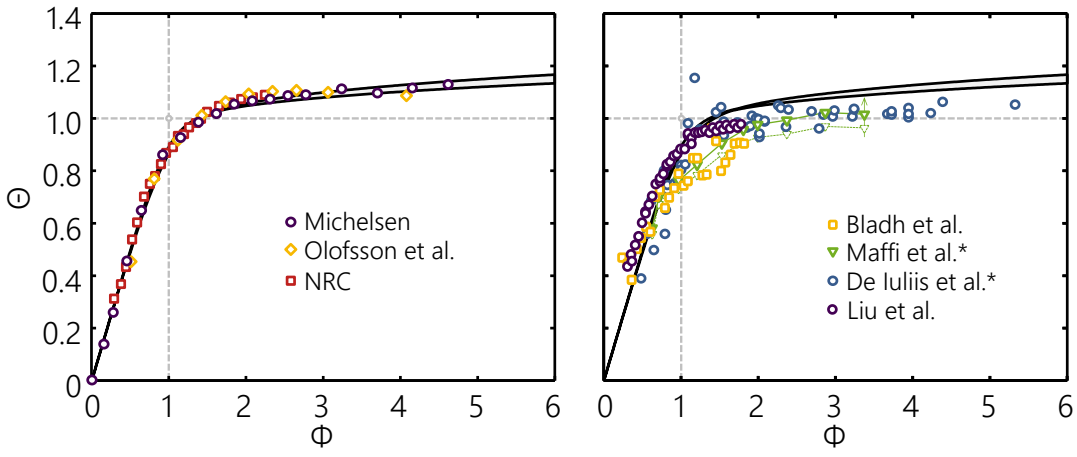

Figure 5.8 Comparison of analytical model to experimental fluence curves reported by Michelsen et al. [97,261], Olofsson et al. [260], Bladh et al. [253], Maffi et al. [110], De Iuliis et al. [258], Liu et al. [54], and unpublished data from the National Research Council (NRC) of Canada. The original Maffi et al. [110] and De Iuliis et al. [274] temperatures are corrected to account for a wavelength-independent $E(\mathbf{m}_\lambda)$. The uncorrected Maffi et al. data [110] is shown for reference.

Table 5.2 Experimental data sets. $E(\mathbf{m}_{\lambda l})$ is inferred from peak temperatures over the low-fluence regime. The laser pulse duration corresponds to the FWHM pulse length specified in each study. Reference temperature and fluence correspond to the solution of Eqs. (5.21) and (5.22), respectively, for each set of experiments. The symbol φ denotes equivalence ratio used in any given study.

Study	Experimental conditions	Model parameters				F_{ref} [J/cm^2]	T_{ref} [K]
		$E(m_{\lambda l})$	d_p	T_g	t_{lp}		
Michelsen et al. [97,261]	Santoro burner, C_2H_2, HAB = 50 mm	0.44	33	1675	10.2	0.115	4205
Olofsson et al. [260]	McKenna burner, C_2H_2, HAB = 10 mm, φ = 0.23	0.29	12	1500	9	0.175	4044
De Iuliis et al. [258]	Laminar coannular diffusion flame, CH_4 and C_2H_2	0.35	20	1820	7	0.133	4167
Bladh et al. [253]	McKenna burner, C_2H_4, HAB = 10 mm, φ = 1.85	0.48	12	2000	9	0.083	4002
Maffi et al. [110]	McKenna burner, C_2H_4, HAB = 13 mm, φ = 0.23	0.29	20	1700	7	0.170	4178
Liu et al. [176]	MiniCAST Model 5201 Type C, C3H8, Laser 1 in [176]	0.60	32	600	6	0.189	4383
NRC data [222]	Gülder burner, C_3H_8, HAB = 42 mm	0.52	35	1700	6	0.101	4328

noted that the adjustment made to the temperatures reported by Maffi et al. [110] and De Iuliis et al. [258], which is consistent with more recent experimental measurements of the $E(\mathbf{m}_{\lambda l})$ function [42,273], brings the corresponding data into better alignment with the analytical model and experimental fluence curves reported by other sources.

5.7 Conclusions

This chapter presents the first comprehensive analytical model of the relationship between laser fluence and peak nanoparticle temperature during pulsed laser heating. Three fluence regimes are identified: the low/linear fluence regime; the moderate/transition fluence regime; and the high/plateau fluence regime. Analytical expressions are derived for the low and high fluence regime, while an interpolating function is specified for the transition regime. Based on these expressions, a set of non-dimensional parameters is proposed that reduces many of the experimentally measured peak temperature fluence curves to a single curve and allows for the formal definition of the fluence regimes about a non-dimensional fluence of unity.

These results highlight the large amount of information contained in fluence curves. Important physical insights that can be obtained by examining the relationship between laser fluence and peak temperature, while

deviations between the derived model and experimental results identifies deficiencies in the spectroscopic and heat transfer submodels that can form the basis of future study and interlaboratory comparison.

Chapter 6
Intensity scaling factor analysis[3]

Our attention now shifts from discussing trends in LII signals with respect to fluence, to trends in these signals with time. Starting from the pioneering work of Roth and Filippov [91], researchers have used some scaling factor to relate the spectral incandescence from the aerosol to a measured voltage. Section 2.1.3 presents some of these formulations. The definition and terminology have varied widely throughout the literature and has encompassed a number of parameters, including the volume fraction, gain, and optical geometry. Mewes and Seitzman [80] inferred such a parameter from their measurements of soot in a laminar diffusion flame, which they called a *proportionality constant* and defined as the ratio of the LII signal to the volume fraction. Mewes and Seitzman were also the first note unexpected temporal anomalies in experimental measurements of this quantity, without hypothesizing on their underlying cause. Snelling et al. [145] presented an alternate phrasing that explicitly defined a calibration factor, η_λ, to relate the spectral incandescence to detector voltage and which excluded the volume fraction. They then present trends over time in the *apparent volume fraction*, that is the value of volume fraction inferred from the spectroscopic model. The parameter is so named due to unexpected increases in the quantity over time for lower fluences and decreases over time for higher fluences that are inconsistent with the value of the true volume fraction. Figure 6.1 demonstrates the relative change in the apparent SVF presented in that work. They suggest that non-uniformities in the laser profile may be the cause for these variations. Hadwin et al. [222] also included such a parameter, which they denote as C_λ, in their study of soot from a laminar diffusion flame. They used a Kalman filter to highlight temporal variation in the quantity. In their review article, Michelsen et al. [97] define yet another variant of this parameter called the *absolute-intensity-calibration factor*, denoted as Ω, which combines the calibration factor from Snelling et al. [145] with various other system-dependent properties. Liu et al. [176] also noted inconsistencies in the inferred apparent

[3] Information presented in this chapter has been submitted for publication as:
Sipkens, T. A., Menser, J., Mansmann, R., Schulz, C., and Daun, K. J., "Examination of changes in the intensity scaling factor inferred from time-resolved laser-induced incandescence," submitted to Appl. Phys. B.

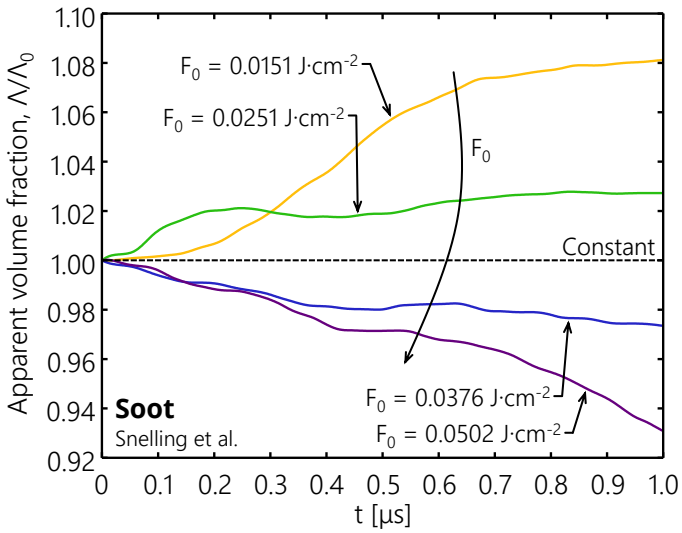

Figure 6.1 The relative change in the apparent volume fraction measured by Snelling et al. [145] during nanoparticle cooling for a range of low-fluence conditions.

volume fraction with laser fluence that are influenced by the choice of laser type and remain unexplained. Variations in these scaling factors have also been observed in TiRe-LII measurements on non-carbonaceous nanoparticles, including molybdenum [131] and silicon [48]. Collectively, these observations lead to the conclusion that this proportionality is not constant at all and therefore includes effects that are not explicitly captured by most LII models. The simplest interpretation is that these phenomena result from *model errors*, that is that these observations are the result of deficiencies in the pyrometry which inaccurately reflect the true physics.

This chapter presents a method for investigating the model errors that result in temporal variations in the *intensity scaling factor* (ISF), the name assigned to the constant that relates the spectral intensity emitted by the probe volume to the detector voltage. Five candidate effects that can influence the ISF are considered: (i) nanoparticle vaporization or sublimation, which is included in standard LII models; (ii) particle annealing; (iii) polydispersity in the nanoparticle size distribution; (iv) a background luminosity effect due to emission from nanoparticles in the line-of-sight (LOS) before and behind the probe volume; and (v) the finite detector response time. These effects are demonstrated by simulating TiRe-LII data for in-flame soot, using new heat transfer and annealing models. This chapter concludes with an analysis of experimental data that not only reveals many of the trends suggested by the theoretical analysis but also notes several remaining anomalies.

6.1 TiRe-LII model

6.1.1 Spectroscopic model

The measured incandescence signal is modeled using Eq. (2.16),

$$\tilde{s}_{\mathrm{j,i}} = \Lambda_{\mathrm{i}} \cdot \eta_{\mathrm{j}} \cdot C_{\mathrm{abs},\lambda_{\mathrm{j}}}\left(d_{\mathrm{p}}\right) \cdot I_{\mathrm{b},\lambda_{\mathrm{j}}}\left[T_{\mathrm{p,i}}\left(d_{\mathrm{p}}\right)\right], \tag{6.1}$$

where Λ is the previously defined, time-varying intensity scaling factor and η_λ the calibration coefficient. For the remainder of this chapter, the absorption cross-section is taken to be the one calculated in the Rayleigh limit. As with Chapter 5, it is assumed that $E(\mathbf{m}_\lambda)$ is independent of λ over the detection wavelengths, which is a common assumption in the TiRe-LII literature [42,96,156]. Accordingly, the ISF can be defined by rearranging Eq. (6.1):

$$\Lambda_{\mathrm{i}} \equiv \frac{\tilde{s}_{\mathrm{j,i}}}{\eta_{\mathrm{j}} \cdot C_{\mathrm{abs},\lambda_{\mathrm{j}}}\left(d_{\mathrm{p}}\right) \cdot I_{\mathrm{b},\lambda_{\mathrm{j}}}\left[T_{\mathrm{p,i}}\left(d_{\mathrm{p}}\right)\right]}. \tag{6.2}$$

There are several ways in which the various quantities that make up the product of $\Lambda(t)\cdot\eta_\lambda$ can be separated. One approach is to set η_λ equal to the definition provided by Snelling et al. [145], which isolates the parameters related to calibrating the LII detector optics and sensors against a continuous signal and is therefore stationary during the measurement. As noted in Section 2.1.3, most instruments are calibrated for their wavelength-dependent sensitivity, so that η_λ is known a priori. The remaining properties, which include the volume fraction and aspects of the optical geometry, are grouped into the ISF, which is, by its definition, a time-varying function that includes the instantaneous particle volume fraction and the effect of sublimation. For the definition of η_λ provided by Snelling et al. [145], this results in a theoretical definition of the ISF as

$$\Lambda = f_{\mathrm{V}} \omega_{\mathrm{b}} \frac{1}{4\pi}. \tag{6.3}$$

In terms of measurements, Chapter 3 notes that the pyrometric temperature is often calculated using ratio pyrometry, Eq. (3.5),

$$T_{\mathrm{p,i}}^{\mathrm{2C}} \approx \frac{hc^2}{k_{\mathrm{B}}}\left(\frac{1}{\lambda_2}-\frac{1}{\lambda_1}\right)\left[\ln\left(\frac{\tilde{s}_{\mathrm{1,i}}^{\mathrm{meas}}\eta_2 E\left(\mathbf{m}_{\lambda_2}\right)\lambda_1^6}{\tilde{s}_{\mathrm{2,i}}^{\mathrm{meas}}\eta_1 E\left(\mathbf{m}_{\lambda_1}\right)\lambda_2^6}\right)\right]^{-1}. \tag{6.4}$$

This approach cancels the ISFs present in Eq. (6.1), so that most researchers often ignore or are unaware of temporal variations in the ISF. However, one can calculate the ISF by substituting the two-color pyrometric temperature from Eq. (6.4) back into Eq. (6.1) and rearranging for Λ to yield

$$\Lambda_{\mathrm{i}}^{\mathrm{meas}} = \frac{\tilde{s}_{\mathrm{j,i}}^{\mathrm{meas}}}{\eta_{\mathrm{j}} \cdot C_{\mathrm{abs},\lambda_{\mathrm{j}}}\left(d_{\mathrm{p}}\right) \cdot I_{\mathrm{b},\lambda_{\mathrm{j}}}\left[T_{\mathrm{p,i}}^{2C}\left(d_{\mathrm{p}}\right)\right]}. \tag{6.5}$$

Alternatively, one can use a minimization scheme, as per Eq. (3.3),

$$\left[T_{\mathrm{p,i}}^{\mathrm{MLE}}, \Lambda_{\mathrm{i}}^{\mathrm{MLE}}\right]^{\mathrm{T}} = \underset{T_{\mathrm{p}},\Lambda}{\arg\min}\left\{\left\|\tilde{s}_{\mathrm{i}}^{\mathrm{meas}} - \tilde{s}_{\mathrm{i}}^{\mathrm{mod}}\left(T_{\mathrm{p,i}}, \Lambda_{\mathrm{i}}\right)\right\|_2^2\right\}. \tag{6.6}$$

As noted in Chapter 3, such a treatment can be used to visualize the relationship between these variables. Figure 6.2 demonstrates this principle for soot signals collected using the apparatus described in Ref. [246] and elaborated on in Section 6.3 at a fluence of 0.129 J/cm^2, 1.5 μs following the peak laser fluence, and using detection wavelengths of λ_1 = 500 nm and λ_2 = 797 nm for inference. The contours show a significant degree of statistical correlation between the inferred parameters, with an elongated valley of candidate solutions that can similarly explain the observed data (though this does not mean that the parameters are correlated according to the underlying physics). Consequently, the results are highly susceptible to measurement errors in the input signals and uncertainties in the model (or nuisance) parameters, including the absorption function [156]. However, it also means that if prior information is introduced on either the ISF or the temperature, the uncertainties in the remaining variable can be reduced considerably, a fact demonstrated in Section 6.3.3.

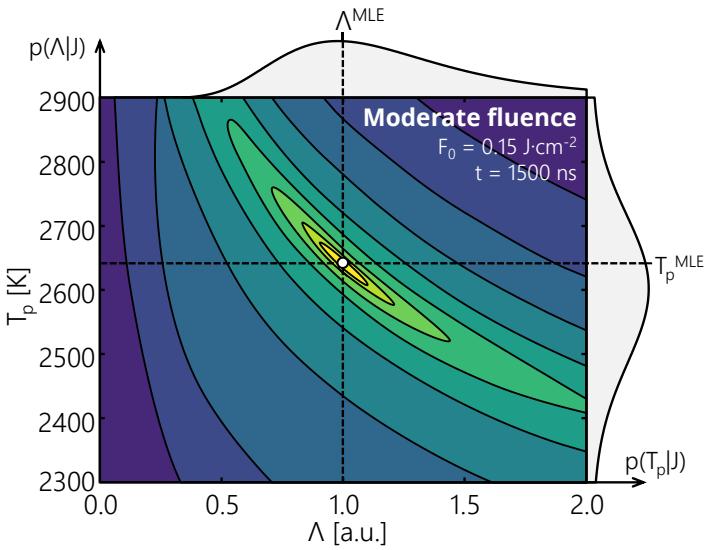

Figure 6.2 Logarithmic contours of the log-likelihood function visualizing the relationship between inferred nanopartice temperature and the ISF. The curved valley identifies the problem as non-linear and demonstrates a degree of correlation between the variables.

6.1.2 Heat transfer model

Here, these principles are first demonstrated on simulated soot signals. For this purpose, a new model for the soot thermophysical properties is defined, which uses the median of the range of values reported in the literature (specifically considering the range of model parameter values given in Michelsen et al. [98]). The model parameter values used in the current study are summarized in Table 6.1. The heat transfer model is defined by solving Eq. (2.20),

Table 6.1 Spectroscopic and heat transfer model parameter values for soot used in generating simulated signals and, excluding the nanoparticle diameter, for interpreting TiRe-LII signals.

Property	Value	Source
Laser energy profile, $f_0(t)$	Gaussian	Having a full width half maximum of 8 ns
Density, ρ	1900 kg/m^3	Taken from the Liu and Boiarciuc models in Michelsen et al. [98], which is considered in the middle of the range of other values given in Michelsen et al. [98]
Specific heat capacity, c_p	T-dependent[a]	Taken from the Will model in Michelsen et al. [98]
Absorption function, $E(\mathbf{m}_\lambda)$	0.34	Constant over all wavelengths, value from Michelsen model in Michelsen et al. [98], which is considered in the middle of the range of other values given in Michelsen et al.
Thermal accommodation coefficient, α	0.30	Average of the values for the models given in Michelsen et al. [98] (other than the original Melton model) and the value given by Sun et al. [275]
Rotational degrees of freedom, ζ_{rot}	2	Based on an N_2 (lin xear polyatomic gas molecule) atmosphere [131]
Gas temperature, T_g	1730 K	Based on experimental conditions and CARS measurements [198,276]
Gas pressure, p_g	101,325 Pa	Based on experimental conditions
Specific latent heat of vaporization, Δh_v	T-dependent[b,c]	See text and notes below.
Critical temperature, T_{cr}	6810 K	Based on the value determined by Leider et al. [203]
Critical exponent, n	0.38	Based on Watson's equation [202]
Román parameter, β_R	0.371	Taken from Román et al. [204]
Molar mass of vapor, m_v	T-dependent	Piecewise constant with sigmoid function for transitions.
Sticking coefficient, β	1	Taken from the Dreier, Kock, and Will models in Michelsen et al. [98]
Vapor pressure, p_v	Kelvin equation	See Eq. (6.12), Eq. (2.45)
Nominal vapor pressure, $p_{v,o}$	Clausius-Clapeyron equation[d,e]	See Eq. (2.44)
Surface tension, γ_s	0.18 J/m^2	Taken from Shih et al. [277]

[a] Given as $c_p = 2900.4 - 36{,}407 \cdot T^{-1/2}$ J/(kg·K).

[b] Below the triple point (4765 K), linear expression is used: $\Delta H_v = 0.6936 \cdot T + 4.214 \times 10^{-5}$ MJ/mol.

[c] Above the triple point (4765 K), Román's equation is used, taken about a reference point of T_{ref} = 5500 K (based on the lower bound for which Leider et al. used Watson's equation) and $\Delta H_{v,ref}$ = 0.3407 MJ/mol (digitized from Leider et al.).

[d] Below the triple point (4765 K), taken about a reference point of T_{ref} = 3000 K, $\Delta H_{v,ref}$ = 0.8215 MJ/mol (from evaluating linear expression at T_{ref}), and P_{ref} = 61.5 Pa (taken from table in Leider et al. [203]).

[e] Above the triple point (4765 K), taken about a reference point of T_{ref} = 4765 K, $\Delta H_{v,ref}$ = 0.3298 MJ/mol (by subtracting the heat of fusion from $\Delta H_{v,ref}$ in c), and Pref = 1.221 × 10^7 Pa (such that the vapor pressure curve is continuous).

$$c_{\mathrm{p}}\rho\frac{\pi d_p^3}{6}\frac{\mathrm{d}T_{\mathrm{p}}}{\mathrm{d}t}=q_{\mathrm{abs}}-q_{\mathrm{cond}}-q_{\mathrm{evap}}. \tag{6.7}$$

The density is taken as constant as 1900 kg/m^3, matching the Liu and Boiarciuc models in Ref. [98], which is considered in the middle of the range of other values given in that work. The specific heat capacity is taken as temperature-dependent from the expression given by the Will model in Ref. [98],

$$c_{\mathrm{p}}=2900.4-36,407T^{-1/2}. \tag{6.8}$$

where c_{p} will be in units of J/(kg·K).

The absorption term is given by Eq. (2.24),

$$q_{\mathrm{abs}}=\frac{\pi^2 d_{\mathrm{p}}^3}{\lambda_1}E\left(\mathbf{m}_{\lambda_1}\right)f_0\left(t\right). \tag{6.9}$$

In this chapter, the laser energy profile is approximated as Gaussian with a full width half maximum (FWHM) of 8 ns and a range of laser fluences. The absorption function, which as noted above is taken as constant over all wavelengths, is $E(\mathbf{m}_\lambda)$ = 0.34, the value from the Michelsen model in Ref. [278], which is again considered in the middle of the range of other values given in that work.

The conduction term is given in the free molecular regime as Eq (2.35),

$$q_{\mathrm{cond}}=-\alpha\frac{\pi d_{\mathrm{p}}^2}{4}n_{\mathrm{g}}c_{\mathrm{g}}k_{\mathrm{B}}\left(2+\frac{\zeta_{\mathrm{rot}}}{2}\right)\left(T_{\mathrm{p}}-T_{\mathrm{g}}\right). \tag{6.10}$$

The thermal accommodation coefficient (TAC) is taken as 0.30, which is the average of the values reported by Ref. [98] (ignoring the original Melton model) and the value given by Sun et al. [275]. The surrounding gas is considered to be N_2, such that ζ_{rot} = 2. The gas temperature and pressure are taken as representative of the experimental conditions in Ref. [246], so that T_{g} = 1730 K, based on the CARS measurements in a laminar diffusion flame [198,276], and p_{g} = 101,325 Pa.

The vaporization term is given by Eq. (2.42),

$$q_{\mathrm{vap}}=-\Delta h_{\mathrm{v}}\beta m_{\mathrm{v}}\pi d_{\mathrm{p}}^2\frac{p_{\mathrm{v}}c_{\mathrm{v}}}{4k_{\mathrm{B}}T_{\mathrm{p}}}=-\Delta H_{\mathrm{v}}\beta\pi d_{\mathrm{p}}^2\frac{p_{\mathrm{v}}c_{\mathrm{v}}}{4RT_{\mathrm{p}}}, \tag{6.11}$$

where β = 1. For the sake of the current work, the latent heat of vaporization, vapor pressure, and molar mass are rederived from the original data of Leider et al. [203], which is the basis for many of the modern expressions [98]. Below the melting temperature, this work uses a linear expression for ΔH_{v} that closely fits the data in Leider and

coworkers. For the rare cases that the temperature exceeds the melting point, the use of the universal expression introduced by Román et al. [204] is proposed, which improves upon Watson's equation used by Leider and coworkers [207] and is discussed further in Chapter 9. Based on the measurements provided by Leider and coworkers, the changes in m_v with temperature are separated into three regimes: (i) low temperatures where C_1 is the dominant species; (ii) beyond 1900 K where C_3 becomes dominant; and (iii) finally, beyond 4500 K where the vapor becomes a mixture of C_3, C_5, and C_7. Accordingly, the molecular mass of the vapor is represented by a step-type function, modified using a sigmoid function so that the transitions between the different regimes are smooth. Finally, the vapor pressure is evaluated using the Kelvin equation, Eq. (2.45),

$$p_v = p_{v,o} \exp\left(\frac{4\gamma_s}{d_p \rho R_s T_p} \right), \tag{6.12}$$

where $\gamma_s = 0.18$ J/cm^2 is the surface tension [277] and $p_{v,o}$ is the nominal vapor pressure above a bulk surface, given by the Clausius-Clapeyron equation, Eq. (2.44). These properties are generally consistent with the other TiRe-LII models presented by Michelsen et al. [98] and the original work of Leider et al. [203], although they predict slightly steeper decays close to the laser pulse.

6.2 Simulating potential model errors in the ISF

Incandescence is simulated at two wavelengths (λ_1 = 500 nm, λ_2 = 797 nm) using the model described in the preceding section. The temperature and ISF are inferred from the simulated data using naïve ratio pyrometry on the modified incandescence. In most cases, the trends with fluence resulting from incorporation of these effects are also considered. This is done relative to the three fluence regimes defined using the method in the preceding chapter. The transition fluence corresponding to the conditions described in Table 6.1 is $F_{ref} = 0.135$ J/cm^2.

6.2.1 Sublimation or evaporation effect

Incorporating sublimation and evaporation effects into the ISF calculation acts as a simple demonstration of how various phenomena can induce temporal variations in the inferred ISF. Figure 6.3 shows the inferred nanoparticle temperature and ISF for fluences ranging from 0.1 J/cm^2 to 0.3 J/cm^2. Changes in the ISF over time are a result of a reduction in the particle volume fraction as the soot sublimates. This occurs close to the laser pulse (prior to 100 ns), when the nanoparticle temperature is high, and only happens at moderate and high fluences. Unlike many of the other effects discussed here, sublimation results in a permanent change in the signal, where the ISF does not return to its original value over time.

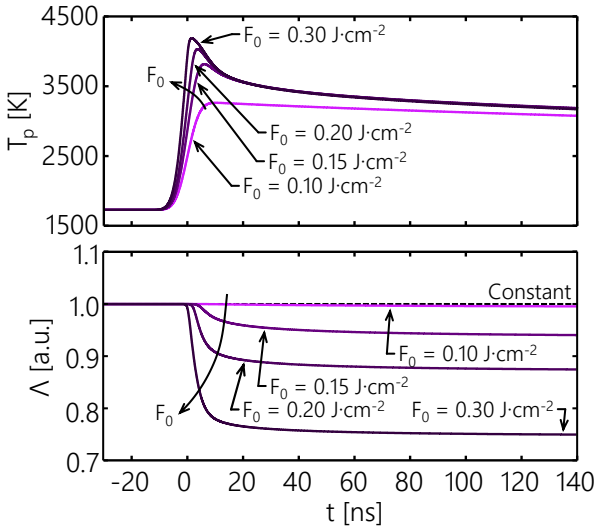

Figure 6.3 Simulated variation in the temperature, T_p, and ISF, Λ, due to vaporization of nanoparticle material. Also shown is the dependence on fluence, with higher fluences resulting in higher temperatures and larger reductions in nanoparticle mass.

6.2.2 Annealing effect

It has been established that soot, when subjected to elevated temperatures, undergoes various transformations that can change its radiative properties and therefore will affect measured ISFs [279]. Transmission electron (TEM) analysis by Vander Wal and coworkers [85,94,280,281], among others [212–214], show that soot anneals from an amorphous structure to an onion-like phase, composed of graphitic layers, during laser heating. Michelsen [104] presents the only model that explicitly accounts for this effect in the context of TiRe-LII, modeling defect annihilation and creation within the carbon matrix. Although this approach qualitatively reflects the annealing process, the model overpredicts the annealing rate at lower temperatures [215], possibly due to overtuning of free parameters, and consequently it predicts fully annealed soot particles even at low fluences. There is also considerable uncertainty regarding how this may affect the radiative properties of soot during cooling. Figure 6.5 demonstrates a partial range of the radiative properties for the different phases of soot. An approximation of the changes determined by line-of-sight attenuation (LOSA) experiments of laser-heated soot [158], in which time-resolved light extinction measurements are made during laser-heating of soot in the flame, are also shown. The LOSA-based values in Figure 6.5 are defined following a linear transformation of the values for soot proposed by Michelsen [104].

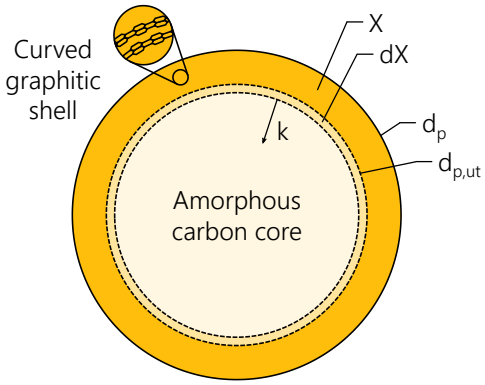

Figure 6.4 Schematic demonstrating the mechanism in the proposed annealing model used in the associated work. The model is based on that proposed for the annealing of diamond by Butenko et al. [282].

In the light of these combined uncertainties, a simplified version of the annealing model is adopted that seeks to improve qualitative agreement with experiments. A reducing sphere model is considered, based on that proposed by Butenko et al. [282] for the graphitization of diamond nanoparticles. The current work adopts different material constants to account for the fact that the initial phase is amorphous soot, rather than diamond. In this model, shown schematically in Figure 6.4, graphitization initiates instantaneously over the primary particle surface. The transformation then progresses into the interior of the primary particle with a single rate, k. The transformed fraction of the individual primary particle X at any given time is described by

$$X = 1 - \frac{d_{\mathrm{p,ut}}^3}{d_{\mathrm{p}}^3}, \tag{6.13}$$

where $d_{\mathrm{p,ut}}$ is the diameter of the untransformed material at any time. It can then be shown that the rate of change in X is given by

$$\frac{\mathrm{d}X}{\mathrm{d}t} = \frac{3\left(1-X\right)^{2/3}}{d_{\mathrm{p}}} \frac{\mathrm{d}d_{\mathrm{p,ut}}}{\mathrm{d}t}. \tag{6.14}$$

The progression of the transformed phase is governed by the Arrhenius equation,

$$\frac{\mathrm{d}d_{\mathrm{p,ut}}}{\mathrm{d}t} = 2k = 2A_0 \exp\left(-\frac{E_{\mathrm{A}}}{RT}\right), \tag{6.15}$$

where E_{A} is an activation energy and A_0 is a pre-exponential factor. The activation energy is taken as 400 kJ/mol, chosen on the lower end of the values reported in the literature (~400-1000 kJ/mol [52]), which brings the model

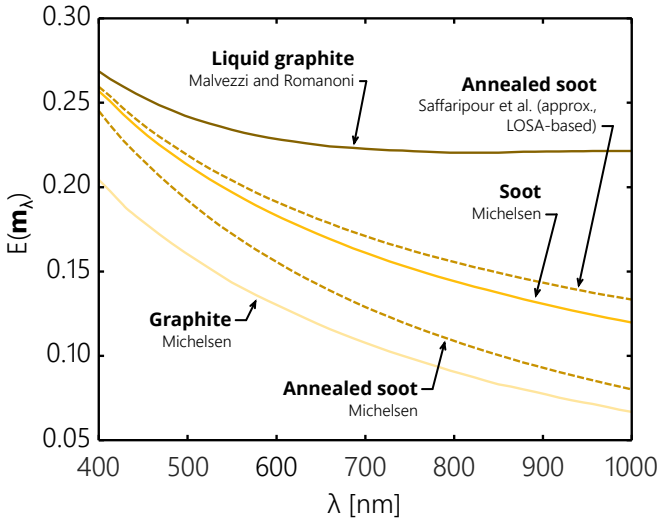

Figure 6.5 Values for the absorption function of various allotropes of carbon and soot. The LOSA-based measurements are digitized from the relative values presented in Figure 12b in [158] for a fluence of F_0 = 0.1 J/cm^2. The shown curve assumes a linear transformation relative to the values for soot defined by Michelsen [104], with the magnitude of the change defined by the digitized LOSA measurements. The remaining values are taken from digitizing Figure 4b in Michelsen [104].

into better agreement with Michelsen's model at high temperatures, while predicting slower annealing times (longer than milliseconds) at flame temperatures, consistent with Ref. [47]. The exponential prefactor is set to 1.0×10^5 s^{-1}, in order to give annealing times consistent with the Michelsen model at moderate fluences, while predicting nearly no annealing in the low fluence regime. The final form of the rate of change in X is

$$\frac{\mathrm{d}X}{\mathrm{d}t}=\frac{6A_0\left(1-X\right)^{2/3}}{d_\mathrm{p}}\exp\left(-\frac{E_\mathrm{A}}{RT}\right). \tag{6.16}$$

This form for the annealing model has the consequence that the rate of $\mathrm{d}X/\mathrm{d}t$ is faster for smaller nanoparticles where there is less material to be transformed. The proposed model also allows for freezing of the transformation at values of $X<1$ for moderate heating. The initial condition for solving is defined as $X=0$, as the annealing rate at flame conditions is slow, and Eq. (6.16) is solved using a 4$^{\mathrm{th}}$ order Runge-Kutta scheme. Figure 6.6 shows the expected progression of the phase fraction, X, over a simulated TiRe-LII experiment for the low, moderate, and high fluence cases. The transformed fraction is observed to match expectations, predicting similar annealing times as Michelsen's model at high fluences and no particle annealing at lower fluences, consistent with results in Ref. [215].

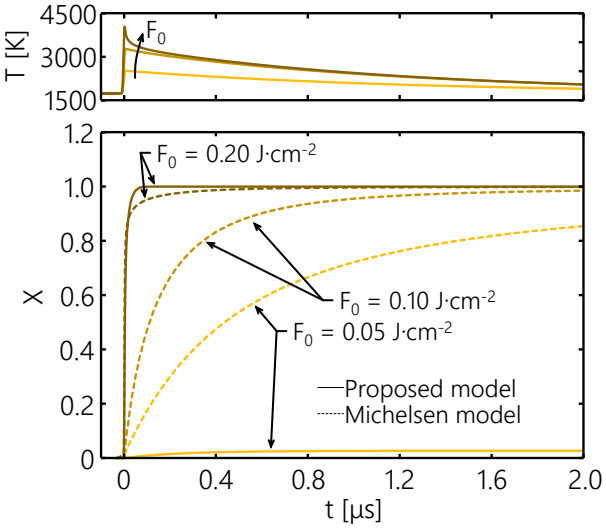

Figure 6.6 Simulated changes in the annealed fraction of the nanoparticle with time over the duration of a TiRe-LII trace and at three different fluences using the heat transfer model presented in Section 6.1.2. The dashed lines correspond to evaluating Michelsen's annealing model [104], and solid lines to the simplified annealing model presented in this chapter. The corresponding temperature traces are shown in the upper plot.

In principle, annealing could influence the soot temperature through the latent heat associated with annealing which could be captured by adding a q_{ann} term into Eq. (6.7),

$$q_{\text{ann}} = \Delta H_{\text{t}} M_{\text{s}} \rho \frac{\pi d_{\text{p}}^3}{6} \frac{dX}{dt}. \tag{6.17}$$

where M_{s} = 12.01 g/mol is the molar mass of carbon and ΔH_{t} is the enthalpy of the phase change. This term is orders-of-magnitude less than sublimation or conduction and is therefore excluded from the heat transfer model. Annealing may, however, have a pronounced effect on the ISF as a result of changing radiative properties (which could also influence the inferred two-color temperature). Considering the large uncertainties in the radiative properties, a range of the possible values suggested in the literature are considered, including the change suggested by Michelsen for annealed soot and those inferred from the LOSA measurements at a fluence of F_0 = 0.1 J/cm^2. For simplicity, $E(\mathbf{m}_\lambda)$ is modeled as a linear combination of the original and transformed values, weighted by volume fraction, X. Figure 6.7 explores the effect of these two cases on the ISF. One can observe that the phenomenon causes a permanent change in the ISF over the same timescale as the annealing process, ~200 ns. As could be expected, an increase in $E(\mathbf{m}_\lambda)$ results in a rise in the ISF, while a decrease in $E(\mathbf{m}_\lambda)$ results in a drop in the ISF, making the temporal variations in the ISF a candidate for investigating changes in $E(\mathbf{m}_\lambda)$ during laser heating, provided that the effect can be isolated from any others present during inference.

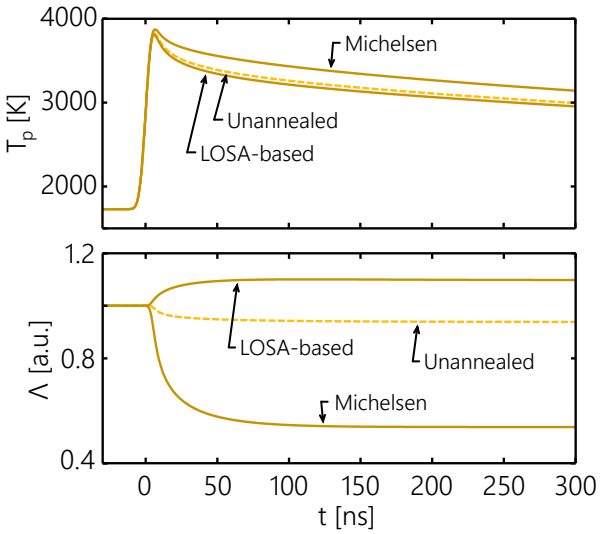

Figure 6.7 Simulated variation in the temperature, T_p, and ISF, Λ, resulting from changes in the radiative properties for a fluence F_0 = 0.15 J/cm^2. The dashed line corresponds to the case of no change in the radiative properties (i.e. vaporization only), while solid lines correspond to the annealed carbon and LOSA-based changes to the radiative properties.

6.2.3 Polydispersity effect

Gas-borne nanoparticles often follow lognormal [283] or Weibull [284] size distributions, depending on the process by which they are synthesized (a fact noted previously in Chapter 5 and later in the experimental analyses of Chapter 8). Incorporating polydispersity into TiRe-LII measurement models has been considered by various practitioners. Cenker et al. [195], for example, considered polydispersity among other effects that influence TiRe-LII signals at higher pressures. Cenker et al. [194] also suggested a procedure to account for polydispersity by fitting two exponential curves to the incandescence decay, demonstrating the approach for both unimodal and bimodal particle size distributions. Including polydispersity has also been shown to be important in inferring synthetic nanoparticle properties [45,48] and influence fluence curves, as noted in Chapter 5.

As noted before, polydispersity can be introduced into the forward model by integrating Eq. (6.1) over the nanoparticle size distribution, matching Eq. (2.15),

$$\tilde{s}_{j,i} = \Lambda(t)\cdot\eta_j\cdot\int_0^\infty C_{abs,\lambda_j}\left(d_p\right)\cdot I_{b,\lambda_j}\left[T_{p,i}\left(d_p\right)\right]\cdot p\left(d_p\right)\cdot \mathrm{d}d_p \,. \tag{6.18}$$

Figure 6.8 shows trends in the temperature and ISF using Eq. (6.18) to generate data, with primary particle diameters that obey a lognormal distribution with a Sauter mean diameter of $d_{p,32}$ = 30 nm and a range of σ_g, and then interpreting the data using ratio pyrometry, Eq. (6.4). The effect of a broadening nanoparticle size

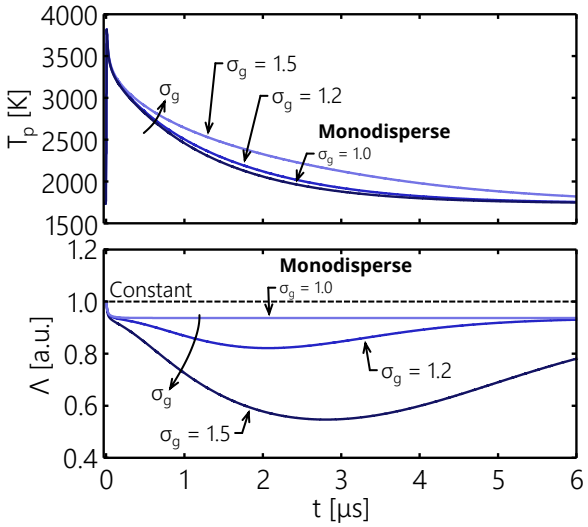

Figure 6.8 Simulated variation in the temperature, T_p, and ISF, Λ, resulting from nanoparticle distributions have widths of σ_g = 1.0 (monodisperse), σ_g = 1.2, and σ_g = 1.5 at a fluence of F_0 = 0.15 J/cm^2.

distribution on pyrometric temperature becomes significant starting 400 ns after the peak laser fluence. As the larger particles cool more slowly than those of average size, the pyrometric temperature decay is biased towards higher temperatures. Such observations are consistent with previous studies [181,194]. More novel is the observation that this phenomenon is also accompanied by a gradual decline in the ISF, where the incandescence emitted by the large nanoparticles dominates over incandescence from the smaller nanoparticles. The ISF recovers as the large nanoparticles also equilibrate with the surrounding gas, on the order of several microseconds depending on the distribution width. These observations match those of Smallwood [221] (cf. Figures 3.34 and 3.35 in that work). Since the variation in ISF is connected to nanoparticle size, it represents additional information that could help recover the distribution width. In fact, unlike the temperature decay, which can be similar for a range of $d_{p,g}$ and σ_g [181,225], the ISF curves are relatively unique for each σ_g and could resolve the ill-posed nature of inferring the quantity from the temperature decay, again assuming the effect can be isolated from any others present in the ISF curves.

6.2.4 Background luminosity and line-of-sight effect

Background emission along the detector LOS includes contributions from both laser-heated soot inside the probe volume and hot soot (luminescing at flame temperature) before and behind the probe volume. Figure 6.9 demonstrates this principle schematically. The total signal from the detector, $\tilde{s}_{j,i}^{tot}$, can be written most generally as

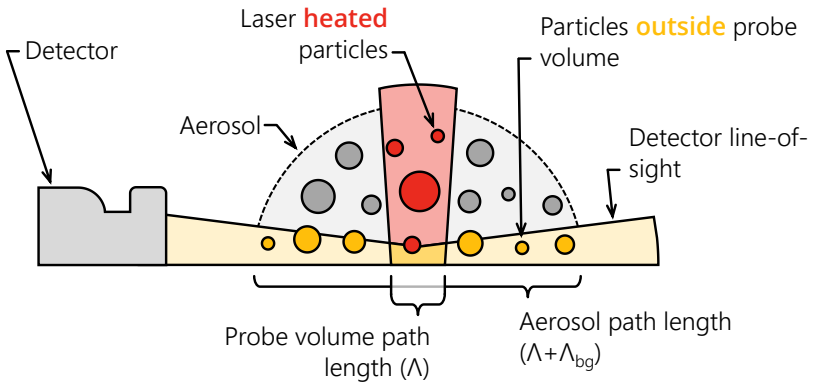

Figure 6.9 A schematic demonstrating the line-of-sight of the detector and the source of the background signal.

$$\tilde{s}_{j,i}^{tot}\left(t\right)=\tilde{s}_{j,i}^{bg}\left(t\right)+\tilde{s}_{j,i}\left(t,T_p\right), \tag{6.19}$$

where $\tilde{s}_{j,i}^{LII}$ is due to incandescence emitted from soot in the probe volume over time and $\tilde{s}_{j,i}^{bg}$ is due to background emission. In this general case, $\tilde{s}_{j,i}^{bg}$ can include incandescence emission from soot in front and behind the probe volume as well as non-incandescent emission (such as plasma emission [270] or fluorescence). Naturally, if the non-incandescent emission is time-dependent, $\tilde{s}_{j,i}^{bg}$ will also be time-dependent. Well-designed experiments aim to select excitation and detection wavelengths so that $\tilde{s}_{j,i}^{bg}$ is limited to time-independent emission. In this case, the background emission can alternatively be written as the total flame radiation prior to the laser pulse, $\tilde{s}_j^{flame}$, reduced by the incandescence from the soot in the probe volume prior to the laser pulse, $\tilde{s}_j^{LII,0}$, so that

$$\tilde{s}_{j,i}^{tot}\left(t\right)=\tilde{s}_j^{flame}\left(t\right)-\tilde{s}_j^{LII,0}\left(t\right)+\tilde{s}_{j,i}\left(t,T_p\right), \tag{6.20}$$

which is the expression adopted by Snelling et al. [198]. In general, researchers must isolate $\tilde{s}_{j,i}$ prior to analysis.

Methods for removing the background luminosity of soot in flames from signals date as far back as Loye et al. [62], who suggested experimental approaches such as lower filter bandwidths and limiting detector exposure time. The simplest approach to remove the background luminosity is for researchers to subtract the flame emission prior to the laser pulse, that is by defining

$$\tilde{s}_{j,i}^{LII*}\left(t,T_p\right)\equiv\tilde{s}_{j,i}^{tot}\left(t\right)-\tilde{s}_j^{flame}=\tilde{s}_{j,i}\left(t,T_p\right)-\tilde{s}_j^{LII,0}. \tag{6.21}$$

In cases where the gas temperature is low or the laser fluence is high and analysis is only considered when the nanoparticles are much hotter than the surrounding gas (that is for cases where $\tilde{s}_j^{LII,0} \ll \tilde{s}_{j,i}$), then $\tilde{s}_{j,i}^{LII*} \approx \tilde{s}_{j,i}$ and this approach is sufficient to proceed with analysis. If that condition is not satisfied, then a method has to be used

to either reintroduce $s_j^{\mathrm{LII},0}$ into Eq. (6.21) or to otherwise accurately simulate the background signal. Snelling et al. [198] proposed an iterative procedure of restoring $s_j^{\mathrm{LII},0}$ by exploiting the fact $\tilde{s}_j^{\mathrm{LII},0} = \tilde{s}_{j,i}(t, T_g)$. Their method is equivalent to defining the following system of three equations about some time, t_i:

$$\frac{\tilde{s}_{j,i}^{\mathrm{LII}^*} + \tilde{s}_j^{\mathrm{LII},0}}{\tilde{s}_j^{\mathrm{LII},0}} = \frac{\exp\left(hc/k_B\lambda_j T_g\right) - 1}{\exp\left(hc/k_B\lambda_j T_{p,i}\right) - 1} \tag{6.22}$$

and

$$T_{p,i}(t) = \frac{hc}{k_B}\left(\frac{1}{\lambda_2} - \frac{1}{\lambda_1}\right)\left[\ln\left(\frac{\lambda_1^6}{\lambda_2^6}\frac{\tilde{s}_{1,i}^{\mathrm{LII}^*} + \tilde{s}_1^{\mathrm{LII},0}}{\tilde{s}_{2,i}^{\mathrm{LII}^*} + \tilde{s}_2^{\mathrm{LII},0}}\right)\right]^{-1}, \tag{6.23}$$

where the former expression is defined for each wavelength to form two equations, and the latter is an adaptation of the pyrometric temperature given by Eq. (3.5) and (6.4). The system is to be solved for $T_{p,i}$ and $\tilde{s}_j^{\mathrm{LII},0}$ at each wavelength. Snelling et al. [198] solved the system iteratively, first evaluating each equation in sequence and then updating $\tilde{s}_{j,i}^{\mathrm{LII}^*}$ by reducing the value at the previous iteration before repeating the procedure. It is noted here, however, that the system can in fact be solved using any optimization scheme. Unfortunately, this method, regardless of the technique used to solve the equations, can incur considerable errors depending on the time at which one chooses to estimate $\tilde{s}_{j,i}^{\mathrm{LII},0}$ and the presence of other effects, as is noted briefly below. Mansmann et al. [200] alternatively used a gated technique to accurately measure $\tilde{s}_j^{\mathrm{flame}}$ and then use the optical geometry to determine what fraction of the flame signal that is expected to be contained in the probe volume. This assumes that the contribution to the background signal is uniform through the flame so that the geometry is sufficient to differentiate these components.

In cases where practitioners inadequately remove the effect of background luminescence, a model error will be incurred during the naïve approach of applying two-color pyrometry to interpret the incandescence data. In the absence of non-incandescent emission, the terms in Eq. (6.19) can be expressed as adaptations of Eq. (6.1), that is

$$\tilde{s}_{j,i}(t,T) = \Lambda(t)\cdot\eta_j\cdot C_{\mathrm{abs},\lambda_j}(d_p)\cdot I_{b,\lambda_j}\left[T_p(d_p,t)\right] \tag{6.24}$$

and

$$\tilde{s}_{j,i}^{\mathrm{bg}}(T_g) = \Lambda_{bg}\cdot\eta_j\cdot C_{\mathrm{abs},\lambda_j}(d_p)\cdot I_{b,\lambda_j}(T_g). \tag{6.25}$$

Here, Λ and Λ_{bg} are the ISFs for the contributions to the signal from soot incandescence inside the probe volume and from the background, respectively (e.g., accounting for the relative concentration path length through the hot, luminescent aerosol and the optical geometry). Note that the Snelling correction procedure can be equivalently interpreted as estimating the value Λ_{bg} about a single point in time. At times around the peak signal intensity, $I_{b,\lambda j}[T_p(d_p,t)]$ is large and $\tilde{s}_{j,i}^{LII}$ dominates Eq. (6.19),

$$\tilde{s}_{j,i}^{tot}(t) \approx \tilde{s}_{j,i}(t,T_p) = \Lambda(t)\cdot\eta_j\cdot C_{abs,\lambda_j}(d_p)\cdot I_{b,\lambda_j}\left[T_p(d_p,t)\right]. \tag{6.26}$$

In these cases, inferring an ISF from pyrometry, using Eq. (6.6), will return Λ. When all of the nanoparticles are at the gas temperature (e.g., before or long after the laser pulse), Eqs. (6.24) and (6.25) are identical except for the scaling factor,

$$\tilde{s}_{\lambda,i}^{tot} = \tilde{s}_{j,i}(t,T_p) + \tilde{s}_{j,i}^{bg}(t,T_p) = \left[\Lambda(t)+\Lambda_{bg}\right]\cdot\eta_j\cdot C_{abs,\lambda_j}(d_p)\cdot I_{b,\lambda_j}(T_g). \tag{6.27}$$

In this case, analysis of TiRe-LII data would result in an ISF equal to the sum of Λ and Λ_{bg}. In other cases, the ISF will lie between Λ and Λ_{bg}. Naturally, corrective procedures can be understood as attempts to estimate Λ_{bg}, so that it can be subtracted from signals.

To illustrate this approach, consider simulated signals generated following the procedure described in Section 6.2.1, except that the signals are corrupted with a background intensity due to incandescence from soot outside of the probe volume at a flame temperature of 1730 K [198,276]. The effect is demonstrated by assuming

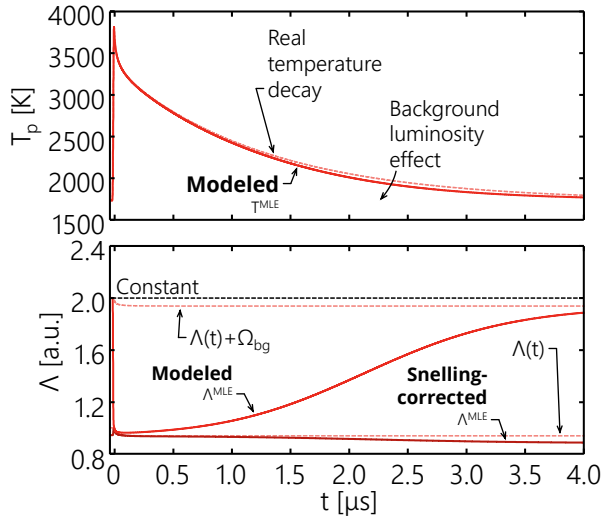

Figure 6.10 Simulated variation in the temperature, T_p, and scaling factor, Λ, showing the effect of background luminosity at a fluence of F_0 = 0.15 J/cm^2 and for a nanoparticle size if d_p = 30 nm. Also shown is the inferred ISF following the Snelling correction defined by the solution of Eqs. (6.22) and (6.23).

an equal concentration path length through the aerosol both inside and outside of the probe volume, so that Λ = 1.0 and Λ_{bg} = 1.0. The temperatures and ISFs inferred from these corrupted signals, without any correction, are shown in Figure 6.10. The effect on the pyrometric temperature is subtle and would be difficult to discern in the presence of noise or without a reference signal. However, the effect on the ISF is immediately apparent, featuring a rapid decline when the laser-heated soot begins to dominate the signal. The extent of the decline varies, depending on the fluence. However, the minimum possible value of Λ would occur when the laser-heated soot completely overwhelms the signal from the unheated soot, rendering the latter negligible. The ISF will recover to $\Lambda + \Lambda_{bg}$ after ~4 μs, when the laser-heated soot has thermally-equilibrated with its surroundings. At high fluences, the temperature decreases more rapidly than at moderate fluences, meaning that the ISF also recovers more quickly. The shape of these curves qualitatively resembles experimental results reported in Ref. [145] derived from measurements on a laminar ethylene diffusion flame at atmospheric pressure, which suggests that the background intensity may not have been adequately removed during that analysis. These ISF curves could also be used to investigate the presence of other possible phenomena, like plasma emission [270] or the local gas heating phenomenon observed by various practitioners (e.g. [200]) that may otherwise be difficult to discern from the temperature decay alone.

As a second illustration of the utility of ISF approach, consider simulated signals generated in an analogous manner as above. However, this time the data is corrected using the procedure of Snelling et al. [198], implementing Eqs. (6.22) and (6.23) about a point 60 ns after the peak laser fluence, before inferring the ISF. This result is also indicated in Figure 6.10. In this case the inferred ISFs well-represent only the LII contribution for the first 1.5 μs. Beyond this point, the ISF still deviates from its true value. This deviation is a consequence of sublimation having reduced Λ at the time used in the Snelling correction (that is, the soot volume fraction in the probe volume is not the same before and after the pulse) resulting in an inaccurate estimate of Λ_{bg} prior to the laser pulse. Similar problems may be encountered if the correction is taken about other points in the signal (for example, close to the laser pulse where the correction may incur errors due to detection system response effects, discussed below).

6.2.5 Detection system response effect

It is well-established that measurements of time-varying optical phenomena are convolved with the response function of the detector system. These effects can vary significantly with sensor type and experimental setup. The response time of gated PMTs, for example, can be limited by the limited voltage that drives the current

needed to restore the photocathode charge. Mansmann et al. [246] recently examined the performance of PMTs in measuring TiRe-LII. They noted various non-linearities in the PMT response that depend on the photocathode material and background light level. Other aspects of the detector system, like incorporating integrating spheres, can also have an influence on the response time of the detector system. For simplicity, the problem is here reduced to considering a simple convolution of the TiRe-LII signal with a Gaussian temporal response function.

Consider a TiRe-LII signal convolved with an instrument response function so that the measured signal, $\tilde{s}_j^{meas}$, is

$$\tilde{s}_j^{meas}(t) = \int_{-\infty}^{\infty} s_j^{tot}(t)\, p_{tr}(t)\, dt\,. \tag{6.28}$$

where $\tilde{s}_j^{tot}$ is the original LII signal and the detector response function is Gaussian, $p_{tr}(t) = \mathcal{N}(t; \mu^{tr}, \sigma^{tr})$, with mean μ^{tr} and standard deviation, σ^{tr}. Figure 6.11 shows trends in the temperature and ISF up to 140 ns after the peak laser energy assigning a standard deviation of σ_{tr} = 1.0 ns to the Gaussian response function (which is representative of some commercially available PMTs) for both channels. This causes a temporal shift in the pyrometric temperature, a reduction in the peak temperature (due the smoothing effect of the time response function), and a slightly faster decay in temperature for the first 10 ns. The latter effect could be partially responsible for the anomalous cooling phenomenon noted in the literature [106,110,194,198]. However, the effect

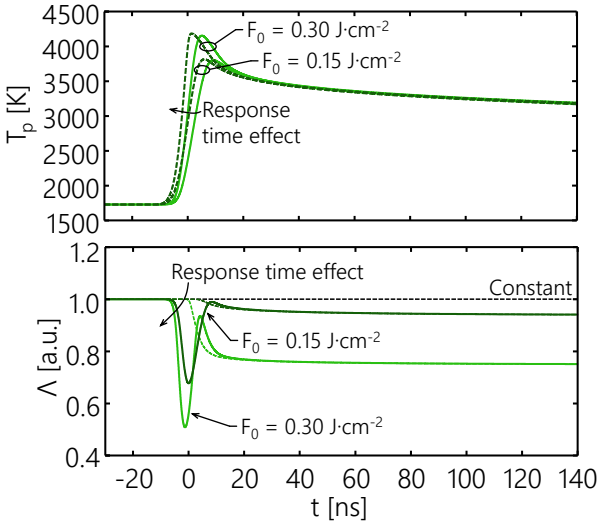

Figure 6.11 Simulated variation in the temperature, T_p, and ISF, Λ, due to a Gaussian instrument response function of the detector at two different fluences. The effect is isolated to times around the laser pulse (generally less than 30 ns).

of the finite sensor response on the temperature is limited to within 10 ns following the peak fluence meaning that it is insufficient to solely describe anomalous cooling to the extent observed in the literature. While the effects on the pyrometrically-inferred temperature are subtle, the ISF, in contrast, shows a pronounced dip that increases in magnitude with increasing fluence. In all cases, this dip is faster than the vaporization process, and, as a result, the ISF can exhibit a secondary peak near the end of the laser pulse after the ISF has recovered from the detector time response effect but before the vaporization effects are most pronounced. Such observations justify the decision of many researchers to ignore the peak signal when inferring the soot volume fraction from LII data. The problem becomes more complex in the case that the channels have different rise times, which can arise from using different types of PMTs. When simulated LII signals are generated using sensors having response times differing by ±20%, the dip in the ISF becomes more pronounced.

6.2.6 Combined effects

The various effects considered above are now combined, noting that the effects have to be included in a specific order. Specifically, one must first compute the annealing and sublimation effects for each size class before they can be combined using Eq. (6.18) to incorporate polydispersity. It is this signal that is corrupted with background luminescence, before the detector response function is finally incorporated. Figure 6.12 shows trends in the prompt and full ISF and temperature curves over a range of fluences after combining the effects considered above, using $d_{p,32}$ = 30 nm, σ_g = 1.5, a Gaussian response function with a standard deviation of σ_{tr} = 1 ns, Λ = 1.0, Λ_{bg} = 1.0, and a modified $E(\mathbf{m}_\lambda)$ representative of LOSA measurements (as per Section 6.2.2).

Close to the laser pulse, the ISF exhibits a sharp decline due the fact that the TiRe-LII signal dominates over the background luminescence. For low fluences, the laser-heated soot particles do not heat up enough to dominate the measured signal and, as a result, the ISF does not decline to Λ = 1.0. As indicated in Section 6.2.4, such effects in the ISF could in significant part be removed by applying a correction to the data. For moderate to high fluences, the ISF curve exhibits a sharp dip around the laser pulse, a consequence of the temporal response function of the detector. At high fluences, the ISF exhibits an artificial *peak* as the ISF recovers from the time-response before declining again due to the change in soot volume fraction with sublimation. For moderate fluences, the enhancement of the optical properties resulting from annealing is observable as a rise in the ISF between the end of the laser pulse and 200 ns following the laser pulse. At higher fluences, this enhancement is hidden by polydispersity and sublimation effects. At moderate-to-high fluences, the ISF is then observed to decline over a period of about 1.5 μs due to polydispersity effects. Finally, in all cases, the ISF is observed to rise

for times in excess of 2.5 μs following the peak as the nanoparticle equilibrate with the gas and background luminescence reappears. These observations are generally qualitatively consistent with those of Snelling et al. [145], who noted a slow decline in the ISF for high fluences and a slow rise in the ISF for low fluences. In an experimental setting, measurement error, such as that noted in Ref. [237], is likely to mask many of these features, particularly those prior to the laser pulse and at later cooling times.

6.3 Examination of experimental signals

Experimental data used to examine the validity of this approach is collected in collaboration with Mr. Raphael Mansmann and colleagues at the University of Duisburg-Essen, using the apparatus described in Ref. [246]. TiRe-LII measurements are carried out on soot in laminar diffusion flame [96,145] operating with 0.194 L/min ethene and 284 L/min air at a height-above-burner of 42 mm. The soot particles are heated by a pulsed Nd:YAG laser at 1064 nm with a full-width half-maximum of 8 ns and an approximately top-hat spatial laser profile. The laser

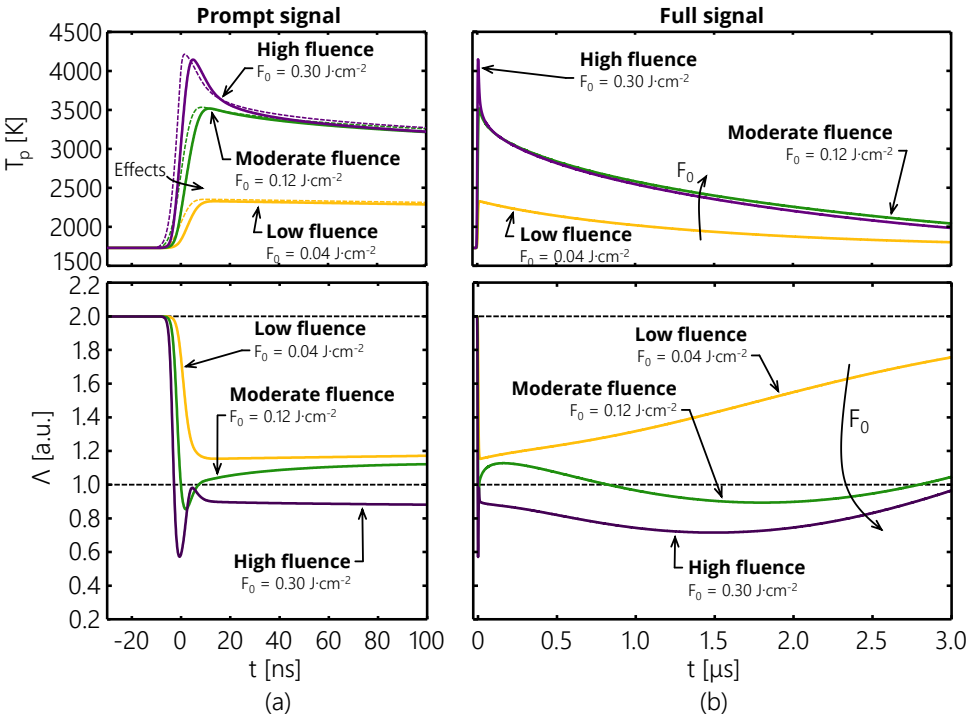

Figure 6.12 Simulated variation in (a) the prompt and (b) longer timescale ISF and temperature curves combining the effects discussed in Section 3, including: sublimation, the annealing model from this work with the LOSA-based changes in the optical properties, polydispersity with a distribution width of σ_g = 1.5, a background luminescence corresponding to Λ = 1.0 and Λ_{bg} = 1.0, and a Gaussian time response with a width of σ^{tr} = 1 ns. Dashed lines in temperature curves correspond to the case where only the polydispersity and sublimation effects are included.

fluence is controlled using a half-wave plate and polarizer and varied between 0.05 and 0.25 J/cm^2 for the current work. However, discussion here is limited to only three fluences representing the low (F_0 = 0.05 J/cm^2), moderate (F_0 = 0.15 J/cm^2), and high (F_0 = 0.25 J/cm^2) fluence regimes defined in Chapter 5. The emission is collected with a series of lenses and is passed through an optical fiber and integrating sphere, that latter of which allows for the complementary investigation of calibration procedures detailed in Ref. [246]. The light is finally focused onto four gated PMTs equipped with bandpass filters at 500 ±13 nm (×2), 684 ±13 nm, and 797 ±9 nm. Figure 6.13 summarizes the experimental apparatus. Channels 2 (500 nm) and 4 (797 nm), as indicated in Figure 6.13, are used for inference in the current work. Signals from 200 laser shots are acquired and averaged for each measurement to reduce measurement error. The oscilloscope is optically triggered to prevent any effects that could enter the measurement due to temporal laser jitter. The measurement errors produced by this apparatus were discussed previously in Chapter 4.

6.3.1 Inferred temperatures

Pyrometrically-inferred temperature curves for low and high fluences are shown in Figure 6.15, displaying many of the characteristics observed in the simulated data. The low fluence case shows slower decays, due in part to absence of cooling by sublimation in the period following the laser pulse. At high fluences, the peak temperature is higher and decays more quickly due to the high amounts of sublimation. The high fluence case also features

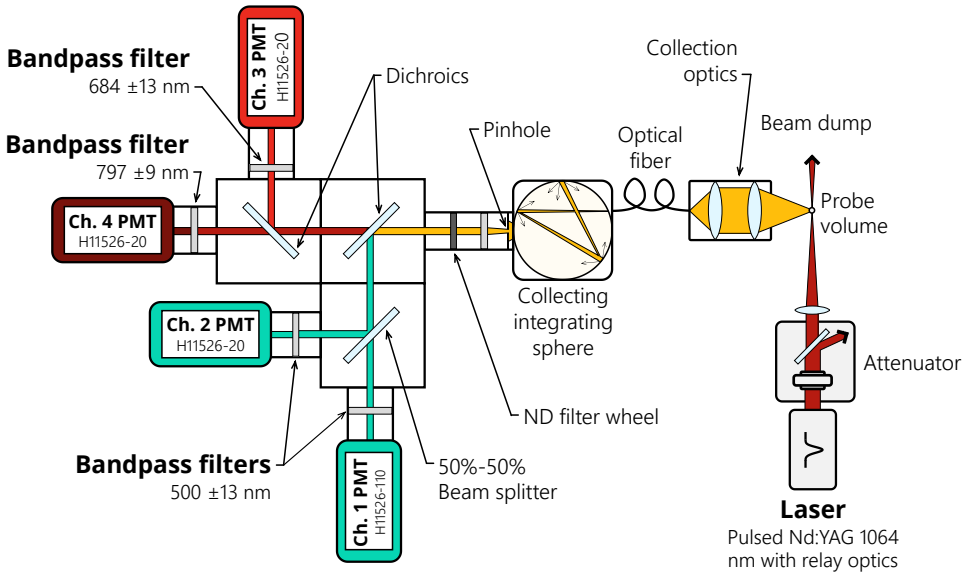

Figure 6.13 Four channel LII apparatus. The integrating sphere was used to simultaneously image other light sources onto the PMTs (see Ref. [246]).

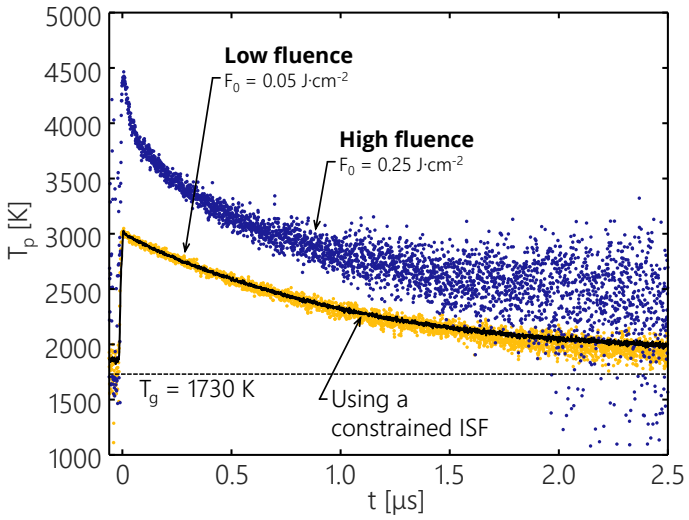

Figure 6.14 Temperature decays for soot at a low fluence (F_0 = 0.05 J/cm^2) and a high fluence (F_0 = 0.25 J/cm^2).

considerably more noise, a result of the signal dropping from its peak value to being nearly undetectable within a short amount of time. The experimental apparatus used here [246] is sufficiently sensitive so that, in the low fluence case, the measured incandescence before the pulse can be used to derive an estimate of the gas temperature prior to the laser pulse, with Figure 6.15 indicating $T_g \approx 1730$ K, consistent with Coherent anti-Stokes Raman spectroscopy (CARS) measurements made at the same location on an identical flame [198,276].

6.3.2 Inferred ISF

Figure 6.15 shows the ISF corresponding to the temperature traces shown in Figure 6.14. Prior to the laser pulse, the ISF is characterized by a high degree of measurement error, fluctuating up to several orders of magnitude. This can be understood by considering that before to the laser pulse, the measured signal will be very low for both channels. The governing Poisson-Gaussian noise model indicates that this will result in low signal-to-noise ratios (cf. Chapter 4), which, when used in conjunction with ratio pyrometry, will result in the amplification of measurement errors in inferred ISFs (this equally results in large fluctuations in the temperature before the laser pulse in Figure 6.14). Such effects get worse for higher fluences, where a larger dynamic range is required to measure the strong peak in the incandescent signal. In this case, the signals from soot at the gas temperature measured before the laser pulse will incur significant errors due to the lower digitization limit of the oscilloscope. For the low fluence regime, the value of the ISF prior to the laser pulse is larger than that observed throughout the remainder of the curve, consistent with the background luminescence effect discussed in Section 6.2.4 for

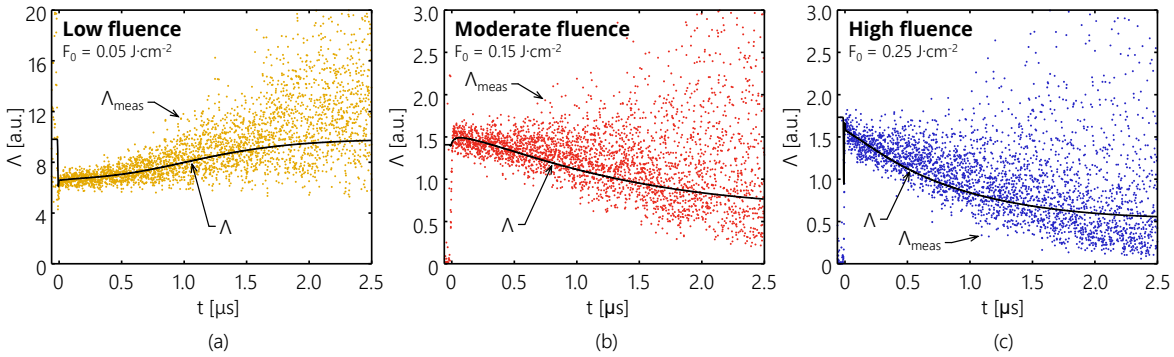

Figure 6.15 Trends in the ISF with time at a low fluence (F_0 = 0.034 J/cm^2), moderate fluence (F_0 = 0.158 J/cm^2), and high fluence (F_0 = 0.250 J/cm^2). Solid lines denote simulations convolving all of the effects described in Section 6.2, with parameters fit to the experimental data.

signals without correction. For higher fluences, the ISF is observed to be lower than that throughout the remainder of the signal, which is likely a consequence of the lower digitization limit of the oscilloscope such that the signal prior to the laser pulse cannot be accurately measured.

During the laser pulse, the signal noise decreases dramatically, and the ISF exhibits several abrupt fluence-dependent characteristics. For low to moderate fluences, the ISF curve is characterized by a sharp decline consistent with the background luminescence effect. As with the simulated case, the ISF inferred for the lowest laser fluence case maintains a higher ISF value close to the peak signal, a consequence of the laser-heated soot contributing a smaller portion of the total signal relative to the high fluence case. As a result, the background luminescence, if not properly accounted for, would inflate the inferred volume fraction at these low fluences. In all cases, the ISF exhibits a sharp drop lasting about 10 ns about the laser pulse, which appears consistent with the finite temporal response of the detector system (expected in this case to be a result of temporal blending from the integrating sphere). This feature is most prominent in the moderate fluence regime where the change in intensity is more dramatic but not influenced by significant annealing effects. This phenomenon would almost certainly confound soot volume fraction measurements made using near-peak incandescence data justifying the choice by researchers to neglect prompt LII signals.

Following the laser pulse, the low fluence ISF curve exhibits a slow rise, consistent with a background luminescence effect wherein the unheated soot begins to corrupt the LII signal. For the moderate and high fluence regimes, one would expect a significant drop in the ISF as sublimation reduces the volume fraction of particulate in the aerosol. On the contrary, the ISF is observed to increases for the moderate fluence regime and decreases only slightly for the high fluence regime. This may rather suggest an increase in the absorption

function as a result of annealing, consistent with LOSA measurements [158] and matching the simulated conditions shown in Figure 6.12. Nevertheless, remaining discrepancies between the model and experimental data suggest the presence of additional unaccounted-for mechanisms (e.g. aggregate reconstruction and collapse [212] or plasma formation and emission [270]) the preclude any definitive conclusions.

Following the above noted effects, the high and moderate fluence ISF curves exhibit a slower, prolonged decline in the ISF lasting on the order of 1.5 μs. This effect is consistent with polydispersity in the primary particle diameters. The decline is more prominent for higher fluences where the larger nanoparticles hold higher temperatures for longer durations. For high fluences, this decline becomes corrupted by signal noise from 500 ns following the pulse. Although there is still a significant downward trend, the contributions of the large particles are often overwhelmed by the background signal and measurement error. This marks the end of the usable, uncorrupted signal.

6.3.3 Reducing uncertainties in inferred temperatures

The ISF can also be viewed as additional information that may improve estimates of other inferred quantities, provided that this effect can be simulated accurately. This is particularly important given the high degree of correlation between the temperature and ISF [157]. Consider simultaneous inference of the ISF and temperature, this time using Eq. (6.6) and constraining the ISF to the simulated value shown in Figure 6.15 (equivalent to applying a very narrow prior on the ISF during inference). Figure 6.14 shows the inferred temperature following this procedure for a low fluence. The temperature decay is marked by a significant reduction in measurement error. Deviations at later times may correct temperatures where the noise falls below the lower discretization level of the oscilloscope. However, further study is required to properly understand the uncertainties in the ISF simulations and propagate them through to the temperatures (i.e. better characterization of model errors, perhaps to be determined in regards to engineered carbon nanoparticles). Accordingly, practitioners could also consider applying a prior with a finite distribution width on the ISF and infer the temperature using a Bayesian procedure (cf. [222] or Chapter 3).

6.4 Conclusions

TiRe-LII practitioners have long been aware of unexplained temporal variations in the scaling factor used to modify Planck's law. This chapter examines the ramifications of the temporal variation in the intensity scaling factor, with outlooks for improving the inference of soot characteristics and providing a more robust understanding of TiRe-LII signals. These observations support the common practice of avoiding the peak LII

signal for volume fraction measurements, as the volatility of the ISF in this region may induce significant errors in measurements. However, they also serve to caution researchers who calculate the ISF from the latter parts of the signal, where sublimation, polydispersity, annealing, and background luminosity effects may influence calculations. Some of these effects can be removed, for example by correcting for sublimation or applying the background correction of Snelling et al. [198]. While some aspects of the experimental ISF curves remain uncharacterized, this chapter demonstrates how the ISF can act as an additional source of information to answer remaining questions in TiRe-LII analysis.

This chapter concludes by showing how the information contained in the ISF may provide an appropriate method of reducing uncertainties in inferred temperatures (by exploiting the high degree of correlation between the ISF and temperature). This must be done with caution as improper prior information can bias the results. Consequently, further work should be done to properly characterize the uncertainties and model errors in the derived ISF curves. This should include advancing the current model to include effects such as the possibility of plasma emission, aggregate shielding, aggregate collapse, and spatial inconsistencies in the laser profile (which could be incorporated using principle component analysis approaches [157]).

Chapter 7
The thermal accommodation coefficient[4]

Free molecular conduction is often the most important form of heat transfer in TiRe-LII analyses and plays an important role in determining quantities-of-interest, such as the nanoparticle diameter. Fundamental to this term is the thermal accommodation coefficient (TAC), introduced in Section 2.2.3.2 and discussed in more detail in Appendix C. Studies quantifying this parameter date back to the 1970s, where the primary application was calculating drag from satellites in the upper atmosphere. An extensive summary of experimentally-derived TACs prior to 1980 is provided by Saxena and Joshi [285]. Goodman and Wachman [286], meanwhile, summarize the classical theoretical treatments developed over a similar period. Most early theoretical studies considered only a single surface atom or approximated the atoms in the surface as hard spheres. The Baule model [287], for example, considers the scattering of a gas atom from a surface atom initially at rest. Such a simple model is limiting, particularly in that it does not account for the motion of surface atoms and requires that the gas atoms be much less massive than the surface atoms (since it presumes only one surface atom is involved in the collision). Cube models [288,289], also discussed in Appendix C, address some of these shortcomings by modeling the interaction between a gas molecule and a moving surface cube that represents an ensemble of surface atoms. These theoretical studies highlight how the TAC depends on various quantities [286,290], including: the mass ratio, $\mu = m_g/m_s$, where m_g is the gas molecular mass and m_s is the surface atomic mass [106,112,286,291]; the temperature ratio, $\tau = T_g/T_s$, where T_g and T_s are the gas and surface temperatures respectively [286,291,292]; the surface roughness observed by the gas molecule [286,290,293]; and the lattice frequency. Unfortunately, while

[4] Information presented in this chapter has been disseminated as:
Sipkens, T. A., and Daun, K. J., 2018, "Effect of surface interatomic potential on thermal accommodation coefficients derived from molecular dynamics", accepted to the J. Phys. Chem. C. doi: 10.1021/acs.jpcc.8b06394

these analytical models allow for a greater understanding of the underlying physics (cf. [294]), the assumptions inherent in these models significantly limits the accuracy of TAC estimates.

Additionally, few scattering experiments and simulations are carried out at the high surface temperatures relevant to TiRe-LII studies (generally >1500 K [285,292]). In this regime, $T_s \gg T_g$, so the scattered gas molecular trajectories are strongly influenced by the thermal motion of the surface atoms. Furthermore, $k_B T_s$ is much larger than the potential well depth, meaning that direct scattering is more probable than trapping or desorption on the surface. Accordingly, in the context of TiRe-LII, TACs are often inferred from pyrometrically-defined cooling rates for cases where the nanoparticle size distribution is known, most often from ex situ analysis [21,24,45,49,106,112]. Unfortunately, the accuracy of LII-inferred TACs is limited by uncertainties in the spectroscopic and heat transfer model parameters, including the radiative and thermodynamic properties of the nanoparticles and the ex situ nanoparticle sizes.

To address this shortcoming, TiRe-LII practitioners have started to apply molecular dynamics (MD) to predict the TAC. MD simulations follow the trajectories of individual atoms in the material, with their motion governed by classical dynamics and interatomic force fields. Early MD simulations of gas-surface scattering in the more traditional scattering regimes by Wachman et al. [295] and Charita et al. [296] demonstrated how the technique could be used to evaluate the TAC. However, these studies did not incorporate realistic surface interatomic potentials and were restricted in the number of candidate gas-surface combinations. Since then, progressively more complex and realistic simulations have been performed for a broader range of gas-surface pairs. Several studies [297–299] used the MD approach to simulate gas molecules moving between parallel plates of platinum to determine energy transfer to gases in nanochannels. This approach results in gas velocity distributions that depend on the pressure and distance between the plates. Hu and McGaughey [300] and Schiffres et al. [301] performed similar simulations but within multiwalled carbon nanotubes. MD simulations have also been used to calculate TACs for equilibrium gases and Au [302,303], Pt [304], and Al [305] surfaces. Moreover, some works have included parametric studies that investigate the sensitivity of MD-derived TACs to gas temperature [108,189,296], surface temperature [189], and potential well depth [108,300,306]. Figure 7.1 demonstrates trends with two of these parameters: (i) trends with the surface temperature, T_s, for gas-surface pairs with a mass ratio, $\mu = m_g/m_s \approx 0.2$, and (ii) trends with the mass ratio for elevated surface temperatures, $T_s > 1500$ K. Trends in MD-simulated TACs [48,107,108,189,306,307] are generally consistent with those observed in experimental studies [21,24,45,48,106,112].

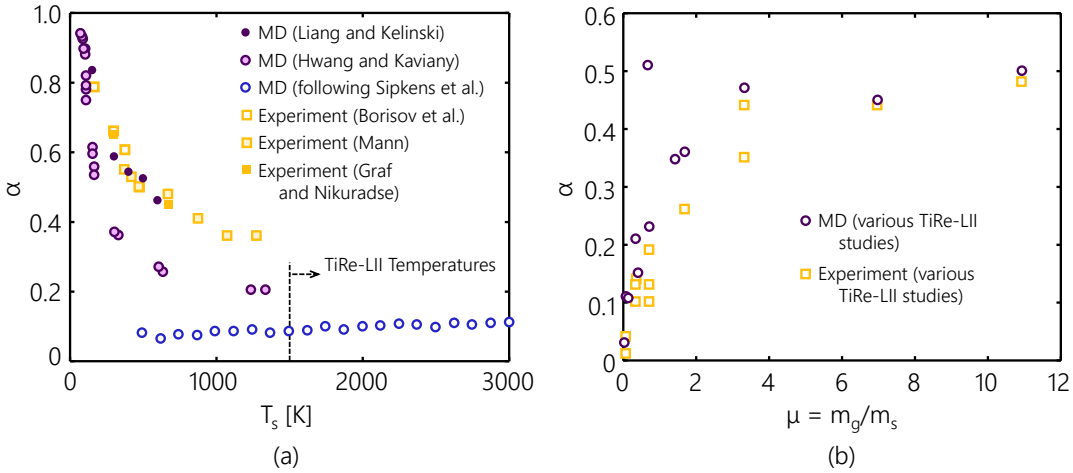

Figure 7.1 Trends in experimentally and MD-predicted thermal accommodation coefficients with (a) T_s for gas-surface pairs around $\mu \sim 0.2$ (specifically Pt-Ar having $\mu = 0.205$, Au-Ar having $\mu = 0.203$, and Si-He having $\mu = 0.143$) and (b) $\mu = m_g/m_s$ for $T_s > 1500$ K and derived for TiRe-LII applications. For (a), experimental sources are Borisov et al. [308] (Pt-Ar), Mann [309] (Pt-Ar), and Graf and Nikuradse [310] (Au-Ar); and MD sources are Liang and Keblinski [311] (Au-Ar), Hwang and Kaviany [312] (Pt-Ar), and Sipkens et al. [48] (Si-He, re-evaluated following the procedure in this work). For (b), experimental sources are Refs. [21,24,45,48,106,112] and MD sources are Refs. [48,107,108,189,306,307].

In the context of TiRe-LII, Daun and coworkers first computed the TAC with MD by modeling the scattering of monatomic [107] and polyatomic [189] gases from graphite, which was used as a surrogate for soot. These simulations were shown to match experimentally-derived TACs from LII measurements on soot. Kamat et al. [313] used a more refined ReaxFF reactive force field to consider multiple gases scattering and reacting with carbon nanoparticles and graphite. Since then, MD has been used to calculate TACs under TiRe-LII conditions for Mo [108], Fe [108], Ni [306,307], and Si [48]. Some of the simulations [48,108] have even been used to interpret experimental TiRe-LII traces [45,48,132], including the analysis presented in Chapter 8.

Uncertainties in MD-derived TACs can stem from various sources, including imperfect knowledge of the incident conditions; unknown gas-surface potential parameters, such as the potential well depth and equilibrium distance; and variations in the functional form of the gas-surface potential itself, which can allow for multiple minima for both physisorption and chemisorption (e.g. [314]). While most of these sources have been characterized in the literature previously, the sensitivity of MD-derived TACs to the chosen surface potential parameterization remains a significant unknown in this process. Surface potential parameterizations often contain large sets of fitting parameters and diverse functional forms that make parametric studies challenging. The present work addresses this by comparing different parameterizations proposed in the literature for a given material. Iron, copper, and silicon surfaces are considered, which are important in the TiRe-LII literature, and

represent a variety of different crystal structures and dynamics. This study includes several gas-surface pairs not considered previously, including Fe-Ne, Cu-He, Cu-Ne, and Cu-Ar. This chapter first reviews the various classes of empirical interatomic potentials that are often used to model to chosen materials, including discussion of three-body, embedded-atom model (EAM), and bond-order potentials. Simulations proceed by implementing these potentials for different surfaces. Differences between the implemented potentials are gauged by visualization of the surfaces and calculation of MD-derived densities. The TAC is finally evaluated using a Monte Carlo procedure over a range of surface temperatures typical of LII measurements (from 1,500 K to 4,000 K). Recommended values of the TAC are given for each of the gas-surface pairs considered in this work. The results not only allow for an estimate of uncertainties in MD-derived TACs that can be propagated through TiRe-LII models (cf. Chapter 8) but also provide additional physical insights into the value of the TAC itself.

7.1 Surface potential parameterizations

The breadth of interatomic potentials in the literature reflects the variety of materials that have been modeled with the MD technique. The most ubiquitous, and one of the simplest, is the Lennard-Jones (LJ) 6-12 potential

$$U_{ij} = 4\varepsilon\left[\left(\frac{\sigma}{r_{ij}}\right)^{12} - \left(\frac{\sigma}{r_{ij}}\right)^{6}\right], \tag{7.1}$$

where ε and σ are the potential well depth and zero potential energy intercept, respectively. This parameterization is generally considered to accurately represent van der Wals interactions. Often smooth cut-off functions are introduced to improve computational efficiency without causing discontinuities in any number of higher order derivatives of the potential. The Morse potential shares similar features with the LJ potential, but foregoes the inverse power law, replacing it with exponential functions

$$U_{ij} = D\exp\left[-2a\left(r_{ij} - R\right)\right] - 2D\exp\left[-a\left(r_{ij} - R\right)\right], \tag{7.2}$$

where D, R, and a are material constants. It is generally considered better at modeling simple bonding-like interactions within materials. Unfortunately, such simple potentials cannot describe all possible material configurations, particularly those involving coordination and manybody type effects. Three other classes of potentials are discussed that provide more accurate descriptions of metals and silicon, the materials of interest in this chapter4.

7.1.1 Embedded atom model potentials

The embedded atom model (EAM) class of potentials, originally attributed to Daw and Baskes [315], are among the most widely used to represent metals. They operate on the principle of embedding atoms in an electron cloud. This results in a potential energy of the form

$$U_i = \frac{1}{2}\sum_{j \neq i} U_2\left(r_{ij}\right) - F\left(\sum_{j \neq i} \rho_j\left(r_{ij}\right)\right), \tag{7.3}$$

where U_2 is a two-body pair potential between the i^{th} and j^{th} atoms, ρ_j is the electron charge density resulting from the j^{th} surrounding atom, and F is the embedding function. The functional forms of U_2, ρ_j, and F vary depending on the parameterization selected. The choice of embedding function must, however, be non-linear, or the potential reduces to a simple two-body form. The Finnis-Sinclair (FS) formulation, for example, uses an embedding function of $F(x) = x^{1/2}$ based on tight-binding theory. Sutton and Chen [316] have since adopted long-range parameterizations of the Finnis-Sinclair potential for various metals, including nickel, which has formed the basis for previous low-energy gas-surface scattering simulations [306]. These potentials are particularly useful in characterizing the melting process and simulating interstitial atoms in many metals.

It is notable that there is not a unique definition for U_{ij} in terms of its pair potential and embedding function contributions [317]. This can lead to ambiguity in defining the fitting parameters presented for the models, particularly in the units prescribed for electron density. One approach is to transform the potential into the effective pair scheme, such that the derivative of the electron density is zero for atoms in an equilibrium lattice, resulting in

$$F^{\text{eff}}\left(\rho\right) = F\left(\rho\right) - F'\left(\rho_0\right) \tag{7.4}$$

and

$$U_2^{\text{eff}}\left(r\right) = U_2\left(r\right) + 2F'\left(\rho_0\right)\rho\left(r\right), \tag{7.5}$$

where ρ_0 is the electron density at an atom position in the case of an undisturbed reference lattice. This has the advantage that, for small perturbations from equilibrium, the forces on the atoms are well approximated by the effective two-body component alone [318]. Accordingly, this pair scheme, calculated on a reference lattice at room temperature, is used for cross-examination against other pair potentials in Section 7.2.

7.1.2 Three-body potentials

Three-body potentials are formed from the linear combination of two-body, U_2, and three-body, U_3, terms,

$$U_{\mathrm{i}} = \frac{1}{2}\sum_{j\neq i} U_2\left(r_{\mathrm{ij}}\right) + \sum_{j\neq i}\sum_{k>j} U_3\left(r_{\mathrm{ij}}, r_{\mathrm{ik}}, \theta_{\mathrm{ijk}}\right), \tag{7.6}$$

where θ_{ijk} is the angle formed between the three atoms denoted as *i*, *j*, and *k*. The two-body and three-body terms are intended to explicitly model bond stretching and bending, respectively, giving rise to preferences for certain atomic configurations that are particularly useful in modeling diamond cubic structures that feature sp^3 hybridization (such as those that occur in silicon and carbon).

The most common potential of this form is the Stillinger-Weber (SW) potential [319], a cluster bonding potential originally parameterized for silicon. The potential adopts an inverse power rule for the two-body contribution reminiscent of the LJ potential

$$U_2\left(r\right) = A\varepsilon\left[B\left(\frac{\sigma}{r}\right)^p - \left(\frac{\sigma}{r}\right)^q\right] f_{\mathrm{c}}\left(r_{\mathrm{ij}}\right), \tag{7.7}$$

where A, ε, B, σ, p, and q are model parameters and

$$f_{\mathrm{c}}\left(r\right) = \exp\left(\frac{\sigma}{r - a\sigma}\right), \tag{7.8}$$

is a cutoff function that ensures a smooth transition to $U_2 = 0$ at the cutoff radius and a is another model parameter. The original parameterization of the SW potential set $q = 0$. The potential then employs a separable three-body component

$$U_3\left(r_{\mathrm{ij}}, r_{\mathrm{ik}}, \theta_{\mathrm{ijk}}\right) = h\left(r_{\mathrm{ij}}\right) h\left(r_{\mathrm{ik}}\right) g\left(\theta_{\mathrm{ijk}}\right), \tag{7.9}$$

where

$$h\left(r\right) = \exp\left(\frac{\gamma}{r - R}\right), \tag{7.10}$$

$$g\left(\theta\right) = \left[\cos\left(\theta\right) + \cos\left(\theta_0\right)\right]^2, \tag{7.11}$$

and γ, R, and θ_0 are additional model parameters.

7.1.3 Bond-order potentials

The bond-order class of potentials, derived from tight-binding theory, was also developed to simulate stable diamond cubic structures. The class consists of multibody potentials in which the interatomic interactions are modeled by pairwise bond-type interactions that are modified by the local environment. This amounts to potentials of the form

$$U_{ij} = U_R\left(r_{ij}\right) - b_{ijk} U_A\left(r_{ij}\right), \tag{7.12}$$

where U_R and U_A are the repulsive and attractive components of the potential, representing the bond, and b_{ijk} modifies the attractive component based on the environment. The form of b_{ijk} varies greatly depending on the application.

The Tersoff potential [320] is one of the simplest bond-order potentials, having repulsive and attractive components reminiscent of the Morse potential, specifically

$$U_R\left(r\right) = A\exp\left(-\lambda_1 r\right) f_c\left(r\right) \tag{7.13}$$

and

$$U_A\left(r_{ij}\right) = B\exp\left(-\lambda_2 r\right) f_c\left(r\right), \tag{7.14}$$

where A, λ_1, B, and λ_2 are fitting parameters, and an explicit cutoff function defined as

$$f_c\left(r\right) = \begin{cases} 1, & r < R - D \\ \frac{1}{2} - \frac{1}{2}\sin\left(\frac{\pi}{2}\frac{r-R}{D}\right), & R - D < r < R + D \\ 0, & r > R + D \end{cases}, \tag{7.15}$$

where R and D are additional model parameters. The cutoff function is much sharper than many other potentials, as demonstrated in Figure 7.3 and Figure 7.13 below. The b_{ijk} term incorporates three-body interactions specifying an explicit angular dependence that acts to weaken the bond in the case of unfavorable configurations by

$$b_{ij} = \left(1 + \beta^n \zeta^n\right)^{-1/2n}, \tag{7.16}$$

where

$$\zeta = \sum_{k,j} f_c\left(r_{ik}\right) g\left(\theta_{ijk}\right) \exp\left[\lambda_3^m \left(r_{ij} - r_{ik}\right)^m\right], \tag{7.17}$$

$$g\left(\theta\right) = \gamma\left(1 + \frac{c^2}{d^2} - \frac{c^2}{d^2 + \left(\cos\theta - \cos\theta_0\right)^2}\right), \tag{7.18}$$

and b, n, λ_3, m, c, d, and θ_0 are fitted parameters.

The environment-dependent interatomic potential (EDIP) [321], has a similar form to the SW potential, containing explicit two- and three-body terms of similar functional forms. Unlike the SW potential, however,

the EDIP potential contains a modified attractive term that adjusts the magnitude of the two- and three-body terms based on a calculated coordination number, that is, the number of immediate neighbors to a given atom. Such a treatment is natural for covalently bonded materials, where interactions are generally well-approximated by considering only those with an atom's closest neighbors. At low coordination numbers, corresponding to diamond cubic structures, the EDIP potential effectively reduces to the Stillinger-Weber potential and strongly reinforces the covalent bonds. As the coordination number increases and the atoms become more tightly packed, the EDIP potential predicts weakened angular dependences, allowing for a transition from covalently bonded structures, like diamond cubic silicon, to metallic-like interactions, like those in liquid silicon. It is worth noting that such a treatment differs in a fundamental sense from the Tersoff potential in that it considers interactions on an atom-by-atom basis, without requiring symmetry, rather than approximating a material as a series of bonds of varying strengths. The EDIP potential is particularly useful in transitioning the angular portion of the potential to prefer different angles depending on the coordination number, which is needed for materials that switch between sp^2 and sp^3 hybridization.

It is also noted that the aforementioned FS potential is unique in that it can be equally represented as a bond-order and EAM potential [322]. The bond-order equivalent forgoes any angular dependence in b_{ijk}, opting rather to have a dependence on the local electron density for multiple surrounding atoms. In fact, the choice of a square root dependence for the embedding function is derived from tight-binding theory, which is the basis for bond-order potentials.

7.2 MD simulations of gas-surface scattering

The above potentials are now deployed to predict the TAC for three surface materials – iron, copper, and silicon – and a range of monatomic gases. Simulations are performed using a similar procedure as was implemented in Ref. [48], and detailed in the following section.

7.2.1 Simulation procedure

Gas atoms are scattered over a theoretically infinite flat surface generated by applying periodic boundary conditions to the lateral surfaces of the simulation domain. Atoms are initialized at equilibrium positions within the crystal structure expected at the specified surface temperature and assigned velocities representative of that temperature. For cases where liquid is expected, the surface is initialized in the crystal structure that exists prior to melting (e.g. face-centered cubic or body-centered cubic). Surfaces are maintained at the specified temperature using the Nose-Hoover thermostat, which allows the surface to evolve under standard number-volume-

temperature (NVT) conditions for 25 ps (or 25,000 timesteps) in LAMMPS [323]. The warmed surfaces are then allowed to continue in the number-volume-energy (NVE) ensemble, corresponding to keeping the total energy of the surface constant, for 5 ps to ensure that the system has reached a steady-state. The final state is saved to a dump file for use in the subsequent scattering simulations. To prevent biases resulting from the warmed surface state, the TAC is calculated using six independently-warmed surfaces at each surface temperature, with each surface having a different seed velocity for the surface atoms.

Scattering simulations proceed by loading a warmed state from a dump file and repeatedly bouncing gas atoms off of the surface. In each case, a single gas atom is initially assigned a velocity randomly sampled from a Maxwell-Boltzmann distribution at the gas temperature, shifted to account for the fact that gas molecules with large normal components are more likely to strike the surface, that is, Eq. (C7),

$$\mathbf{v}_{\mathrm{i}}^{k} \sim f_{\mathrm{i}}\left(\mathbf{v}_{\mathrm{i}}, T_{\mathrm{g}}\right)=\frac{2\beta_{\mathrm{T}}^{4}}{\pi} w_{\mathrm{i}} \exp\left[-\beta_{\mathrm{T}}^{2}\left\|\mathbf{v}_{\mathrm{i}}\right\|_{2}\right]. \tag{7.19}$$

where $\mathbf{v}_{\mathrm{i}} = [u_{\mathrm{i}}, v_{\mathrm{i}}, w_{\mathrm{i}}]^{\mathrm{T}}$ is the initial velocity and $\beta_{\mathrm{T}} = (m_{\mathrm{g}}/2k_{\mathrm{B}}T)^{1/2}$ is the inverse most probable speed of the gas. The gas atom then scatters from the surface, and the scattering simulation continues until the vertical position of the gas atom above the surface exceeds its starting position. At this point, the scattered velocity, $\mathbf{v}_{\mathrm{o}}$, is recorded. The TAC for any given simulation, γ, is then calculated based on the change in the kinetic energy over the scattering event, Eq. (C24),

$$\gamma^{\mathrm{k}}=\frac{E_{\mathrm{o}}-E_{\mathrm{i}}}{\left\langle E_{o}-E_{i}\right\rangle_{\max}}=\frac{m_{\mathrm{v}}\left(\left\|\mathbf{v}_{\mathrm{o}}^{\mathrm{k}}\right\|_{2}^{2}-\left\|\mathbf{v}_{\mathrm{i}}^{\mathrm{k}}\right\|_{2}^{2}\right)}{4k_{\mathrm{B}}\left(T_{\mathrm{s}}-T_{\mathrm{g}}\right)}. \tag{7.20}$$

It is noted that the value of γ for any given scattering event need not be bounded by [0,1], since this constraint (related to the 2nd Law of Thermodynamics) only applies to the average. The TAC can then be calculated by averaging, Eq. (C30),

$$\alpha=\frac{\left\langle E_{\mathrm{o}}-E_{\mathrm{i}}\right\rangle}{\left\langle E_{o}-E_{i}\right\rangle_{\max}} \approx \frac{1}{N}\sum_{k=1}^{N}\gamma^{\mathrm{k}}. \tag{7.21}$$

In the present case, 1500 scattering events, 250 per warmed surface, are used to generate this estimate, and a timestep of 1 fs is employed. An analogous procedure can be used to define the normal and tangential TACs, replacing the velocities used in Eq. (7.20) with the velocity components normal and tangential to the surface (see

Appendix C for more detail). The trajectory for a single scattering event for Fe-Ar at $T_s = 2500$ K is shown in Figure 7.2.

7.2.2 Iron

In this work, four surface potential parameterizations for iron are examined: the LJ potential as parameterized by Filippova et al. [326]; the EAM potential as parameterized by Zhou et al. [324]; the FS potential as parameterized by Mendelev et al. [327]; and the Tersoff potential as parameterized by Müller et al. [328]. The Filippova (LJ) potential was fit to the material properties of α-Fe alone. This, combined with its simple form, is expected to result in poor performance, particularly over large temperature ranges over which iron undergoes multiple phase changes and eventually melts. On the other hand, the simplicity of this potential is appealing

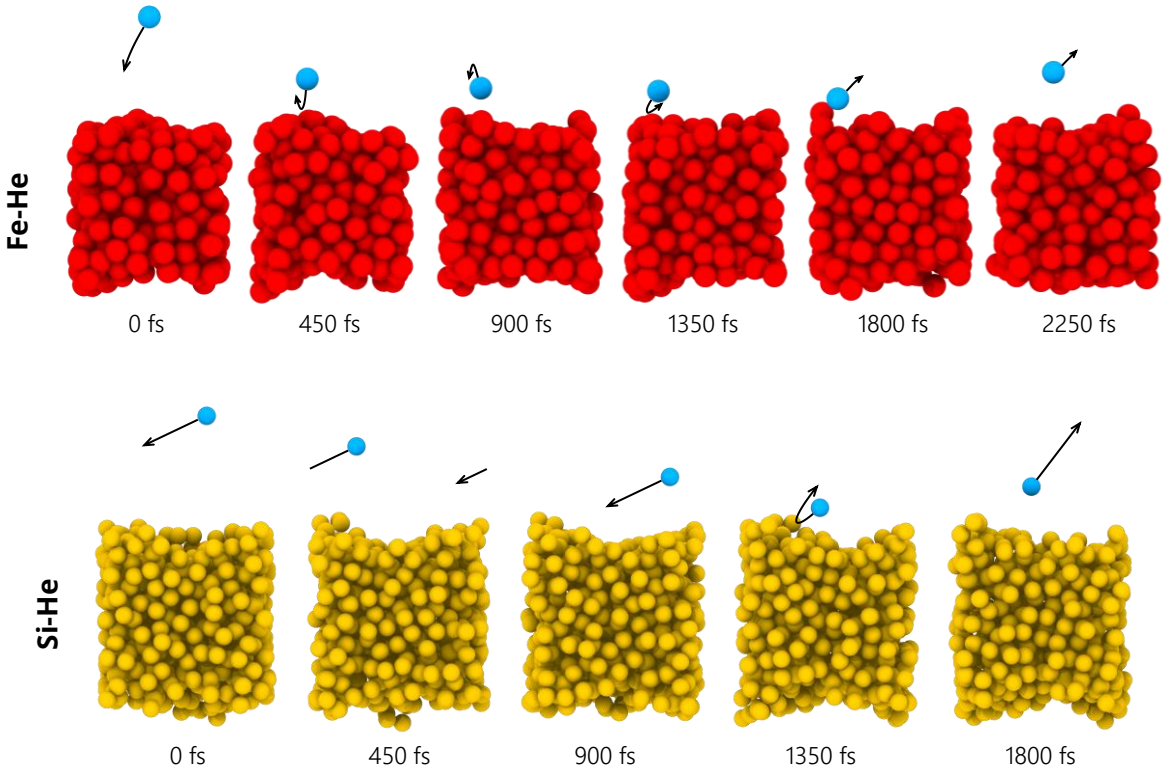

Figure 7.2 A sample MD-predicted trajectory for (top) a helium atom scattering from an iron surface for T_s = 2500 K, T_g = 300 K, and using a surface potential parameterization of the EAM form from Zhou et al. [324], and (bottom) a helium atom scattering from an silicon surface for T_s = 2500 K, T_g = 300 K, and using a surface potential parameterization of the EAM form from Stillinger and Weber [319]. This specific Fe-He trajectory involved a single bounce on the surface and a backscattering event where much of the tangential velocity is reversed. Visualizations here, and throughout this chapter, are created in OVITO [325].

from a computational perspective and so represents a valuable test case for whether simpler potentials are sufficient for calculating the TAC.

Figure 7.3 shows the pairwise potential (or effective pairwise potential for EAM and FS) for the parametrizations considered in this work, as well as the FS potentials of Ackland et al. [332] and Finnis and Sinclair [329,330] (used in previous scattering MD simulations [108]) and the Morse potential parameterized by Girifalco and Weizer [333]. For visualization purposes, the value of b_{ijk} for the Müller (Tersoff) potential is set to unity. The shape of the Tersoff pair interaction in Figure 7.3 is strongly influenced by the cutoff function explicitly defined in the potential. This is the reason for the abrupt change in the slope of the potential about r = 3 Å. The Zhou (EAM) and Mendelev (FS) effective pair potentials feature shallower potentials wells and are very similar, sharing similar equilibrium radii and well depths. The Müller and Filippova (LJ) potentials both have much deeper wells, although the depth of the former varies based on the specific atomic configuration. The deeper well for the LJ potential is likely required to maintain the solid phase in the absence of accounting for manybody effects.

Figure 7.4 shows realizations of iron surfaces at four surface temperatures corresponding to the α, γ, δ phases of solid iron, as well as liquid iron. Surface are initiated in the phase expected at that temperature, in this case

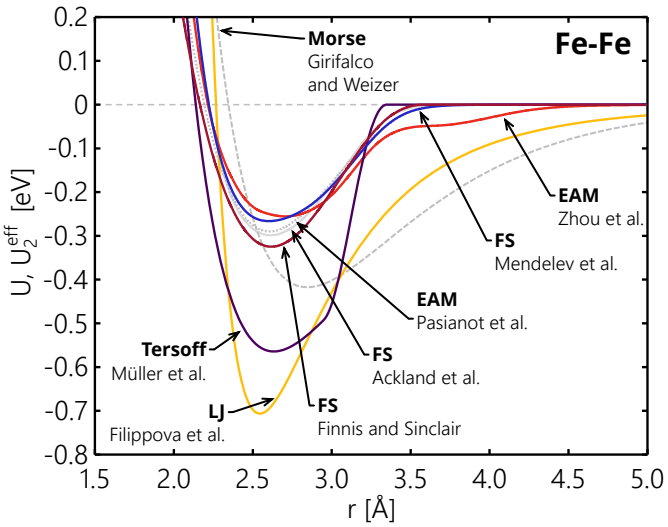

Figure 7.3 Pair potentials for Fe-Fe interactions from Filippova et al. [326], Finnis and Sinclair [329,330], Mendelev et al. [326], Zhou et al. [324], Müller et al. [328], Pasianot et al. [331], Ackland et al. [332], and Girifalco and Weizer [333]. The effective pair scheme is used for the EAM and FS potentials. For the Tersoff potential, bijk is calculated considering the equilibrium lattice positions of a BCC structure. Faded lines correspond to potentials for which TACs were not calculated in this work.

using a lattice constant calculated from density values given in Mills [334]. Discussions are enhanced by consideration of MD-derived densities, which are compared to experimental values in Figure 7.5.

Realizations of the Filippova (LJ) potential [326] reveal visible distortion for the α and δ body-centered cubic (BCC) phases. While this distortion is not visible in the γ phase, Figure 7.5 indicates that the Filippova potential significantly overpredicts the density. This is not unexpected as the potential was intended to model room temperature iron. The solid structure is maintained well beyond the melting temperature, which indicates further limitations in using this potential for elevated temperatures. Similar results would be expected from the Morse potential [333], though the shallower well shifted to slightly larger radii would allow for lower densities and for a quicker transition to liquid (estimated for the to be 2290 K for the Girifalco and Weizer potential by Imamova et al. [335] compared to 1811 K, measured experimentally).

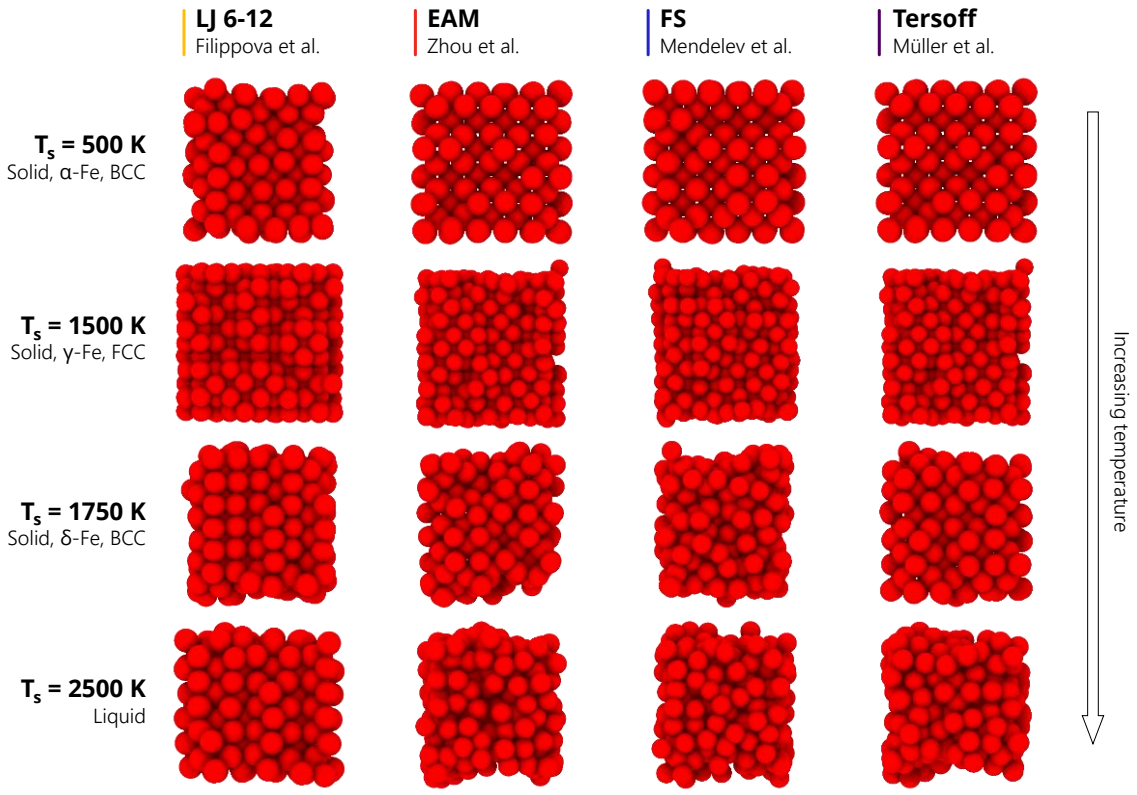

Figure 7.4 Realizations of iron surfaces using a range of surface potentials, including the Filippova (LJ) [326], Zhou (EAM) [324], Mendelev (FS) [326], and Müller (Tersoff) [328] potentials. Surface temperatures are chosen so that all four phases (α, γ, δ, and liquid) of iron should be realized (though these phases do not always represent the actual phases observed during simulation). Images show a lateral surface, with the top surface used for scattering gas atoms.

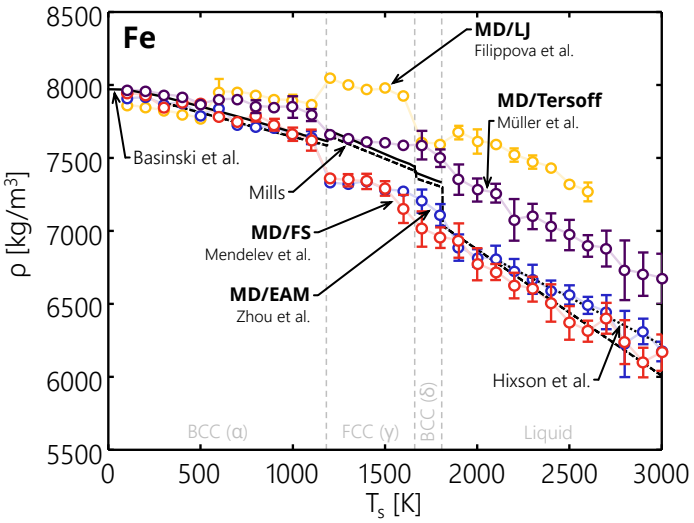

Figure 7.5 Trends in MD-derived density of iron surfaces for the Filippova (LJ) [326], Zhou (EAM) [324], Mendelev (FS) [326], and Müller (Tersoff) [328] potentials. Also shown are experimental densities from Mills [334], Basinski et al. [336], and Hixson et al. [337].

Surfaces predicted using the Zhou (EAM) potential [324] are more physically-realistic compared to those modeled with the LJ potential. Figure 7.4 indicates that the appropriate BCC structure is obtained for α-Fe without distortion after warming. The densities also match the experimental values over the entire α-Fe temperature range. Figure 7.5 indicates that the FCC γ-Fe phase is also modeled reasonably well, although the potential yields lower densities than those found experimentally. In the BCC δ-Fe phase, the potential also appears to predict an undistorted BCC lattice, but with noticeable differences at the surfaces where some of the short-range order is disrupted. The results also indicate that the potential predicts a liquid surface above the melting temperature with appropriate densities.

The results for the Mendelev (FS) potential [327] are generally consistent with those for Zhou's potential. Unlike the Zhou potential, however, the Mendelev potential predicts a continuous decrease in the density starting at 1625 K until the liquid phase is reached. Such observations are consistent with Figure 7.4, where the potential predicts a liquid-like surface instead of δ-Fe. In spite of this, the melting temperature is still predicted within 200 K, consistent with Ref. [338], and presents an improvement over the original FS potential, which was found to predict a melting temperature around 2540 K [339]. At temperatures beyond the melting point, the results are again consistent with Zhou's potential.

Figure 7.4 indicates that the Müller (Tersoff) potential [328] correctly predicts all of the appropriate phases of iron. It is noted, however, that the potential appears to overpredict the melting temperature by several hundred Kelvin. Figure 7.5 also indicates that the Tersoff potential overpredicts the density of all phases except for α-Fe. For the liquid phase, this isn't necessarily surprising as the form of the potential provides little manner of distinguishing between the closest-packed FCC and liquid structures, which share a coordination number of 12. The higher densities are consistent with the deeper potential as seen in Figure 7.3, and, in that regard, represent a potential well depth between the LJ and EAM potentials. It is noted that the density of the surface appears to be positively correlated with potential well depth.

Scattering simulations are carried out using pairwise Morse gas-surface potentials reported in Refs. [108,340] and repeated in Table 7.1 for reference. They were derived from fits to DFT calculations of the ground state energy of systems consisting of a single gas atom above a supercell of surface atoms.

Figure 7.6 shows trends in the normal and tangential components of the MD-derived TACs for the Fe-Ne case. Error bounds correspond to two standard deviations of the mean of the TAC across the six realizations of the surface. In all cases, error bounds expand as the surface temperature approaches the gas temperature (T_g = 300 K), a consequence of amplification of statistical uncertainties in $\langle E_o - E_i \rangle$ as the denominator in Eq. (7.20) approaches zero. For both components, the Filippova (LJ) potential [326] predicts noticeably different TACs over the entire temperature domain. This is unsurprising given the simplicity of its functional form and suggests that the potential cannot be used as a shortcut to faster evaluation of the TAC. The normal component of the TAC increases gradually with increasing T_s, with a sharper change between the α-Fe to γ-Fe transition, likely as a result of changes in the phonon dispersions in the surface. Predictions of the Zhou (EAM) [324], Mendelev (FS) [327], and Müller (Tersoff) [328] potentials are generally consistent with each other. Differences in the normal TAC between these parameterizations are inversely correlated with surface potential well depth. The tangential component is similarly correlated, with a gradual rise in the TAC with T_s. Sharper increases are observed about

Table 7.1 Parameterizations of the Morse potential for iron-gas pairs. The Fe-He and Fe-Ar parameterizations are taken directly from Ref. [108].

Gas-surface pair	D [meV]	a [Å^{-1}]	R [Å]
Fe-He	2.483	1.290	4.281
Fe-Ne	1.860	1.340	4.160
Fe-Ar	2.238	1.204	4.779

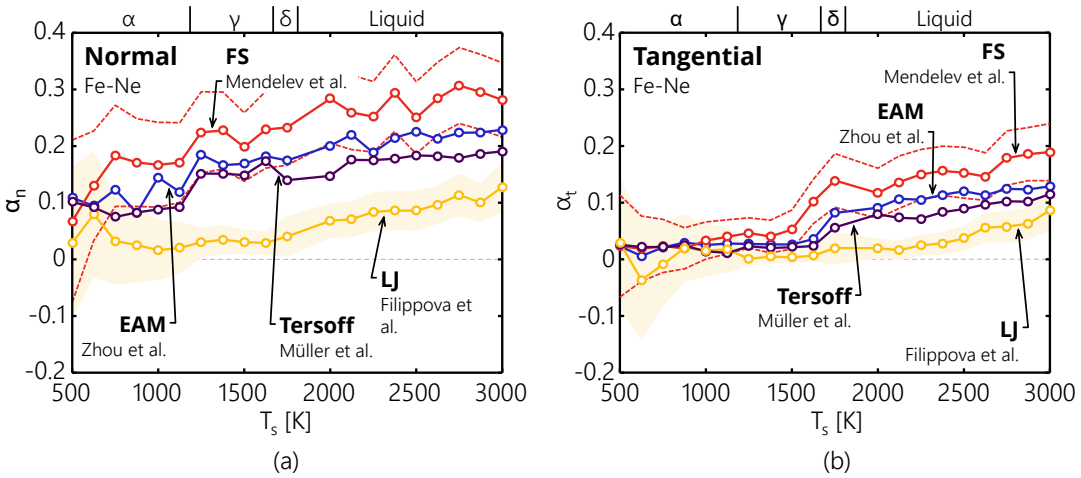

Figure 7.6 Trends in the (a) normal and (b) tangential TACs with T_s for T_g = 300 K and Fe-Ne. Surface potentials include the Filippova (LJ) [326], Zhou (EAM) [324], Mendelev (FS) [326], and Müllexr (Tersoff) [328] potentials. The temperatures corresponding to the phase changes of bulk iron are indicated on the upper axis. TACs are plotted on the same vertical scale for comparison. Included error bounds (shaded region and dashed lines) correspond to two standard deviations of the mean of the six surface realizations.

the γ-Fe, δ-Fe, and liquid Fe transitions (with the location of the discontinuity depending on the potential, e.g. Zhou's EAM potential [324] does not predict δ-Fe and therefore does not predict a corresponding discontinuity in the TAC at the phase transition temperature). As opposed to the normal TAC, Figure 7.4 indicates that the liquid phase transition represents a change from a relatively smooth surface to one having considerable *superatomic roughness* (i.e. roughness on the order of several surface atoms). This allows the gas atom to interact with the lateral edges of surface atoms and increases the interaction time, collectively resulting in an increase in the tangential accommodation.

Figure 7.7 shows trends in the total TAC with T_s predicted for Fe-He, Fe-Ne, and Fe-Ar using Eq. (7.20) and (7.21). The Fe-He curves are nearly flat. Invariance in the TAC as the surface phase changes is likely because helium atoms are small enough to *see* corrugation resulting from individual atoms in the surface, even at lower temperatures. As a result, the increased amount of roughness after melting has little effect on the TAC. This also explains why more energy transfer is predicted for Fe-He than the heavier gases at low temperature, where the tangential mode is frozen for the large gas atoms (cf. Figure 7.6). The TACs predicted by the Zhou (EAM) [324], Mendelev (FS) [327], and Müller (Tersoff) [328] potentials are again consistent with one another over the entire temperature range. The TACs predicted by the Filippova (LJ) potential [326] are smaller than those predicted by the more refined potentials, again suggesting that the form is too simplistic to give accurate values of the TAC

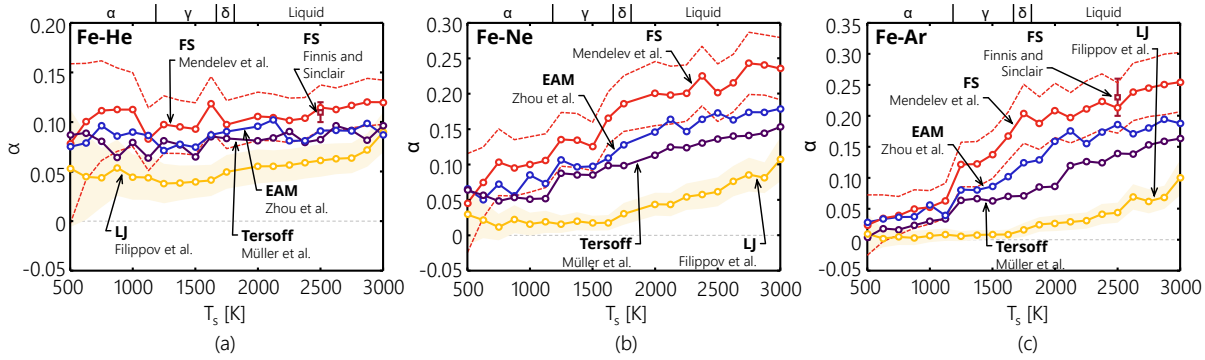

Figure 7.7 Trends in the total TAC with surface temperature, T_s, for (a) Fe-He, (b) Fe-Ne, and(c) Fe-Ar at T_g = 300 K. Surface potentials include the Filippova (LJ) [326], Zhou (EAM) [324], Mendelev (FS) [326], and Müller (Tersoff) [328] potentials. Also included are the results using the original Finnis-Sinclair (FS) parameterization for iron [329,330], which was used previously by Daun et al. [108]. TACs are plotted on different vertical scales for each gas. Included error bounds (shaded region and dashed lines) correspond to two standard deviations of the mean of the six surface realizations.

for iron surfaces, even for the lighter gases. Other differences between the TACs predicted by the different surface potentials are correlated with potential well depth, with those parameterizations featuring deeper surface potential wells (i.e. the LJ and Tersoff potentials) generally predicting lower TACs. It is finally noted that the value calculated using the original FS parameterization [329,330] by Daun et al. [108] is consistent with the value from the FS parametrization by Mendelev et al. [327].

In the case of Fe-Ne and Fe-Ar, the TAC increases with T_s and feature noticeable discontinuities about the phase changes, as discussed for Fe-Ne in reference to Figure 7.6 above. The Filippova potential significantly under predicts the TAC for all temperatures except for those below 750 K, i.e. at temperatures for which it was derived. The remaining potentials are generally consistent with each other and, with the exception of surface temperatures below 600 K, predict TACs that increase with mass ratio. As with Figure 7.6, differences in the TAC across different surface potentials are inversely correlated with density and potential well depth. It is also noted that, as with Fe-He, the value predicted with the newer FS parametrization by Mendelev et al. [327] is again consistent with the original FS parameterization [108,329,330].

The TACs predicted by the Zhou potential are taken as the most reliable with the parameterization predicting both the most credible phase transitions and values of the TAC that are bounded by the Mendelev and Müller potentials. The recommended values of the TAC at T_s = 750 K (solid) and 2500 K (liquid) are provided in Table 7.2, taken as a weighted average of the results obtained from the Zhou, Mendelev, and Müller potentials, weighting the latter two potentials half as heavily and incorporating stochastic uncertainties accordingly. The

results for the original FS parameterization [108,329,330] are also included in the T_s = 2500 K case, again weighted half as heavily as the Zhou potential predictions.

7.2.3 Copper

The atomic structure of copper surfaces over the temperature range of interest is relatively simple compared to iron, including only a single phase change and a crystalline form that is closest packed. Nevertheless, a large set of candidate parameterizations have been proposed in the literature. Figure 7.8 shows the LJ pair potential, as parameterized by Filippova et al. [326], and EAM effective pair potentials, using a range of parameterizations [332,341,342,345], as a function of interatomic distance. Other parameterizations of the EAM form not shown [346,347] are approximately bounded by the Universal 4 and Foiles potentials. A comparison of Figure 7.3 (for iron) and Figure 7.8 reveals several similarities. For instance, in both cases, the LJ potential [326] features a much deeper potential well than any other potential. The Morse parameterizations also feature well depths bounded by the LJ and effective EAM potentials and have equilibrium distances that are the greatest of the parameterizations considered. The EAM and FS potentials for copper are generally consistent with each other,

Table 7.2 Recommended values of the total TACs for various gases above iron, copper, and silicon for T_g = 300 K and for T_s = 750 K and liquid (T_s = 2500 K for iron and silicon and T_s = 2000 K for copper). Error bounds correspond to two standard deviations on the mean. For iron, values are a combination of predictions from Zhou (EAM) [324], Mendelev (FS) [326], and Müller (Tersoff) [328] potentials, with the latter two potentials weighted half as heavily. The results for the original FS potential [329,330] calculated by Daun et al. [108] are also included in Fe-He and Fe-Ar values for the liquid case, also weighted half as heavily. For copper, values are the average of Zhou (EAM) [341] and Foiles (EAM) [342] potentials. For silicon, solid values are the average of the SW [319], T2 (Tersoff) [320], Justo (EDIP) [343], and Jelinek (MEAM) [344] potentials and the liquid values are the average of the SW, Justo, and Jelinek potentials.

Gas-surface pair	Solid, T_s = 750 K			Liquid		
	α	α_n	α_t	α	α_n	α_t
Fe-He	0.095 ±0.021	0.149 ±0.041	0.042 ±0.024	0.095 ±0.008	0.113 ±0.016	0.072 ±0.013
Fe-Ne	0.070 ±0.020	0.119 ±0.039	0.022 ±0.021	0.168 ±0.016	0.219 ±0.027	0.117 ±0.018
Fe-Ar	0.031 ±0.014	0.029 ±0.056	0.013 ±0.006	0.181 ±0.014	0.245 ±0.028	0.110 ±0.017
Cu-He	0.036 ±0.015	0.052 ±0.029	0.018 ±0.021	0.077 ±0.011	0.089 ±0.019	0.066 ±0.017
Cu-Ne	0.092 ±0.024	0.134 ±0.041	0.051 ±0.029	0.229 ±0.024	0.253 ±0.035	0.205 ±0.030
Cu-Ar	0.250 ±0.024	0.352 ±0.066	0.148 ±0.048	0.493 ±0.037	0.540 ±0.054	0.447 ±0.046
Si-He	0.089 ±0.011	0.124 ±0.025	0.054 ±0.019	0.110 ±0.008	0.137 ±0.013	0.083 ±0.011
Si-Ar	0.105 ±0.012	0.134 ±0.027	0.076 ±0.022	0.382 ±0.021	0.485 ±0.032	0.273 ±0.021

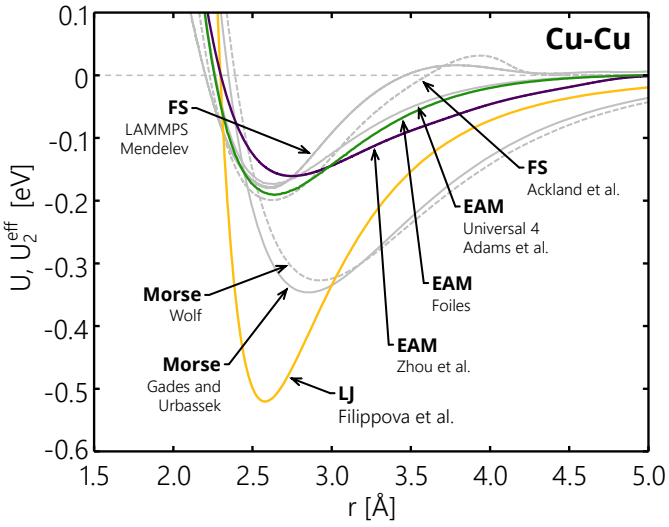

Figure 7.8 Potentials describing Cu-Cu interactions from Zhou et al. [341]; Foiles [342]; the Universal 4 potential by Adams et al. [345]; an unknown source, but included with LAMMPS distrisbutions [323]; Ackland et al. [332]; and Filippova et al. [326]. The Universal 3 [346] and Mishin [347] EAM potentials generally bounded by the potential by Foiles and the Universal 4 potentials. Faded lines correspond to potentials for which TACs were not calculated in this work.

featuring similar equilibrium distances and potential well depths. They also have slightly shallower effective pair potentials than those obtained from the EAM and FS potentials for iron.

Only two of the EAM parameterizations are considered here, specifically those by Zhou et al. [341] and Foiles [342], and are implemented alongside the Filippova (LJ) potential [326]. Examination of the density predicted by these potentials, shown in Figure 7.9, reveals that both EAM parameterizations predict very similar densities over the entire temperature range considered and produce values that are also consistent with experiments. These observations are consistent with the findings of Ryu and Cai [348] for a range of similar potentials, including the Universal 3 parameterization [346]. The surface realizations shown in Figure 7.10 highlight the solid and liquid surface structures at 500 K and 1500 K respectively. Without multiple phase changes, Figure 7.10 indicates that the potentials tend to be more consistent and do not predict significant disruptions from the standard lattice positions compared to iron. The LJ potential presents an exception, predicting lower densities over much of the domain, likely due to the fact that the LJ potentials does not realistically capture manybody effects. As with iron, Figure 7.10 indicates that the Filippova (LJ) potential predicts a crystalline structure well above the melting point. However, unlike iron, the LJ potential also results in a considerable number of free atoms that evaporate from the surface for temperatures exceeding 1000 K. Consequently, the calculated density

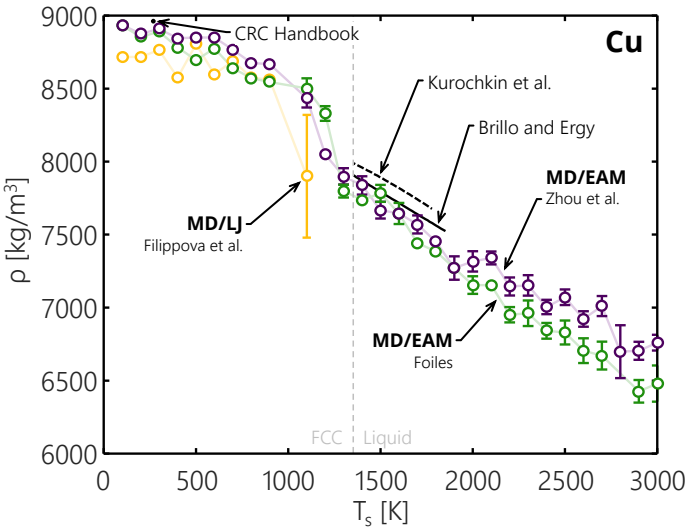

Figure 7.9 Density of copper as predicted by MD simulations using the EAM potential parameterized by Zhou et al. [341] and Foiles [342] and the LJ potential parameterized by Filippova et al. [326]. Also shown are experimental densities from the CRC Handbook [341], Kurochkin et al. [351], and Brillo and Ergy [352].

of the material declines rapidly as the temperature increases. While some degree of evaporation may be expected, these free atoms may interfere with initial placement of the gas molecule and cause other problems with scattering simulations.

Explicit gas-surface potentials for Cu-He, Cu-Ne, and Cu-Ar are not available in the literature. Instead, a pairwise Morse potential is fit to the physisorption potential given by Chizmeshya and Zaremba [349], using a static FCC lattice of copper atoms with a lattice constant of a_0 = 3.615 Å during fitting. The Morse potential parameterization for each gas is provided in Table 7.3 and plotted as a function of interatomic distance for Cu-He, Cu-Ne, and Cu-Ar in Figure 7.11. These potentials are shallower than those given for Cu-Ar by Vorontsov et al. [350] (D= –12 meV), who did not elaborate on the origin of their potentials.

Figure 7.12 shows the total TACs predicted for Cu-He, Cu-Ne, and Cu-Ar as a function of surface temperature for the chosen potentials. The Cu-He case reveals similar features to the Fe-He case, with little observable change about the melting temperature. The TACs predicted using the Filippova potential [326] are an exception where the TAC changes considerably about the melting point. This is likely due to the evaporated copper atoms, which interfere with scattering simulations and results in non-physical TACs. Unlike the Fe-He case above, both EAM potentials predict a small, nearly linear rise in the TAC with surface temperature. This rise mostly occurs in the tangential component, perhaps because of gradual increases in atomic-scale surface corrugation with surface temperature. As noted previously, the apparent increase in the TAC as the surface temperature approaches the

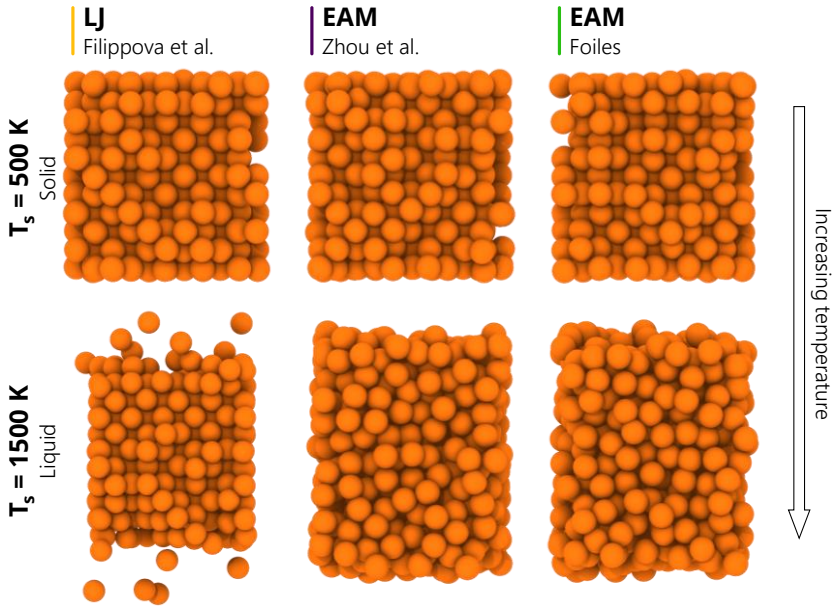

Figure 7.10 Realizations of copper surfaces using a range of surface potentials, including the LJ potential parameterized by Filippova et al. [326] and the EAM potential parameterized by Zhou et al. [341] and Foiles [342]. Surface temperatures are chosen so that the crystalline and liquid phases should be realized (though these phases do not always represent the actual phases observed during simulation). Images show a lateral surface, with the top surface used for scattering gas atoms. For T_s = 1500 K and the LJ potential, considerable evaporation means that numerous atoms exist outside of the shown domain.

gas temperature (300 K) in Figure 7.12 is associated with an increase in the error bounds and is expected to be non-physical, rather resulting from amplification of stochastic and modeling errors in the numerator of Eq. (7.20) as the denominator approaches zero.

For Cu-Ne and Cu-Ar, like the Fe-Ne and Fe-Ar cases above, the TAC features abrupt changes about the melting temperature. This is again attributed to a change in the superatomic roughness of the surface, which is visible in Figure 7.10. TACs predicted by both EAM potentials are again consistent, while the Filippova potential

Table 7.3 Parameterizations of the Morse potential for copper-gas atomic pairs as derived from the physisorption potentials of Chizmeshya and Zaremba [349].

Gas-surface pair	D [meV]	a [Å^{-1}]	R [Å]
Cu-He	0.5255	1.1033	3.9372
Cu-Ne	1.5769	1.1082	3.4947
Cu-Ar	6.0557	1.0779	3.3464

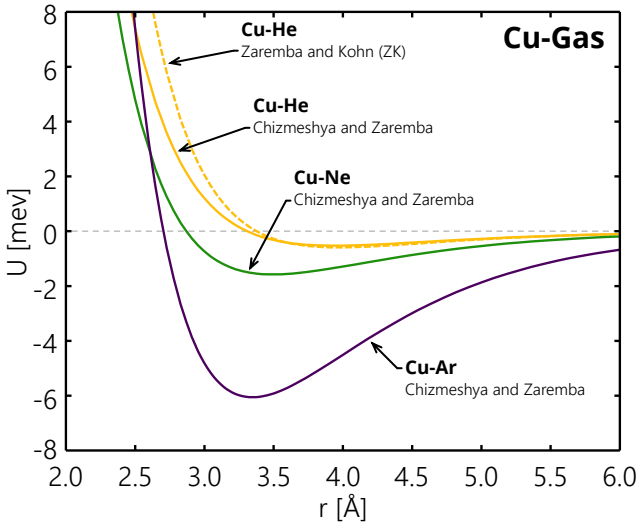

Figure 7.11 Inferred Morse potential for Cu-gas interactions based on physisorption potentials given in Chizmeshya and Zaremba [349]. Also shown is a Morse potential derived using the same procedure, but from the physisorption potential given by Zaremba and Kohn [353].

[326] predicts significantly lower thermal accommodation. It is again noted that results obtained from the Filippova potential above 1000 K must be taken with an air of caution, due to the presence of a free copper atoms above the surface. The value of the TAC below the melting point is nearly constant with respect to temperature, while that above has a slight upward trend with increasing temperature, consistent with observations for Fe-Ne and Fe-Ar above the melting point. The TAC predicted by all potentials increases with increasing μ as expected [48,108,286], resulting in values of approximately 0.25 and 0.49 for Cu-Ne and Cu-Ar above the melting point. The TAC again appears correlated with the surface potential well depth, with the Filippova potential having the deeper potential well and smallest TACs and the EAM parameterization by Zhou et al. [341] having the shallowest effective well depth and largest TACs.

7.2.4 Silicon

Studies comparing silicon potential parameterizations are relatively plentiful in the literature [348,354–360], examining a wide variety of parameterizations. In this work, considerations are limited to the following parameterizations: (i) the Stillinger-Weber (SW) potential, using the original parameterization [319]; (ii) the T2 (Tersoff) potential [320]; (iii) the EDIP potential, as implemented for silicon by Justo et al. [343]; and (iv) the MEAM potential, as parameterized by Jelinek et al. [344]. Figure 7.13 shows the two-body and angular components of these potentials, as well as the T3 (Tersoff) [361] and Erhart-Albe (Tersoff) [362] potentials. The angular functions are plotted in terms of an effective angular dependence, $g_{\text{eff}}(\theta)$, where the functions are each

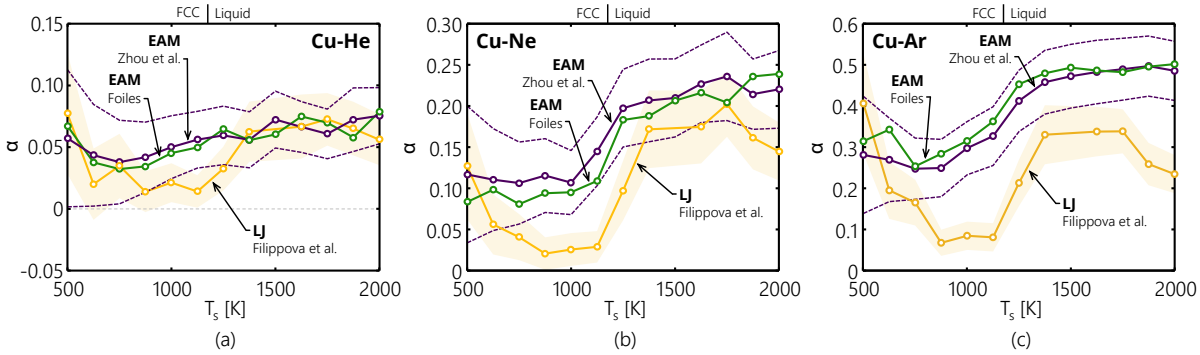

Figure 7.12 Trends in MD-derived total TACs for (a) Cu-He and (b) Cu-Ne using two parameterizations of the EAM potential [341,342] and the LJ potential as parameterized by Filippova et al. [326]. Error bounds correspond to two standard deviations of the mean of scattering from six realizations of the copper surface.

normalized by their maximum. For the Justo potential, Figure 7.13 shows both the ideal liquid (Z_{eff} = 12, which will rarely be reached in reality) and diamond cubic (Z_{eff} = 4) cases, indicating how the transition to higher coordination numbers shifts the potential from enforcing bonding at specific angles at low coordination numbers to only repulsive interactions without any angular dependence at high coordination numbers. This is not true at the phase interface, where the coordination number will always be lower (due to the absence of atoms either above or below the considered atom). This allows atoms at the surface to encounter high attractive forces towards to surface even when the bulk phase exhibits the higher coordination numbers associated with the liquid phase. One can also note that the two-body component of the T2 and T3 potentials are very similar, while the angular components are quite different.

All of the silicon surfaces are initiated in a crystalline, diamond cubic (*c*-Si) structure with five unit cells in all directions. Figure 7.14 shows the MD-derived density of silicon surfaces as a function of surface temperature, compared to experimentally-derived values [363]. Below the melting point, the SW, T2, and Justo (EDIP) potentials predict very similar densities. The Justo potential exhibits slight thermal contraction, which is not present in the other potentials. Realization of the silicon surfaces at T_s=1500 K, shown in Figure 7.15, suggests that this may be a result of significant displacement from the standard crystal configuration of several atomic layers adjacent to the top and bottom surface, likely due to the different coordination number compared to the bulk. This also causes increased surface roughness relative to the other potentials, which impacts the TAC. The Jelinek (MEAM) potential predicts thermal expansion that causes it to deviate from the other potentials for silicon. Visualization of the surface indicates that this is a result of high surface energies and an early onset of melting. It

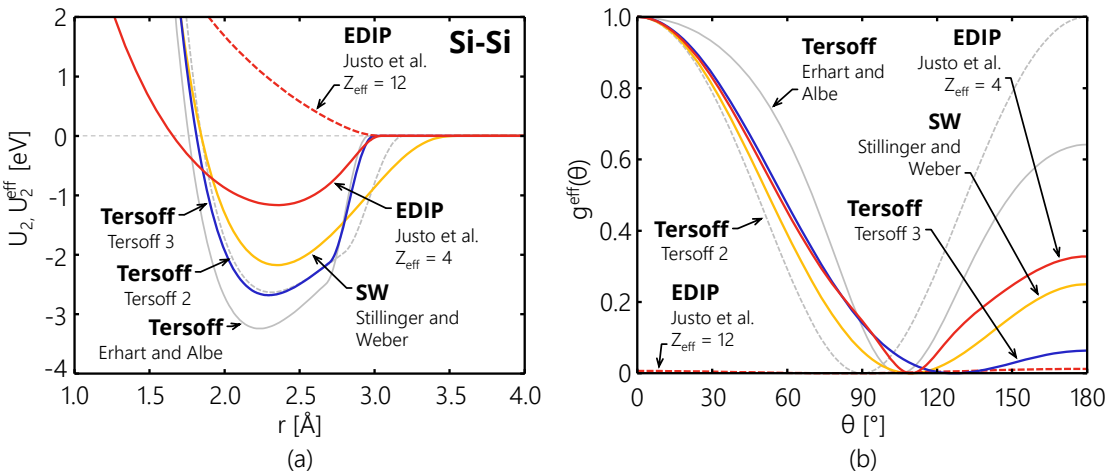

Figure 7.13 Pair potentials for Si-Si interactions from Tersoff (T2 [320] and T3 [361]), Stillinger and Weber (SW) [319], Justo et al. (EDIP) [343], and Erhart and Albe (Tersoff) [362]. For the Tersoff potentials, b_{ijk} = 1. For the Justo potential, two effective coordination numbers are shown: Z_{eff} = 4 corresponding to an ideal diamond cubic phase and Z_{eff} = 12 corresponding to an ideal liquid phase. The angular functions, $g_{eff}(\theta)$, are scaled against their maximum (except for the Z_{eff} = 12 case of the Justo potential which is scaled by the maximum of the Z_{eff} =4 case). Faded lines correspond to potentials for which TACs were not calculated in this work.

is noted that the roughness appears on a smaller scale for the Jelinek potential (where it appears to be almost atomic in scale) than the Justo potential (where the roughness is on the scale of the simulation box).

The densities predicted by the potentials diverge significantly above the melting temperature. The SW potential, as stated above, predicts the melting point with a high degree of accuracy. The SW potential is also the only one to predict that the density increases abruptly upon melting, which is consistent with experimental observations. Furthermore, Figure 7.15 indicates a liquid-like structure at T_s = 2500 K. In contrast, the T2 potential shows a density consistent with that of solid silicon at temperatures well above the melting temperature. This is consistent with Figure 7.15, which indicates that the T2 potential predicts a solid structure even at T_s = 2500 K. Overprediction of the melting temperature by the T2 potential is consistent with the literature [355,364], where the phenomenon is attributed to the strength of the bond bending term (partially manifested in the deeper potential well in Figure 7.13).

The Justo (EDIP) potential appears to predict a melting point within a couple hundred Kelvin of the experimental value. Unlike the SW potential, however, the Justo potential predicts a relatively sparse structure, similar to what would be expected of *a*-Si (e.g. Ref. [365,366]). This expansion is likely a result of the bonds becoming weak as the coordination number increases for liquid silicon, allowing the material to expand until

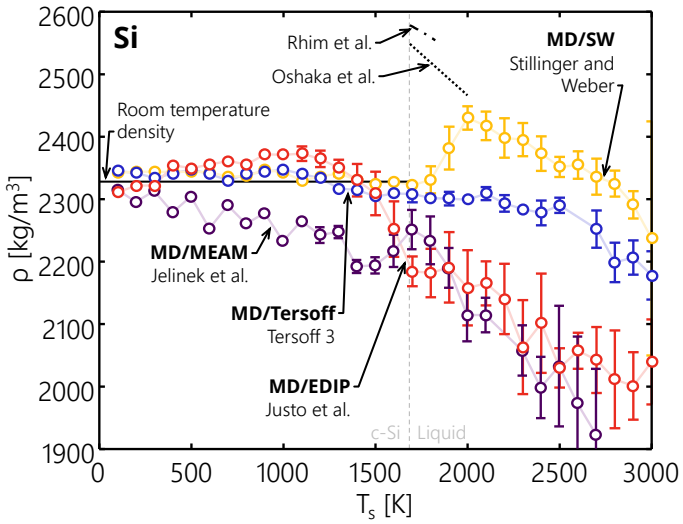

Figure 7.14 Trends in MD-derived density of silicon surfaces for the SW [319], T2 (Tersoff) [320], Justo (EDIP) [343], and Jelinek (MEAM) [344] potentials. Error bars correspond to one standard deviation of the density of six realizations of a silicon surface. Also shown are experimental densities for liquid silicon from Rhim et al. [367] and Oshaka et al. [368] and the room temperature density from [369].

lower coordination numbers are achieved, that is, when the surface takes on a more amorphous character. This will accelerate as the atoms move farther apart, resulting in an increasingly sparse structure as the surface temperature increases. The surface remains intact as atoms at the surface will always have lower coordination numbers and feature strong bonding to subsurface atoms. Figure 7.15 indicates that these effects result in visibly rougher surfaces than those predicted by the SW and T2 potentials at 2500 K.

The liquid density predicted by the Jelinek (MEAM) potential is similar in nature to that predicted by the Justo potential, exhibiting considerable expansion. Visualization of surfaces suggests that the melting occurs near 1500 K, significantly lower than the experimentally-determined melting point. This phenomenon was also observed by Ryu and Cai [348] and Cook and Clancy [355], who observed melting points of 1411 and 1475 K, respectively, albeit for a different parameterization of the MEAM potential [370].

The gas-surface potential for the silicon scattering simulations are considered in the same manner as the iron case above, using a Morse form to fit DFT calculations (in this case from Ref. [48]). This potential shows improvements over the treatment of Zhao et al. [360], who used a purely repulsive potential for the gas-surface interaction in simulations where argon atoms were used as a thermostat.

Figure 7.16 shows trends with surface temperature in the normal and tangential TACs for Si-Ar. The SW potential predicts temperature invariant values for both normal and tangential TAC components above and

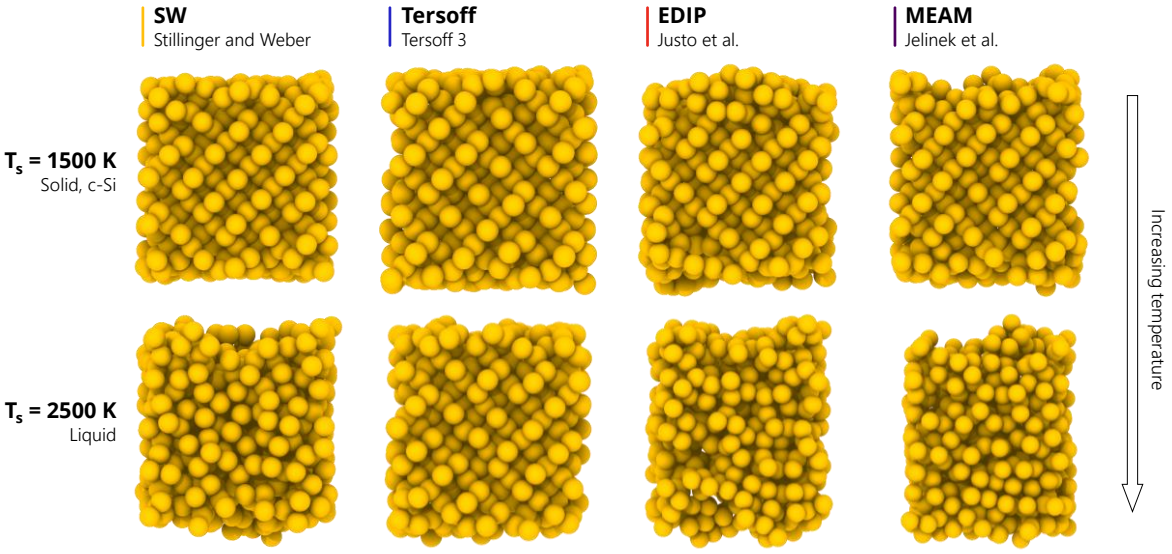

Figure 7.15 Realization of silicon surfaces using the SW [319], T2 (Tersoff) [320], Justo (EDIP) [343], and Jelinek (MEAM) [344] potentials at T_s = 1500 K (where a solid, diamond cubic structure is expected) and T_s = 2500 K (where a liquid structure is expected). Images shows a lateral surface, with the top surface used for scattering gas atoms.

below the melting point, with sharp transitions at the melting point as in the case of the copper surface. This highlights the fact that the TAC is significantly influenced by superatomic roughness in the surface, which Figure 7.15 shows increases considerably when the SW-predicted surface melts. In contrast, the TACs predicted by the T2 potential are relatively constant with increasing temperature up to 2250 K, at which point they gradually increase towards the value predicted by the SW potential. This is consistent with observations that the T2-derived surfaces remain solid up to those temperatures. The low temperature or *c*-Si TAC is consistent between the SW and T2 potentials up to 1500 K. The Justo (EDIP) potential, in contrast, undergoes a gradual increase from the low temperature value predicted by the SW and T2 potentials, to one slightly higher than the SW and T2 potentials for high temperatures. The more gradual increase is well correlated with changes in the bonding at the surface predicted as a result of the different coordination number, again shown in Figure 7.15. The Jelinek (MEAM) potential predicts similar characteristics to the SW potentials with a sharp transition in both components of the TAC about the anticipated melting point noted above.

Figure 7.17 shows how the total TAC varies with surface temperature for Si-He and Si-Ar. The Si-Ar case highlights the abrupt change at the melting temperature, which itself varies depending on the potential. The Si-He case, in contrast, exhibits very little change in the TAC over the temperature range considered. As with the Fe and Cu cases, the difference can be attributed to the smaller size of the helium atom, which is scattered by the

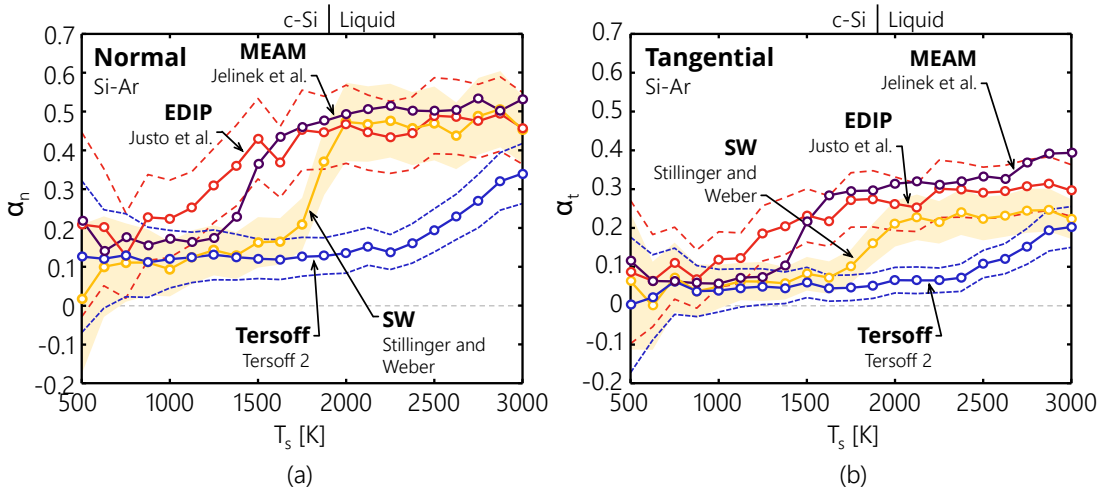

Figure 7.16 Trends in MD-derived (a) normal and (b) tangential TACs for Si-Ar using the SW [319], T2 (Tersoff) [320], Justo (EDIP) [343], and Jelinek (MEAM) [344] potentials. Error bounds correspond to two standard deviations of the mean of scattering from six realizations of the silicon surface. The vertical axis is consistent between (a) and (b).

atomic level corrugation in the surface that makes the tangential translational energy mode accessible even for low temperatures. As the diamond structure is sparser than the FCC case for copper, one would anticipate a higher level of atomic-scale roughness that would further limit the influence of surface temperature on the TAC. Also consistent with the other materials, there again appears to be a loose correlation between the TAC and surface potential well depth.

7.3 Outlooks for TiRe-LII analysis

The TACs calculated by this method at surface temperatures above 2000 K can now be compared to those available in the literature from TiRe-LII experimentation. Figure 7.18 shows trends in the MD- [107,108,306,307], hard cube model- [294], and TiRe-LII-derived [21,24,45,48,49,112] TACs at high temperatures. The MD-derived TACs in the present study generally increase monotonically with increasing μ following previous MD simulations and TiRe-LII experimentation, including those calculated in Chapter 8. A notable exception to this trend is the Ni-Ar case from Ref. [306,307], which is attributed to the Casmir-Polder effects that result in much larger MD-derived TACs. It is also worth mentioning that fundamental differences in surface physics across multiple classes of materials causes a significantly amount of scatter about this trend. This suggests that surface features must be considered in order to accurately predict the TAC with theoretical models. Thus, any model that only considers how the TAC varies with μ (such as the hard cube and Baule models), is expected to incur

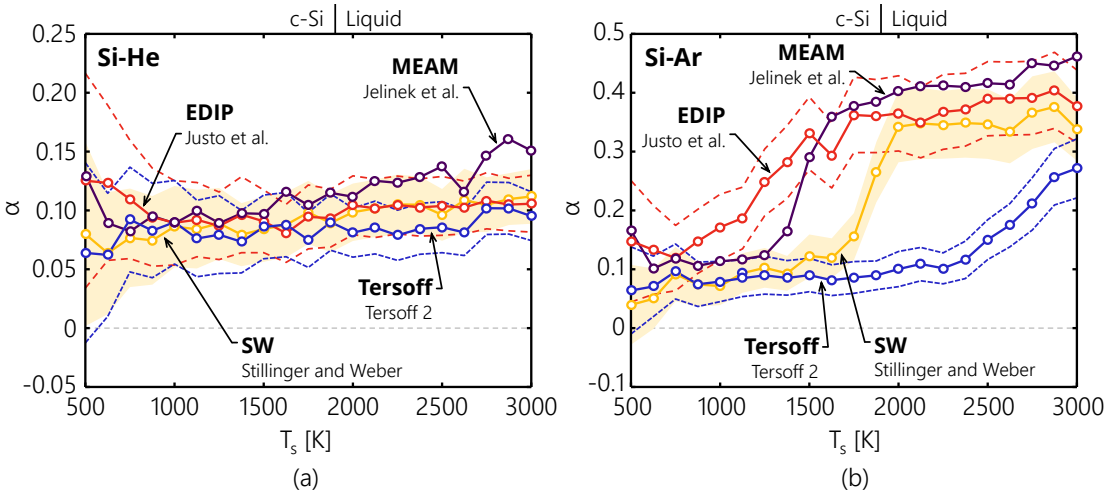

Figure 7.17 Trends in MD-derived total TACs for (a) Si-He and (b) Si-Ar using the SW [319], T2 (Tersoff) [320], Justo (EDIP) [343], and Jelinek (MEAM) [344] potentials. Error bounds correspond to two standard deviations of the mean of scattering from six realizations of the silicon surface.

significant model errors. Remaining scatter in TiRe-LII-derived TACs are quite likely a consequence of model and experimental measurement errors in the TiRe-LII analyses that should act as a caution to practitioners.

Another observation relevant to TiRe-LII analyses is that, within the scattering regime relevant to TiRe-LII and in the absence of phase changes, the TAC is mostly constant with surface temperature, only increasingly slightly over more than 1000 K. This is in contrast to the treatment of Michelsen [109] who proposed that the TAC would decline with surface temperature by extrapolating the results of molecular beam studies at lower surface temperatures. This small upward trend is, however, consistent with Goodman and Wachman [286] (see Figure 10.23 in that work) who noted that the TAC will begin to increase and plateau after reaching a minimum around the Debye temperature. This observation is useful for TiRe-LII analyses, justifying the common practice of assuming that a single value of the TAC can be used for the duration of the cooling curve.

Finally, the work in this chapter suggests that the surface phase can significantly impact the value of the TAC. In consequence, it is expected that any laser-induced annealing or so-called *aging* of soot could have an impact on the value of the TAC. This has several consequences. In the case of laser-induced annealing, the degree of annealing depends significantly on laser fluence. As a result, TiRe-LII studies at low fluences may correspond to different TACs then those at high temperatures. The aging of soot could have a similar effect, resulting in soot at different points in a flame or in the atmosphere having different values for the TAC. Future work will extend the method presented in this chapter to the different phases of carbon in order to investigate these effects.

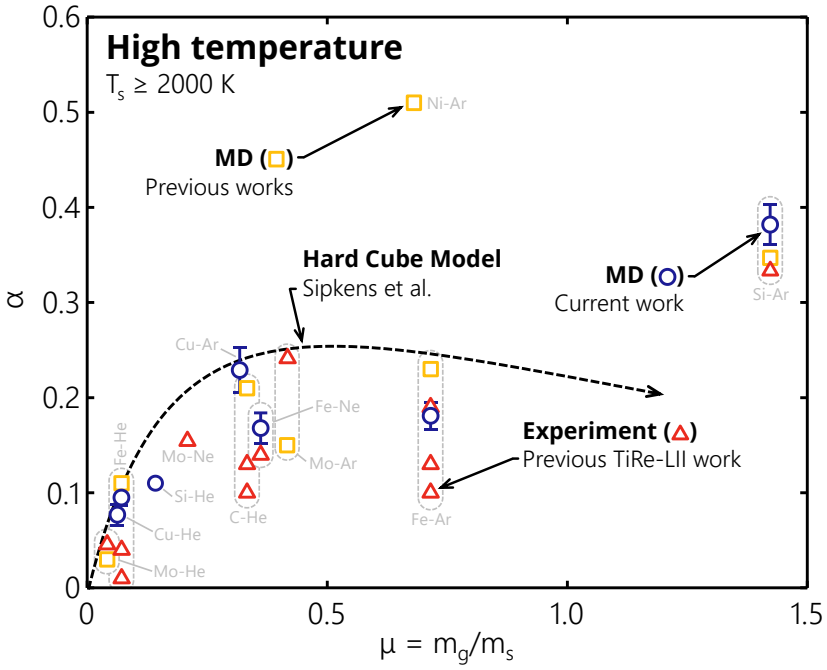

Figure 7.18 Trends in MD-derived total TACs with mass ratio for the current MD simulations, previous MD simulations [107,108,306,307], TiRe-LII experimentation from Refs. [21,24,45,48,112] and Chapter 8, and hard cube models (as per Ref. [294]).

Chapter 8
Inference of nanoparticle properties from temperature decay[5]

This chapter discusses a more traditional analysis of TiRe-LII signals: that of inferring nanoparticle properties, such as size, from the inferred nanoparticle temperature decay. This is to be done in regards to a comparative assessment of two-color laser-induced emission measurements on a range of engineered nanoparticles – namely iron, silver, and molybdenum – in a variety of bath gases. These materials were selected to highlight the different types of information contained in the TiRe-LII data for metal nanoparticles with cooling models dominated by different heat transfer modes. Following Ref. [112], and in contrast to other LII studies that exclusively consider nanoparticles synthesized in the gas phase, the aerosols examined in this study originate from a nanocolloid solution that is aerosolized using a pneumatic atomizer. This approach enables investigation of a range of aerosols that could not be synthesized in the gas phase. Moreover, unlike in gas-phase synthesis, where the bath gas composition strongly influences the nanoparticle size distribution, the sizes of each type of nanoparticle in this experiment are expected to be identical for all bath gases, allowing one to isolate the TAC for specific gas-surface pairs.

8.1 TiRe-LII model

8.1.1 Spectroscopic model

In the present chapter, the incandescence signal is given by Eq. (2.15),

[5] Experimental aspects of this work were led by Mr. Nigel Singh as part of his MASc work with assistance from the author. Some experimental details are included to inform the reader of the experimental conditions and provide proper context to the analysis, while further details are available in Mr. Singh's thesis [627]. This work was also disseminated in part as Sipkens, T. A., Singh, N. R., and Daun, K. J., 2017, "Time-resolved laser-induced incandescence characterization of metal nanoparticles," Appl. Phys. B, **123**(1), pp. 14-30. doi: 10.1007/s00340-016-6593-7

$$\tilde{s}_{\mathrm{j,i}} = \Lambda \cdot \eta_{\mathrm{j}} \int_{d_{\mathrm{p}}} C_{\mathrm{abs},\lambda_{\mathrm{j}}}\left(d_{\mathrm{p}}\right) \cdot I_{\mathrm{b},\lambda_{\mathrm{j}}}\left[T_{\mathrm{p,i}}\left(d_{\mathrm{p}}\right)\right] \cdot p\left(d_{\mathrm{p}}\right) \cdot \mathrm{d}d_{\mathrm{p}} \,. \tag{8.1}$$

The analyses in the current chapter will apply the Rayleigh approximation to Mie theory for all three metals, so that Eq. (2.4) applies,

$$Q_{\mathrm{abs},\lambda} = \frac{C_{\mathrm{abs},\lambda}}{\pi / d_{\mathrm{p}}^2} = 4x \cdot E\left(\mathbf{m}_{\lambda}\right) = -4x\,\mathrm{Im}\left(\frac{\mathbf{m}_{\lambda}^2 - 1}{\mathbf{m}_{\lambda}^2 + 2}\right) = -4x\,\mathrm{Im}\left(\frac{\varepsilon_{\lambda} - 1}{\varepsilon_{\lambda} + 2}\right), \tag{8.2}$$

where the latter term rephrases the refractive index of refraction in terms of the electrical permittivity, $\boldsymbol{\varepsilon}_{\lambda} = \varepsilon_{1,\lambda} + \varepsilon_{2,\lambda}$. This treatment follows the standard approach in the TiRe-LII literature, where it has been applied to iron and other engineered nanoparticles previously (e.g. Refs. [21,48,49,112,129]). This assumption is predicated on the fact that the nanoparticle size criterion,

$$x = \frac{\pi d_{\mathrm{p}}}{\lambda} \ll 1 \,, \tag{8.3}$$

is satisfied [151,153]. Very recent work [371] suggests that this approach may not be valid for metals due to violation of the phase shift parameter criterion [151], noted in Section 2.1.1:

$$x \cdot \left|\mathbf{m}_{\lambda}\right| \ll 1 \,. \tag{8.4}$$

The impact of removing the Rayleigh approximation is the subject of ongoing research, as noted in Section 8.4.

The optical properties of metallic nanoparticles are, in principle, known with much greater certainty than those of soot in that they have a well-defined, homogenous composition and that the dielectric properties of the bulk material apply directly to nanoparticles (provided the nanoparticle diameter is much larger than the mean free electron path [372,373]). Moreover, the bulk dielectric properties of most metals at high temperatures have been derived from ellipsometry measurements made under carefully-controlled conditions and, in the case of some liquid metal nanoparticles, have an underpinning in Drude theory, as discussed in Section 2.1.1. As an example, molten silver, with an energy gap between the highest core electron state ($4d$) and the conduction band [374] that corresponds to ultraviolet wavelengths, has optical properties in the visible and infrared wavelengths that are well-described by Drude theory. This is affirmed by Figure 8.1b, where the refractive indices and absorption function determined from Drude theory are shown to be consistent with ellipsoidal measurements on molten silver [374]. The Drude parameters, namely the plasma frequency, ω_{p}, and relaxation time, τ, are determined from [375]

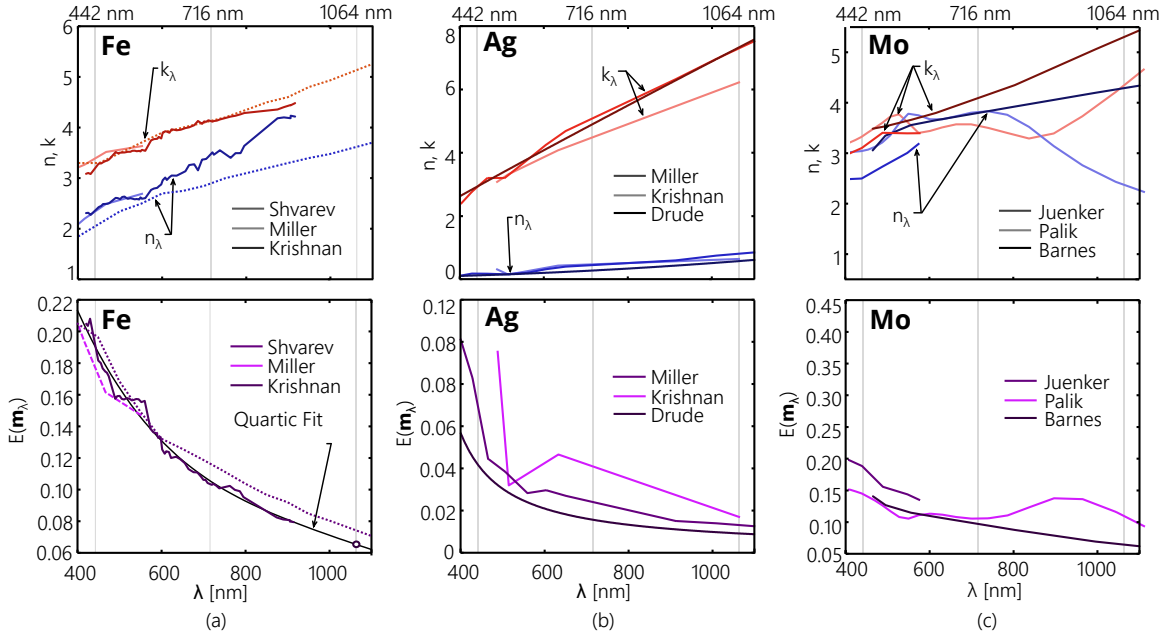

Figure 8.1 Real and imaginary components of the refractive index, $\mathbf{m}_\lambda$, and absorption function, $E(\mathbf{m}_\lambda)$ for (a) molten iron, (b) molten silver, and (c) solid molybdenum. Solid curves denote values used to analyze TiRe-LII data.

$$\omega_p = \frac{n_e^2 e^2}{m_e \varepsilon_0} \tag{8.5}$$

and

$$\tau = \frac{\sigma_{DC} m_e}{n_e^* e^2}, \tag{8.6}$$

where n_e^* is the effective number of free electrons per unit volume, $m_e = 9.109\times10^{-31}$ kg and $e = 1.602\times10^{-19}$ C are the rest mass and charge of an electron, respectively, $\varepsilon_0 = 8.854\times10^{-12}$ F/m is the vacuum permittivity, and σ_{DC} is the direct current conductivity. The latter expression derived considering the limit of $\omega \to 0$, that is applying a direct current. The free electron density can be found from the atomic density, assuming that the number of electrons contributing to the conduction band by each atom is equal to the valence, adjusted by a factor that accounts for band structure. The effective electron number density is $n_e^*/n_e = 1.05$ [374,376], where $n_e = 5.218$ electrons/m^3, and the direct current conductivity is $\sigma_{DC} = 5.84\times10^6$ S/m [374] (which corresponds to $\omega_p = 1.3175\times10^{15}$ rad/s and $\tau = 3.7823\times10^{-15}$ s).

The situation for molten iron nanoparticles is more complicated. As a transition metal, the *d*-band electrons overlap the conduction band, so the radiative properties in the visible and infrared spectrum are due to both interband and intraband transitions. Consequently, while the general trends in $\boldsymbol{\varepsilon}_\lambda$ (or $\mathbf{m}_\lambda$) are consistent with Drude theory, Eqs. (2.6) and (2.7) are not expected to provide an accurate representation of $E(\mathbf{m}_\lambda)$. Previous TiRe-LII measurements by Sipkens et al. [16] on molten iron nanoparticles used a Drude model from Kobatake et al. [377] that was later noted to be nonphysical [378]. In this work, values for the absorption function are initially considered with respect to ellipsometry measurements from Krishnan et al. [155] and Shvarev et al. [379], shown in Figure 8.1a, which are consistent with the data given in Miller [374].

While the laser-energized iron and silver nanoparticles are in the molten state during detection, the molybdenum nanoparticles presumably remain solid due to the high melting temperature of molybdenum (2896 K [380]). The n_λ, k_λ and $E(\mathbf{m}_\lambda)$ values for solid molybdenum depend on temperature through the DC conductivity via Drude/Hagen-Rubens theory [381], although these theories cannot be applied directly, mainly due to the strong impact of the electronic band structure in the solid state. Instead, n_λ, k_λ are taken from reflectance measurements on solid molybdenum at 2200 K between 465 nm and 2000 nm from Barnes [382]. Figure 8.1c compares this data to similar data reported by Juenker et al. [383] at 2200 K and wavelengths shorter than 576 nm and data compiled by Palik [384] at room temperature.

Values of n_λ, k_λ, and $E(\mathbf{m}_\lambda)$ at the detection and excitation wavelengths are summarized in Table 8.1. A comparison of the results reveals that the trends in n_λ and k_λ for molten iron and silver are similar ($n_\lambda < k_\lambda$, both increase monotonically with wavelength), which is expected from Drude free electron theory (though the *d*-band electron contributions in molten iron preclude a quantitative treatment by Drude theory). In contrast, n_λ and k_λ

Table 8.1 Bulk radiative properties used to interpret TiRe-LII measurements on iron, silver, and molybdenum nanoparticles.

	λ = 442 nm			λ = 716 nm				λ = 1064 nm		
Material	**n**	**k**	**E(m)**	**n**	**k**	**E(m)**	**$E(m)_r$**	**n**	**k**	**E(m)**
Ag (Drude)	0.10	2.92	0.041	0.25	4.89	0.015	2.67	0.55	7.31	0.009
Fe [155]	2.37	3.22	0.191	3.49	4.12	0.103	1.85	5.64*	5.01*	0.065*
Fe [379]	2.06	3.30	0.198	2.90	4.13	0.116	1.70	3.62	5.13	0.073
Mo [382]	2.83	3.45	0.152	3.83	4.09	0.097	1.59	4.29	5.30	0.065

*Values are obtained by extrapolation.

are similar in magnitude for solid molybdenum, possibly due to strong interband contributions. In terms of the spectral absorption cross-section, $E(\mathbf{m}_\lambda)$ for silver nanoparticles is much smaller than the value for iron and molybdenum nanoparticles due to its higher electrical conductivity. Such an observation has consequences on the peak temperature analysis presented in Section 8.3.1.

8.1.2 Heat transfer model

Under most LII conditions, the conductive and evaporative cooling terms are the only cooling terms that are important, so that from Eq. (2.20),

$$c_\mathrm{p}\rho\frac{\pi d_p^3}{6}\frac{\mathrm{d}T_\mathrm{p}}{\mathrm{d}t}=q_\mathrm{abs}-q_\mathrm{cond}-q_\mathrm{vap}\,. \tag{8.7}$$

The spectral absorption cross-section is modeled assuming Rayleigh regime physics, cf. Eq. (8.2), so that from Eq. (2.24)

$$q_\mathrm{abs}=C_{\mathrm{abs},\lambda_1}\left(d_\mathrm{p}\right)\cdot f_0\left(t\right)=\frac{\pi^2 d_\mathrm{p}^3}{\lambda_1}\cdot E\left(\mathbf{m}_{\lambda_1}\right)\cdot f_0\left(t\right). \tag{8.8}$$

Conduction is considered in the free molecular regime for monatomic gases, so that from Eq. (2.35) and using $\zeta_\mathrm{rot} = 0$,

$$q_\mathrm{cond}==-\alpha\frac{\pi d_\mathrm{p}^2}{2}n_\mathrm{g}c_\mathrm{g}k_\mathrm{B}\left(T_\mathrm{p}-T_\mathrm{g}\right). \tag{8.9}$$

From Eq. (2.42), evaporation, assuming the sticking coefficient is unity, $\beta = 1$, is given by

$$q_\mathrm{vap}=-\Delta h_\mathrm{v}\beta m_\mathrm{v}\pi d_\mathrm{p}^2\frac{p_\mathrm{v}c_\mathrm{v}}{4k_\mathrm{B}T_\mathrm{p}}. \tag{8.10}$$

The vapor pressure is given by the Clausius-Clapeyron equation, taking the form

$$p_\mathrm{v}=A\cdot\exp\left(-\frac{\Delta h_\mathrm{v}}{R_\mathrm{s}T_\mathrm{p}}\right). \tag{8.11}$$

The vapor pressure is further corrected for surface curvature using the Kelvin equation, Eq. (2.45), and the latent heat of vaporization is given by Watson's equation, Eq. (2.43). The relevant material properties used in evaluating these models are provided in Table 8.2. Figure 8.2 shows simulated heat transfer modes plotted over the expected temperature range observed during the cooling stage for laser-energized silver, iron, and molybdenum nanoparticles in argon, assuming $\alpha = 0.1$, $d_\mathrm{p} = 50$ nm, $T_\mathrm{g} = 300$ K, and $p_\mathrm{g} = 101.3$ kPa. In the case of molten iron and

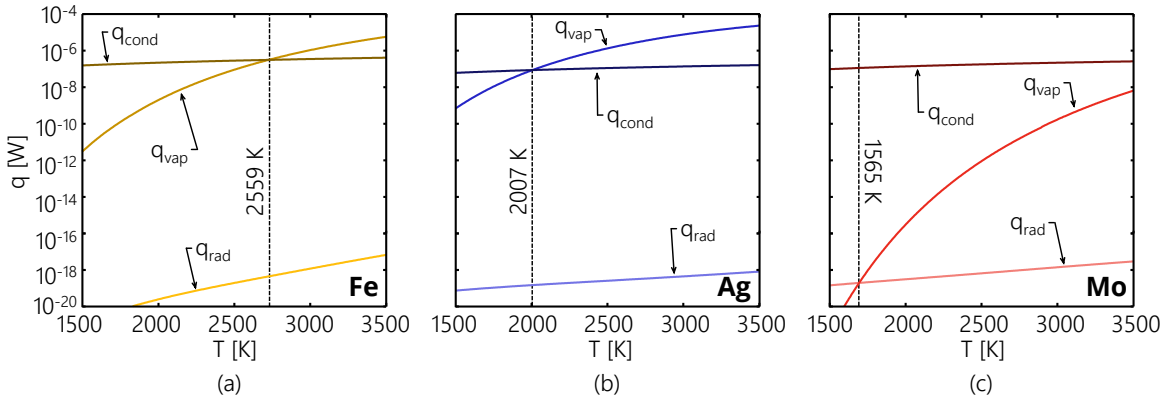

Figure 8.2 Heat transfer from (a) iron, (b) silver, and (c) molybdenum nanoparticles in argon at T_g = 300 K and p_g = 101.3 kPa, assuming d_p = 50 nm and α = 0.1. Vertical lines show the temperatures at which the dominant heat transfer mode changes. The relative importance of the heat transfer modes over the observed temperature decays determines the quantities that can be inferred from the TiRe-LII data.

silver, evaporation heat transfer dominates at temperatures beyond approximately 2728 K and 2007 K, respectively. It is significant that, in the case of silver, evaporation heat transfer dominates over the entire range of LII-detectable temperatures, while, for iron nanoparticles, some of the observed cooling curve is dominated by conduction. Heat transfer from molybdenum is due almost entirely to conduction over the entire range of measurement temperatures. These observations impact the parameters that can be inferred from the TiRe-LII data, as discussed later in this chapter.

8.2 Experimental details

The experiments described in this chapter are designed to allow for control over the buffer gas surrounding the nanoparticles by aerosolizing nanoparticle colloids. A buffer gas flow is introduced through a TSI Model 3076 pneumatic atomizer operating in recirculation mode connected to a sample vessel containing a colloid suspension of either iron, silver, or molybdenum nanoparticles. Motive gases are supplied to the atomizer at a pressure of 200 kPa; under these conditions the atomizer is expected to produce an aerosol of droplets having a median diameter of 0.3 μm with a geometric standard deviation of less than 2.0 [385]. The colloid is diluted so that, on average, each droplet contains one nanoparticle. The droplets pass through a diffusion drier containing a silica gel desiccant to remove any water in the aerosol stream. The dried aerosol then enters the sample chamber within which the laser-induced emission measurements are carried out. The pressure within the sample chamber is monitored using a pressure transducer and was observed to be within ±5 kPa of atmospheric pressure throughout all experiments. There were also notable fluctuations in the volume fraction of particulate in the

Table 8.2 Thermophysical properties of iron, silver, and molybdenum compiled from various sources that are used in evaluating the heat transfer model.

Property	Iron	Silver	Molybdenum
Density, ρ [kg/m^3]	8171–0.64985·T_p [337]	9346–0.9067·(T_p–1234) [386]	9100-0.6·(T_p–T_m), $T_p >= T_m$ 9100-0.5·(T_p–T_m), $T_p < T_m$ [380]
Specific heat capacity, c_p [J/(kg·K)]	835 [387]	531 [388]	56.5+0.01177·(T_p–T_m), $T_p >= T_m$ a(T_p)*, $T_p < T_m$ [380]
Melting temperature, T_m [K]	1811 [387]	1234 [386]	2896 [380]
K [J/kg], Eq. (2.43)	7.11×10^6	2.83×10^6	7.29×10^6
Boiling temperature, T_b [K]	3134 [389]	2466 [390]	4913 [391]
Latent heat of vaporization, $\Delta h_{v,b}$ [J/kg]	6.09×10^6 [389]	2.35×10^6 [390]	6.23×106 [392]
Critical temperature, T_{cr} [K]	9340 [393]	6410 [386]	14,588 [393]
A [Pa], Eq. (2.44)	4.70×10^{10}	2.43×10^{10}	2.31×10^{11}
Surface tension, γ_s [N/m]	1.865–(T_p–1823)·(0.35)·(10^{-3}) [394]	1.0994–0.0002·T_p [395]	2.11 [396]

* $a(T_p) = (1582+0.0589\cdot(T_p-T_m))\cdot(3.0+1.03\cdot(10^{-3})\cdot(T_p-T_m))$

sample cell between laser shots, causing a distinctly non-linear relationship between the signal mean and variance noted in Chapter 4. A schematic of this experimental apparatus is shown in Figure 8.3.

Laser-induced emission measurements are carried out with an Artium 200M system, which uses a pulsed Nd:YAG laser operating at 1064 nm and 10 Hz. Relay imaging is used to obtain a square 2.5 mm × 2.5 mm beam profile at the probe volume having a nearly top-hat temporally-averaged fluence profile. The nominal laser fluence used in this study is 0.29 ±0.03 J/cm^2 (found by measuring the pulse energy with a Coherent J-25MB-IR pyroelectric sensor and dividing by the beam area) and is adjusted by varying the Q-switch delay. The spectral incandescence is imaged onto two photomultipliers equipped with narrow bandpass filters centered at 442 and 716 nm (each with a full width at half maximum of 50 nm). PMT voltages are sampled every two nanoseconds using a fast oscilloscope.

Iron nanoparticle colloids were prepared shortly before the experimentation to avoid agglomeration or oxidation of the nanoparticles. Zero-valent iron nanoparticles were synthesized by reducing ferrous iron ions (Fe^{2+}) in a solution of sodium borohydride ($NaBH_4$), used as the reducing agent, and carboxymethylcellulose (CMC), to prevent agglomeration in deionized water, following Refs. [397,398]. Silver nanoparticle colloids were also prepared shortly before experimentation and were synthesized in solution using the procedure described in Ref. [399]. A silver nitrate aqueous solution was combined with a citrate solution under boiling conditions, after

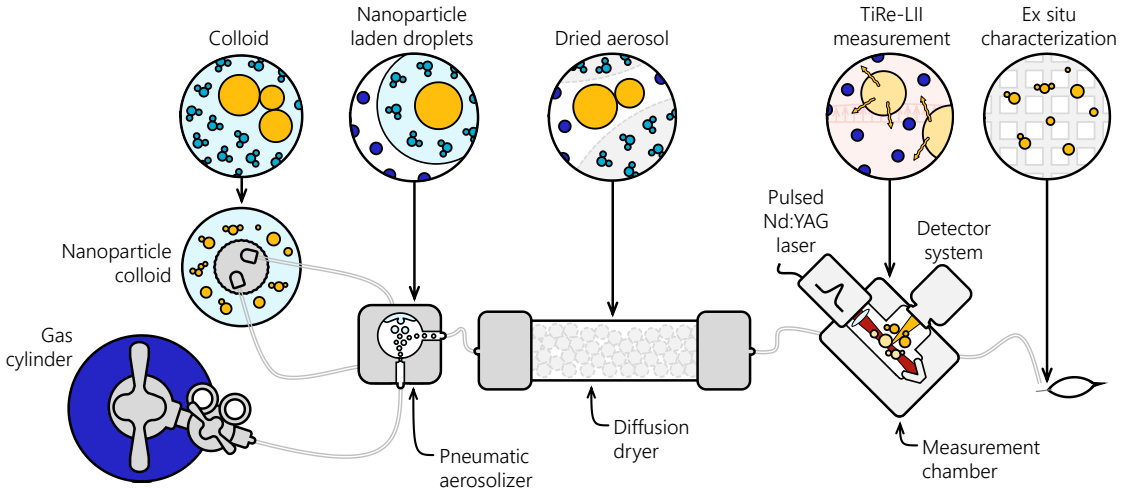

Figure 8.3 Schematic of the experimental apparatus used in this study. A motive gas and nanoparticle colloid streams are combined in a pneumatic aerosoliser. Water from the colloid is removed from the sample using a diffusion dryer. The nanoparticles are then characterised with an TiRe-LII measurement in a sample chamber used with an Artium 200 M system. Finally the nanoparticles are impacted onto a TEM grid for ex situ characterization.

which the solution was left to reflux under vigorous mechanical stirring for one hour. The molybdenum colloid was formed by dispersing a commercially-available molybdenum nanopowder in deionized water. The nanopowder (<100 nm) was purchased from Sigma-Aldrich (batch number MKBR4618V) and used without further purification. A 0.5 g sample of the nanopowder was dispersed in 100 mL of deionized water and ultrasonicated for 10 minutes.

Additional ex situ characterization of the nanocolloids was performed to complement or inform on TiRe-LII inference. TEM is used to image iron and molybdenum nanoparticles, and SEM is used to image the silver nanoparticles. In all cases, a diluted aliquot of the colloid was allowed to dry on a 200-mesh copper grid. Figure 8.5 shows sample electron microscopy images for each of the three materials. Figure 8.4 shows the nanoparticle size histograms obtained from a subsequent image analysis of the electron micrographs. The TEM image of iron shows the CMC coating produced during synthesis. It is assumed that this coating will rapidly ablate during the onset of laser heating and, while it may influence nanoparticle heating, is not expected to affect nanoparticle cooling. Image analysis of the iron colloid to determine a nanoparticle size distribution proved impractical, due in significant part to oxidation of the nanoparticles that occurred between TEM grid preparation and imaging. SEM imaging of the silver nanoparticles revealed isolated nanospheres that followed a narrow, Weibull-type size distribution [284], with a mean diameter of 65 nm. The distribution is sufficiently narrow that for the remainder

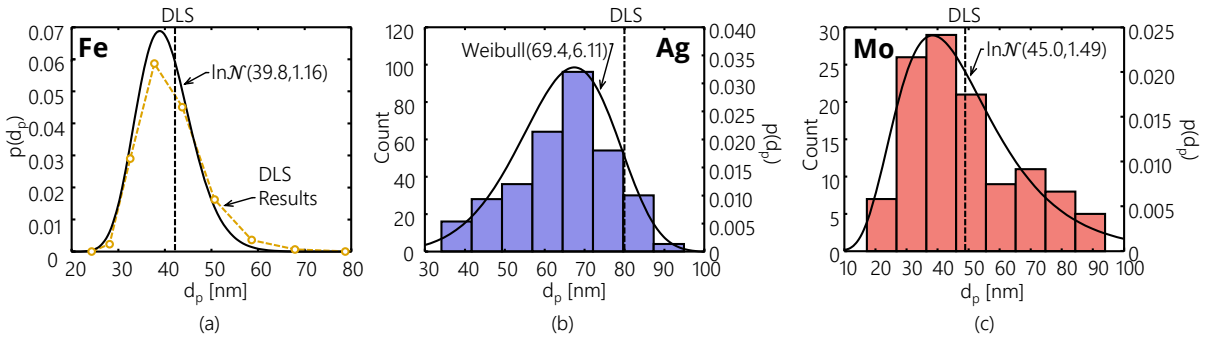

Figure 8.4 Histogram showing an analysis of ex-situ measured nanoparticle sizes for (a) iron (DLS), (b) silver (SEM), and (c) molybdenum (TEM). Histograms bins are obtained from electron microscopy image analysis.

of the analysis in this work, the silver nanoparticles are assumed to be monodisperse. TEM imaging of the molybdenum nanoparticles revealed aggregates of nanospheres. The primary particles in the aggregates approximately obey a lognormal distribution having a geometric mean (median) of 49 nm and a geometric standard deviation, σ_g, of 1.49, consistent with a self-preserving particle size distribution [283].

Dynamic light scattering (DLS) analysis was also performed on samples of each nanocolloid, which were diluted by a 1:1000 ratio in deionized water and then ultrasonicated for approximately 10 minutes immediately prior to measurement. The measurements are carried out using a Vasco DL 135 instrument and a Padé-Laplace model to fit the data. The solid index of refraction is used for silver [400] and molybdenum [401] nanoparticles and a value of 2.87 is used to account for the CMC-coating on the iron nanoparticles [402]. All three samples showed a nanoparticle size that quickly increased during the DLS measurements. These observations can be attributed to settling and aggregation of the nanocolloid during the measurement. Mean nanoparticle diameters observed near the time of ultrasonication were found to be 42, 80, and 51 nm for the iron, silver, and molybdenum colloids respectively. An approximation of the distribution for iron nanoparticles determined from the DLS analysis is also provided in Figure 8.4a. Like the silver nanoparticles, the iron nanoparticle sizes obey a narrow distribution which is approximated as monodisperse throughout the remainder of this work.

8.3 Comparative analysis of iron, silver, and molybdenum TiRe-LII

Laser-induced emission is measured following excitation of iron, silver, and molybdenum nanoparticles. The entirety of this section follows the original work of Ref. [45] in assuming that the laser-induced emission is incandescence from nanoparticles that satisfy the conditions for the Rayleigh approximation. The effect of this assumption and other anomalies noted in the analysis below receive explicit attention in Section 8.4. Signals are

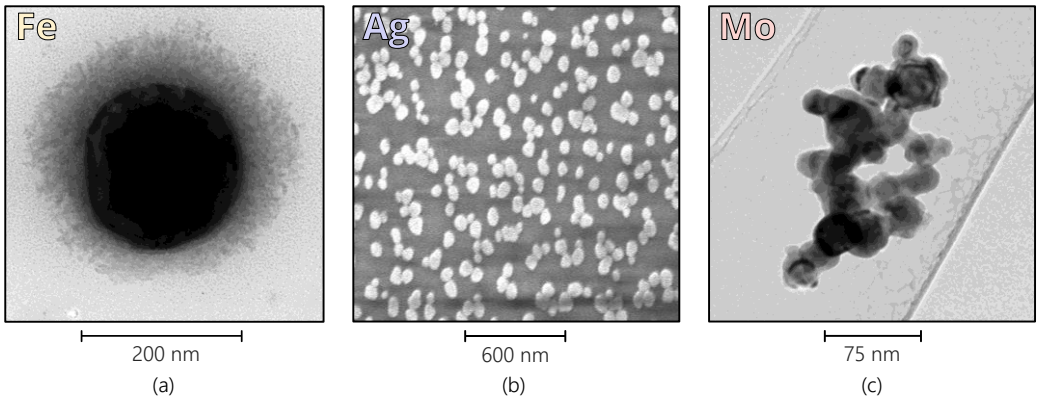

Figure 8.5 Sample TEM images of (a) iron and (c) molybdenum nanoparticles and (c) a SEM image silver nanoparticles resulting from the experimental procedure described in the text. The imaged iron nanonparticle appears surrounded by CMC capping. The silver nanoparticles appear as isolated spheres, while the molybdenum nanoparticles exhibit a significant degree of aggregation.

collected from 250, 500, and 500 individual shots of laser excitation for iron, silicon, and molybdenum respectively. The measured signals are then subdivided into groups of three, with each group being averaged to reduce signal variance. Two-color pyrometry, Eq. (3.5), is applied to the average of each group to calculate a series of temperature decays. Outliers in the temperature decays are removed using a Thompson Tau procedure [403], before the mean and standard deviation of the mean are calculated on the remaining temperature decays to be used as input to a Bayesian procedure. According to the Central Limit Theorem, the mean will obey a narrower normal distribution, which lends itself to the form of the likelihood discussed previously in Chapter 3. Sample temperature decays generated by this procedure are included with the discussion in Section 8.3.2. Peak nanoparticle temperatures for use in Section 8.3.1 are taken as the mean pyrometric temperature at the time of the peak signal. This section proceeds by applying many of the tools developed in the previous chapters. Section 8.3.1 presents a peak temperature fluence curves analysis, following Chapter 5, for the three materials. Section 8.3.2 presents an analysis of the pyrometrically-defined nanoparticle temperature decay, for which the MD-derived TACs from Chapter 7 become a source of information. Finally, Section 8.3.3 concludes with a discussion of the intensity scaling factor (ISF), following the technique described in Chapter 6.

8.3.1 Peak temperature and fluence curve analysis

Considerable information can be derived by analyzing the pyrometrically-inferred peak nanoparticle temperatures. Here, they are first used to infer the absorption efficiency required for a nanoparticle to heat up to the observed peak temperatures. Consider the energy balance on the nanoparticle having neglected evaporation prior to the peak and with energies integrated over the duration of the laser pulse (similar to the analysis

performed in Chapter 5 for the low fluence regime). With a known peak temperature, this expression can be rearranged for the absorption efficiency at the laser wavelength,

$$\left(Q_{\text{abs},\lambda_1}\right)_{\text{meas}} = \frac{4}{6}\frac{c_p \rho d_p}{F_0}\left(T_{\text{peak}} - T_g\right). \tag{8.12}$$

This represents the minimum absorption efficiency required to reach the observed peak temperature. In neglecting the evaporation term, this treatment will result in a conservative estimate of the absorption efficiency, with the real efficiency being larger for low boiling point materials. Figure 8.6 presents trends in this quantity, normalized by the one derived from Rayleigh theory using the optical properties available in the literature. For the case of iron, silver, and molybdenum, the optical properties for the Rayleigh absorption efficiencies are taken from data reported in Refs. [155], [374], and [382], respectively. The height of the bar symbols for the values in the current study correspond to the range of $(Q_{\text{abs},\lambda 1})_{\text{meas}}$ inferred over the range of fluences considered in this study. This quantity is also indicated for soot, following measurements by Snelling et al. [111]. The results indicate that the experimentally-derived absorption efficiency at 1064 nm far exceeds the spectroscopic values predicted by Rayleigh theory for iron and silver; the same is true for molybdenum nanoparticles, although to a lesser extent. The ones for carbon, in contrast, are much closer to the predicted values. The reason for this discrepancy is not currently understood and is the topic of future work. One possible

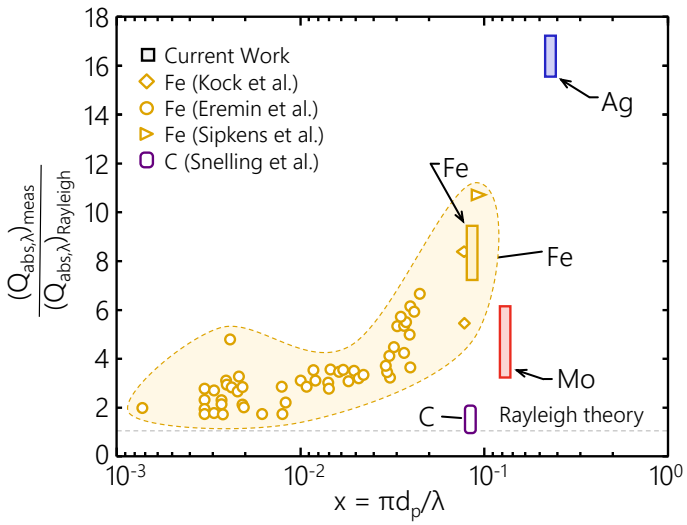

Figure 8.6 Trends in the ratio of the LII-derived to spectroscopic absorption cross section at the laser wavelength (1064 nm) with increasing dimensionless size parameter, *x*. Data is taken from fluence studies by Eremin et al. (iron)[129], Kock et al. (iron) [21], Sipkens et al. (iron) [112], Snelling et al. (carbon) [111] and the current work (iron, silver, and molybdenum).

explanation is that the discrepancy comes as a result of adopting the Rayleigh approximation in the place of Mie theory, which Figure 2.1 would suggest gives trends similar to that observed for iron in Figure 8.6. However, even in this case, the optical properties of silver only predict a temperature rise of several hundred Kelvin, which would not result in measurable incandescence.

An alternative approach to analyzing the peak temperature data is to consider the variation with laser fluence. Figure 8.7 considers this relationship, where the laser energy is controlled by varying the laser flashlamp Q-switch delay between 137 μs and 250 μs, corresponding to laser fluences from 0.058 to 0.263 J/cm^2. Error bars are excluded for clarity and generally correspond to less than 10% of the recorded value. Equation (5.32),

$$T_{\text{peak}}\left(F_0\right)=\left\{\left(B_1F_0+T_{\text{g}}\right)^n+\left[\frac{B_2}{W_{-1}\left(B_3F_0^2\right)}\right]^n\right\}^{1/n}, \tag{8.13}$$

is fit to the data using B_1, B_2, and B_3 as free parameters and assigning n = –20. The peak nanoparticle temperatures are expected to plateau slightly above the boiling point of each material due to the fact that the laser energy is added to the nanoparticle faster than it can be removed through evaporation. Consequently, the excess laser energy accumulated during the pulse causes a superheat, typically on the order of several hundred degrees Kelvin.

The trends in T_{peak} versus fluence for iron nanoparticles shows the progression from the linear region towards the plateau region described above. While the general shape of T_{peak} versus F_0 for iron nanoparticles complies with the expected trend, the temperature of the plateau region calculated using $E(\mathbf{m})_r$ = 1.85 is approximately 3000 K,

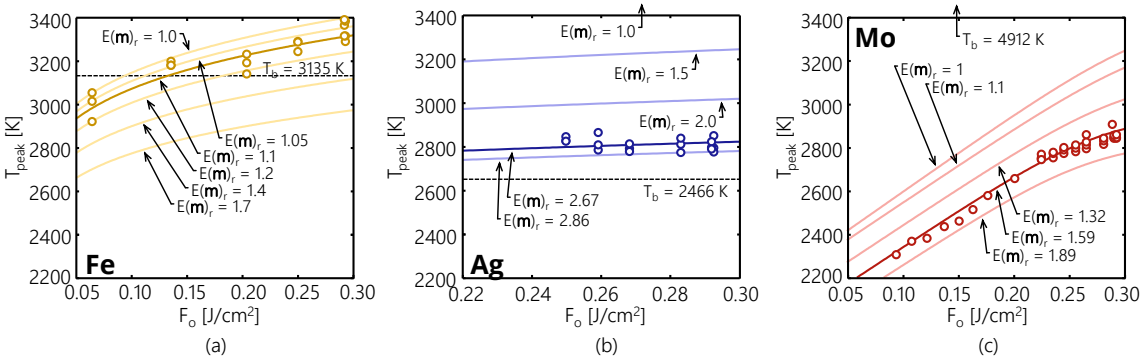

Figure 8.7 Examination of the peak temperature, T_{peak}, as a function of laser fluence for (a) iron, (b) silver, and (c) molybdenum. Circles represent experimental peak temperatures for $E(\mathbf{m})_r$ = 1.10, 2.67, and 1.59 for iron, silver, and molybdenum respectively. Remaining lines correspond to fits of Eq. (8.13) to data interpreted with different values of $E(\mathbf{m})_r$.

below the boiling point of bulk iron, 3135 K [389]. It is useful to note that the reduction in the boiling point predicted by the Kelvin equation is only ~10 K for the ex situ-determined nanoparticle sizes. More reasonable peak temperatures can be obtained using $E(\mathbf{m})_r = 1.1$, which is smaller than that expected using experimentally-derived radiative properties of molten iron [155,374] but consistent with previous TiRe-LII studies that matched TiRe-LII inferred nanoparticle sizes to TEM-derived values by assuming $E(\mathbf{m})_r = 1$ [21,24]. This treatment will be revisited when inferring nanoparticle diameters and TACs in Section 8.3.2.

The peak temperature of the silver nanoparticles remains nearly constant with increasing laser fluence over the relatively short range considered. This could be interpreted in several different ways. Perhaps the simplest explanation is that the silver nanoparticles are superheated and the additional laser heating roughly balances with an increased evaporation rate. In this case, interpreting the spectral incandescence data with $E(\mathbf{m})_r = 2.67$ obtained from Drude theory results in a maximum peak temperature ~200 K above the boiling temperature, in line with the expected superheat, while using a value of $E(\mathbf{m})_r = 1$ results in a temperature of ~3600 K, which is likely nonphysical. Alternatively, however, the insensitivity to the laser fluence could suggest that some other form of fluence-independent emission phenomenon is responsible for the observed signal.

The peak temperature of the molybdenum nanoparticles exhibits less evidence of a plateau than the iron case, which is expected given the high boiling point. Fitting Eq. (8.13) to the curves remained challenging, however, as extrapolation of the linear trend at the lower fluences would suggest gas temperatures around 2000 K, when, in fact, they are known to be ~300 K. The reason for this remains unknown and is discussed further in Section 8.4. As a result, the lines are only intended to guide the eye and to indicate the effect of changing $E(\mathbf{m})_r$. Some degree of curvature in the fluence curve at higher fluences suggests the onset of sublimation. This observation occurs in spite of the fact that using $E(\mathbf{m})_r = 1.59$ derived from ellipsometry measurements on polished molybdenum [382] gives peak temperatures below the melting point of molybdenum, $T_m = 2896$ K [380]. While the increased surface energy of the nanoparticles can reduce their melting point relative to that of the bulk material by an amount proportional to $1/d_p$ [404,405], the relatively large size of the molybdenum nanoparticles anticipated from ex situ analysis suggests that this effect is negligible. In contrast, it seems more reasonable that the small degree of observed curvature in the peak temperature fluence curve may be a result of temperature-dependent sensible energy or conductive cooling properties.

8.3.2 Nanoparticle sizing and the thermal accommodation coefficient

The nanoparticle size and TAC are inferred from a subset of the observed temperature decay curves, samples of which for Fe-Ar, Ag-Ar, and Mo-Ar are included in Figure 8.8. For this portion of the study the nominal fluence of 0.29 J/cm^2 is used for all measurements. The analysis is carried out using temperatures starting from 30 ns after the peak temperature (unless otherwise noted), to avoid residual laser heating and known uncertainties associated with the spectroscopic model that occur close to the peak incandescence signal [48], and extending to a time at which a specified signal-to-noise ratio is exceeded. In this chapter, uncertainties in the estimates are considered independently in the context of: (i) measurement errors as discussed in Chapter 4 and caused by photonic shot noise, electronic noise, and fluctuations in laser intensity; and (ii) parameter uncertainties in the spectroscopic and heat transfer model parameters. Simultaneous incorporation of both of these uncertainties into a single Bayesian procedure requires formal definition of priors and a higher-order inference, which is considered for iron nanoparticles in Chapter 9.

Measurement errors in the average temperature are incorporated directly into the likelihood, which is modeled as normal. In this case, the likelihood is given by Eq. (3.25),

$$p\left(\mathbf{b}|\mathbf{x},\boldsymbol{\theta}\right)=\left|2\pi\boldsymbol{\Sigma}^{\mathrm{b}}\right|^{-1/2}\exp\left\{-\frac{1}{2}\left\|\mathbf{L}^{\mathrm{b}}\left[\mathbf{b}^{\mathrm{meas}}-\mathbf{b}^{\mathrm{mod}}\left(\mathbf{x},\boldsymbol{\theta}\right)\right]\right\|_2^2\right\}, \tag{8.14}$$

where $\mathbf{b}$ is a vector of average temperatures, $\mathbf{x}$ contains the quantities-of-interest, and $\boldsymbol{\theta}$ is the nuisance parameters, taken about their nominal values (see Table 8.2). Initially, an uninformed prior is applied, such that maximum a posteriori (MAP) estimate corresponds to the maximum likelihood estimate (MLE), that is Eq. (3.26),

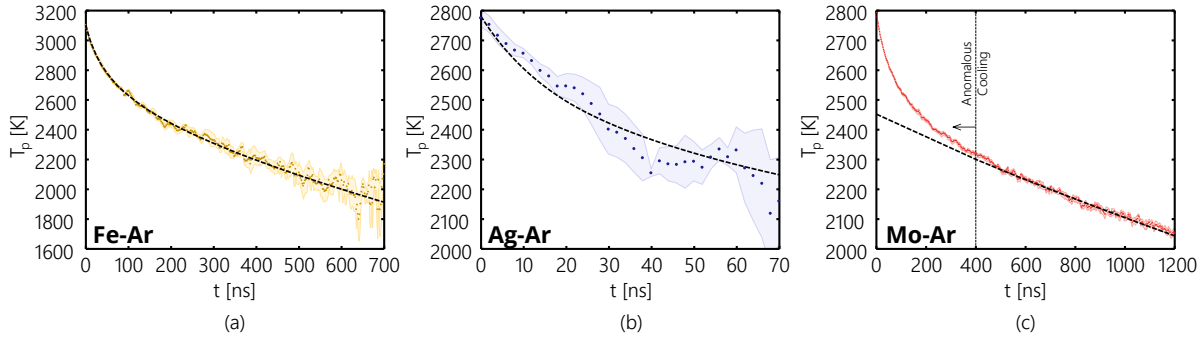

Figure 8.8 Mean pryometric temperature decay inferred from TiRe-LII measurements of (a) iron, (b) silver, and (c) molybdenum nanoparticles in argon buffer gas. Error bounds correspond to two standard deviations of the mean at each time. Dashed lines correspond to MLE fits to the data.

$$\mathbf{x}^{\mathrm{MAP}} = \mathbf{x}^{\mathrm{MLE}} = \arg\min_{\mathbf{x}} \left[p\left(\mathbf{b}|\mathbf{x},\boldsymbol{\theta}\right) \right]. \tag{8.15}$$

The likelihood probability densities are summarized by 95% credibility intervals, which, for a normal distribution with respect to $\mathbf{x}$, corresponds to two standard deviations.

Contours of the log-likelihood function resulting from this procedure are plotted in Figure 8.9 for iron, silver, and molybdenum nanoparticles in argon. The plots reveal a robust MLE for the iron nanoparticles but not for silver and molybdenum nanoparticles. The different likelihood topographies arise from the fact that different cooling regimes are observable for each type of nanoparticle (cf. Figure 8.2). In the case of iron nanoparticles, the observed temperature decay is due to both evaporation heat transfer, which depends on d_p, and conduction heat transfer, which depends on d_p and α. In contrast, if the observed emission for silver is interpreted as incandescence, the inferred temperature decay would result almost entirely from evaporative cooling (unless α is excessively large), which depends on d_p but not α. Finally, the likelihood function for molybdenum nanoparticles is maximized not by a single point, but rather by a locus of solutions corresponding to a fixed value of α/d_p. One would expect this since the observed temperature decay is entirely due to free molecular conduction and, under these circumstances, rearrangement of Eq. (8.7) approximately results in $\mathrm{d}T_\mathrm{p}/\mathrm{d}t \propto C{\cdot}\alpha/d_\mathrm{p}{\cdot}[T_\mathrm{p}(t) - T_\mathrm{g}]$ where independent estimates of α and d_p would not be possible [131].

The propagation of the model parameter uncertainties, that is the uncertainties due to $\boldsymbol{\theta}$, through to the quantities-of-interest, $\mathbf{x}$, is done using a Monte Carlo procedure, similar to that employed by Crosland et al. [228]. In this approach, normal probability densities are specified for the model parameters centered on the nominal

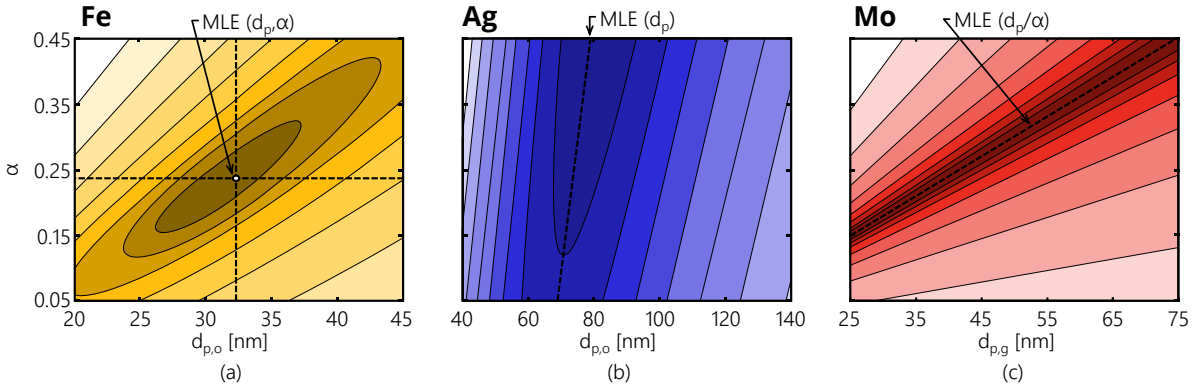

Figure 8.9 Log contours of the log-likelihood function for (a) Fe-Ar, (b) Ag-Ar, and (c) Mo-Ar. The length of the domain of α is a consistent across all three plots. In the case of Mo-Ar, σ_g = 1.49 for the entirety of the plot.

values in Table 8.2 and having assigned distribution widths shown in Table 8.3. These distribution widths are chosen based on expected parameter uncertainties (e.g. variations in literature values and reported experimental uncertainty). Randomly-sampled model parameters are substituted into the heat transfer model, and $\mathbf{x}^{\mathrm{MLE}}$ is found by repeatedly solving Eq. (8.15). The recovered parameters obey near-Gaussian probability densities with widths that define the uncertainties in d_p and α, which are included along with the estimates in subsequent tables.

8.3.2.1 Iron

Table 8.4 summarizes the nanoparticle size and TAC found from TiRe-LII measurements on iron nanoparticles in argon, nitrogen, and carbon dioxide. Estimates correspond to $E(\mathbf{m})_r$ values of 1.10, 1.70, and 1.84, with the latter two values taken from the ellipsometry measurements in Refs. [379] and [155], respectively. The recovered nanoparticle sizes are consistent for all three motive gases, as one would expect given that nanoparticle synthesis is independent of the gas type in this study. The sizes obtained using $E(\mathbf{m})_r = 1.1$ are also consistent with those found through ex situ analysis, while sizes obtained using the other $E(\mathbf{m})_r$ values are much smaller. Likewise, the recovered TACs using $E(\mathbf{m})_r = 1.1$ are similar to those reported through previous experimental [21,24] and

Table 8.3 Distribution width of multiplicative factors on model input parameters, θ_i. Values correspond to two relative standard deviations, $2\sigma_{\theta i}/\mu_{\theta i}$ and are listed for all three materials.

	$2\sigma_{\theta i}/\mu_{\theta i}$		
θ_i	**Iron**	**Silver**	**Molybdenum**
$d_{p,g}$	-	-	0.10
σ_g	-	-	0.10
α	-	0.38	0.10*
T_g	0.01	0.01	0.01
ρ	0.10	0.10	0.10
c_p	0.10	0.10	0.10
ΔH_v	0.10	0.10	-
ln(A)	0.01	0.01	-
T_i	0.004	0.004	0.004
$E(\mathbf{m})_r$	0.10	0.10	0.20

* This value is only used when inferring $d_{p,g}$ and σ_g. In this case, α is inferred and therefore not perturbed as part of $\boldsymbol{\theta}$.

molecular dynamics [108] studies, including those in Chapter 7. They also follow the expected trends with molecular mass and structural complexity [106,189]. In contrast, values for the TAC found using $E(\mathbf{m})_r = 1.70$ and 1.84 are much smaller. This finding is consistent with results presented in Section 8.3.1 and previous experimental studies that assumed $E(\mathbf{m})_r = 1$ [21,24]. Figure 8.8a shows that the modeled temperature decay, corresponding to $\mathbf{x}^{MLE}$, is in excellent agreement with the observed pyrometric temperatures calculated assuming $E(\mathbf{m})_r = 1.1$. It is worth noting that the uncertainties due to incomplete information about the model parameters greatly exceed those coming from measurement error. This is a consequence of the fact that: (i) the variance of the data is inversely proportional to the number of shots taken in averaging the data; and (ii) the length of $\mathbf{b}$, representing a large number of measurements of the temperature decay over the duration of a single-shot measurement.

8.3.2.2 Silver

Proceeding assuming that emission from the laser-heated silver nanoparticles is, in fact, incandescence, the inferred sizes of the silver nanoparticles aerosolized in argon, carbon dioxide, and nitrogen are shown in Table 8.5. The sizes are consistent with one another, DLS analysis (80 nm), and electron microscopy analysis (65 nm), in the context of the large uncertainties induced by the measurement noise and model uncertainties. However, it should be noted that, while at first glance the nanoparticle characteristics inferred from the TiRe-LII model match expectations, a detailed inspection of the signals casts doubt on this interpretation. Figure 8.8b shows that the modelled temperature decay for silver nanoparticles in argon is very rapid, consistent with the findings of Fillipov et al. [44]. While one interpretation is that this rapid temperature decay is due to the dominance of

Table 8.4 Maximum likelihood estimates of parameters of interest, x_i, for iron in different gases. Estimates of uncertainty are broken into those resulting from noise in the measured signal and those resulting from sensitivity to input parameters, θ_i. Uncertainties correspond to 95% confidence level (two standard deviations). Nanoparticle sizes are given in nanometers.

		$E(m)_r = 1.1$				$E(m)_r = 1.70$	$E(m)_r = 1.84$	α, MD
Gas	**x_i**	**MLE**	**Measurement ±**	**Parameter ±**	**Corr.**	**MLE**	**MLE**	**(Chapter 7)**
Ar	d_p	32.3	0.5	9.2	0.91	11.4	9.6	-
	α	0.24	<0.01	0.06		0.08	0.07	0.181 ±0.014
N_2	d_p	30.2	0.4	8.3	0.91	10.7	9.0	-
	α	0.07	<0.01	0.02		0.02	0.02	~0.125
CO_2	d_p	28.2	0.6	8.2	0.91	10.1	8.5	-
	α	0.12	<0.01	0.03		0.04	0.03	-

evaporative cooling, the limited duration and large amount of measurement error in the signals makes definitive conclusions challenging.

8.3.2.3 Molybdenum

Inspection of the pyrometric temperature decay for molybdenum nanoparticles (see Figure 8.8c) reveals a super-exponential decay in the effective temperature that lasts for approximately 400 ns after the laser pulse. This decay cannot be explained by the free molecular conduction heat transfer model alone. Superficially, the initial temperature decay curve suggests evaporation-dominated cooling, such as that seen in Figure 8.8a for iron nanoparticles in argon. However, the observed temperatures are well below the boiling point and, as per Figure 8.2, in a region in which conductive cooling is expected to dominate. Furthermore, the peak nanoparticle temperatures and the fluence curve in Figure 8.7 do not support this hypothesis, since one would expect to see a significant plateau region if evaporative cooling were that important in the fluence ranges used in this study. It is worth noting that the initial non-exponential temperature decay resembles the *anomalous cooling* effect that is particularly prominent in TiRe-LII measurements carried out at ambient temperatures on soot (cf. [106]), although it typically has a shorter duration (~50 ns). Accordingly, data analysis focuses on effective temperatures starting from 400 ns after the laser pulse.

As noted above, the TAC and the nanoparticle size distribution parameters cannot be inferred simultaneously from TiRe-LII measurements made on molybdenum nanoparticles due to the fact that d_p and α appear in a fixed ratio for conduction-dominated cooling. Instead, two scenarios are considered: (i) the nanoparticle size is inferred, assuming prior knowledge of α; or (ii) α is inferred, assuming prior knowledge of the nanoparticle size distribution. In the first scenario, the TAC is set equal to the MD-derived value of $\alpha = 0.15$ for Mo-Ar reported in Daun et al. [108]. MD-derived TACs for Mo-N_2 and Mo-CO_2 are unavailable, so nanoparticle sizing is restricted to the Mo-Ar case. The size distribution found through ex situ analysis (Figure 8.4) suggests a

Table 8.5 Maximum likelihood estimates of the nanoparticle size, d_p, in nanometers for silver in various gases assuming the emission signal is incandescence. Estimates of uncertainty are broken into those resulting from measurement error and those resulting from model input parameter uncertainty, θ_i. Uncertainties correspond to 95% confidence level (two standard deviations).

Gas	MLE, d_p	Measurement ±	Parameter ±
Ar	76	3	23
N_2	98	6	26
CO_2	78	6	21

lognormal distribution, which is used in the current analysis. The corresponding log-likelihood contours for this case are plotted in Figure 8.10. They reveal a MLE of $d_{p,g}$ = 43 nm and σ_g = 1.34, consistent with $d_{p,g}$ = 45 nm and σ_g = 1.49 found by electron microscopy. The contours resemble those observed in Figure 3.2. Corresponding credibility intervals due to measurement and model parameter uncertainty are summarized in Table 8.6. Similar observations can be noted to iron, where model parameter uncertainties dominate over those from measurement error.

In the second scenario, the TAC is inferred form the data having assumed a lognormal size distribution corresponding to that found through electron microscopy ($d_{p,g}$ = 45 nm, σ_g = 1.49). Table 8.6 shows the TAC for molybdenum nanoparticles in helium, neon, argon, carbon dioxide, and nitrogen. Measurements for molybdenum nanoparticles in monatomic (He, Ne, Ar) and polyatomic (N_2, CO_2) gases were carried out on two non-consecutive days, and Mo-Ar aerosols were measured on both occasions to assess the repeatability of this procedure. The results show that the TAC for Mo-Ar inferred from the TiRe-LII data (α = 0.24) is larger than that derived from molecular dynamics by Daun et al. [108] (α = 0.15), perhaps due to the inappropriateness of Mie theory or aggregation effects.

8.3.3 Intensity scaling factor analysis

Figure 8.11 shows the temporal evolution of the ISF corresponding to the Fe-Ar, Ag-Ar, and Mo-Ar temperature traces shown in Figure 8.8. In contrast to the soot ISF curve shown in Chapter 6, these ISF curves are relatively flat and remain nearly constant with respect to time. The Fe-Ar curve features a slight incline over the first 100 ns, which is unexplained. For Ag-Ar, a constant ISF is unexpected since, were the measured signal incandescence,

Table 8.6 Maximum likelihood estimates of parameters of interest, x_i, for molybdenum in various gases. Estimates of uncertainty are broken into those resulting from noise in the measured signal and those resulting from sensitivity to input parameters, θ_i. Uncertainties correspond to 95% confidence level (two standard deviations). Diameters are given in nanometers. Reported values are the result of two sets of experiments, with overlapping argon results.

θ_i	Gas	x_i	MLE	Measurement ±	Parameter ±	Correlation
α = 0.15	Ar	$d_{p,g}$	58	4	44	-0.98
		σ_g	1.19	0.01	0.23	
$d_{p,g}$ = 45.0 σ_g = 1.49	He	α	0.05	<0.005	0.01	-
	Ne	α	0.16	<0.005	0.04	-
	Ar	α	0.24	<0.005	0.05	-
	N_2	α	0.18	<0.005	0.06	-
	CO_2	α	0.23	<0.005	0.07	-

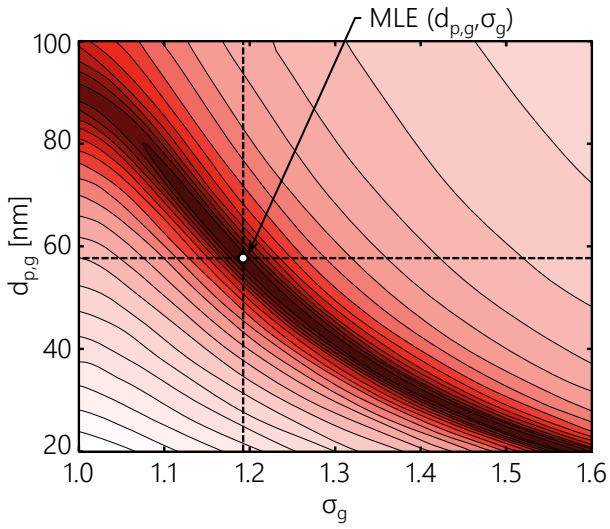

Figure 8.10 Log contours of the log-likelihood function considering variation in σ_g and $d_{p,g}$ for Mo-Ar. The contours exhibit similar non-linear behaviour to that observed for silicon by Sipkens et al. [48].

the pyrometrically-inferred temperatures imply considerable vaporization which would cause the ISF to drop over this period. This adds credence to the hypothesis that the observed signal may not be incandescence. Beyond 60 ns, the Ag-Ar curve also exhibits a sharp rise in the ISF. While the reason for the inflection is currently unknown, it is important to note that the signals are very noisy at this point. For Mo-Ar, the ISF curve exhibits a slight decline over the duration of the considered signal. This observation is consistent with the polydispersity effect identified by Smallwood [221] and described in Chapter 6. Furthermore, the magnitude suggests only a small degree of polydispersity in the aerosol, consistent with the interpretation of the nanoparticle temperature decay in Section 8.3.2.

8.4 Unresolved questions

While many aspects of the TiRe-LII measurements on Fe, Ag, and Mo aerosols conform to expectations, there are other aspects that suggest that the physical model underlying these experiments is incomplete or incorrect. A moment is taken to summarize the anomalies noted through this analysis and the possible explanations that should be pursued in future work.

In the case of the iron aerosol, the TiRe-LII experimental traces could be replicated using the measurement model with small residuals, and the inferred nanoparticle sizes matched those found through ex situ sizing. However, it is noted that one should consider the phase parameter, Eq. (8.4), as well as the size parameter, Eq. (8.3), when assessing the validity of the Rayleigh approximation [151]. Calculating the phase parameter reveals that

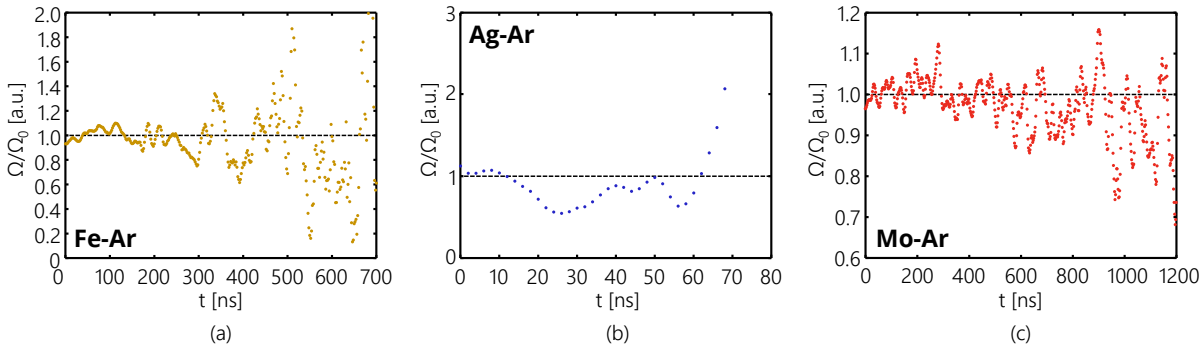

Figure 8.11 Temporal evolution of the ISF for (a) Fe-Ar, (b) Ag-Ar, and (c) Mo-Ar, normalized by the average of the first 100 ns for Fe and Mo and the first 10 ns for Ag.

the Rayleigh approximation should not be used to interpret TiRe-LII measurements on iron nanoparticles. Upon invoking Mie theory in the place of the Rayleigh approximation, two observations can be made. First, the absorption efficiency of iron nanoparticles at 30 nm increases considerably, which reduces the difference between the theoretically-predicted and observed absorption cross sections from a factor of eight to a factor of two. The remaining discrepancy may be a result of the variation in optical properties encountered by the nanoparticles during laser heating, most notably upon nanoparticle melting, or due to the presence of a thin oxide layer that can enhance the absorption cross-section. Second, adopting Mie theory in place of Rayleigh theory changes the ratio of the absorption efficiencies at the measurement wavelengths used in pyrometry. (This can be understood as changing the effective value of $E(\mathbf{m})_r$, though it must be noted that, without the use of the Rayleigh approximation, $E(\mathbf{m}_\lambda)$ no longer holds a physical interpretation). Applying Mie theory for $d_p = 30$ nm and the complex index of refraction from Ref. [155], the calculated absorption efficiencies imply an effective $E(\mathbf{m})_r \approx 1.85$. This value is effectively unchanged from that calculated using the Rayleigh approximation and, accordingly, has little effect on pyrometry. Accordingly, the reason for the adequacy of using $E(\mathbf{m})_r \approx 1$ remains an unknown. Further study is also needed to determine whether the slight increase in the ISF over the 100 ns following the laser pulse is physical and to investigate potential reasons for the phenomenon.

For measurement of silver, numerous observations in the current analysis suggest that the measured laser-induced emission is not incandescence. Most prominently, the calculated absorption efficiencies for silver, even after correctly applying Mie theory, only imply a temperature rise on the order of a few hundred Kelvin. Further, ISF analysis indicates no significant drop in the volume fraction during the signal. This is inconsistent with pyrometrically-defined nanoparticle temperatures that would suggest very significant evaporative mass loss from the nanoparticles. The very rapid temperature decay casts further doubt on the appropriateness of any

TiRe-LII analysis. Ongoing collaboration with Mr. Sina Talebi Moghaddam has focused on developing the hypothesis that the observed laser-induced emission may be bremsstrahlung, which decays shortly after the laser pulse due to work-function limited electron release, a decay in the emitted electron temperature, and diffusion of electrons out of the detector LOS.

For molybdenum nanoparticles, two anomalies are noted. First, the observed temperature decay features an anomalous cooling effect, shown in Figure 8.8, lasting 400 ns following the laser pulse. Recent, unpublished work by Mr. Talebi Moghaddam focuses on identifying the phenomena responsible for this effect, most notably the restructuring of aggregates by sintering of the primary particles. Second, extrapolation of the peak nanoparticle temperature versus fluence curves backward to zero fluence suggests gas temperatures inconsistent with experimental conditions. Several hypotheses exist to explain this phenomenon, including changes in the nanoparticle structure due to sintering and the invalidity of the Rayleigh approximation, which has significant consequences for polydisperse aggregates where the primary particles in the aggregate reach significantly different peak temperatures.

8.5 Conclusions and future work

While time-resolved laser-induced incandescence is mainly used to characterize soot primary particles in combustion applications, it shows promise as a tool for measuring aerosolized metal nanoparticles. Interpreting TiRe-LII data requires reliable spectroscopic and heat transfer models for these types of aerosols. This study presents a comparative analysis of TiRe-LII measurements on iron, silver, and molybdenum nanoparticles within monatomic and polyatomic gases, with the main objective of advancing development of these models. These aerosols are produced by pneumatically atomizing nanocolloids, which permits synthesis of a virtually unlimited combination of nanoparticle and bath gas, and also decouples the nanoparticle synthesis process from the bath gas, which allows a direct comparison of TiRe-LII derived nanoparticle sizes and other related quantities between the aerosols.

The three types of metal nanoparticles chosen for this study have very different thermophysical properties, which are reflected in the variation of observed peak temperatures. Peak temperatures for molybdenum nanoparticles increase approximately linearly with increasing fluence, indicating that the absorbed laser energy is transformed into sensible energy of the nanoparticle. In contrast, when the observed laser-induced emission from silver is interpreted as incandescence, the peak nanoparticle temperature plateaus above the boiling point of bulk silver, consistent with the observations of Chapter 5. The peak temperature for iron nanoparticles, in

contrast, reveals a transition between the low and plateau fluence regimes, leveling out above the boiling point of bulk iron. It is noted, however, that this result can only be obtained by assuming that a ratio of $E(\mathbf{m}_\lambda)$ values at the two detection wavelengths that is close to unity, an observation shared in previous studies [21,112,201]. Using the radiative properties for bulk molten iron, derived from ellipsometry measurements reported in the literature, provides nonphysical temperatures.

The observed pyrometric temperature decays for these materials are also characteristic of their respective melting points: the observed temperature decay for molybdenum nanoparticles is consistent with conduction-dominated cooling, while the pyrometrically-defined temperature decay for the silver nanoparticles appears consistent with evaporation-dominated cooling. The temperature decay for iron nanoparticles results from a combination of both evaporative and conductive heat transfer. The active heat transfer modes during cooling determines the information that can be inferred from TiRe-LII data, as indicated by log-likelihood contour plots. Robust estimates for d_p and α can be obtained from measurements on iron nanoparticles, while only d_p can be found from the pyrometrically-defined temperature of silver nanoparticles and independent values of α and d_p cannot be isolated from TiRe-LII measurements on molybdenum nanoparticles. When the TiRe-LII data for molybdenum nanoparticles is analyzed using lognormal size distribution parameters found from ex situ analysis, the resulting TACs follow the expected trends with gas molecular mass and structure, as is the case with the TACs inferred from TiRe-LII measurements on iron nanoparticles. Likewise, the nanoparticle sizes recovered from iron are consistent with those found from ex situ analysis, though again only by assuming an $E(\mathbf{m})_r$ ratio close to unity for iron.

The results of this study support the assertion that TiRe-LII can potentially be developed into a reliable diagnostic for measuring the size and concentration of aerosolized metal nanoparticles and demonstrates how TiRe-LII can also be thought of as a scientific instrument for carrying out experiments of fundamental interest. However, the measurements also suggest that the understanding of the physical processes underlying these measurements is incomplete. Most notably, there is a strong indication that the measured spectral incandescence from laser-energized silver nanoparticles may not, in fact, be incandescence at all. Future work will investigate these remaining discrepancies using the various tools presented throughout this thesis.

Chapter 9
Bayesian model selection and TiRe-LII[6]

In an effort to improve the robustness of their estimates, TiRe-LII practitioners continuously seek to improve the nanoparticle heating and cooling submodels used to interpret data. This has resulted in a plethora of models, the range of which is noted in Section 2.2 and often includes different treatments for the various heat transfer terms included in Eq. (2.20). While simple models fail to capture all the salient features of experimental cooling curves, progressively complex models, which may include temperature-dependent expressions for the thermophysical properties, have been shown to account for these features [97]. Some researchers have interpreted this improved fit between measured and modeled data as sufficient evidence that a new model is more realistic. However, this procedure ignores the fact that more complex models often rely on additional parameters that can significantly amplify uncertainties [45,89,228] (a fact made further evident by the dominance of model parameter uncertainty in the estimates presented in Chapter 8). This circumstance is demonstrated rather significantly for soot, where the models in the literature have been *tuned* to data sets from specific laboratories without robust consideration of the uncertainties. The result, noted by Michelsen et al. [98], is a series of models that diverge significantly from one another and cannot be used in an interlaboratory context. Accordingly, this approach to model development has generally led to misplaced confidence in the robustness of parameter estimates and represents one of the largest challenges currently facing the LII community.

In the consideration of metal nanoparticles, similar circumstances can be encountered. Many of the thermophysical properties that act as inputs to TiRe-LII models are poorly characterized for the temperatures relevant to analysis. Take, for example, the latent heat of vaporization. In the case of iron, much of the available data for this quantity is summarized by Desai [387], who reports data for temperatures up to 3200 K. Studies cited

[6] Information presented in this chapter has been disseminated as:
Sipkens, T. A., Hadwin, P. J., Grauer, S. J., and Daun, K. J., 2018, "Predicting the heat of vaporization of iron at high temperatures using time-resolved laser-induced incandescence and Bayesian model selection," J. Appl. Phys., **123**(9), 95103. doi: 10.1063/1.5016341

employ techniques that include the Langmuir and Knudsen effusion methods. More recently, Beutl et al. [406] measured the enthalpy of liquid iron up to 5000 K following a calorimetric technique, by comparing the electrical power supplied by an electrode to the pyrometrically-inferred temperature of the molten steel. Wille et al. [407] applied a similar technique to laser-heated iron droplets levitated using a gas stream. Nevertheless, data for the latent heat of vaporization of liquid metals is still sparsely available in the literature, particularly in regards to how the quantity changes with respect to temperature [408]. Many studies, including those cited by Desai [387], report a single latent heat of vaporization by deriving a single value from a vapor pressure curve, often from vapor data collected below the melting point. As a result, determining the latent heat of vaporization above the melting temperature has historically been determined using models. This has resulted in a plethora of expressions with varying levels of sophistication [408,409], with little consensus as to which expression is most suitable for TiRe-LII analysis.

In response, this chapter explores the use of *Bayesian model selection*. Bayesian model selection, as a technique, extends the Bayesian approach introduced in Chapter 3 to consider uncertainties in the models themselves, incorporating the data and model parameters in the process. This approach has been used to assess and compare models in applications including astrophysics and cosmology [410,411], applied physics [230,412], sociology [413], economics [414], ecology [415,416], and biology [417,418]. Bayesian model selection automatically incorporates the concept of *Occam's razor*, accounting for trade-offs between model simplicity and fit to the data, informing on the relative plausibility of alternative physical mechanisms. Here, the technique is applied to the TiRe-LII data from laser-excitation of iron nanoparticles described in Chapter 8. In this regard, the current chapter serves several purposes, namely (i) to demonstrate the Bayesian model selection technique for aerosolized iron nanoparticles prior to considering the complexities involved in modeling soot (a topic of future work), (ii) to improve the robustness of TiRe-LII analyses carried out on iron, and (iii) to obtain additional theoretical insight into the thermophysical properties of liquid iron by identifying the most probable expression available in the literature to describe the latent heat of vaporization over wide temperature ranges.

This chapter begins with an overview of the spectroscopic and heat transfer submodels that make up the TiRe-LII measurement model. The statistical framework underlying Bayesian model selection is explained, before being demonstrated using simulated TiRe-LII measurements of iron nanoparticles in an argon buffer gas. Comparisons are made for a range of peak temperatures to highlight the regimes in which alternate conduction and evaporation cooling submodels are relevant. Finally, the TiRe-LII data from Chapter 8 for iron nanoparticles

in argon is considered. The results show that Román's equation, while more complex than other models considered in this paper, best describes the behavior of iron across the large temperature range of TiRe-LII. More generally, this procedure illustrates how TiRe-LII can be used to robustly determine fundamental thermophysical properties of metals at high temperatures.

9.1 TiRe-LII model

The TiRe-LII model employed in this chapter is a modified version of the one presented in Chapter 8. The spectroscopic model is identical to that presented in Chapter 8 and is only used in interpreting the experimental incandescence data. Unlike that chapter, however, the Thompson Tau outlier procedure is here applied to the incandescence data directly rather than to the pyrometrically-inferred temperatures. In regards to the heat transfer model, the present chapter only examines nanoparticle cooling, allowing for simplification of Eq. (2.20) to

$$c_{\mathrm{p}}\rho\frac{\pi d_p^3}{6}\frac{\mathrm{d}T_{\mathrm{p}}}{\mathrm{d}t}=-q_{\mathrm{cond}}-q_{\mathrm{vap}}\,. \tag{9.1}$$

The peak temperature then acts as the initial condition for solving this equation. The form of the conduction and evaporation models shares a form with Chapter 8, only varying in the treatment of the latent heat of vaporization and some model parameter values as described in Section 9.2.

In terms of the latent heat of vaporization, it has long been established that the quantity is a function of temperature, monotonically decreasing towards zero at the critical point [419]. As Δh_{v} is zero at the critical temperature, most expressions for this quantity are phrased in terms of a dimensionless temperature,

$$\tilde{T}=\frac{T_{\mathrm{cr}}-T_{\mathrm{p}}}{T_{\mathrm{cr}}-T_{\mathrm{ref}}}\,, \tag{9.2}$$

where T_{cr} is the critical temperature of the nanoparticle material and T_{ref} is a reference temperature. Renormalization group theory predicts that the heat of vaporization asymptotically approaches [420]

$$\Delta h_{\mathrm{v}}=D_{\mathrm{n}}\tilde{T}^{\,n}\,, \tag{9.3}$$

at the critical point, where n is a universal critical exponent and D_{n} is a material constant. This expression has seen support in the literature dating back to Thiesen [419] in 1897, who proposed n = 1/3. Numerous empirical variants of the critical exponent have been proposed, including: n = 0.38 [202], n = 0.386 [421], n = 0.3889 [422], and n = 0.4 [423,424]. Silverberg and Wenzel [425] proposed that n is not a universal constant, but rather a material-

specific property, reporting values of n that range from 0.237 to 0.589, with most values clustered tightly about a mean of 0.378. Most analysts who consider the temperature-dependence of Δh_v use $n = 0.38$, which gives Watson's equation [202], Eq. (2.43),

$$\Delta h_v = K\left(1-\frac{T_p}{T_{cr}}\right)^{0.38} = \Delta h_{v,ref}\tilde{T}^{0.38}. \tag{9.4}$$

This expression has been used directly in several TiRe-LII studies of synthetic nanoparticles [45,48,112] and in related fields, including laser ablation of nanoparticles [426] and droplet evaporation in combustion [427].

Watson's equation also forms the basis for other, more recent expressions. For example, Zhong [428] propose a generalization of Eq. (9.4), dividing the temperature domain into regimes, where Watson's equation is valid in the higher temperature regime. Others incorporate additional factors into the more general Eq. (9.3). Svoboda et al. [409,429] suggest a temperature-dependent prefactor. Román et al. [204] use the assumption that thermodynamic properties change linearly with temperature near the triple point to propose a more general form of this equation,

$$\Delta h_v = \Delta h_{v,ref}\exp\left[\left(n-\beta_R\right)\left(\frac{T_p-T_{ref}}{T_{cr}-T_{ref}}\right)\right]\tilde{T}^n, \tag{9.5}$$

where β_R is related to the slope of Δh_v at the reference point. In the case that $n = \beta_R$, this form reduces to Eq. (9.3) and then, for $n = 0.38$, to Watson's equation. Meyra et al. [205] proposed that n is a function of temperature,

$$\Delta h_v = \Delta h_{v,ref}\tilde{T}^{Z_c^2\left[\left(T_{cr}-T_p\right)/\left(T_{cr}-T_{ref}\right)\right]+Z_c}, \tag{9.6}$$

where $Z_c = 0.292$ is the universal critical ratio. Such an expression can be shown to approach Watson's equation about the reference temperature, most often taken as the triple point. Other candidates deviate from the form of Eq. (9.3). Fish and Lielmezs [430] suggested

$$\Delta h_v = \Delta h_{v,ref}\frac{T_p}{T_{ref}}\left(\frac{\tilde{T}+\tilde{T}^q}{T_{ref}/T_p+\tilde{T}^{m_{FL}}}\right), \tag{9.7}$$

with $q = 0.20957$ and $m_{FL} = -0.17464$, based on data from five metals and one metalloid, giving errors less than 3% from experimental data. Velasco et al. [431] performed a comparison of Eqs. (9.4) to (9.7) for metals and metalloids over a wide range of temperatures (limited to the data from Desai for iron), showing a preference for the expression proposed by Román et al. [204]. The objective of this work is to determine which of Eqs. (9.4) to (9.6)

and a model consisting of a constant Δh_v is the most plausible treatment, using TiRe-LII measurements on aerosolized iron nanoparticles to do so.

9.2 Priors on the thermophysical properties of iron

Implementation of Bayesian model selection, which is introduced below in Section 9.3, requires that each of the model parameters, be it a QoI or nuisance parameter, have a prior that accurately quantifies the information available for that parameter before the measurement. A multivariate normal prior is used for all the parameters here, having a mean and covariance corresponding to the expected values and uncertainties derived from values given in the literature (thereby adhering to the Principle of Maximum Entropy). When this information is not explicitly available in the literature, a Bayesian procedure is used to estimate the mean and covariance from published experimental data. This procedure amounts to the following steps:

1. A functional form is chosen for the model parameters in question (in this case with respect to temperature or holding the quantity in question constant).
2. Where possible, priors are applied to the parameters in these functions (e.g., prior measurements of the critical temperature in estimating the temperature dependence of the latent heat of vaporization).
3. The posterior distribution that is determined for the parameter using Bayes' equation, Eq. (3.21), forms the prior for subsequent TiRe-LII inference.

Results of the literature review are summarized in Table 9.1. Here, the posterior covariance matrix is alternatively stated in terms of a standard deviation, which has the advantage sharing units with the parameter in question, and a Pearson correlation coefficient between the i^{th} and j^{th} parameter, $R_{ij} = \Sigma_{ij}/(\Sigma_{ii}\Sigma_{jj})^{1/2}$, which contains dimensionless coefficients bounded by [-1, 1]. Also included in Table 9.1 is an indication of which model parameter values are used in which of the case studies considered in Section 9.4.

The density of iron is taken from Hixson et al. [337], so that

$$\rho = \rho_0 + \rho_1 T \,, \tag{9.8}$$

where ρ_0 and ρ_1 are fitted constants representing the density at 0 K (or the y-intercept) and the slope with respect to temperature, respectively. In order to determine the uncertainty attached to these parameters, a nonlinear regression of Eq. (9.8) is carried out to the original experimental data presented in Ref. [387]. The posterior covariance of these parameters, having assumed an uninformed prior, describes our new state-of-knowledge of

Table 9.1 Parameter values and covariance used in evaluations of the heat transfer models for iron. A distinction is made between the properties applied as priors to the different models in Table 9.2.

Property	Relevant models	Relevant model parameters	Center	Standard deviation	Correlation, R
Nanoparticle size	A-G	d_p [nm]	30	10	-
Thermal accommodation coefficient	A-G	α	0.236	0.026	-
Density, $\rho(T) = \rho_0+\rho_1 T$	A, B	ρ_0 [kg/m^3]	6350	259	-0.9840
	A	ρ_1 [kg/(m^3·T)]	0	0.0823	
	C-G	ρ_0 [kg/m^3]	8171	259	-0.9840
		ρ_1 [kg/(m^3·T)]	-0.6499	0.0823	
Heat capacity, $M \cdot c_p(T) = c_{p,0}+\kappa T$	A, B	$c_{p,0}$	1	0.0300	-0.6672
	A	κ	0	0.3912	
	C-G	$c_{p,0}$	1	0.0300	-0.6672
		κ	1	0.3912	
Gas temperature	A-G	T_g [K]	298	2.98	-
Gas pressure	A-G	p_g [Pa]	1.013×105	1013	-
Vapor pressure, Clausius-Clapeyron eq.	A, B, D-G	$\Delta h_{v,b}$ [kJ/kg]	6571	79.26	-0.7986
		T_b [K]	3073	21.02	
Surface tension	A, B, D-G	γ_s [N/m]	1.865	0.05	-
Critical temperature	A, B, E-G	T_{cr} [K]	9330	75	-
Critical exponent	A, B, E, F	n	0.38	0.0084	-
Román parameter	A, B, F	β_R	0.371	0.0845	-
Universal critical ratio	A, B, G	Zc	0.292	0.0044	-

these parameters. Table 9.1 shows the standard deviation and correlation coefficient for ρ_0 or ρ_1. The parameters are highly correlated, a consequence of the linear relationship and the structure of the data.

The volumetric heat capacity of the nanoparticle is considered as a piecewise linear function of temperature [387]

$$M\cdot c_{\mathrm{p}}\left(T\right)=\begin{cases}46.6\cdot c_{\mathrm{p},0}, & T\geq 1811\,\mathrm{K}\\ 40.4\cdot c_{\mathrm{p},0}+0.0322\cdot\kappa\cdot\left(T-1667\right), & 1667\,\mathrm{K}\leq T<1811\,\mathrm{K}\\ 33.8\cdot c_{\mathrm{p},0}+0.00916\cdot\kappa\cdot\left(T-1181\right), & 1181\leq T<1667\,\mathrm{K}\end{cases}, \tag{9.9}$$

where $c_{\mathrm{p},0}$ and κ are multiplicative constants having a default value of unity and M is the molar mass of iron in kg/mol. A covariance matrix on these parameters is taken as the worst-case scenario in fitting data to individual pieces of Eq. (9.9), assuming the data has a 3% error at the end points (as stated in Ref. [387]). The corresponding standard deviation of $c_{\mathrm{p},0}$ and κ, as well as the correlation between the parameters are again given in Table 9.1.

The vapor pressure is given by the Clausius-Clapeyron equation, where T_{ref} and $\Delta h_{\mathrm{v,ref}}$ are unknowns. Bayesian inference was performed on vapor pressure data obtained from Refs. [369,387,406,432–434] to attain the most suitable expected values and covariance for these properties. Although such sources can in some cases be traced back to some subset of the sources cited by Desai [387], they do represent the spread in the modern interpretation of this data and thereby still provide information about the current state-of-knowledge of the vapor pressure. In the case that the source gave an equation, the vapor pressure was evaluated at intervals of 50 K (for CRC [369] and SMI [432]) or 200 K (for Beutl et al. [406], which covers a larger range). A Gaussian prior was applied to the boiling temperature by taking the mean (3060 K) and standard deviation (42 K) of predictions in Refs. [387,432,433,435]. Figure 9.1 shows the data and resultant Clausius-Clapeyron equation fit, and Figure 9.3 shows the corresponding posterior distribution. The linear approximation to the posterior covariance of this procedure is used as the prior covariance during TiRe-LII analyses considered in subsequent sections.

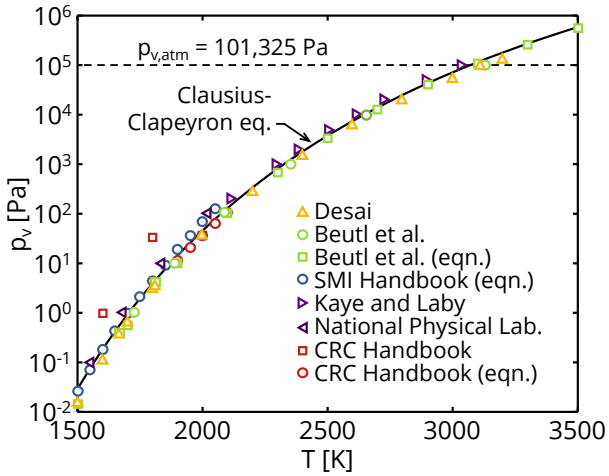

Figure 9.1 Vapor pressure as a function of temperature from a range of studies [369,387,406,432–434] and a realization of the Clausius-Clapeyron equation corresponding the MAP estimate of T_{b} and $\Delta h_{\mathrm{v,b}}$.

To account for the variation in Δh_v with respect to temperature, three expressions proposed in the literature are considered, specifically those of Watson [202], Román et al. [204], and Meyra et al. [205]. In each case, a prior on the critical temperature is taken as the mean (9330 K) and standard deviation (75 K) of the values given in Refs. [393,406,436,437]. The reference point is taken as the boiling point at atmospheric pressure, that is T_{ref} and $\Delta h_{v,ref}$, having uncertainties defined in the previous paragraph. For the expression given by Watson and Román et al., a Gaussian prior on the critical exponent, n, is centered at 0.38 with a standard deviation of 0.0084, based on the range of values for the critical exponent reported in the literature [421–424]. A Gaussian prior on the additional parameter in Román's equation is centered on 0.371 having a width chosen so that the 0.54 limit originally suggested by Román et al. is two standard deviations away from the mean (giving a standard deviation of 0.0845). The universal critical ratio, Z_c, required for the Meyra's equation, is given by Guggenheim [438] to be 0.292 with an estimated 1.5% error. Figure 9.2 shows the difference between the temperature dependence predicted by these three expressions, using the mean values stated in Table 9.1.

Priors on the remaining properties are considered independently based on ranges given in the literature. Prior information for the thermal accommodation coefficient is taken from a weighted combination of MD simulations [108], such as those presented in Chapter 7, and previous TiRe-LII experiments [45], in which error bounds were reported and used as weights. The TAC is modeled as independent of temperature based on the conclusions of cube model analysis [294] and the MD simulations presented in Chapter 7. This yields a mean and standard deviation of 0.236 and 0.026 respectively. The range of values for the surface tension of iron is discussed

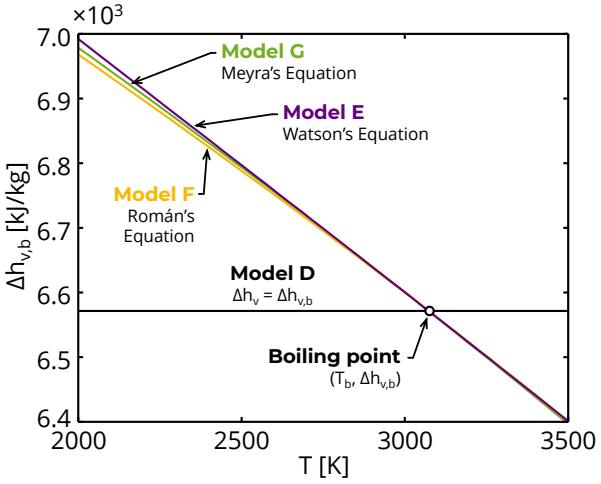

Figure 9.2 The temperature dependence of the heat of vaporization for iron based on the equations proposed by Watson [202] (Model E), Román et al. [204] (Model F), and Meyra et al. [205] (Model G) using the boiling point as a reference.

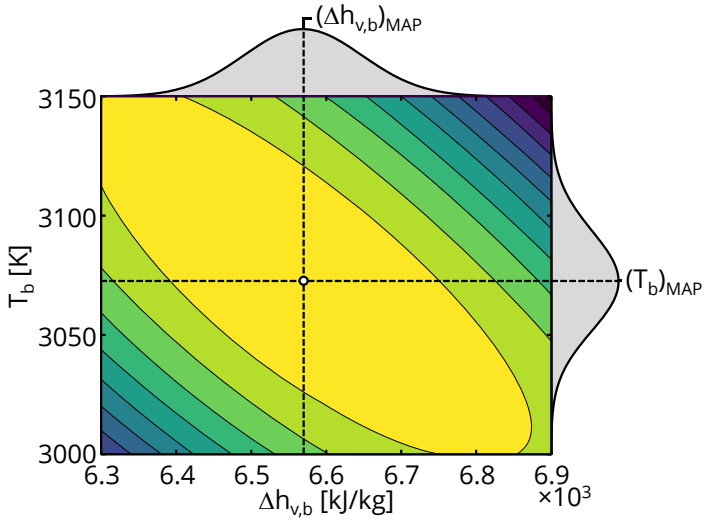

Figure 9.3 Log contours of the posterior distribution of $\Delta h_{v,b}$ and T_b inferred from vapor pressure data. The marginalized distributions of $\Delta h_{v,b}$ and T_b are shown on the right and top axes respectively. The MAP is indicated by the white circle.

extensively in Keene et al. [394], and the recommended mean and standard deviation are adopted directly from that work.

9.3 Bayesian model selection

Bayesian model selection acts to extend the Bayesian framework introduced in Section 3.3 to determine the optimal model of those presented in the preceding sections. Inherent in Bayes' equation, Eq. (3.34), is a model, M_i, that is used to evaluate $\mathbf{b}^{\text{mod}}$ for the parameter set $\boldsymbol{\phi}_i$. This underlying model dependency can be explicitly incorporated into Eq. (3.24) by conditioning every term on the model

$$p\left(\boldsymbol{\phi}_i \,|\, \mathbf{b}, M_i\right) = \frac{p\left(\mathbf{b} \,|\, \boldsymbol{\phi}_i, M_i\right) p_{\text{pr}}\left(\boldsymbol{\phi}_i \,|\, M_i\right)}{E_i}, \tag{9.10}$$

where $\boldsymbol{\phi}_i$ refers to the parameter set specific to model M_i and the evidence, $E_i = p(\mathbf{b}|M_i)$, is the probability of observing the data $\mathbf{b}$ given the model M_i and involves integration over $\boldsymbol{\phi}_i$ (see Eq. (3.35)). Model adequacy is gauged by phrasing a Bayesian inference problem in terms of an optimal model rather than an optimal value for the QoI. The solution to this problem is then the model posterior,

$$p\left(M_i \,|\, \mathbf{b}\right) = \frac{p\left(\mathbf{b} \,|\, M_i\right) p_{\text{pr}}\left(M_i\right)}{\sum_i p\left(\mathbf{b} \,|\, M_i\right) p_{\text{pr}}\left(M_i\right)} \propto E_i \, p_{\text{pr}}\left(M_i\right), \tag{9.11}$$

where $p(\mathbf{b}|M_i)$ refers to the model likelihood, which describes the probability density of observing the data based on the assumptions encoded in the model, and the denominator normalizes the results based on the set of all possible models. It is important to note that the model likelihood in this problem corresponds to the evidence in Eq. (9.10). If no model is preferred a priori, Eq. (9.11) reduces to

$$p\left(M_i|\mathbf{b}\right) \propto E_i \,. \tag{9.12}$$

Generally, this problem is rephrased in relative terms to remove the proportionality and to avoid evaluating the denominator in (9.11), so that

$$B_{ij} = \frac{p\left(\mathbf{b}|M_i\right)}{p\left(\mathbf{b}|M_j\right)} = \frac{E_i}{E_j} \,, \tag{9.13}$$

where the Bayes factor, B_{ij}, is the odds that M_i produced the data over M_j. The model selection problem then becomes a matter of comparing the evidence for two competing models. Thus, while the evidence need not be explicitly calculated when estimating the posterior after invoking Laplace's approximation (see Section 3.3.3) or sampling methods, it plays a critical role in model selection.

The evidence can be computed different ways [439], most traditionally by carrying out the integral in Eq. (3.35) using quadrature or Monte Carlo sampling. A different approach is taken here. Equation (9.10) is rearranged as

$$E_i = \frac{p\left(\mathbf{b}|\boldsymbol{\phi}_i, M_i\right) p_{pr}\left(\boldsymbol{\phi}_i|M_i\right)}{p\left(\boldsymbol{\phi}_i|\mathbf{b}, M_i\right)} \,. \tag{9.14}$$

After invoking Laplace's approximation to linearize the problem (see Section 3.3.3), each of the probabilities on the right-hand side of Eq. (9.14) is known (as per Section 3.3) and the expression can be evaluated directly. It is noted that, after invoking Laplace's approximation, the numerator and denominator have the same functional dependence on $\boldsymbol{\phi}_i$. Accordingly, the evidence is constant, irrespective of the choice of $\boldsymbol{\phi}_i$, and can be computed directly for any $\boldsymbol{\phi}_i$. The evidence is chosen to be evaluated about the MAP estimate, which simplifies the expression of the posterior pdf. For large data sets, the exponential of the negative of the norm in the likelihood will be nearly zero, which can introduce numerical instabilities when evaluating the ratio of evidence functions. For this reason, model selection is often phrased in terms of the logarithm of the evidence, which can be decomposed into three key components

$$\ln\left(E_i\right)=C_i+F_{b,i}+F_{pr,i}\,, \tag{9.15}$$

where

$$C_i=\frac{1}{2}\ln\left(\left|2\pi\cdot\boldsymbol{\Sigma}_i^{po}\right|\right)-\frac{1}{2}\ln\left(\left|2\pi\cdot\boldsymbol{\Sigma}_i^{pr}\right|\right)-\frac{1}{2}\ln\left(\left|2\pi\cdot\boldsymbol{\Sigma}^{b}\right|\right), \tag{9.16}$$

is the product of the normalizing factors of the various distributions, called the *measurement credence*[440];

$$F_{b,i}=-\frac{1}{2}\left\|\mathbf{L}^{b}\left[\mathbf{b}_i^{mod}\left(\boldsymbol{\phi}_i^{MAP}\right)-\mathbf{b}^{meas}\right]^{T}\right\|_2^2, \tag{9.17}$$

is the fit of the model to the data evaluated at the MAP; and

$$F_{pr,i}=-\frac{1}{2}\left\|\mathbf{L}_i^{pr}\left(\boldsymbol{\phi}_i^{MAP}-\boldsymbol{\phi}_i^{0}\right)\right\|_2^2, \tag{9.18}$$

is the fit of the MAP to the prior [440]. It should also be noted that the fit and MAP will change with each realization of random noise, making them inherently random variables. Accordingly, it is best to repeat the inference on different sets of $\mathbf{b}^{meas}$ (resulting from multiple measurements of shots) to develop a distribution for *E*. In the absence of multiple shots, robust conclusions about the results may not be possible.

Before continuing, a note is made on the definition of the *measurement credence*. The measurement credence contains the determinants that normalize the distributions, ensuring that they follow the Law of Total Probability. Large determinants occur when the distributions are diffuse, that is when the distributions describe highly uncertain properties, contain less information, or have a higher number of parameters (reflected in the dimension of $\boldsymbol{\phi}_i$ or degrees-of-freedom of a given model). This lends itself to a simple interpretation in the context of the likelihood and prior, where larger determinants resulting from diffuse distributions will cause the evidence to be smaller and the model less favorable. Interpretation of the determinant of the posterior is less intuitive, particularly in that the posterior covariance inherently depends on the covariance of the likelihood and prior and the form of the model. To understand this relationship, consider a special case resulting from several simplifications to the problem. First, consider the case of a linear model. Using the definition of the posterior covariance, Eq. (3.38), the measurement credence can then be written as

$$C=-\frac{1}{2}\ln\left(\left|\frac{1}{2\pi}\mathbf{A}^{T}\left(\boldsymbol{\Sigma}^{b}\right)^{-1}\mathbf{A}+\frac{1}{2\pi}\left(\boldsymbol{\Sigma}^{pr}\right)^{-1}\right|\right)-\frac{1}{2}\ln\left(\left|2\pi\cdot\boldsymbol{\Sigma}^{b}\right|\right)-\frac{1}{2}\ln\left(\left|2\pi\cdot\boldsymbol{\Sigma}^{pr}\right|\right). \tag{9.19}$$

Now, also consider the simple case of a single QoI, so that $\boldsymbol{\Sigma}^{pr}=\sigma_{pr}$. It can then be shown that

$$C = -\frac{1}{2}\ln\left[\left|2\pi\cdot\boldsymbol{\Sigma}^{\mathrm{b}}\right|\sigma_{\mathrm{pr}}\mathbf{A}^{\mathrm{T}}\left(\boldsymbol{\Sigma}^{\mathrm{b}}\right)^{-1}\mathbf{A}+\left|2\pi\cdot\boldsymbol{\Sigma}^{\mathrm{b}}\right|\right]. \tag{9.20}$$

Finally, consider the trivial case of having a single data point, so that $\boldsymbol{\Sigma}^{\mathrm{b}} = \sigma_{\mathrm{b}}$, which further simplifies the expression to

$$C = -\frac{1}{2}\ln\left[2\pi\sigma_{\mathrm{pr}}A^2 + 2\pi\sigma_{\mathrm{b}}\right]. \tag{9.21}$$

This simple case demonstrates how the width of the likelihood and prior remains a negative term in the credence and will, overall, penalize models with highly uncertain parameters. The inclusion of A in this expression also indicates the significance of the model itself in determining the credence. Interpretations of the more general linear case, Eq. (9.19), are less immediate, though similar principles will apply.

Proceeding, the Bayes factor, Eq. (9.13), can also be separated into its components, which, when written in terms of the natural logarithm of the Bayes factor, are expressed as

$$\ln\left(B_{\mathrm{ij}}\right) = \underbrace{\left(C_{\mathrm{i}} - C_{\mathrm{j}}\right)}_{\substack{\text{Relative}\\ \text{measurement}\\ \text{credence, } \Delta C_{\mathrm{ij}}}} + \underbrace{\left(F_{\mathrm{b,i}} - F_{\mathrm{b,j}}\right)}_{\substack{\text{Relative fit}\\ \text{to the data}}} + \underbrace{\left(F_{\mathrm{pr,i}} - F_{\mathrm{pr,j}}\right)}_{\substack{\text{Relative fit}\\ \text{to the prior}}} = \Delta C_{\mathrm{ij}} + \Delta F_{\mathrm{ij}}\,. \tag{9.22}$$

For ease of discussion, $\ln(B_{\mathrm{ij}})$ is written in terms of two competing quantities. First, $\Delta C_{\mathrm{ij}} = C_{\mathrm{i}} - C_{\mathrm{j}}$ is the relative measurement credence. This term roughly quantifies the relative uncertainties contained in the models and will penalize models based on the number of degrees of freedom. Second, $\Delta F_{\mathrm{ij}} = (F_{\mathrm{b,i}} - F_{\mathrm{b,j}}) + (F_{\mathrm{pr,i}} - F_{\mathrm{pr,j}})$ is the relative fit, describing both how close the MAP is to the prior and $\mathbf{b}^{\mathrm{mod}}(\boldsymbol{\phi}_{\mathrm{i}}^{\mathrm{MAP}})$ is to the data. The preferred model will best navigate the trade-off between these two quantities, forming a basis for discussion in subsequent sections. As with the fit and measurement credence, the Bayes factor is also a random variable.

9.4 Case studies on simulated data

To demonstrate this approach, a set of candidate models, $\{M_{\mathrm{i}}\}$, is constructed. The set of models used to interpret and generate synthetic data are summarized in Table 9.2, categorized according to three case studies. The first two case studies are devised to demonstrate the attributes and effectiveness of Bayesian model selection, while the third is designed to infer variation of Δh_{v} with temperature based on TiRe-LII data.

In all cases, data is simulated for iron nanoparticles in argon under conditions identical to the experiments described in Chapter 8 and Refs. [45,112]. In each scenario, one model is chosen as a source model to generate synthetic nanoparticle temperature histories. The source model parameters are taken at the center or mean of the

Table 9.2 Candidate models used in generating simulated data and for inference throughout the current work. Case study refers to where the models are used in Section 9.4.

Case study	Model	Evaporation submodel	Heat of vaporization submodel	Density submodel	Specific heat capacity submodel
1	A	Yes	Watson [202]	$\rho=\rho_0+\rho_1 T$, mean(ρ_0)=0	$c_p=c_{p,0}+\kappa T$, mean($c_{p,0}$)=0
1	B	Yes	Watson [202]	$\rho=\rho_0$	$c_p=c_{p,0}$
2	C	No	-	Desai [387]	Desai [387]
3	D	Yes	Constant	Desai [387]	Desai [387]
2, 3	E	Yes	Watson [202]	Desai [387]	Desai [387]
3	F	Yes	Román et al. [204]	Desai [387]	Desai [387]
3	G	Yes	Meyra et al. [205]	Desai [387]	Desai [387]

priors (for example, a nanoparticle size of 30 nm is used). The spectral incandescence data is corrupted with measurement noise according to the general measurement error model presented in Chapter 4 (and Refs. [237,242]). For simplicity, measurement error is added directly to the temperature decays rather than to incandescence traces. Due to correlation between subsequent timesteps in the measured signals, an exponential decay is included in the covariance matrix as one moves away from the diagonal, with a cutoff of 11 timesteps away from the current timestep (for computational efficiency). Temperature decays are generated by random sampling the measurement error from a multivariate normal distribution with this covariance. A simulated temperature decay following this technique, using Model E as a source model, is shown in Figure 9.4 for reference. Also shown is the model fit using Model E as the interpretive model. In each case, this is repeated 250 times to estimate the distribution of the Bayes factor.

9.4.1 Case 1: Considering constant density and specific heat capacity

This first case study compares two models, A and B, where A is more complex. This case is conceived to verify that model selection will choose the simpler model when the complex model offers only a modest improvement to goodness-of-fit. The difference between the two models lies in their treatment of density and specific heat capacity. Model A assumes both parameters are linearly-dependent on temperature, whereas Model B considers these parameters to be constant. Model A is designed so that Model B is nested, that is, it can be completely described by Model A, a requirement for traditional likelihood-ratio tests [441]. This manifests in that the density and specific heat capacity in Model A have priors that prefer no slope with temperature but allow for a linear temperature dependence should the data support it.

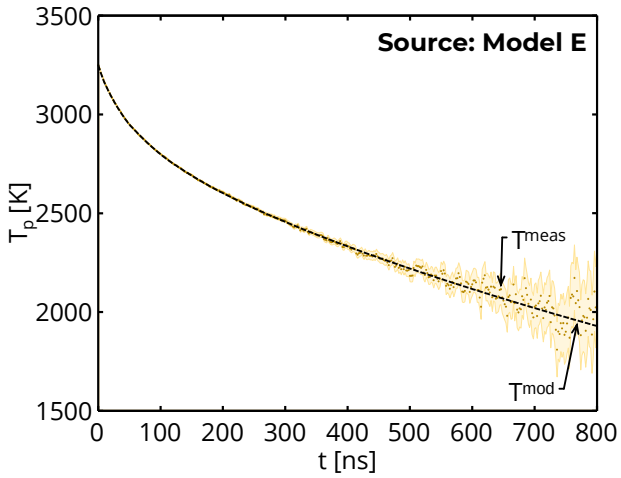

Figure 9.4 A single realization of a simulated average temperature decay based on the memasurement error model given in Chapter 4. Error bounds about the temperature represent one standard deviation of the mean.

The more complex Model A is used as the source model and Thompson Tau outlier removal [403] is performed on the data to eliminate cases that did not properly converge. Outliers amounted to fewer than 1% of the cases considered. Table 9.3 reports the mean and two standard deviation of 250 samples of the natural logarithm of the Bayes factor, $\ln(B_{BA})$; relative fit, ΔF_{BA}; and relative measurement credence, ΔC_{BA}. Model A is chosen as the denominator so that negative values indicate cases in which Model A is more probable given the data and chosen parameter set.

The error bounds reported in Table 9.3 show that the distribution of relative fits encompasses zero. This indicates, as expected, that both models can reproduce the data nearly equally well. The mean of the relative fit is slightly less than zero, suggesting a slight preference for the more complex Model A, where the increased degrees-of-freedom allows for a slightly better fit to the data. The relative measurement credence, by contrast, shows a strong preference for Model B, indicating that the data does not contain sufficient information to inform

Table 9.3 The mean of the natural logarithm of the Bayes factor, $\ln(B_{BA})$; relative fit, ΔF_{BA}; and relative measurement credence, ΔC_{BA}, for models A and B over multiple realizations. Model A is used as the source model throughout and is in the denominator during calculation of the Bayes and other relative factors. Error bounds correspond to two standard deviations of multiple realizations of each quantity.

Models compared	Relative measurement credence, ΔC	Relative fit, ΔF	Logarithm of Bayes factor, ln(B)
B, A	7.91 ±1.26	-0.29 ±0.63	7.62 ±1.38

on the additional model parameters in Model A. In combining these quantities to calculate a Bayes factor, the strong preference for Model B coming from the relative measurement credence overwhelms the slight preference for Model A coming from the relative fit. The conclusion is that the simpler Model B is more effective in deriving information from the data.

9.4.2 Case 2: Considering the effect of evaporation

This second case study contains a set of two models (C and E) and is intended to demonstrate the importance of the evaporation submodel. The peak nanoparticle temperature obtained through laser-heating, which acts as an initial condition to Eq. (9.1), is varied to reflect the range of cooling curves that can be realized by changing the laser fluence. Model C excludes the evaporation model, greatly reducing the number of input parameters, but limiting its ability to reconstruct TiRe-LII data at high temperatures. Model E includes evaporation.

Figure 9.5 shows trends in the mean of 250 realizations of the natural logarithm of the Bayes factor, $\ln(B_{CE})$; relative fit, ΔF_{CE}; and relative measurement credence, ΔC_{CE}. Model E is chosen as the denominator so that negative values indicate cases in which Model E is more probable given the data and chosen parameter set. In all cases, the sum of the $\langle \Delta F \rangle$ and $\langle \Delta C \rangle$ curves is approximately equal to the value of the $\langle \ln(B) \rangle$ curve. At low peak temperatures, where the evaporation term is negligible, all three quantities are close to zero, indicating no preference between the two models. This result is not necessarily intuitive, as one might expect that the simpler model that excludes evaporation to be preferred when the fit is the same and requires some additional discussion.

This result is explained by the fact that Bayesian model selection is only affected by parameters that influence the measurement model. To show this, $\boldsymbol{\phi}$ can be decomposed into a vector of parameters related to the sensible energy and conduction submodel ($\mathbf{c}$) and a vector of evaporation submodel parameters ($\mathbf{e}$),

$$\boldsymbol{\phi} = \left[\mathbf{c}, \mathbf{e} \right]^{\mathrm{T}}. \tag{9.23}$$

Assume these variables are independent, as is the case in this chapter, such that the prior covariance is given by

$$\boldsymbol{\Sigma}^{\mathrm{pr}} = \mathrm{diag}\left(\boldsymbol{\Sigma}_{\mathrm{c}}^{\mathrm{pr}}, \boldsymbol{\Sigma}_{\mathrm{e}}^{\mathrm{pr}} \right). \tag{9.24}$$

where diag(·) indicates a block-diagonal matrix with zeros in the off-diagonal blocks, and $\boldsymbol{\Sigma}_{\mathrm{c}}^{\mathrm{pr}}$ and $\boldsymbol{\Sigma}_{\mathrm{e}}^{\mathrm{pr}}$ are prior covariance matrices for the parameter subsets. Using Laplace's approximation (see Section 3.3.3), the posterior covariance can now be expressed as

$$\left(\boldsymbol{\Sigma}^{\text{po}}\right)^{-1}=\mathbf{L}^{\text{po}}\left(\mathbf{L}^{\text{po}}\right)^{\text{T}}\simeq\left(\mathbb{J}_{\text{c}},\mathbb{J}_{\text{e}}\right)^{\text{T}}\left(\boldsymbol{\Sigma}^{\text{b}}\right)^{-1}\left(\mathbb{J}_{\text{c}},\mathbb{J}_{\text{e}}\right)+\text{diag}\left[\left(\boldsymbol{\Sigma}_{\text{c}}^{\text{pr}}\right)^{-1},\left(\boldsymbol{\Sigma}_{\text{e}}^{\text{pr}}\right)^{-1}\right]. \tag{9.25}$$

where $\mathbb{J}_{\text{i}}$ refers to the Jacobian of the i^{th} parameter subset. When the measurement model is insensitive to the evaporation model, as in the current example, the Jacobian for these terms goes to zero, that is $\mathbb{J}_{\text{e}} = 0$. As a consequence, the only information about the parameters comes from the information provided in the prior.

This result has two implications for the Bayes factor. First, as the Jacobian is zero for parameters to which a model is insensitive, the data fit will be unaffected by changes in this parameter, and the MAP will always be at the center of the prior (which then acts as the only source of information). Consequently, the fit will be identical for any model that is insensitive to these parameters, and the relative fit will be zero. Second, since the posterior uncertainties in these parameters will also be the same as those specified in the prior (again a consequence of the prior being the only source of information), the measurement credence is also identical for both models, and the relative measurement credence will also be zero. The final conclusion then is that neither model is more probable. In the present case, both models are either insensitive to or exclude the evaporation model, resulting in neither model being preferred.

Figure 9.5 shows that as the peak temperature increases to the point that evaporation contributes to the cooling, the relative fit quickly decreases. This is because Model C cannot account for the evaporative cooling

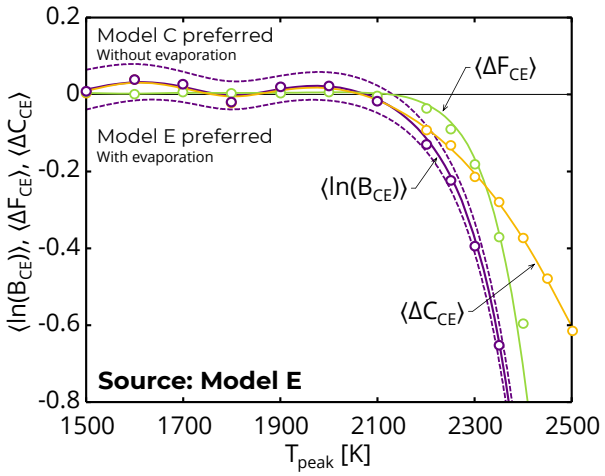

Figure 9.5 Trends in the natural logarithm of the Bayes factor, $\ln(B_{\text{CE}})$; relative fit, ΔF_{CE}; and relative measurement credence, ΔC_{CE}, with peak temperature for data simulated using Model E. Model C does not include the evaporation submodel; Model E includes the evaporation submodel. Values below zero represent cases where Model E is more probable and vice versa. Dashed lines correspond to plus and minus two standard deviation of the realizations of $\ln(B_{\text{CE}})$.

predicted by Model E, which is used to generate the data. This lack of fit also manifests in widening uncertainties in posterior estimates and a small decline in the relative measurement credence with increasing peak temperature. This results in an even more rapidly decreasing Bayes factor, indicating a strong preference towards Model E for peak temperatures beyond 2200 K.

9.4.3 Case 3: Considering the temperature dependence of the heat of vaporization

This third case study is designed to investigate the validity of expressions for predicting the temperature dependence of the latent heat of vaporization, including a constant value (Model D), Watson's equation (Model E), Román's equation (Model F), and Meyra's equation (Model G). Again, the peak nanoparticle temperature is varied to identify how these equations perform in different temperature regimes.

Figure 9.6 shows trends in the mean of 250 realizations of the natural logarithm of the Bayes factor, $\ln(B_{BA})$; relative fit, ΔF; and relative measurement credence, ΔC, with peak temperature, using Model E (containing Watson's equation) as the source model and in the denominator (so that negative values correspond to a preference for Watson's equation). There is no clear preference when the cooling rate is unaffected by evaporation (for peak temperatures less than 2200 K, based on Figure 9.5), as per the discussion in Section 9.4.2 above. Even as the peak temperature exceeds this value, the logarithm of the Bayes factor remains zero until the peak temperature exceeds 2800 K, indicating that the temperature decay is insensitive to the temperature dependence of Δh_v up until that point. Other trends in Figure 9.6 are considered on a case-by-case basis.

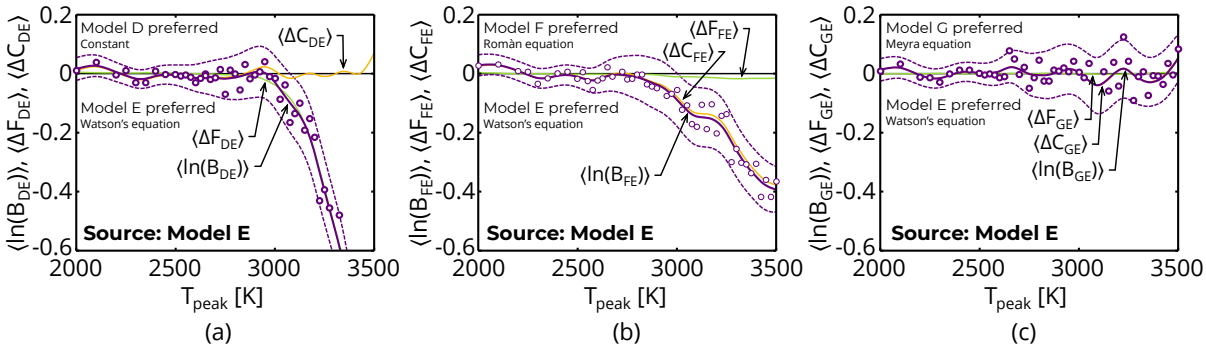

Figure 9.6 Trends in the natural logarithm of the Bayes factor, $\ln(B)$; relative fit, ΔF; and relative measurement credence, ΔC, with peak temperature for data simulated using Model E, which uses Watson's equation. Model D considers a constant Δh_v, Model E uses Watson's equation, Model F uses the expression from Román et al. [204], and Model G uses the expression from Meyra et al. [205]. Values below zero represent cases where Model E is more probable. Dashed lines correspond to plus and minus two standard deviation of the realizations of $\ln(B)$.

Figure 9.6a examines the difference between Watson's equation (Model E) and a constant Δh_v (Model D). The trend with increasing peak temperature shares many of the characteristics to the case considered in Section 9.4.3 and Figure 9.5. As the model is generated with a temperature-varying heat of vaporization, a model that excludes this effect cannot describe the data. Consequently, the relative fit quickly declines as peak temperatures rise beyond 2800 K, indicating a strong preference for the source model.

Figure 9.6b examines the difference between Watson's equation (Model E) and Román's equation [204] (Model F). Both equations predict similar variation in the heat of vaporization (see Figure 9.2), with Román's equation having an additional degree of freedom. This leads to an unsurprising result: Román's equation can equally describe data produced using Watson's equation and the relative fit is effectively zero across the entire domain. However, due to the additional degree of freedom, the relative measurement credence declines as the temperature increases beyond 2800 K, since this parameter is unnecessary to describe the data. This leads to a declining Bayes factor that indicates a preference for the simpler Watson's equation. This is in stark contrast to the case considered above in Figure 9.6a, where the decision is entirely dependent on the fit.

Figure 9.6c examines the difference between Watson's equation (Model E) and Meyra's equation [205] (Model G). Both expressions have the same degrees-of-freedom, and only differ by the exponent. Figure 9.6c indicates no preference between these two models with both the relative fit and relative measurement credence being zero across the entire domain. The former is a result of the expressions sharing the same number of degrees-of-freedom and the latter is a result of similarities in the temperature dependence of the heat of vaporization predicted by both expressions (see Figure 9.2).

9.5 Determining an expression for the latent heat of vaporization from experimental data

Consider now applying the same methodology to the experimental data from Chapter 8, where the true underlying physics are unknown. As the Bayes factor changes between realizations of the noise, an accurate picture of the Bayes factor requires several noisy signals. To realize the distribution of the Bayes factor, the original data set is resampled, randomly selecting 225 shots from the original 250 shots. These signals are then randomly subdivided into nine groups of 25, which are averaged and converted to pyrometric temperatures. Finally, statistics on the noise in the temperature decays, including the likelihood covariance and mean, are computed on these nine temperature decays. A sample of a temperature decay following this procedure is shown in Figure 9.7. The peak temperatures are consistently around 3350 K.

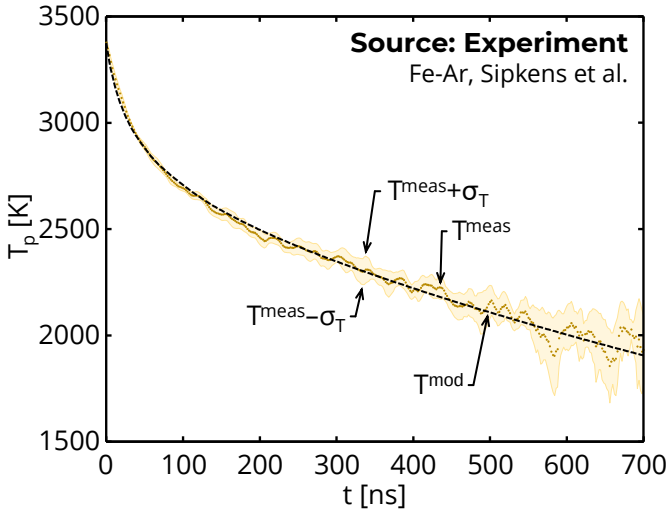

Figure 9.7 A single realization of an experimental average temperature decay for iron nanoparticles in an argon buffer gas as per Chapter 8 and Sipkens et al. [45]. Error bounds about the temperature represent one standard deviation of the mean.

Now consider the series of models considered for Case 3 above, where the data is interpreted with models D through G. Priors on the parameters are the same as those stated in Table 9.1 for the proposed models, except that the prior for the nanoparticle diameter is centered on 33 nm (based on the analysis in Chapter 8). The resultant averages of the natural logarithm of the Bayes factor, $\ln(B)$; relative fit, ΔF; and relative measurement credence, ΔC, are indicated in Table 9.4. Unlike Section 9.4.3, Model F (containing Román's equation) is placed in the denominator. Also, unlike Table 9.3, error bounds here are stated as two standard deviations of the mean (rather than just of the unaveraged parameter). In all cases, the distribution of the Bayes factor is considerably wider than in the simulated case, covering several orders of magnitude, while the relative measurement credence distributions are very similar.

Table 9.4 The mean of the natural logarithm of the natural logarithm of the Bayes factor, $\ln(B)$; relative fit, ΔF; and relative measurement credence, ΔC, for models D through G using experimental data from iron nanoparticles in argon from Chapter 8. In all cases, Model F, which uses Romàn's equation [204], is preferred when quantities are negative. Error bounds correspond to two standard deviations of the mean.

Models compared	Relative measurement credence, ΔC	Relative fit, ΔF	Logarithm of Bayes factor, ln(B)
D, F	0.058 ±0.086	-6.68 ±0.55	-6.63 ±0.53
E, F	0.047 ±0.079	-0.888 ±0.395	-0.840 ±0.388
G, F	0.013 ± 0.093	-0.828 ±0.445	-0.815 ±0.432

Table 9.4 indicates the difference between holding the heat of vaporization constant with temperature and using Román's equation. The relative fit dominates the Bayes factor, indicating a strong preference towards a temperature-dependent heat of vaporization. As such, while one may be inclined to use a constant latent heat of vaporization based on the principle of model parsimony, this result shows that temperature-dependence of Δh_v is statistically important and should be included in TiRe-LII models.

Table 9.4 also compares Watson's equation to Román's equation. Román's equation is preferred, based entirely on improvements in the relative fit. This indicates that the experimental data contains sufficient information to distinguish between these expressions and to support the additional degree-of-freedom in Román's model. As implementation of Román's equation is straightforward, it is recommended that this expression be used in future TiRe-LII analyses and in any other applications that feature a similar range of temperatures. Our observation is consistent with Velasco et al. [408], who suggested that Román's equation is more suitable for describing the heat of vaporization of metals and metalloids.

Finally, Table 9.4 compares Meyra's and Román's equation. These results are very similar to the comparison of Watson's equation and Román's equation, with Román's equation being preferred based on similar improvements to the relative fit. This result is unsurprising given the similarity between Watson's and Meyra's equations.

Phrasing all of these comparisons in terms of Model F allows us to conclude that Román's equation outperforms all of the other proposed expressions and is thus the most probable expression for defining the temperature-dependence of Δh_v for molten iron over a wide range of temperatures. The average MAP estimates for the Román model parameters calculated during the model selection procedure are included in Table 9.5,

Table 9.5 Average maximum a posteriori (MAP) estimates and credibility intervals (corresponding to two standard deviations of the samples) of the parameters in Román's equation calculated during the model selection procedure.

Parameter	Symbol	Value	Credibility bounds
Heat of vaporization at boiling point [kJ/kg]	$\Delta h_{v,ref}=\Delta h_{v,b}$	6367	±113
Boiling temperature [K]	$T_{ref}=T_b$	3073	±4
Critical temperature [K]	T_{cr}	9328	±15
Critical exponent	n	0.380	±0.002
Román parameter	β_R	0.479	±0.108

indicating a preference for a relatively high value of β_R that improves the fit to the TiRe-LII data. Moreover, these results demonstrate: (i) the ability of TiRe-LII to inform on nanoscale physics and (ii) indicates experimental support for the enhancements contained in Román's equation, specifically adding a degree-of-freedom describing the slope in the latent heat of vaporization at the reference temperature.

9.6 Conclusions

Model complexity is one of the largest problems currently facing the LII community and has led to TiRe-LII models being susceptible to *tuning*. In response, this chapter describes a Bayesian model selection procedure that can be applied to TiRe-LII analyses to ensure that uncertainties are considered during the development of novel models. Moreover, this chapter addresses the fact that little experimental data is available for metals at high temperatures, increasing dissention in the models available for TiRe-LII analysis in this context.

Bayesian model selection is first outlined, and three key components that make up the Bayes factor are identified: (i) the relative measurement credence; (ii) the relative fit between the modeled and measured data; and (iii) the consistency of the inferred parameters with prior information. To implement Bayesian model selection, priors are defined that quantify the state-of-knowledge of both the quantities-of-interest and model parameters before the measurement. The limitations and capabilities of Bayesian model selection are demonstrated by applying the technique to synthetic data across a range of case studies. Bayesian model selection is shown to prefer the simpler model in the absence of sufficient contradictory information in the data. It is also demonstrated that the technique correctly identifies the source model used to generate the data in the cases where additional degrees-of-freedom are unnecessary, such as those in Román's equation, or when the candidate model is incapable of reproducing the data.

Finally, Bayesian model selection is applied to experimental TiRe-LII data collected from iron nanoparticles in an argon buffer gas [45]. The distribution of the Bayes factor is shown, with fits varying significantly depending on the realization of signal noise. Consequently, this procedure should be repeated on multiple measurements to obtain robust results. The results support Román's equation as the most realistic form for predicting the latent heat of vaporization for iron in the set of expressions considered. Further, four significant conclusions can be made. First, TiRe-LII has been identified as a tool for fundamental scientific inquiry that can elucidate fundamental thermophysical properties across a wide range of temperatures. Second, Román's equation is statistically distinct in describing the temperature dependence of the latent heat of vaporization of iron and should be used in future analyses. Third, the principle put forward by Román et al. [204], allowing for

flexibility in the slope of the latent heat of vaporization at the reference temperature, is supported experimentally over a wide temperature range. Finally, this chapter has demonstrated how Bayesian model selection can be used as a statistically-robust tool in model development and can settle model disputes that are of detriment to the progress of TiRe-LII as a technology.

Chapter 10
Conclusions and future work

Time-resolved laser-induced incandescence (TiRe-LII) is a powerful diagnostic for characterizing aerosolized nanoparticles. This thesis explores several facets of the TiRe-LII measurement technique and presents novel approaches of extracting information from signals that improve our overall understanding of laser-induced emission.

10.1 Summary and key findings

This thesis begins with a discussion of the basic form of the spectroscopic and heat transfer submodels widely implemented throughout the TiRe-LII literature. The spectroscopic submodel defines how the nanoparticles heat up during the laser pulse and how they emit spectral incandescence. For the sake of the current work, the spectral absorption cross-section is calculated using the Rayleigh approximation, which applies when the wavelength of light interacting with the nanoparticle is significantly larger than the nanoparticle diameter. The Rayleigh approximation itself models absorption and emission from the nanoparticles as a volumetric phenomenon and, through extension via Rayleigh-Debye-Gans Fractal Aggregate theory, simplifies the interaction with aggregates as the superposition of independent primary particles. The spectroscopic submodel also includes Planck's Law, which relates the nanoparticle temperature to the emitted blackbody spectral intensity. The temporal evolution of the nanoparticle temperature is governed by a heat transfer submodel that includes terms for nanoparticle heating due to laser absorption and cooling due to conduction with the surrounding gas and vaporization of the nanoparticle material. Both conduction and evaporation are assumed to occur in the free molecular regime, in which that gas or vapor molecules travel ballistically between the nanoparticle surface and the equilibrium gas without undergoing intermolecular collisions close to the nanoparticle surface.

These spectroscopic and heat transfer submodels define the measurement model used in TiRe-LII analyses to relate the quantities-of-interest (QoI) (which can include the nanoparticle size, volume fraction of particulate

in the aerosol, thermal accommodation coefficient, and other thermophysical properties) to the measured time-resolved spectral incandescence. Inferring the QoI from the observed data amounts to inverting the spectroscopic and heat transfer submodels, often in sequence by applying two-color pyrometry to invert the spectroscopic submodel and using a least-squares analysis to invert the heat transfer submodel. The present work uses the Bayesian approach of model inversion, first applied to TiRe-LII by Sipkens et al. [48]. The Bayesian framework treats all quantities, including the data, QoI, and model parameters, as random variables that obey distributions. Under certain circumstances this treatment amounts to weighted nonlinear least-squares regression. The Bayesian approach also allows for an intuitive way to propagate uncertainties through the inversion process and can be used to incorporate prior information to reduce these uncertainties. Accordingly, Chapter 3 discusses inversion and provides the necessary background for the Bayesian approach that is used throughout the remainder of this thesis.

Chapter 4 proposes a new technique for analyzing TiRe-LII signals, with a focus on the information contained in the measurement noise or error in observed signals. LII measurements are governed by a Poisson-Gaussian noise model, which is a combination of photonic shot noise arising from the quantized nature of light (which obeys a Poisson distribution) and Gaussian noise sources that include thermal noise. In practice, however, practitioners often average multiple laser shots to improve the signal-to-noise ratio. This treatment introduces additional sources of measurement error that both corrupt the signals and provide information about the measurement device or the observed process. Chapter 4 extends the traditional Poisson-Gaussian noise model to a generalized measurement error model that incorporates these shot-to-shot variations. It is shown that Gaussian variations in the volume fraction of particulate in the aerosol will transform the relationship between the mean signal and the variance of the signal from a linear relationship, which applies for simple Poisson-Gaussian noise, to a quadratic one. Furthermore, the coefficient on the quadratic is shown to contain information about the underlying variability of the measured process. This information is useful for characterizing the stationarity of a turbulent process or diagnosing problems in an experimental setup. The validity of this model is demonstrated on experimental data collected from soot and engineered nanoparticles, with more variable measurements demonstrating the expected quadratic relationship. The generalized measurement error model also provides a basis for realistically corrupting simulated TiRe-LII signals, an approach taken to generate simulated data in Chapter 9.

Chapter 5 proceeds with a discussion of fluence curves, a tool commonly used by TiRe-LII practitioners to further characterize nanoparticle systems and diagnose measurement problems. The curves elucidate the relationship between the peak temperature (or incandescence) and the laser fluence. They are characterized by a sharp rise in the peak temperature at lower fluences, corresponding to an increase in the sensible energy of nanoparticles, followed by a *plateau* regime as vaporization or latent energy effects become significant. While fluence curve analyses are a common feature of individual LII studies reported in the literature, Chapter 5 presents one of the first systematic comparisons of fluence curves obtained from different aerosols under different measurement conditions. To do so, simplifications are applied to the TiRe-LII heat transfer model to derive closed form expressions for the low and plateau fluence regimes. The intersection of these two expressions provides a simple method of determining a transition fluence, at which the *plateau* regime is expected to begin. This allows for the formal definition of three fluence regimes: (i) the low fluence regime, where vaporization is negligible and an increase in laser fluence corresponds directly to an increase in nanoparticle temperature and sensible energy; (ii) the moderate fluence regime, where there is significant vaporization but not enough to balance the laser input to the nanoparticle during the laser pulse; and (iii) the high or plateau fluence regime, where vaporization will balance the laser input to the nanoparticle during the laser pulse. Furthermore, normalizing the fluence and peak temperature by the transition fluence and peak temperature lends itself to a natural set of dimensionless parameters that act to collapse existing fluence curves onto a single curve for comparison. The analysis reveals that much of the existing fluence curve data published in the literature, including measurements carried out on non-carbonaceous nanoparticles [442], can be collapsed onto a single curve. Furthermore, it is noted that remaining discrepancies flag potential issues that could influence data interpretation.

Chapter 6 presents a novel approach for analyzing TiRe-LII data using the intensity scaling factor (ISF). Most practitioners derive an effective nanoparticle temperature through ratio pyrometry on the spectral incandescence measurements at two detection wavelengths, which bypasses calculation of the scaling factor used to convert the measured signal to nanoparticle incandescence. This approach throws away valuable information about the aerosol, which is encoded into the temporal variation of the scaling parameter (or the so-called *apparent volume fraction* [145,176]). Chapter 6 formally defines this parameter as the intensity scaling factor (ISF) and examines five effects that result in temporal variations in this quantity. These effects include: (i) vaporization, which results in a reduction in the volume fraction of particulate in the aerosol; (ii) annealing, where the internal structure of the nanoparticles changes during laser heating, further influencing the emissive properties of the

nanoparticles; (iii) polydispersity, where the distribution of nanoparticles sizes results in large nanoparticles dominating aerosol emission at later times; (iv) background luminescence, an additive effect resulting from non-LII emission along the line-of-sight of the detector, and (v) the detector system time response, which smooths over sharp features in the observed signals. Combining these various effects allows practitioners to, for the first time, explain many of the temporal features observed in ISF curves. Moreover, variations in the ISF can act as a warning to practitioners who fail to correctly remove additive background luminescence.

The temporal decay of the spectral incandescence traces, or, more often, the effective temperature, provides even more information about the nanoparticle size and thermophysical properties. Analyzing this data requires the heat transfer submodel parameters. One of the most important and uncertain of these quantities is the thermal accommodation coefficient (TAC), which quantifies the efficiency of energy transfer when gas molecules scatter from the nanoparticle surface. Unfortunately, little information is available about this parameter for the surface temperatures relevant to TiRe-LII. Accordingly, molecular dynamics (MD) can be used to investigate this parameter before proceeding with the analysis of TiRe-LII data. Chapter 7 is an advance upon past MD treatments in that it examines how the choice of surface potential affects the value of the TAC over a range of surface temperatures. The MD simulations yield several useful conclusions: (i) at lower surface temperatures, the tangential mode of large gas atoms is inaccessible to the surface atoms, and consequently energy is accommodated more effectively for the lighter gas molecules; (ii) the value of the TAC is highly sensitive to the surface phase, with a marked increase in the TAC when the surface melts; (iii) above the melting point, the MD-predicted TACs increase with mass ratio, $\mu = m_g/m_s$, consistent with observations from TiRe-LII experimentation; and (iv) above the melting point, the TAC also appears to be insensitive to surface temperature, affirming the common practice of using a temperature-independent TAC when interpreting TiRe-LII data. Chapter 7 also presents the TAC for several new gas-surface pairs, including: Fe-Ne, Cu-He, Cu-Ne, and Cu-Ar. These additional gas-surface pairs will be useful in ongoing TiRe-LII analyses on iron and copper [443] nanoparticles.

Chapter 8 shows how the techniques and insights developed in the preceding chapters can be used to infer the nanoparticle size and TAC from TiRe-LII measurements on metallic aerosols. The chapter demonstrates the experimental approach of Sipkens et al. [112] wherein nanoparticle colloids are aerosolized into a range of buffer gases. In contrast to gas-phase synthesis where the bath gas influences both nanoparticle nucleation and growth as well as the TiRe-LII cooling model through the TAC, this approach isolates the synthesis technique from the

buffer gas, and consequently allows for independent assessment of the TAC for specific gas-surface pairs. TiRe-LII measurements on engineered iron, silver, and molybdenum nanoparticles are reviewed, and a cross-examination of these different materials in controlled environments highlights some of the unresolved aspects of TiRe-LII model development. For example, all three nanoparticle materials exhibit excessive absorption, where, in order to obtain the peak pyrometric nanoparticle temperature, the absorption cross-section at the laser wavelength would need to be considerably larger than the one predicted by the combination of the Rayleigh approximation and published radiative properties of the bulk material. This enhanced absorption is found to depend significantly on the nanoparticle material, with molybdenum, iron, and silver nanoparticles having approximately 4, 8, and 16 times enhanced absorption, respectively. This can be partially resolved by implementing Mie theory in the place of the Rayleigh approximation and is a topic of ongoing work. Moreover, the especially large enhancement to the absorption cross-section of silver nanoparticles, along with some other observations, suggests that the observed emission is not incandescence, but some other form of laser-induced emission, such as fluorescence or bremsstrahlung. Chapter 8 also shows that for conduction-dominated cooling, such as that observed for molybdenum nanoparticles, it is not possible to infer the nanoparticle size and TAC independently. This is due to the nanoparticle size and TAC appear as a fixed ratio in the energy balance on the nanoparticle. In contrast, the considerable increase in vaporization for iron nanoparticles allows for a statistically robust estimate of both the nanoparticle size and TAC. The chapter concludes by noting remaining anomalies, including the material-dependent excessive absorption noted above, an anomalous cooling effect exhibited by the molybdenum nanoparticles, and other factors that suggest that the signals from laser-excited silver are not incandescence.

This thesis concludes with a discussion of model complexity. The plurality of models available in the literature presents one of the largest challenges to advancing TiRe-LII technology. Chapter 9 proposes Bayesian model selection as a solution and discusses how it can be applied practically to TiRe-LII analyses. Specifically, Chapter 9 provides a proof-of-concept study, applying the Bayesian model selection approach to TiRe-LII data collected from iron nanoparticles. Priors are first defined on each of the model parameters considered in the analysis, drawing on data available in the literature. Then, simulated TiRe-LII data from iron nanoparticles is used to examine the capabilities of the model selection procedure, demonstrating how models must balance the number of degrees-of-freedom and model parameter uncertainties with goodness-of-fit. The chapter concludes by demonstrating the technique on experimental data from Chapter 8. The results shows that Román's equation [204] is statistically distinct from and favored over other expressions and also highlights how TiRe-LII is

increasingly used as a tool for fundamental scientific inquiry (e.g. characterizing thermodynamic properties) as opposed to a *turn-key* particle sizing diagnostic. More importantly, Chapter 9 demonstrates how Bayesian model selection can be implemented in the future as a solution to properly account for model complexity in establishing the properties of soot and robustly interpreting TiRe-LII data.

10.2 Ongoing and future work

Moving forward, TiRe-LII practitioners are presented with several challenges. Most prominently, there is a need to (i) resolve the dissention between the models developed between different laboratories and (ii) explain remaining anomalies in measured signals in order to have confidence in LII as a diagnostic. In this regard, the current work presents several novel approaches to TiRe-LII data analysis that can be used to meet these challenges, increase the range of aerosols that can be measured, and diversify the quantities that can be inferred from the data. This section reviews ongoing and recommended work that can advance upon this narrative.

10.2.1 The generalized error model

The generalized error model presented in Chapter 4 represents a new form of analysis that can be applied to TiRe-LII signals. Most immediately, the approach can be used by practitioners to troubleshoot problems with their experiments. The next step would involve applying the general error model to signals collected under a more diverse set of conditions. Of particular interest would be the analysis of TiRe-LII signals collected from turbulent flames. In turbulent flames, soot is advected through the flame as small, approximately homogenous, pockets [444]. In this scenario, the particle volume fraction within the spatially-fixed probe volume is unlikely to vary according to a Gaussian distribution. Accordingly, modifications will need to be made to interpret the signal variance for these cases. If successful, however, this kind of analysis could provide an approach to determining turbulent flow statistics simply by analyzing nonlinearities in signal variance versus mean curves. One could also consider a shift from phrasing the error model with time to with space, examining the variance in the two-dimensional spatial distribution of volume fraction throughout flames. Figure 10.1 demonstrates this approach, plotting the expected value versus spatial variance for signals collected on a turbulent flame. The curve reveals a significantly nonlinear trend that also deviates from the quadratic relationship expected if variations in the measured process were Gaussian. Interpreted, this trend corresponds to a relationship in which the variance is exceptionally high when soot is present and consistently low when soot is not present.

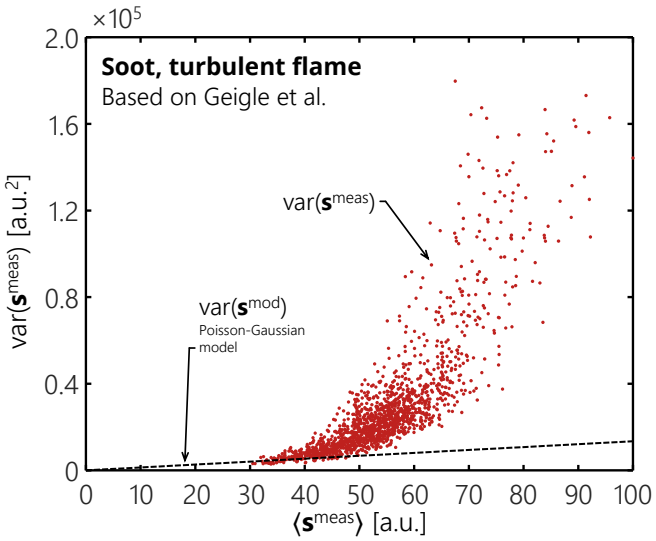

Figure 10.1 Expected signal versus spatial variance curve for data collected by Dr. Klaus-Peter Geigle and co-workers on a turbulent flame using the apparatus described in Ref. [54].

10.2.2 Dimensionless fluence analysis

The dimensionless fluence analysis demonstrated in Chapter 5 allows for the comparison of peak temperature fluence curves from different laboratories. The natural extension of this work, therefore, is to use it to facilitate an interlaboratory comparison of LII data. Most notably, it could be used to explore why several of the studies surveyed in Chapter 5 appear to plateau about different temperatures. The model could also be extended to consider spatially-nonuniform distributions in the laser energy, which will vary depending on the laser used for excitation and the optics used for attenuation and beam shaping. Liu and Smallwood [445] have recently suggest that this effect may explain anomalies in previously calculated fluence curves [176]. Other avenues of future work could include calculating detailed peak temperature fluence curves for a greater variety of engineered nanoparticles, an approach that is already being developed [442], and an extension of the applied approach to incandescence-based fluence curves, such as those in Refs. [65,72,99,121,249,257].

10.2.3 Intensity scaling factor curve analysis

The analysis of ISF curves presented in Chapter 6 demonstrates another way through which TiRe-LII practitioners can either: (i) extract more information from their signals; or (ii) determine if signals need to be corrected for various effects, like background luminescence. In this regard, ISF curves can serve as an additional source of information to resolve anomalies in TiRe-LII signals. Consider, for example, the fluence anomaly reported by Liu et al. [176] and noted in Section 10.2.2 wherein experimentally-inferred volume fractions are observed to change significantly with laser fluence. Extending the current technique to considering spatial

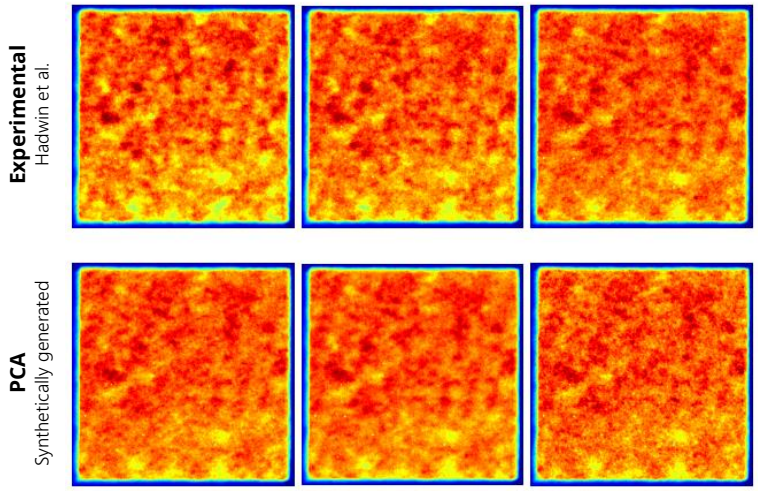

Figure 10.2 Three samples of spatial laser fluence profiles of a Nd:YAG laser (top) measured experimentally measured and (bottom) generated syntehtically using a principle component analysis. Figures are adopted from Hadwin et al. [157].

variations in the laser energy may explain this anomaly. Including the effect of spatial aberration in the laser profile should build on the work of Hadwin et al. [157], who used a principle component analysis to generate realistic laser profiles (as demonstrated in Figure 10.2). This technique can be used to accommodate the effect of spatial inconsistencies in the laser profile in a probabilistic manner that facilitates uncertainty quantification. ISF curves may also prove useful in detecting if laser-induced emission from engineered nanoparticles is indeed incandescence (as demonstrated, albeit briefly, in Chapter 8).

10.2.4 Molecular dynamics-derived thermal accommodation coefficients

MD-derived TACs are an especially promising area of future research, with significant potential in reducing uncertainties in TiRe-LII models and in developing a greater understanding of the physics underlying the quantity. Here, two major avenues of future work are considered.

First, the formulation for the TAC presented in this chapter can easily be extended to polyatomic gas molecules (e.g. [189]), simply by including an additional sum over the kinetic energy of all of the atoms in the gas molecule, that is

$$E = \sum_j \frac{1}{2} m_g \left\| \mathbf{v}^j \right\|_2^2 . \tag{10.1}$$

This accounts for the rotational energy of the gas molecule, which increases the maximum amount of energy that can be stored in the gas molecule. Molecules dynamics can thus be used to predict scattered velocity

Table 10.1 Parameterizations of the Morse potential derived from ab initio calculations for iron and polyatomic gas pairs. The Fe-N_2 values can also be found in Ref. [446].

Gas-surface pair	D [meV]	a [Å^{-1}]	R [Å]
Fe-N_2 (N)	2.162	0.932	4.819
Fe-CO (C)	31.2	1.04	3.76
Fe-CO (O)	64.8	1.95	4.92

distributions for polyatomic gas molecules. Recently, gas-surface potentials have been derived from ab initio calculations for Fe-N_2 and Fe-CO by Dr. Titantah and Prof. Karttunen in collaboration with the current author (cf. [446]). The Morse potential parameterizations for these cases are included in Table 10.1. For Fe-CO, preliminary MD simulations predict nearly complete absorption as a result of the relatively high potential well depth between the oxygen and iron atoms. This could have significant consequences for the Fe-CO experiments in Ref. [112], where the nanoparticles are likely to be covered in a layer of CO molecules or otherwise undergo chemical reactions. Preliminary MD simulations of Fe-N_2 scattering yield an estimate of the total TAC of $\alpha = 0.12$ for the EAM parameterization by Zhou et al. [324] and $\alpha = 0.13$ the FS parameterization of Mendelev et al. [327] for $T_s = 2500$ K and $T_g = 300$ K. Beyond providing a more robust understanding of the TAC as a fundamental property, these simulations will aid directly in interpreting TiRe-LII collected from iron in nitrogen and carbon dioxide environments and provide an appreciation of how polyatomic gases may interact with carbon surfaces.

Second, more research is needed to examine the surface potential parameterization affects the TAC between various gases and carbon to carbon, including a study of the effect that the graphitic and amorphous phases have on the TAC. Such a study would be particularly important in understanding how the TAC may change as soot either ages (e.g. [260]) or anneals within the flame. MD-derived TACs have been obtained P between various gases and amorphous carbon, generated by rapidly heating a diamond crystal of carbon atoms to temperatures in excess of 4000 K before quenching the surface to the temperature of interest. Figure 10.3 shows realizations of the resultant surface predicted using a range of surface potentials: two Tersoff potentials [362,447], the long-range carbon bond order (LCBOP) potential parameterized by Los and Fasolino [448], the MEAM potential provided with the LAMMPS distributable [323], and the EDIP potential parameterized by Lucas et al. [449]. The Erhart-Albe and EDIP parametrizations are particularly effective at generating sparse structures with no long-range order, while the MEAM potential could not generate an amorphous phase, rather maintaining the initial

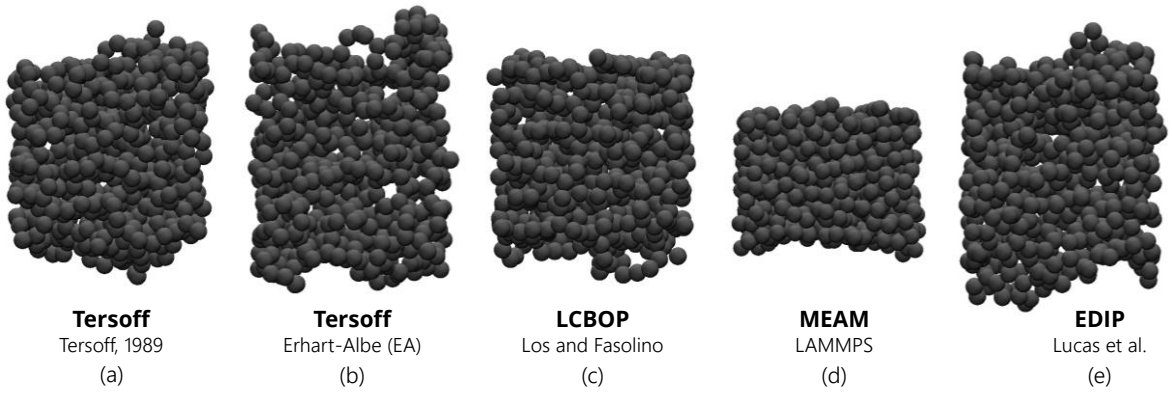

Figure 10.3 Realization of carbon surfaces following a procedure aimed at producing the amorphous phase. Implemented potentials are those of [323,362,447–449].

diamond cubic phase. This demonstrates a sensitivity of the surface phase to the interatomic potential and could be a topic of future investigations.

MD-derived scattered velocity distributions, whether they be for polyatomic gas molecules scattering from metals or monatomic gas molecules scattering from carbon, could also be useful in direct simulation Monte Carlo (DSMC) simulations aimed at improving our understanding of the shielding effect for conductive cooling of aggregates [113,114,118,197], which is still an area of active research [450].

10.2.5 Comparisons of laser-induced emission from engineered nanoparticles

The analysis of LII data from iron, silver, and molybdenum nanoaerosols has raised several unresolved questions that require further analysis. Why do the radiative properties of molten iron nanoparticles deviate from those of bulk molten iron? What is responsible for the enhanced absorption cross-section of the molten metal nanoparticles? What is the origin of the *anomalous cooling* observed for molybdenum nanoparticles? Answering these questions will require additional experimental and theoretical analysis, which will exploit the tools developed in this thesis as well as recent innovations in optical diagnostics (e.g. streak cameras, which provide spectrally and temporally-resolved emissions from the nanoparticles). One significant topic of interest is the validity of the Rayleigh approximation. The approximation was originally justified on the basis that $x \ll 1$. It is noted, however, that the phase shift condition cited in Chapter 2, $x \cdot |\mathbf{m}_\lambda| \ll 1$, is not adequately satisfied for some of the metals considered here. As such, future work will re-examine this data in the light of this observation, including the influence of aggregation on the laser-excitation of molybdenum analyses. Ongoing work [371] is also aimed at understanding laser-induced emission from silver nanoparticles and resolving whether the

observed signal is due to incandescence or another phenomenon like bremsstrahlung. Analysis of these signals may even lead to a brand-new diagnostic that can be used for nanoparticle characterization.

10.2.6 The application of Bayesian model selection to TiRe-LII

Perhaps the most promising avenue of future research is the application of Bayesian model selection to TiRe-LII, as outlined in Chapter 9 of this thesis. While the discussion in that chapter is limited to consideration of iron nanoparticles for which the material properties are well-established, soot provides a much richer field of study. The thermophysical properties of soot are highly uncertain and hotly debated in the literature, resulting in a plethora of competing models [98] that are often tuned to a specific set of benchmark data. This dissention is one of the largest challenges in the TiRe-LII community and represents a barrier to making further advancements in the reliability of LII-derived quantities. Bayesian model selection presents a solution to this problem, providing a statistically-robust method by which models can be compared and by which anomalies can be resolved. The first step in this procedure is to establish methods for quantifying the uncertainties in the model parameters, which is required to apply the model selection procedure to TiRe-LII collected from soot. Such work has the capacity to create a significant impact in the TiRe-LII community, not only providing an update to the current state of TiRe-LII modeling but also by providing a framework by which uncertainties can be propagated through these models.

10.3 Final remarks

Laser-induced incandescence has been applied to soot and engineered nanoparticles and, in this respect, is an established method for determining the volume fraction of particulate in an aerosol and the nanoparticle size, which is important in determining nanoparticle toxicity and utility. More recently, LII is being applied as a tool of fundamental scientific inquiry, capable of providing insights into the thermophysical properties of materials at high temperatures. Moreover, the *in situ*, real time, and inexpensive nature of TiRe-LII promises to make nanoparticle characterization more accessible than ever. TiRe-LII could thus be employed both for online control of nanoparticle synthesis as well as for regulating soot pollution in an effort to meet global climate change commitments and reduce the negative effects on human health. To this end, this thesis provides novel tools for the interpretation of TiRe-LII signals that brings these objectives closer to reality and provides the basis for new methods of nanoparticle characterization that can be used to understand physical mechanisms on the nanoscale.

Appendix A
A review of complementary aerosol and combustion diagnostics

The suite of diagnostics available from the characterization of nanoparticle laden aerosols is extensive, employing a broad range of application-dependent mechanisms. As such, a short word on scope in this appendix is required. This appendix focuses on those techniques that are used to characterize high melting point nanoparticles, such as metallic nanoparticles and soot. This excludes nanomaterials like lipids or nanostructured polymers, which cannot be characterized using LII due to the high temperatures required to incite measurable incandescence. This appendix also limits discussion to those characterization techniques used to determine thermal and physical properties of nanoparticles, this in contrast to those focused on characterizing nanoparticle surfaces (which is an important characteristic in the functionalization of nanoparticles for catalysis and drug delivery applications) or their chemical properties (some techniques for which are reviewed in Refs. [451,452]). The techniques are categorized either as *ex situ* and *in situ*, adopting the definition in the main text where this categorization pertains to whether measurements can be made of an observed process directly (in situ) or must happen afterwards (ex situ).

A.1 Ex situ, sampling-based, and downstream diagnostics

Ex situ diagnostics offer an unparalleled amount of information about aerosolized nanoparticles, ranging from detailed chemistry to aggregate morphology. However, they are, by their nature, intrusive to the measured aerosol. Moreover, sampling procedures are limited in their temporal and spatial resolution and can be plagued with preferential sampling resulting from inertial, gravitational, diffusional, thermophoretic, or electrostatic deposition [453]. This misrepresents the true distribution of nanoparticle characteristics. The list of ex situ diagnostics used for aerosol characterization is, in and of itself, extensive. Accordingly, attempts are not made to provide an exhaustive list of the aerosol characterization techniques, but rather focus on the most common techniques (such as those discussed in review papers on physical characterization of aerosols [453–456]) and those

Table A.1 Ex situ aerosol cahracterization techniques reviewed in this work, including their acronyms and studies concurrent with LII, if available.

Technique	Types and acronyms	Diamaeter range	Concurrent to LII
Electron microscopy	SEM, TEM, HRTEM	-	[21,24,69,77–79,84,85,112,119,127,199]
Probe microscopy	STM, AFM, MFM	-	-
Condensation nanoparticle counter	CPC, CNC	10-3000 nm [457]	[458]
Gravimetric analysis	-	-	[75,86,459]
Scanning mobility nanoparticle sizer	SMPS, SEMS	3-700 nm [454]	[119,137–139,460,461]
Mobility spectrometers	DMS, EAS, FMPS, EEPS, MEAS, FIMS	5-1000 nm [454,457,462]	[458,459]
Electrical low pressure impactor	ELPI, DMM	10-30,000 nm [454,457]	[463–466]
Centrifuges	-	> 200 nm [467]	-
Particle mass analyser	PMA, APM, CPMA	50-800 nm [468]	[119]
Optical, filter-based devices	Aethelometer, PSAP, SOAP, MAAP	20-600 nm [469]	[458]
Continuous-wave laser-induced incandescence	CW-LII, SP^2	70-500 nm	-
Photoacoustic devices	PA, PAS, PASS	-	[219,459]
Aerosol mass spectrometer	AMS, HR-TOF-AMS, SP-AMS	-	-
Brunauer-Emmett-Teller	BET	-	[48,128,470]
Microbalances	TEOM, QCM	-	[465]
Diffusion batteries	EDB	0.8-200 nm [471,472]	-

techniques that have been compared to LII measurements. These techniques, and the cases where they have been used in studies with LII, are provided in Table A.1.

A.1.1 Microscopy

One of the most common methods of characterizing nanoparticles is electron microscopy. Electron microscopy involves firing a beam of electrons at a sample and measuring various aspects of their interaction with the material. The shorter wavelength of electrons compared to light results in higher resolutions, down to the nanoscale. The term first saw use in Knoll and Ruska [473], who developed the principle of electron lenses. The

principle was quickly commercialized. The scanning electron microscopy (SEM) is one such microscope that involves measuring electrons scattered from the sample. By scanning the electron beam across the surface and measuring the number of scattered electrons from any given location, one can create a map of the sample topography and can thus determine aggregate structure and nanoparticle size. China et al. [474], for example, performed SEM using a field emission source to differentiate between four different kinds of soot nanoparticles emitted from a wildfire. Figure A.1a shows one of these types of soot, revealing the expected fractal aggregate structure. Due to the amount of information allowed by imaging, electron microscopy is often taken as the standard by which many of the other technique presented here are compared. Further, one can use the same apparatus to perform x-ray diffraction (XRD) analysis or energy dispersive x-ray spectroscopy (EDX), involving an analysis of emitted x-rays instead of electrons. As the characteristics of the x-ray emission will depend on the atomic makeup of a material, these complementary techniques can be used to enhance the images by determining elemental composition of the sample.

SEM analyses are generally limited by the finite interaction volume of the electron beam. Transmission electron microscopes (TEM) push the capabilities of electron microscopes to much higher resolutions, making them better accustomed to nanoparticle characterization. In TEM, the electrons interact with only a thin slice of the material, where they either pass through the material or are diffracted due to interaction with the material. In total, there are nearly 40 different operational modes for the TEM [476], including electron energy-loss spectrometers (EELS) and tomographic microscopy. Those most often used for physical characterization of nanoparticles are imaging using the diffracted (dark field) or transmitted (bright field) electrons. Figure A.1b and

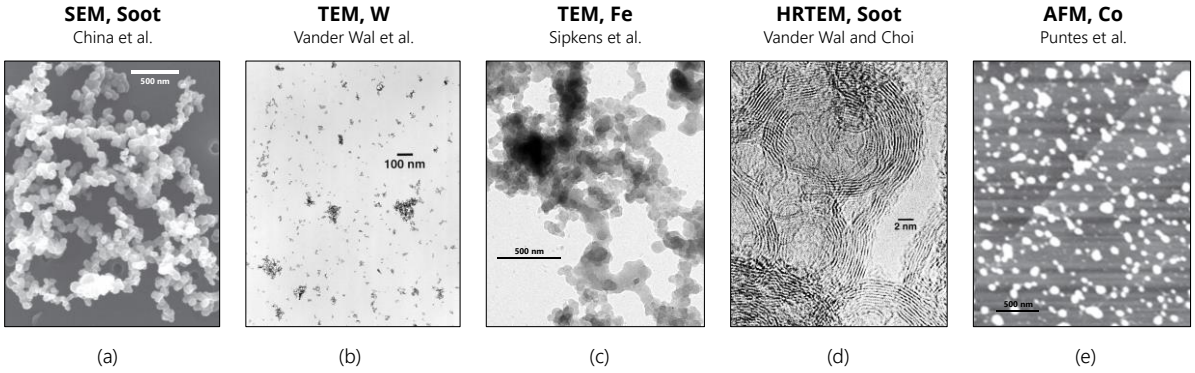

Figure A.1 Examples of electron and atomic force microscopy applied to various kinds of high melting point nanoparticles. The images depict (a) SEM images of soot from wildfires [474], (b) bright field TEM images of tungsten nanoparticles [94], (c) bright field TAM mages of aerosolized iron nanoparticles [112], (d) HRTEM images of the interior of carbon nanoparticles [85], and (e) AMF images of cobalt nanoparticles [475].

c exemplify bright field TEM images of tungsten [84] and iron [112] aggregates. In either case, the aggregate structure and primary nanoparticle size can be visually accessed from the images. Calculating the statistics around nanoparticle size distributions from TEM images remains a field of active development, requiring sophisticated image analysis algorithms [477]. This if often complicated by aggregation, which can induce certain biases [478]. Bright field TEM images have been similarly used to characterize nanoparticles in connection with a variety of other LII studies, including [21,24,69,77–79,84,85,112,127], where they are used to restrict inference or verify LII models. For these reasons, TEM images are used for comparison purposes in Chapter 8 of the associated work.

More recently, high-resolution transmission electron microscopes (HRTEM) have provided higher resolution [281,479]. This mode of imaging relies on phase-contrast, where both the transmitted and diffracted electrons are used to generate an image. The phase interference between these electrons creates fringes that can be interpreting using Fourier analysis, for resolutions down to the atomic level. Although such a level of detail is not critical to determining larger-scale information about aggregates or nanoparticle size distributions, it does allow for investigation of the internal structure of nanoparticles including core-shell and crystal structure. Vander Wal and Choi [85] used HRTEM to investigate the internal structure of soot following laser heating, with on such image shown in Figure A.1d. Here, one can clearly see the soot particles as well as their internal structure, consisting of layers of graphite. Such studies are particularly useful in investigating the changes that soot nanoparticles undergo during laser heating and can act to inform on LII models. Others have used HRTEM to investigate soot annealing [85,278,281] and oxidation [480].

Scanning probe microscopes (SPMs) is a summary term for a category of microscopes that use a probe to interrogate nanomaterials, most prominently including the scanning tunneling microscope (STM) and atomic force microscope (AFM). STM operates based on measuring a tunneling current, which depends on the distance between the probe and the surface and requires a highly conductive sample. As this interaction is generally limited to the atom closest to the probe, the surface topography can be imaged down to atomic resolution [481]. When scanning across the surface, the vertical position of the sample is updated to achieve a nearly constant tunneling current. The AFM, by contrast, images the profile of a surface based on atomic attraction and repulsion of the probe. Puntes et al. [475] demonstrated the use of AFM to characterize cobalt nanoparticles, producing images including that of Figure A.1e. Variations on these two models of SPMs have extended the usefulness of the technique. For example, magnetic force microscopy (MFM) operates on the same principle as AFM but relies on

magnetic forces in the place of atomic forces. Puntes et al. [475] also used MFM to image the cobalt nanoparticles shown in Figure A.1e. They note that although there is some loss of resolution relative to AFM, MFM has the advantage of large lateral resolution and the allowance of insulating surfaces. Of course, SPMs can only measure surface topologies, which can be limiting when considering aggregates, where entire nanoparticles can be hidden under the imaged surface. This also means that only surface features can be imaged, rather than the internal structure allowed by HRTEM. Moreover, absorbed species on the tip or surface can also cause problems [482]. As a result of these limitation, SPM is rarely implemented as a complementary technique to LII.

In general, nanoparticle characterization by microscopy is relatively time intensive and often incurs some of the longest delays between sample collection and characterization.

A.1.2 Condensation nanoparticle counting

Condensation nanoparticle counters (CPC) or condensation nucleus counters (CNC) count the number of nanoparticles in an aerosol by enlarging them until they can be counted, often using a camera or photoelectric detector. The technique was originally pioneered by Aitken [483] who measured atmospheric nuclei between 20 and 200 nm. Several designs of CPC are available [471]: (i) an expansion-type, using water, a humidifier, and an expansion chamber in cyclic fashion for cooling; (ii) conductive cooling-type, using a saturator, thermal condenser, and nanoparticle detector for continuous, steady-state operation; and (iii) mixing-type, involving mixes a hot saturated stream with the aerosol [484] that allows flexible flow rates [485] and minimal diffusional loss. The general principle is shown schematically in Figure A.2a. CPC is a standard technique for various forms of environmental compliance. The technique is limited in its lower detectability limits, which ranges from 2 to 15 nm. Moreover, the presence of nanoparticles around or below this limit can render measurements unreliable [453]. This, combined with the fact that nanoparticle number measurements are more sensitive to aggregation than other techniques, has pushed researchers to investigate other methods of aerosol characterization.

A.1.3 Gravimetric method

In practice, total particulate mass measurements are most often made using gravimetric analysis, where nanoparticles of all sizes are collected on a filter. The filter's mass is measured before and after being exposed to an exhaust stream, with the difference in mass being attributed to the mass of captured nanoparticles. Despite widespread use for regulation purposes, new combustion technologies have reduced the particulate matter released from engines to the lower detectability limit of the analysis, prompting investigation into replacement techniques [454]. Snelling et al. [86] found a high degree of correlation between LII measurements and the

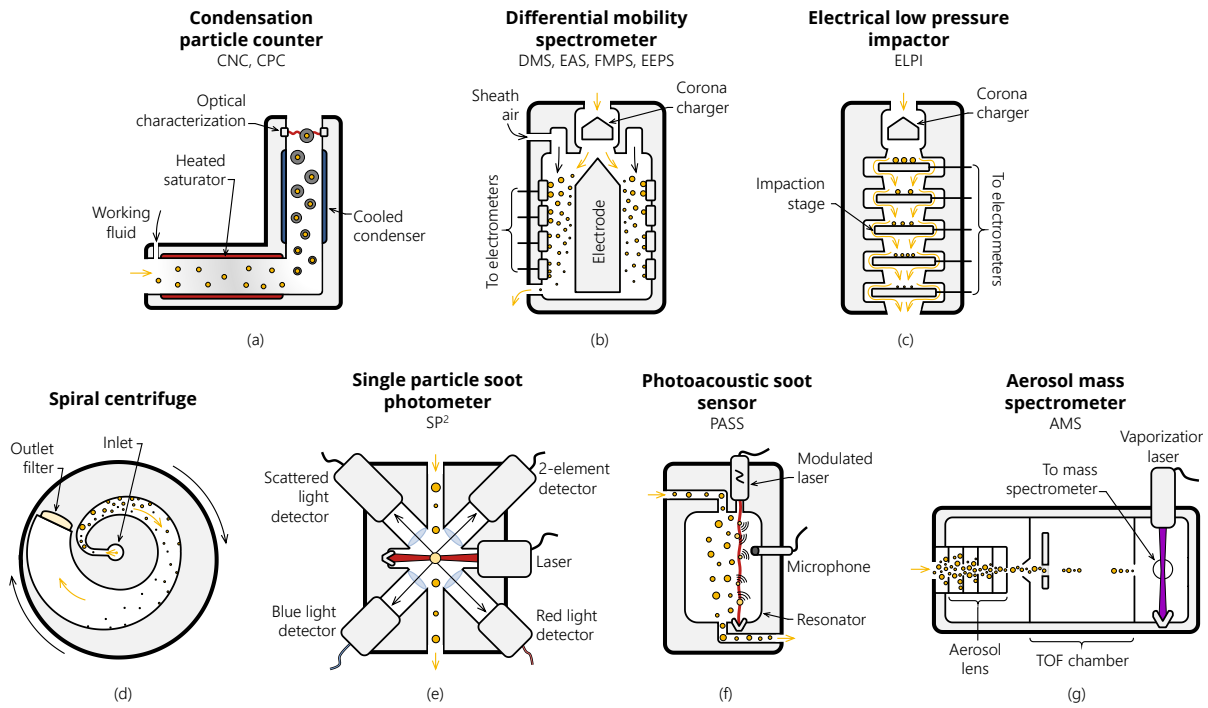

Figure A.2 Schemtics of select ex situ devices used in aerosol characterization, including (a) the condensation nanoparticle counter, (b) the fast mobility nanoparticle sizer, (c) the electrical low pressure impactor, (d) the spiral centrifuge, (e) the single photon soot photometer (SP^2), (f) the photoacoustic soot sensor (PASS), and (g) aerosol mass spectrometer (AMS).

gravimetric method over a range of engine modes. Due to the frequent use in emission standards, the gravimetric method has been particularly useful in the context of calibrating LII devices [486,487].

A.1.4 Electromobility sizing

The nanoparticle size distribution can alternative be inferred from nanoparticle electromobility. These techniques rely on the differential mobility analyzer (DMA), following the pioneering work of Knutson and Whitby [488], where nanoparticles in a polydisperse aerosol are subjected to an electrical field, most often in a vertical chamber consisting between two concentric cylinders. The applied field will invoke a lateral velocity on the nanoparticles in the chamber that is proportional to their electric mobility, which is in turn related to the nanoparticle size and charge. Using a narrow opening at the bottom, a specific size class can be selected, allowing one to generate a nearly monodisperse aerosol at the outlet. These often form the basis for electric mobility spectrometers (EMS), which measure the spectrum of electric mobility diameter in an aerosol. For example, differential mobility nanoparticle sizers (DMPS) combine a DMA with a CPC and step the voltage in the DMA to count nanoparticles with a specified mobility diameter. Scanning mobility nanoparticle spectrometers (SMPS),

also known as scanning mobility nanoparticle sizers or scanning electrical mobility sizers (SEMS), advance on this idea by scanning the voltage continuously rather than stepping [489]. Scan times can range from 16 s to several minutes, depending on the instrument, nanoparticle loading, and desired resolution [490] and are limited by smearing of the size distribution in the CPC [491]. Comparisons between different kinds of SMPS are prevalent in the literature [492–495]. Michelsen et al. [278] used SMPS, with complementary TEM, to investigate the changes soot undergoes during laser heating. As a result of the near real time response of the instrument, the technique has been compared to TiRe-LII analyses of combustion [119,137–139,460,461]. It is noted that mobility sizers are expected to perform poorly for complicated nanoparticle morphologies, such as for soot aggregates [490].

Differential mobility spectrometers (DMS) [496] or electrical aerosol spectrometers (EAS) [497] (which have been commercialized as fast mobility nanoparticle sizers, FMPS, and engine exhaust nanoparticle sizers, EEPS) replace the CPC used in a SMPS for nanoparticle counting with a series of electrometers arranged along the height of the chamber, as demonstrated in Figure A.2b. This results in measurement frequencies up to 1 Hz. The technique has several limitations still, however. Some authors have noted opacity in the inversion methods used in the device software [490]. The electrometers used in the DMS devices are also generally less sensitive than the CPCs that are used in SMPS. As a result, when the technique is compared to SMPS and other characterization techniques [490,492,498], it was found to underpredict the mean nanoparticle size. The miniaturized electrical mobility aerosol spectrometer (MEAS) [499] replaces the sheath flow with an electrostatic precipitator, allowing for a smaller device that may enable deployment of these kinds of devices in a broader range of applications. The fast integrated mobility spectrometer (FIMSs) is yet another variant of these devices, where the mobility separator and condenser are integrated into a single column [462,500]. Using a laser beam at the end of the column, a camera captures the scattering from the resultant nanoparticles and can count the number of nanoparticles in each size class. This procedure gives the FIMS even higher time resolution, up to 10 Hz, while measuring nanoparticles in the range of 5-1000 nm [462]. The FIMS can also be used to determine the distribution of naturally charged nanoparticles by removing the nanoparticle charger [501].

A.1.5 Inertial or impaction sizing

Inertial techniques mostly aim at measuring the aerodynamic diameter of nanoparticles in an aerosol, relying on the ability of nanoparticles to cross streamlines in a flow. This generally involves two strategies: impactors and centrifuges.

The electrical low pressure impactor (ELPI) [502,503] is a device consisting of: (i) a unipolar diode charger, that charges the nanoparticles in a sample aerosol; (ii) a cascade impactor, in which each impactor captures nanoparticles of a specific aerodynamic diameter; and (iii) a multichannel electrometer to measure the charge build up caused by the nanoparticles on each impactor. This is demonstrated schematically in Figure A.2c. New stages have lowered the detectability to 7 nm [504]. ELPI has an advantage over SMPS in that it can resolve distributions on the order of seconds, which makes it better suited to measuring transient processes. However, the technique has several limitations in that it requires knowledge of the effective density of the measured nanoparticles (which can be resolved with complementary use of a DMA [505]); can be influenced by charge transfer during nanoparticle bounce off of the stages [506]; and other loading-induced size shifts [507,508]. The technique has been compared to many of the other aerosol characterization techniques presented here, including DMPS [505], SMPS [490,509], and LII [463–465]. The Dekati Mass Monitor (DMM) adds an electromobility sizer to improve the description of particulate matter [454], yielding reasonable agreement with gravimetric measurements [510]. The DMM has also been studied concurrent to LII [466].

Centrifuges, in contrast, seek to separate nanoparticles based on their differential aerodynamic diameters. The spiral centrifuge is one of the most common such devices used for nanoparticle sizing [467]. In the device, the aerosol is introduced in the center of a spiral channel. As the device rotates, the aerosol is driven outwards through the spiral channel resulting in the heavier nanoparticles being driven towards the channel wall close to the center of the device and the smallest nanoparticle impacting the wall near the exit. This is demonstrated schematically in Figure A.2d. One advantage of such a device is that it can be used to determine the aerodynamic size distribution even of irregular shaped nanoparticles, such as fibers [511] or aggregates. They are generally limited to larger nanoparticles (down to 200 nm [467], depending on the device).

Particle mass analyzers (PMA), which include the aerosol nanoparticle mass analyzer (APM) [512] and Couette centrifugal nanoparticle mass analyzer (CPMA) [513], are devices containing two rotating cylinders over which a voltage is applied. The instruments thus measure a balance between the electromobility and centrifugal forces on nanoparticles, representing a hybrid between electromobility and inertial nanoparticle sizing. These devices are generally accurate in the range of 50-800 nm [468] and can also be combined with a DMA or SMPS to allow for independent evaluation of the nanoparticle mass and electrical mobility diameter. Moreover, combining a PMA with one of these other devices can help identify errors incurred by multiple charged nanoparticles [514].

A.1.6 Optical methods

Light-based ex situ techniques offer high temporal resolution by optically characterizing a sample aerosol. Filter-based optical techniques are an improvement to the standard gravimetric method in which nanoparticles are collected on a filter and the properties of the filter are measured over time. The sensitivity of the technique is highly influenced by the choice of filter, which can enhance multiple scattering from the sample, errors due to the deposited nanoparticle morphology, and induced unexpected angular distributions of light scattered by the nanoparticles [160]. Aethalometers [515] are one of the earliest examples of such a technique, wherein the nanoparticles are collected on a filter and the filter transmissivity is monitored over time. Calibration can be performed using physical and chemical characterization of the nanoparticles deposited on the filter following measurements. Such calibration is important, as several studies have shown that aethalometer measurements can differ by 20-50% [454]. Most systems are limited in temporal resolution to minutes, though some newer devices can reduce this to a matter of seconds. Commercial systems are available for both single and multiple wavelength measurements [516]. The nanoparticle soot absorption photometer (PSAP) operates on a similar principle, measuring the transmissivity of the filter with a temporal resolution up to 0.1 Hz [517]. The spectral optical absorption photometer (SOAP) further expands the PSAP to incorporate multiple wavelengths, using a broadband light source and a spectrometer for detection [518]. Use of these techniques is often limited by the aforementioned multiple scattering effects of the filter (which increases device sensitivity, but also makes calibration more challenging), humidity, and unusual noise properties (see references and discussion in Ref. [160]). The multi-angle absorption photometer (MAAP) [519] overcomes some of the shortcomings of these other techniques by combining filter transmission measurements with direct and diffuse scattering measurements at multiple angles.

Continuous-wave laser-induced incandescence (CW-LII) is a technique in which individually sampled nanoparticles pass through a continuous laser beam [60]. The resultant incandescence appears as measured pulses for individual nanoparticles and is highly sensitive even for low nanoparticle loadings. As a result, the technique has been used to characterize a wide variety of laboratory-generated carbonaceous nanoparticles [520,521], engineered metal nanoparticles [217], and atmospheric nanoparticles [522] and has been compared to many other devices (e.g. [523]). The technique has, for the most part, been standardized to the commercially available Single Particle Soot Photometer (SP^2) instrument, which also includes a scattering detector. A schematic demonstrating this device is included in Figure A.2e, based on the setup of shown in Ref. [521]. Unlike pulsed LII, CW-LII counts single nanoparticles making it necessarily an ex situ technique requiring considerable dilution and a narrow

passage to isolate the nanoparticles. However, similar models are used to interpret both pulsed and CW-LII data. Further information can be found in Michelsen et al. [97], which summarized both the pulsed and CW-LII literature.

Photoacoustic methods use a modulated laser pulse to periodically heat nanoparticles in the aerosol [524]. The heat is transferred to the surrounding gas, causing periodic gas expansion and contraction (or acoustic waves). The acoustic waves are amplified by resonance in the measurement chamber and are detected using a microphone. The resultant acoustic signal is proportional to the volume concentration in the aerosol for nanoparticles less than 300 nm and the surface of the nanoparticles for nanoparticles larger than the 300 nm [454]. Cross sensitivities with absorption by the gas can cause problems in nanoparticle detection; this can often be resolved by choosing appropriate frequencies. The technique has been commercialized as photoacoustic soot spectrometers (PA or PASS), which is shown schematically in Figure A.2f based on Ref. [525], and the Micro Soot Sensor. Photoacoustic methods have been compared to LII on several occasions [219,459] and are generally considered a low-cost alternative to make measurements for low nanoparticle concentration aerosols. The method can also be implemented as an in situ diagnostic.

A.1.7 Other notable ex situ diagnostics

Aerosol mass spectrometers (AMSs) are dual function devices that perform both nanoparticle time-of-flight (TOF) analysis for nanoparticle sizing and mass spectrometry for elemental analysis [526]. The technique relies on the aerodynamic lens, which both focuses the nanoparticles in the aerosol into a narrow beam and results in different size nanoparticles having different speeds. The original device used a shutter to create short bursts of nanoparticles, thereby syncing the initial position of the nanoparticles entering the chamber (as shown in Figure A.2g). As larger nanoparticles are moving more slowly upon leaving the aerodynamic lens, they take longer to arrive at the end of the chamber (i.e. they have a longer TOF), allowing for nanoparticle sizing. Upon arriving at the end of the chamber, the nanoparticles are vaporized by a UV laser for elemental analysis in a mass spectrometer. The commercialized variant from Aerodyne is based on the design from Ref. [526] and employs a quadruple mass spectrometer (QMS). Several variants on this AMS have been developed by replacing the QMS with other types of spectrometers. The high-resolution time-of-flight AMS (HR-TOF-AMS) [527] and soot nanoparticle AMS (SP-AMS) [528], for example, replace the QMS with a high-resolution TOF mass spectrometer that allows for a real time and field deployable device. These variants have seen considerable use in atmospheric measurements and have been used complementary to other nanoparticle sizers [529,530].

Brunauer-Emmett-Teller (BET) analysis [531] measures the physisorption of inert gases by a sample of nanoparticle powder, which are kept at an elevated temperature under vacuum to remove residual water and absorbed species before measurement. If one assumes that the nanoparticles are monodisperse spheres, the specific surface area can be converted to a Sauter mean diameter with knowledge of the sample mass and density. The technique has occasionally been used to verify LII-derived nanoparticle sizes for engineered nanoparticles [48,128,470]. Extension to soot is impractical given the high degree of aggregation and non-uniformity in thermophysical properties for those samples.

Microbalance methods involve measuring the change in resonant frequency of an oscillating platform as nanoparticles are deposited. Microbalance methods are limited in part due to problems with impaction and humidity, pressure changes, and filter artifacts [454]. As a result, the sensitivity of the device doesn't compare to photoacoustic techniques or LII. The most common such device is the tapered element oscillating microbalance (TEOM) [532], which uses a tapered quartz wand where nanoparticle are deposited on the tip. The TEOM technique was used to add information to LII and ELPI investigations by Witze et al. [465]. In another common arrangement, the quartz crystal microbalance (QCM), nanoparticles are deposited by electrostatic precipitation onto a thin quartz crystal. Proper functioning of this technique requires frequent cleaning of the device, as the soot layer can oscillate relative to the collection crystal. The QCM also has a smaller mass range than the TEOM, which resulted in the devices being less dominant in practice [533]. Differential TEOMs, such as those described in Refs. [534,535], are designed to overcome some of the problems with the TEOM.

Diffusion batteries operate on the principle of selective diffusion of an aerosol through filters with progressively tighter meshes [472]. The technique can be used to categorize nanoparticles in aerosols ranging from 0.8-200 nm [471,472], which overlaps considerably with the sizes measured by TiRe-LII. However, the size and temporal resolution of diffusion batteries is quite limited, the former by the number of stages which results in very large bins. The electrical diffusion battery (EDB) [536] adds a corona charger before the diffusion battery. In this case, the charge builds up on each stage as the nanoparticles collect, making the size distribution faster and more efficient to quantify.

A.2 In situ optical diagnostics

In situ diagnostics, in contrast to ex situ techniques, offer high temporal and spatial resolution of an observed process and almost exclusively use optical probing to attain information about an aerosol. This is particularly advantageous in combustion applications, where the dynamics of a process are to be probed. Accordingly, much

of the discussion in this section is directed at soot and combustion diagnostics. It is noted, however, that these techniques are often less intrusive, cheaper, and have higher temporal resolution that makes them useful beyond combustion applications (e.g. synthesis of inorganic nanoparticles [537]). The optical diagnostics here can be broadly categorized based on whether scattering, extinction, or emission is measured. A short discussion on how nanoparticles interact with light, which may prove useful to the unfamiliar reader, is provided in Chapter 2. Works reviewing subsets of the in situ methods for characterizing aerosolized nanoparticles are provided in Refs. [152,454,538,539] (and complementary information on the surrounding gas in Refs. [540–542]). A summary of the techniques discussed in this section is provided in Table A.2.

A.2.1 Extinction diagnostics

Light extinction (LE), line-of-sight attenuation (LOSA), or laser absorption spectroscopy (LAS, which is light extinction measurement in which a laser source is used) diagnostics represent an impressive suite of optical techniques that can be used to probe aerosols. The techniques are, by their nature, line-of-sight (LOS) or path integrated techniques in that they examine light-matter interactions of rays of light that transect the measurements domain. In its simplest form then, extinction techniques simply measure the amount of light from some source that attenuates through an aerosol. Models involve solving the radiative transfer equation (RTE), which describes how matter causes light extinction, emission, and scattering along the ray.

Table A.2 In situ aerosol or combustion cahracterization techniques reviewed in this work, including their acronyms and studies concurrent with LII, if available.

Category	Technique	Types and acronyms	Concurrent to LII
Extinction	Light extinction	LE, LOSA, LAS, CRDS, CRDLAS	[49,65,71,81,158,543–547]
Scattering	Elastic light scattering, nanoparticles	ELS, ES, Rayleigh scattering, MAELS, WALS	[87,92,543,548–552]
	X-ray scattering	WAXS, SAXS, USAXS	[553]
	Dynamic light scattering	PCS, DLS, DBS, QELS	-
	Raman spectroscopy	SERS, CARS	[102,143,218,554,555]
Absorption and emission	Laser-induced flourescence	LIF, PLIF, VLIF	[66,68,73,77,78,85]
	Laser-induced breakdown spectroscopy	LIBS, LIPS, PS-LIBS	-
	Two-colour method (thermometry)	2C	-
	Laser-induced incandescence	LII, SP^2, TiRe-LII	-

As a nanoparticle diagnostic, extinction methods produce signals that are roughly proportional to the number of soot nanoparticles available to scatter or absorb light along any given ray. The technique is ubiquitous in the combustion literature and used extensively to study flames (e.g. [556–559]) and can include spectral measurements (e.g. [42,543,560]). Moreover, the technique is often used in conjunction with LII analyses [65,543–545]. Menser et al. [49], for example, performed extinction measurements of silicon nanoparticles in a plasma reactor. Heated LOSA (HLOSA), a variant in which extinction is measured temporally during the laser-heating of the nanoparticles, has proven particularly useful in the context of determining the changes nanoparticles undergo during LII [158]. The technique resembles that used by Dasch [60] for soot concentration measurements. This is shown schematically in Figure A.3a. Cavity ring-down laser absorption spectroscopy (CRDS or CRLAS) involves introducing a mirror system into the optical setup [561] so that light passes through the aerosol many times. This effectively increases the path length and results in the measured light decreasing exponentially over time after the laser pulse. Measurement of the characteristic decay time, known as the ringdown time, results in highly sensitive measurements, due to the number of passes the light makes through the aerosol. This technique has been applied concurrent to LII by Vander Wal et al. [546,547] and Moreau et al. [562].

As a complementary gas diagnostic, extinction techniques are designed to incite electronic, vibrational, and rotational energy transitions in the gas molecules. Depending on the target species, measurements can be in the UV, visible, or infrared regions of the spectrum. The relative absorption into different quantized energy levels depends on the temperature, facilitating gas thermometry that can act as an input to TiRe-LII analyses. Further, the amount of absorption in specific bands can be related to species concentrations that could impact the value of the thermal accommodation coefficient used in the TiRe-LII cooling model. Reviews on the topic are available in the literature [563,564]. Techniques include direct absorption spectroscopy (DAS), which analogous to LOSA above, and wavelength modulated spectroscopy (WMS), which employs a combination of a high and low frequency laser input and a frequency analysis [565,566]. Either technique can be applied both using a fixed wavelength of by scanning across multiple wavelengths (for example, in tunable diode laser spectroscopy, TDLAS), which can improve resolution. The resultant information can be useful in reducing uncertainties in TiRe-LII cooling models.

These line-of-sight techniques are often used in conjunction with computer tomography (CT) to determine the spatial distribution of temperature or concentration of soot or gaseous species in an observed process. Depending on the conditions various algorithms are available for inverting the LOS data to spatial

concentrations. For axisymmetric flames, the problems can be reduced to one dimension by implementing onion peeling, shown schematically in Figure A.3b. The resultant inversion problem was named for Abel and can be performed using any number of algorithms available in the literature (e.g. [567,568]). Various other techniques have been developed to perform tomography for turbulent or non-symmetric flows [569].

A.2.2 Scattering diagnostics

Light can also be scattered by nanoparticles or gases in the aerosol. Scattering can occur either elastically or inelastically. For nanoparticles, elastic light scattering (ELS or ES) maintains an identical wavelength as the incident light which is picked up by a detector. Scattering experiments vary in the light they use to induce scattering from the nanoparticles, but most are sensitive to the degree of aggregation in the aerosol. This makes the technique complementary to LII, where LII can give information about the primary particle size and scattering the aggregate radius of gyration. Studies of this sort are superfluous in the literature [87,254,548–552]. Often, infrared light is used as the wavelength is sufficiently long that interactions with the nanoparticle can be modeled with Rayleigh-Debye-Gans (RDG) theory (see Section 2.1.2 in the main text). Rayleigh scattering is a

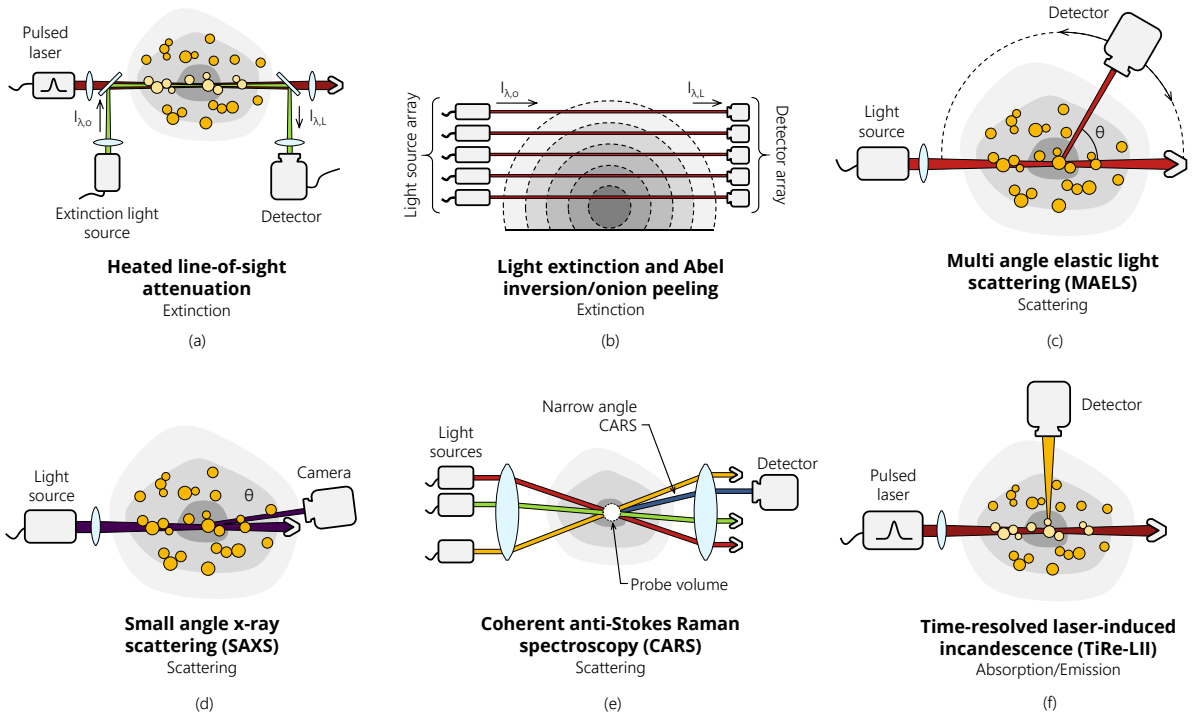

Figure A.3 Schemtics demonstrating select in situ techniques, including: (a) heated LOSA, (b) 1D light extinction measurement using onion peeling, (c) multi-angle elastic light scattering (MAELS), (d) small-angle x-ray scattering (SAXS) and (d) TiRe-LII.

further special case of elastic scattering where the features or interest, in this case the diameter of the nanoparticles or aggregate, are sufficiently smaller than the laser wavelength [151]. In this case, the light incites an electric polarization on the nanoparticles or aggregate inducing some electron oscillation. This can equivalently be understood as an excitation of the electrons in the nanoparticle as they interact with the applied electromagnetic field. The character of scattering is such that this excited state is only a virtual state through which the nanoparticle passes before reaching some ground state. A vast majority of electrons will return to their initial state, resulting in strong elastic or Rayleigh scattering. Rayleigh scattering forms the basis for the so-called RAYLIX system [92,93] that performs simultaneous LII, Rayleigh scattering, and extinction measurements to characterize soot. It has been noted that in the visible region of the spectrum, elastically scattered light can be sufficiently significant that it can cause problems in the detection of LII [96]. Such problems can generally be avoided by proper experimental design.

Mutli-angle elastic light scattering (MAELS or MALS) adds information by measuring the elastically scattered light at multiple angles relative to the incident beam, normally by rotating the detector or source around the observed flow [570,571]. A sample experimental setup is shown schematically in Figure A.3c. The added information allows for the determination of additional aggregate morphology parameters. The technique has commonly been applied in this regard to soot [570,572] and has been used in conjunction with extinction measurements [539] and LII [543]. Wide angle light scattering (WALS) removes the requirement of having to mechanically move the detector by using an ellipsoidal mirror to simultaneously capture scattering at many angles [573–575]. This light can be captured by a camera where it appears as a ring. This results in more robust measurements and improved temporal resolution.

Occasionally, elastic scattering is measured at other wavelengths. At shorter wavelengths into the visible range, the nanoparticles interact by Mie scattering (assuming they are spherical) and aggregate effects become more complex to model [153]. At even shorter wavelengths in the x-ray region, small angle x-ray scattering (SAXS) [576] measurements can be made in which elastic scattering is measured at angles close to the primary transmitted beam (shown schematically in Figure A.3d). As a result of the shorter wavelength, the light interacts with nanoscales features in the aerosol, making the technique particularly useful in detecting early stage soot too small to be detected by other techniques [577,578]. The technique also has limited use in conjunction with LII [553]. Ultra-small angle x-ray scattering (USAXS), which was used in Ref. [579] to characterize soot aggregates, pushes the limitation of x-ray scattering to larger features, often beyond 100 nm. The main challenge in these

techniques is distinguishing the primary transmitted beam of x-rays from those scattered at ultra-small angles. SAXS is rarely applied in this regard due to cost and mobility limitations.

Photon correlation spectroscopy (PCS), also known as dynamic light scattering (DLS), diffusion-broadening spectroscopy (DBS), or quasielastic light scattering (QELS), is a technique capable of sizing nanoparticles in the range of 1 nm to 1 μm [580]. Measurements of scattered light at a specific angle are made over time. The intensity in the scattered light will vary over time due to spectral broadening of light scattered from nanoparticles undergoing Brownian motion. The oscillation period increases as the nanoparticles get larger and slower. Various algorithms have been developed to calculate the nanoparticle size form these fluctuations. The technique has been applied to flames on several occasions [581–583]. Like many other scattering techniques, PCS is more sensitive to aggregate characteristics, rather than primary nanoparticle size.

Inelastic scattering occurs when the energy of the scattered light is different than that of the incident light. Raman scattering is the inelastic equivalent of Rayleigh scattering, where the nanoparticles relax into a different state than their initial state. In contrast to Rayleigh scattering, the Raman scattered light has a different frequency from the excitation light, with either a lower (Stokes) or higher energy and frequency (anti-Stokes). The available transitions in which electrons can participate are limited, resulting in a species-dependent spectrum exploited by Raman spectroscopy. Raman spectra has been used on soot to determine structural information about the nanoparticles [554,584]. Unfortunately, traditional Raman scattering techniques are often limited by noise in the collected data and the scattering is spherical, requiring the collection optics to be placed close to the observed process to measure a significant amount of scattered radiation. Surface-enhanced Raman spectroscopy (SERS) is a surface-sensitive technique expected to arise from either surface-plasmon or charge-transfer effects that enhances Raman signals from objects like metal nanoparticles considerably [585].

For gases, light interacts with the molecules in a similar way as nanoparticles, except that the wavelength of light is sufficiently large for the Rayleigh approximation to be applied over a wider range of wavelengths. In Rayleigh scattering, the scattered light takes on the same frequency as the incident light, with a certain about of line broadening due to effects like Doppler shift [586,587]. The amount of Rayleigh scattering from a gas is directly proportional to the number of scatterers and the concentration of the gas in any location. In the case that the gas pressure is known, the concentration can also be used for gas thermometry (cf. [588]), with similar ramifications on TiRe-LII analyses as extinction measurements on the gas phase. Unfortunately, the Rayleigh signal from the gas can easily be overwhelmed by elastic scattering from small nanoparticles such as soot, which may make

measurements in sooting flames infeasible or requiring spectral filtering. The scattering signal can also be overshadowed with laser-induced fluorescence (discussed in Section A.2.3), which results from the preferential absorption of photons that bring the electrons in the gas into an excited state. This can be avoided using gating [589] or tuning the excitation light to a wavelength that does not incite fluorescence.

Occasionally, the excited electrons in the gas will relax into a different state than their initial state, resulting in inelastic or Raman scattering. Raman spectroscopy is a mainstay combustion diagnostic used in determining gas species concentrations and for thermometry [590]. Combined measurements of Raman and Rayleigh scattering can improve analysis, where Raman scattering is used for species concentrations that act as inputs to thermometry by Rayleigh scattering [540,591]. Unfortunately, Raman scattering from gases suffers from the same signal problems as in the nanoparticle case, namely that the signals are often weak and require that the optics be placed close to the flame. Coherent anti-Stokes Raman spectroscopy (CARS), shown schematically in Figure A.3e, overcomes limitations in traditional Raman spectroscopy by inciting Raman scattering using three simultaneous, powerful laser pulses and making use of phase matching [592,593]. The Raman scattered light is then emitted in a relatively small angle (due to momentum constraints), resulting in a stronger signal. The spectrum can be split into its vibrational components to be fit to Boltzmann equation, allowing for accurate thermometry. As such, CARS is often used to provide gas temperatures as input to TiRe-LII analyses [143,218,555]. Bengtsson et al. [555] also noted how incandescence signals can corrupt CARS measurements, suggesting limiting the collection angle to differentiate between the different types of signals. The high accuracy of CARS comes at a high financial cost, however, requiring multiple lasers aligned at precise angles. The technique is also generally limited to point measurements (though studies employing 1D and 2D CARS have been performed at great cost to the practitioner [594,595]).

A.2.3 Absorption and emission diagnostics

Light can finally be absorbed and subsequently reemitted as a result of various phenomena. Laser-induced fluorescence (LIF), for example, involves excitation of electrons in the gas molecules by laser irradiation. The gas molecules will then spontaneously relay back to the ground state, first by vibrationally relaxation and then by emitting fluorescence. Excitation only occurs if the wavelength of incident light matches a transition available to the gas molecule so that LIF focuses on a single species at a time. The choice of incident wavelength depends on the target species. For example, OH, CH, and HCO (e.g. [596]) are intermediates that can gauge the progress of hydrocarbon combustion and the flame front [540]. Other intermediates, such as CN [597] and NO [598], can be

used to gauge the progress of nitrogen reactions in the flame. Determination of species concentrations is often limited to qualitative values due to complex physics of the fluorescence quenching process. However, by taking the ratio of the fluorescence at two specific wavelengths, researchers have been able to achieve quantitative estimate of temperature, cancelling out the uncertainties resulting of unknown quenching rates. Results can be improved by seeding flows with tracers (tracer LIF), which can be tuned for specific applications [599]. Planar (PLIF) [600–602] and volumetric (VLIF) [603–605], wherein a laser sheet is used to illuminate a plane or volume of flame that is imaged by a camera normal to the laser sheet, allow for the simultaneous measurement of a species concentration or temperature across the entire measurement domain, providing a wealth of spatial information about flames and other aerosol synthesis techniques. Under specific conditions, LIF from the C_2 swan bands has the capacity to corrupt LII signals, which is something LII practitioners must be aware of during experimentation. It should be noted, however, that this can be avoided with proper experimental design [72] (e.g. using a 1064 nm laser beam to avoid the C_2 swan bands). Further, Vander Wal [77] used simultaneously measurement of LII and LIF to track the formation of in-flame soot.

If the laser fluence is sufficiently high, the nanoparticle will vaporize and be ionized to form a plasma. Laser-induced breakdown spectroscopy (LIBS) (or, identically, laser-induced plasma spectroscopy, LIPS) examines the spectral emission from the plasma, which is characterized by broadband inverse Bremsstrahlung radiation and line emission that correspond to the chemical footprint of the nanoparticle and surrounding gases [606–608]. This is particularly useful within the context of fuels that contain trace amount of metals and other elements. Blevins et al. [609], for example, use LIBS to identify a range of elements, including Fe, Na, and Si, inside an industrial furnace. LIBS can be combined with LIF to simultaneously measure multiple species, while providing a high sensitivity towards a single species [606]. Phase-selective LIBS (PS-LIBS) or low-fluence LIBS is a modification to the traditional LIBS procedure at lower fluences that can distinguish between nanoparticle-based and gas emission. Such a technique is particularly useful within the context of metal-oxide nanoparticles in flames where one can distinguish between a metal precursor and the nanoparticle material [610–612].

Incandescence, that is thermal radiation (though, it is noted that *incandescence* is often limited to thermal radiation emitted in the visible spectrum), from flames is often measured without requiring laser excitation. This so-called *two-color method* is relatively simple, requiring measurement of the flame incandescence at two wavelengths. This can be used to define a pyrometric temperature and approximate SVF in the flame. A review of the contribution and methodology of the two-color method is provided by Payri et al. [613]. The technique, like

most extinction approaches, is inherently a LOS technique, measuring the culminative radiation emitted by soot along a path through the flame. This inherently introduce various uncertainties in the measurements, not the least of which is assumption regarding homogeneity of the soot in the flame. Despite these limitations, the simplicity and affordability of the technique makes it a common combustion diagnostic. LII builds off of the traditional two-color method by heating only a portion of the aerosol, thereby removing the LOS limitations of the original technique. Further, LII involves heating the nanoparticles to higher temperatures such that stronger signals are achieved.

Appendix B
List of LII studies on engineered nanoparticles

Table B.1 Summary of LII studies on engineered nanoparticles in the literature.

Study	Year	Materials	Experimental notes	Model	QoI
Weeks and Duley [614]	1974	Al_2O_3, C	Powders in a drift tube, 300 nm	Conduction, radiation, and absorption submodels	-
Vander Wal et al. [94]	1999	Fe, W, Mo, Ti	Laser ablation, examined fluence dependencies and emission spectra	-	-
Filippov et al. [44]	1999	C, Ag, TiN	Spark generator, powder in a shock tube	Conduction, evaporation, and absorption submodels	d_p
Altman et al. [46]	2001	SiO_2	Flame reactor	-	-
Starke et al. [23]	2003	Fe, C	Shock wave reactor, ~10 nm	Conduction (transition regime) submodel, temperature independent properties	d_p
Eom et al. [125]	2003	Si	Low-pressure plasma reactor	Melton model (conduction, evaporation, radiation, and absorption submodels)	d_p
Eom et al. [126]	2004	Si	Low-pressure plasma reactor	Melton/Holfeldt model (conduction, evaporation, radiation, and absorption submodels)	d_p
Kock et al. [21]	2005	Fe	Hot wall flow reactor, ~30 nm	Conduction, evaporation, and radiation submodels	d_p, α
Lehre et al. [127]	2005	MnO	Powders in an evaporation chamber, ~40 nm	Conduction, evaporation, radiation, and absorption submodels	Clausius-Clapeyron equation parameters

Study	Year	Materials	Experimental notes	Model	QoI
Murakami et al. [124]	2005	Mo	UV laser photolysis, fluence curves are included	Conduction submodel (temperature independent properties)	d_p
Eremin et al. [24]	2008	Fe	UV laser photolysis, a range of nanoparticle diameters	-	d_p, α
Maffi et al. [128]	2008	TiO_2	Flame reactor	-	-
Cignoli et al. [70]	2008	TiO_2	Flame reactor, 17-48 nm	-	-
Reimann et al. [133]	2010	Ni	-	-	-
Eremin et al. [129,201]	2011	Fe, C	Shock wave reactor, a range of nanoparticle diameters	Conduction, evaporation, and radiation submodels	d_p, $E(\mathbf{m}_\lambda)$
Tribalet et al. [134]	2012	Fe_2O_3	Low-pressure flame reactor	At least an evaporation submodel	d_p, α
Eremin et al. [130]	2013	Fe, C	Shock wave reactor, simultaneous extinction measurements, focus on evaporation model	Conduction, evaporation (with Kelvin equation), and radiation submodels	d_p, f_v, T_{peak}
Sipkens et al. [131]	2013	Mo	UV laser photolysis, reanalysis of data from Murakami et al. [124]	Conduction and evaporation (negligible) submodels	d_p/α
Sipkens et al. [48]	2014	Si	Low-pressure plasma reactor	Conduction and evaporation (Kelvin, Tolman, and Watson equations) submodels	d_p, σ_g
Sipkens et al. [112]	2015	Fe	Aerosolized colloid, 30-70 nm	Conduction and evaporation (with Kelvin, Tolman, and Watson equations) submodels	d_p, α
Eremin and Gurentsov [132]	2015	Mo	UV laser photolysis, study of nanoparticle formation	Conduction, evaporation, and radiation submodels	d_p, T_{peak}
Menser et al. [49]	2016	Si	Low-pressure plasma reactor, considered uncertainties in vapor pressure, LOSA measurements	Conduction, evaporation (Kelvin equation) submodels, and absorption submodels	d_p, α

Study	Year	Materials	Experimental notes	Model	QoI
Sipkens et al. [45]	2017	Fe, Ag, Mo	Aerosolized colloid, 30-70 nm, comparative study	Conduction and evaporation (with Kelvin and Watson equations) submodels	d_p, α
Daun et al. [443]	2016	Cu, Si	Plasma reactor (Si), arc discharge reactor (Cu), LOSA measurements	Spectroscopic model	-
Sipkens et al. [207]	2018	Fe	Aerosolized colloid, 30-70 nm, focus on model selection	Conduction and evaporation (with Kelvin equation) submodels	Δh_v
Menser et al. [135]	-	Ge	-	-	-

Appendix C
Notes on the thermal accommodation coefficient[7]

This appendix describes background on the definition and calculation of the thermal accommodation coefficient. The thermal accommodation coefficient is defined with respect to the conduction submodel in Section 2.2.3. From Eq. (2.32)

$$\alpha = \frac{\left\langle E_\mathrm{o} - E_\mathrm{i} \right\rangle}{\left\langle E_\mathrm{o} - E_\mathrm{i} \right\rangle_\mathrm{max}} = \frac{\left\langle E_\mathrm{o} \right\rangle - \left\langle E_\mathrm{i} \right\rangle}{\left\langle E_\mathrm{o} \right\rangle_\mathrm{max} - \left\langle E_\mathrm{i} \right\rangle_\mathrm{max}}. \tag{C2}$$

where the latter part of the expression is derived from the definition of an average. To calculate the TAC, one must now quantify the numerator and denominator of this expression.

C.1 The denominator: the maximum energy transfer

The maximum energy is defined by Eq. (2.33) in terms of thermodynamic degrees-of-freedom (DOF) and can be stated as

$$\left\langle E_\mathrm{o} - E_\mathrm{i} \right\rangle_\mathrm{max} = \frac{1}{2} k_\mathrm{B} \left(4 + \zeta_\mathrm{rot} \right) \left(T_\mathrm{p} - T_\mathrm{g} \right) = k_\mathrm{B} \left(2 + \frac{\zeta_\mathrm{rot}}{2} \right) \left(T_\mathrm{p} - T_\mathrm{g} \right). \tag{C3}$$

For simplicity, this appendix will only discuss monodisperse molecules, for which there are no rotational DOF, that is $\zeta_\mathrm{rot} = 0$. Considering the translational DOF, such an expression can be derived by considering the kinetic energy of the gas atom

$$E = \frac{1}{2} m_\mathrm{g} \left\| \mathbf{v} \right\|_2^2 = \frac{1}{2} m_\mathrm{g} \left(u^2 + v^2 + w^2 \right), \tag{C4}$$

[7] Information presented in this chapter overlaps work disseminated as:
Sipkens, T. A., and Daun, K. J., 2017, "Using cube models to understand trends in thermal accommodation coefficients at high surface temperatures," Int. J. Heat Mass Transf., **111**, pp. 54–64. doi: 10.1016/j.ijheatmasstransfer.2017.03.090

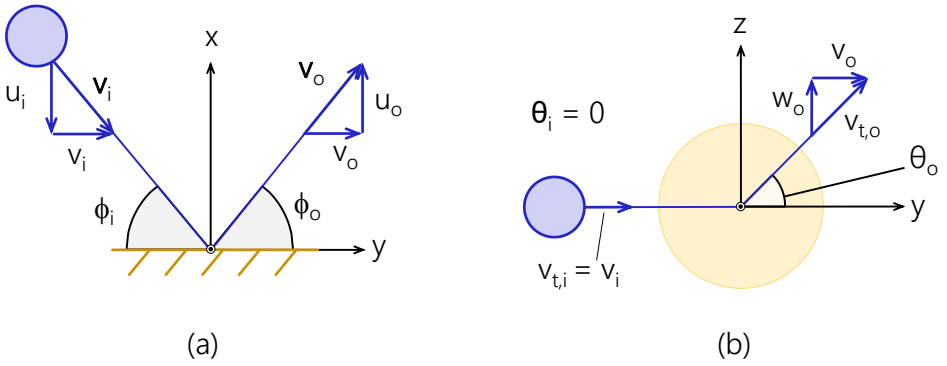

Figure C.1 Coordinate system used for the cube model analyses of Ref. [294] and for molecular dynamics simulations in the current work.

where $\mathbf{v} = [u, v, w]^T$ is a vector containing the gas atom velocity, which can be resolved into $\mathbf{v} = [v_n, v_t]^T$ where the normal, v_n, and tangential, v_t, components are defined relative to the local surface coordinate system in which the normal component is aligned with the x-axis, such that $v_n = u$ and $v_t = (v^2 + w^2)^{1/2}$. This matches the treatment of Ref. [294] and is shown schematically in Figure C.1. Here each component of the velocity; that is u, v, and w; represents a single thermodynamic DOF over which energy is distributed evenly. The average kinetic energy can then be calculated by integrating over the velocity distribution

$$\langle E \rangle = \int_{\mathbf{v}} \frac{1}{2} m_g \left(u^2 + v^2 + w^2 \right) f\left(\mathbf{v}, T \right) \mathrm{d}\mathbf{v} \,, \tag{C5}$$

where $f(\mathbf{v}, T)$ is the velocity distribution of the gas molecule. For TiRe-LII applications, the gas atom velocities will follow a Maxwell-Boltzmann distribution at the gas and surface temperatures for the incident and scattering conditions respectively, that is [187]

$$f_{\mathrm{MB}}\left(\mathbf{v}, T \right) = \frac{\beta_T^3}{\pi^{3/2}} \exp\left[-\beta_T^2 \left\| \mathbf{v} \right\|_2 \right], \tag{C6}$$

where $\beta_T = (m_g / 2 k_B T)^{1/2}$ is the inverse most probable speed of the gas. In the presence of a surface, this distribution is shifted to account for the fact that gas atoms with large velocity components normal to the surface are more likely to strike the surface, thus

$$f\left(\mathbf{v}, T \right) = \frac{2\beta_T^4}{\pi} w \exp\left[-\beta_T^2 \left\| \mathbf{v} \right\|_2 \right], \tag{C7}$$

The average energy transfer available can then be derived by integrating the kinetic energy over this distribution, that is by evaluating Eq. (C5) with this new distribution. This can be equally derived by considering the transport of kinetic energy across the boundary, in which case Eq. (C5) becomes [187]

$$\left\langle E\right\rangle=\int_{\mathbf{v}}\frac{1}{2}m_{\mathrm{g}}w\left(u^2+v^2+w^2\right)f\left(\mathbf{v},T\right)\mathrm{d}\mathbf{v}\,, \tag{C8}$$

where, in this case, the velocity distribution is Eq. (C6). In either case, upon evaluating the average energy transfer, one finds

$$\left\langle E\right\rangle_{\mathrm{MB}}=2k_{\mathrm{B}}T\,. \tag{C9}$$

Evaluating this expression at the gas and surface temperatures gives

$$\left\langle E_{\mathrm{o}}-E_{\mathrm{i}}\right\rangle_{\mathrm{max}}=2k_{\mathrm{B}}\left(T_{\mathrm{p}}-T_{\mathrm{g}}\right), \tag{C10}$$

which is Eq. (C3) for $\zeta_{\mathrm{rot}}=0$. Thus, the total TAC considering only the translational modes of DOF is

$$\alpha=\frac{\left\langle E_{\mathrm{o}}-E_{\mathrm{i}}\right\rangle}{2k_{\mathrm{B}}\left(T_{\mathrm{p}}-T_{\mathrm{g}}\right)}\,. \tag{C11}$$

Similar considerations can be used to define modes of energy transfer. For example, it is known that each of the velocity components in an unconstrained gas obey

$$f_{\mathrm{y}}\left(v,T\right)=\frac{\beta_{\mathrm{T}}}{\pi^{1/2}}\exp\left(-\beta_{\mathrm{T}}^2v^2\right), \tag{C12}$$

resulting in an energy for each of the translational modes or DOF of a free gas given by

$$\left\langle E_{\mathrm{o}}-E_{\mathrm{i}}\right\rangle_{\mathrm{max,x}}=\frac{1}{2}k_{\mathrm{B}}\left(T_{\mathrm{s}}-T_{\mathrm{g}}\right). \tag{C13}$$

For the normal component, the presence of the surface again causes the distribution to shift, such that

$$f_{\mathrm{n}}\left(w,T\right)=2\beta_{\mathrm{T}}^2\exp\left(-\beta_{\mathrm{T}}^2v^2\right), \tag{C14}$$

resulting in a maximum energy in the normal mode of

$$\left\langle E_{\mathrm{o}}-E_{\mathrm{i}}\right\rangle_{\mathrm{max,n}}=k_{\mathrm{B}}\left(T_{\mathrm{s}}-T_{\mathrm{g}}\right). \tag{C15}$$

Accordingly, the normal TAC is defined as

$$\alpha_{\mathrm{n}}=\frac{\left\langle E_{\mathrm{o}}-E_{\mathrm{i}}\right\rangle_{\mathrm{n}}}{k_{\mathrm{B}}\left(T_{\mathrm{s}}-T_{\mathrm{g}}\right)}\,. \tag{C16}$$

The tangential component can be considered analogous to the normal component as a flux through a plane normal to the surface, thus

$$\left\langle E_{\mathrm{o}}-E_{\mathrm{i}}\right\rangle_{\mathrm{max,t}}=k_{\mathrm{B}}\left(T_{\mathrm{s}}-T_{\mathrm{g}}\right) \tag{C17}$$

and

$$\alpha_{\mathrm{t}}=\frac{\left\langle E_{\mathrm{o}}-E_{\mathrm{i}}\right\rangle_{\mathrm{t}}}{k_{\mathrm{B}}\left(T_{\mathrm{s}}-T_{\mathrm{g}}\right)}. \tag{C18}$$

By this definition, the total TAC is defined as the average of the normal and tangential TACs, that is $\alpha = (\alpha_n + \alpha_t)/2$.

C.2 The numerator: the true energy transfer

The numerator can be phrased in terms of changes in the observed kinetic energy of the gas atoms, that is

$$\left\langle E_{\mathrm{o}}-E_{\mathrm{i}}\right\rangle=\frac{1}{2}m_{\mathrm{g}}\left\langle\left\|\mathbf{v}_{\mathrm{o}}\left(\mathbf{v}_{\mathrm{i}},\Phi\right)\right\|_2^2-\left\|\mathbf{v}_{\mathrm{i}}\right\|_2^2\right\rangle=\frac{1}{2}m_{\mathrm{g}}\left[\left\langle\left\|\mathbf{v}_{\mathrm{o}}\left(\mathbf{v}_{\mathrm{i}},\Phi\right)\right\|_2^2\right\rangle-\left\langle\left\|\mathbf{v}_{\mathrm{i}}\right\|_2^2\right\rangle\right]. \tag{C19}$$

where $\mathbf{v}_{\mathrm{o}}$ and $\mathbf{v}_{\mathrm{i}}$ are the scattered and incident velocities respectively, with the scattered velocity depending on the surface state, denoted as Φ, and the incident velocity, $\mathbf{v}_{\mathrm{i}}$. The *surface state* here refers to the arrangement and velocity of the atoms over the duration of the gas-surface interaction, and, in this regard, there is not a simple way of parameterization for Φ. Rather, it is more likely to be defined in a probabilistic sense. These can be equivalently defined for the normal and tangential components as

$$\left\langle E_{\mathrm{o}}-E_{\mathrm{i}}\right\rangle_{\mathrm{n}}=\frac{1}{2}m_{\mathrm{g}}\left[\left\langle\left[w_{\mathrm{o}}\left(\mathbf{v}_{\mathrm{i}},\Phi\right)\right]^2\right\rangle-\left\langle w_{\mathrm{i}}^2\right\rangle\right] \tag{C20}$$

and

$$\left\langle E_{\mathrm{o}}-E_{\mathrm{i}}\right\rangle_{\mathrm{t}}=\frac{1}{2}m_{\mathrm{g}}\left[\left\langle\left[v_{\mathrm{t,o}}\left(\mathbf{v}_{\mathrm{i}},\Phi\right)\right]^2\right\rangle-\left\langle v_{\mathrm{t,i}}^2\right\rangle\right], \tag{C21}$$

respectively. These averages can then be stated in terms of an integral over the distribution of surface states and incident velocities,

$$\left\langle E_{\mathrm{o}}-E_{\mathrm{i}}\right\rangle=\frac{1}{2}m_{\mathrm{g}}\int_{\Phi}\int_{\mathbf{v}_{\mathrm{i}}}\left(\left\|\mathbf{v}_{\mathrm{o}}\left(\mathbf{v}_{\mathrm{i}},\Phi\right)\right\|_2^2-\left\|\mathbf{v}_{\mathrm{i}}\right\|_2^2\right)f_{\mathrm{i}}\left(\mathbf{v}_{\mathrm{i}},T_{\mathrm{g}}\right)p_{\Phi}\left(\Phi,T_{\mathrm{s}}\right)\cdot\mathrm{d}\mathbf{v}_{\mathrm{i}}\cdot\mathrm{d}\Phi\,. \tag{C22}$$

When propagating Eq. (C22) forward to a TAC, practitioners often define a value of the TAC for a specific set of input conditions, such that

$$\alpha=\int_{\Phi}\int_{\mathbf{v}_{\mathrm{i}}}\gamma\left(\mathbf{v}_{\mathrm{i}},\Phi\right)\cdot f_{\mathrm{i}}\left(\mathbf{v}_{\mathrm{i}},T_{\mathrm{g}}\right)\cdot p_{\Phi}\left(\Phi,T_{\mathrm{s}}\right)\cdot\mathrm{d}\mathbf{v}_{\mathrm{i}}\cdot\mathrm{d}\Phi\,, \tag{C23}$$

where, for a monatomic gas,

$$\gamma\left(\mathbf{v}_{\mathrm{i}},\Phi\right)=\frac{E_{\mathrm{o}}-E_{\mathrm{i}}}{\left\langle E_{o}-E_{i}\right\rangle_{\max}}=\frac{m_{\mathrm{v}}\left(\left\|\mathbf{v}_{\mathrm{o}}\left(\mathbf{v}_{\mathrm{i}},\Phi\right)\right\|_{2}^{2}-\left\|\mathbf{v}_{\mathrm{i}}\right\|_{2}^{2}\right)}{4k_{\mathrm{B}}\left(T_{\mathrm{s}}-T_{\mathrm{g}}\right)}. \tag{C24}$$

Analogous treatments can be applied for the different translational modes. This shifts the problem to determining an appropriate distribution for the scattered velocity.

C.3 The scattering kernel

In general, the scattered velocity distribution required for Eq. (C22) and (C23) can be described by

$$w_{\mathrm{o}}f_{\mathrm{o}}\left(\mathbf{v}_{\mathrm{o}}\right)=\int_{\Phi}\int_{u_{\mathrm{i}}<0}w_{\mathrm{i}}f_{\mathrm{i}}\left(\mathbf{v}_{\mathrm{i}},T_{\mathrm{g}}\right)p_{\Phi}\left(\Phi,T_{\mathrm{s}}\right)K\left(\mathbf{v}_{\mathrm{i}},\Phi,\mathbf{v}_{\mathrm{o}}\right)\cdot\mathrm{d}\mathbf{v}_{\mathrm{i}}\cdot\mathrm{d}\Phi. \tag{C25}$$

where $K(\mathbf{v}_{\mathrm{i}},\Phi,\mathbf{v}_{\mathrm{o}})$ is the scattering kernel that probabilistically maps the incident velocity and surface state to an output velocity. In many cases, the probabilistic nature of variations in the surface state are absorbed into the kernel, effectively marginalizing over the surface state so that,

$$w_{\mathrm{o}}f_{\mathrm{o}}\left(\mathbf{v}_{\mathrm{o}}\right)=\int_{u_{\mathrm{i}}<0}w_{\mathrm{i}}f_{\mathrm{i}}\left(\mathbf{v}_{\mathrm{i}},T_{\mathrm{g}}\right)K\left(\mathbf{v}_{\mathrm{i}},\mathbf{v}_{\mathrm{o}}\right)\mathrm{d}\mathbf{v}_{\mathrm{i}}. \tag{C26}$$

In many cases, mathematical forms for the kernel are chosen for convenience, while still satisfying certain basic physical principles (e.g. the Principle of Detailed Balancing [615]). The best known of these kernels is the Maxwell kernel [616,617], which is a linear combination of (i) diffuse (Lambertian) emission that is typical of complete thermal accommodation and (ii) a specular component in which the normal incident velocity is reflected and the tangential component is unchanged. The more elaborate Cercignani-Lampis kernel [618,619] is defined empirically based on detailed balancing and assumes that energy is accommodated independently into the normal and tangential energy modes of the gas molecule. Both of these kernels take the TAC as an input variable and, while useful in simplifying the physical mechanism underlying scattering and the scattered velocity distribution (which may be important when considering heat conduction from aggregates [113,114,118,197]), cannot be used directly to calculate the TAC.

The Baule model [287], in contrast, maps the initial velocity to the scattered velocity by applying conservation of linear momentum to a head-on elastic collision between a gas atom and a single surface atom initially at rest [286]. An expression for the thermal accommodation coefficient can then be derived as

$$\alpha = \frac{4\mu}{\left(1+\mu\right)^2} = \frac{4\mu}{\mu^2+2\mu+1}, \tag{C27}$$

where $\mu = m_g/m_s$ is the mass ratio. This expression can be generalized to consider off-normal collisions [286,620] such that

$$\alpha = \frac{A\mu}{\left(1+\mu\right)^2} = \frac{A\mu}{\mu^2+2\mu+1}, \tag{C28}$$

where A ranges from 2 to 4 [286,621] depending on the conditions of incidence and problem geometry. This treatment can be extended to a larger lattice of initially stationary atoms connected by linear springs, corresponding to a harmonic potential (that is, lattice theory) [286,622,623]. Unfortunately, these simple theories presume that the surface atoms are approximately stationary relative to the gas molecules [286], which is not the case at high surface temperatures where the thermal motion of the surface atoms strongly influence gas-surface scattering. Modeling this scenario requires more advanced dynamics models.

C.4 Sampling methods and dynamics models

While closed-form scattering kernels reproduce observed scattering probability distributions, they are empirically-derived and do not replicate the true scattering physics. Instead many practitioners bypass Eq. (C25) and use dynamics models of gas-surface scattering. While these models generally cannot be manipulated into closed-form analytical solutions for the scattering kernel, scattered velocity distribution, or TAC [624], they are more explicit in their treatment of the problem physics relative to the approximate kernels. Evaluating the double integral in Eq. (C22) can then be performed using Monte Carlo integration. In this method, k samples of the initial velocity and surface state are drawn from the appropriate distributions, that is $\mathbf{v}_i^k \sim p_i(\mathbf{v}_i)$ and $\omega^k \sim p(\omega)$. The scattered velocity for any given sample is then calculated using the proposed samples, and Eq. (C22) is approximated by

$$\left\langle E_o - E_i \right\rangle \approx \frac{1}{N}\sum_{k=1}^{N}\frac{1}{2}m_g\left[\left\|\mathbf{v}_o^k\left(\mathbf{v}_i^k,\Phi^k\right)\right\|_2^2 - \left\|\mathbf{v}_i^k\right\|_2^2\right]. \tag{C29}$$

where $N$is the number of samples. This can be equally phrased in terms of the TAC for each trial

$$\alpha \approx \frac{1}{N}\sum_{k=1}^{N}\gamma^k\left(\mathbf{v}_i^k,\Phi^k\right). \tag{C30}$$

This approximation asymptotically approaches Eq. (C22) or Eq. (C23) as the number of samples increases. Various approaches can now be applied. Most are dynamics-based models that use physics to model the gas-surface

interaction and calculate γ. These techniques include the cube models and molecular dynamics simulations, the latter of which features in Chapter 7 in the main text.

C.4.1 The cube models

Cube models incorporate the thermal motion of surface atoms [286,288,289,625]. The name *cube* derives from the fact that most of these models assume a strictly one-dimensional *normal* interaction, which one would expect if the surface were flat or cube-like. Recent work by the author [294] demonstrated the usefulness of three types of cube models in interpreting MD simulations. The simplest of these model is the hard cube (HC) model [288], which approximates the surface using a cube that moves with a constant velocity between two bounds. In this way, the distribution of the surface states is parameterized using the velocity of the surface cube in each sample. The second, the soft cube (SC) model [289], attaches the surface cube to a spring that is fixed to a stationary surface, representing forces from the remaining lattice. This feature is intended to more closely approximate the dynamics of a real surface and allows for another free quantity to parameterize the surface estate: the elastic constant of the spring. Finally, the authors considered the washboard model [626], which is identical to the hard cube model except in that the cube is allowed to be oriented at an angle to incorporate corrugation in the surface. A schematic summarizing these three models is provided in Figure C.2. Sipkens and Daun [294] showed that, while these simple dynamics models could predict the trends in the TAC with some of the key parameters, such as with mass ratio and temperature, the models could not be used to produce realistic quantitative estimates of the TAC.

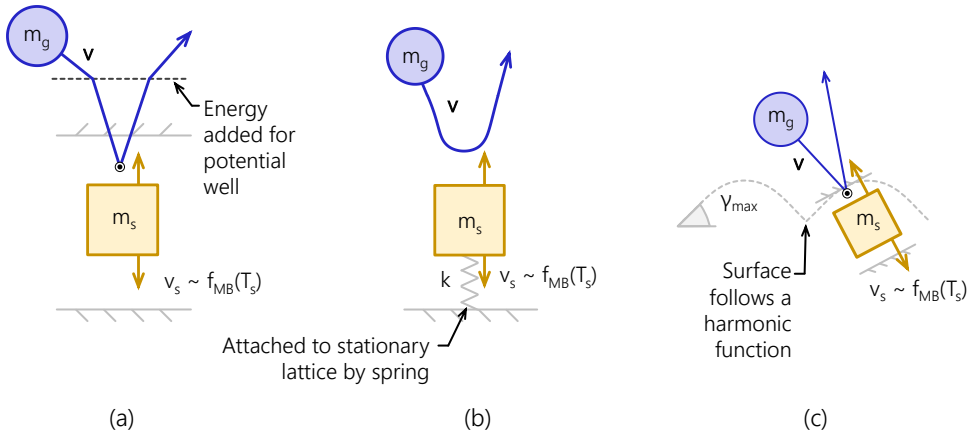

Figure C.2 Schematics describing the cube models, including (a) the hard cube (HC) model, (b) the soft cube (SC) model, and (c) the washboard model.

C.4.2 Molecular dynamics simulations

Molecular dynamics (MD) presents a higher fidelity approximation to the true gas surface interaction, by modeling the interaction of gas atoms with a subset of the full lattice. In MD, atomic positions are iteratively updated based on atomic velocities and forces, the latter of which is obtained by differentiating interatomic potentials with respect to displacement. Further information on this approach to calculating the TAC is provided in Chapter 7 of the main text.

References

[1] Huber, D. L., 2005, "Synthesis, Properties, and Applications of Iron Nanoparticles," Small, **1**(5), pp. 482–501.

[2] O'Farrell, N., Houlton, A., and Horrocks, B., 2006, "Silicon Nanoparticles: Applications in Cell Biology and Medicine," Int. J. Nanomedicine, **1**(4), pp. 451–472.

[3] Kummer, M., Badillo, J. P., Schmitz, A., Bremes, H. G., Winter, M., Schulz, C., and Wiggers, H., 2014, "Silicon/Polyaniline Nanocomposites as Anode Material for Lithium Ion Batteries," J. Electrochem. Soc., **161**(1), pp. A40–A45.

[4] Pavesi, L., and Turan, R., 2010, *Silicon Nanocrystals: Fundamentals, Synthesis and Applications*, John Wiley & Sons, Weinheim.

[5] Konstantatos, G., and Sargent, E. H., 2010, "Nanostructured Materials for Photon Detection," Nat. Nanotechnol., **5**(6), pp. 391–400.

[6] Rai, M., Yadav, A., and Gade, A., 2009, "Silver Nanoparticles as a New Generation of Antimicrobials," Biotechnol. Adv., **27**(1), pp. 76–83.

[7] Gaylarde, C. C., Morton, L. H. G., Loh, K., and Shirakawa, M. A., 2011, "Biodeterioration of External Architectural Paint Films–A Review," Int. Biodeterior. Biodegradation, **65**(8), pp. 1189–1198.

[8] Abou El-Nour, K. M. M., Eftaiha, A., Al-Warthan, A., and Ammar, R. A. A., 2010, "Synthesis and Applications of Silver Nanoparticles," Arab. J. Chem., **3**(3), pp. 135–140.

[9] Bolzinger, M. A., Briançon, S., and Chevalier, Y., 2011, "Nanoparticles through the Skin: Managing Conflicting Results of Inorganic and Organic Particles in Cosmetics and Pharmaceutics," Wiley Interdiscip. Rev. Nanomedicine Nanobiotechnology, **3**(5), pp. 463–478.

[10] Kango, S., Kalia, S., Celli, A., Njuguna, J., Habibi, Y., and Kumar, R., 2013, "Surface Modification of Inorganic Nanoparticles for Development of Organic-Inorganic Nanocomposites - A Review," Prog. Polym. Sci., **38**(8), pp. 1232–1261.

[11] Kruis, F. E., Fissan, H., and Peled, A., 1998, "Synthesis of Nanoparticles in the Gas Phase for Electronic, Optical and Magnetic Applications—a Review," J. Aerosol Sci., **29**(5–6), pp. 511–535.

[12] Zeng, S., Yong, K. T., Roy, I., Dinh, X. Q., Yu, X., and Luan, F., 2011, "A Review on Functionalized Gold Nanoparticles for Biosensing Applications," Plasmonics, **6**(3), pp. 491–506.

[13] Pradeep, T., and Anshup, 2009, "Noble Metal Nanoparticles for Water Purification: A Critical Review," Thin Solid Films, **517**(24), pp. 6441–6478.

[14] Savage, N., and Diallo, M. S., 5AD, "Nanomaterials and Water Purification: Opportunities and Challenges," J. Nanoparticle Res., **7**(4–5), pp. 331–342.

[15] Ambashta, R. D., and Sillanpää, M., 2010, "Water Purification Using Magnetic Assistance: A Review," Jounral Hazard. Mater., **180**(1–3), pp. 38–49.

[16] Duguet, E., Vasseur, S., Mornet, S., and Devoisselle, J. M., 2006, "Magnetic Nanoparticles and Their Applications in Medicine," Nanomedicine, **1**(2), p. 157.

[17] Granqvist, C., Kish, L., and Marlow, W., 2004, *Gas Phase Nanoparticle Synthesis Gas Phase Nanoparticle*, Springer, Dordecht.

[18] Swihart, M. T., 2003, "Vapor-Phase Synthesis of Nanoparticles," Curr. Opin. Colloid Interface Sci., **8**(1), pp. 127–133.

[19] Kammler, H. K., Mädler, L., and Pratsinis, S. E., 2001, "Flame Synthesis of Nanoparticles," Chem. Eng. Technol., **24**(6), pp. 583–596.

[20] Mariotti, D., and Sankaran, R. M., 2010, "Microplasmas for Nanomaterials Synthesis," J. Phys. D. Appl. Phys., **43**(32), p. 323001.

[21] Kock, B. F., Kayan, C., Knipping, J., Orthner, H. R., and Roth, P., 2005, "Comparison of LII and TEM Sizing during Synthesis of Iron Particle Chains," Proc. Combust. Inst., **30**(1), pp. 1689–1696.

[22] Knipping, J., Wiggers, H., Rellinghaus, B., Roth, P., Konjhodzic, D., and Meier, C., 2004, "Synthesis of High Purity Silicon Nanoparticles in a Low Pressure Microwave Reactor," J. Nanosci. Nanotechnol., **4**(8), pp. 1039–1044.

[23] Starke, R., Kock, B., and Roth, P., 2003, "Nano-Particle Sizing by Laser-Induced-Incandescence (LII) in a Shock Wave Reactor," Shock Waves, **12**(5), pp. 351–360.

[24] Eremin, A., Gurentsov, E., and Schulz, C., 2008, "Influence of the Bath Gas on the Condensation of Supersaturated Iron Atom Vapour at Room Temperature," J. Phys. D. Appl. Phys., **41**(5), p. 055203.

[25] Choi, C. J., Tolochko, O., and Kim, B. K., 2002, "Preparation of Iron Nanoparticles by Chemical Vapor Condensation," Mater. Lett., **56**(3), pp. 289–294.

[26] Gresback, R., Holman, Z., and Kortshagen, U., 2007, "Nonthermal Plasma Synthesis of Size-Controlled, Monodisperse, Freestanding Germanium Nanocrystals," Appl. Phys. Lett., **91**(9), p. 93119.

[27] Petermann, N., Stein, N., Schierning, G., Theissmann, R., Stoib, B., Brandt, M. S., Hecht, C., Schulz, C., Wiggers, H., Stein, N.; Schierning, G., Theissmann, R., Stoib, B., Brandt, M. S., Hecht, C., Schulz, C., and Wiggers, H., 2011, "Plasma Synthesis of Nanostructures for Improved Thermoelectric Properties," J. Phys. D. Appl. Phys., **44**(17), p. 174034.

[28] Bondarenko, O., Juganson, K., Ivask, A., Kasemets, K., Mortimer, M., and Kahru, A., 2013, "Toxicity of Ag, CuO and ZnO Nanoparticles to Selected Environmentally Relevant Test Organisms and Mammalian Cells in Vitro: A Critical Review," Arch. Toxicol., **87**(7), pp. 1181–1200.

[29] Srivastava, V., Gusain, D., and Sharma, Y. C., 2015, "Critical Review on the Toxicity of Some Widely Used Engineered Nanoparticles," Ind. Eng. Chem. Res., **54**(24), pp. 6209–6233.

[30] Shi, H., Magaye, R., Castranova, V., and Zhao, J., 2013, "Titanium Dioxide Nanoparticles: A Review of Current Toxicological Data," Part. Fibre Toxicol., **10**(1), pp. 15–47.

[31] Mueller, N. C., and Nowack, B., 2008, "Exposure Modelling of Engineered Nanoparticles in the Environment," Environ. Sci. Technol., **42**(12), pp. 4447–4453.

[32] Gottschalk, F., Sonderer, T., Scholz, R. W., and Nowack, B., 2009, "Modeled Environmental Concentrations of Engineered Nanomaterials (TiO2, ZnO, Ag, CNT, Fullerenes) for Different Regions," Environ. Sci. Technol., **43**(24), pp. 9216–9222.

[33] Dwivedi, A. D., Dubey, S. P., Sillanpää, M., Kwon, Y. N., Lee, C., and Varma, R. S., 2015, "Fate of Engineered Nanoparticles: Implications in the Environment," Coord. Chem. Rev., **287**, pp. 64–78.

[34] Navarro, E., Baun, A., Behra, R., Hartmann, N. B., Filser, J., Miao, A. J., Quigg, A., Santschi, P. H., and Sigg, L., 2008, "Environmental Behavior and Ecotoxicity of Engineered Nanoparticles to Algae, Plants, and Fungi," Ecotoxicology, **17**(5), pp. 372–386.

[35] Maurer-Jones, M. A., Gunsolus, I. L., Murphy, C. J., and Haynes, C. L., 2013, "Toxicity of Engineered Nanoparticles in the Environment," Anal. Chem., **85**(6), pp. 3036–3049.

[36] Seaton, A., Godden, D., MacNee, W., and Donaldson, K., 1995, "Particulate Air Pollution and Acute Health Effects," Lancet, **345**(8943), pp. 176–178.

[37] Raaschou-Nielsen, O., Andersen, Z. J., Beelen, R., Samoli, E., Stafoggia, M., Weinmayr, G., Hoffmann, B., Fischer, P., Nieuwenhuijsen, M. J., Brunekreef, B., and Xun, W. W., 2013, "Air Pollution and Lung Cancer Incidence in 17 European Cohorts: Prospective Analyses from the European Study of Cohorts for Air Pollution Effects (ESCAPE)," Lancet Oncol., **14**(9), pp. 813–822.

[38] Moskal, A., Makowski, Ł., Sosnowski, T. R., and Gradoń, L., 2006, "Deposition of Fractal-like Aerosol Aggregates in a Model of Human Nasal Cavity," Inhal. Toxicol., **18**(10), pp. 725–731.

[39] Kittelson, D. B., 1998, "Engines and Nanoparticles: A Review," J. Aerosol Sci., **29**(5–6), pp. 575–588.

[40] Mayer, A., Egli, H., Burtscher, H., Czerwinski, J., and Gehrig, D., 1995, "Particle Size Distribution Downstream Traps of Different Design," J. Engines, **104**, pp. 732–742.

[41] Bond, T. C., and Bergstrom, R. W., 2006, "Light Absorption by Carbonaceous Particles: An Investigative Review," Aerosol Sci. Technol., **40**(1), pp. 27–67.

[42] Coderre, A. R., Thomson, K. A., Snelling, D. R., and Johnson, M. R., 2011, "Spectrally Resolved Light Absorption Properties of Cooled Soot from a Methane Flame," Appl. Phys. B, **104**(1), pp. 175–188.

[43] Vander Wal, R. L., 1996, "Laser-Induced Incandescence: Detection Issues," Appl. Opt., **35**(33), pp. 6548–6559.

[44] Filippov, A. V, Markus, M. W., and Roth, P., 1999, "In-Situ Characterization of Ultrafine Particles by Laser-Induced Incandescence: Sizing and Particle Structure Determination," J. Aerosol Sci., **30**(1), pp. 71–87.

[45] Sipkens, T. A., Singh, N. R., and Daun, K. J., 2017, "Time-Resolved Laser-Induced Incandescence Characterization of Metal Nanoparticles," Appl. Phys. B, **123**(1), pp. 14–30.

[46] Altman, I. S., Lee, D., Chung, J. D., Song, J., and Choi, M., 2001, "Light Absorption of Silica Nanoparticles," Phys. Rev. B, **63**(16), p. 161402.

[47] Lehre, T., Bockhorn, H., Jungfleisch, B., and Suntz, R., 2003, "Development of a Measuring Technique for Simultaneous in Situ Detection of Nanoscaled Particle Size Distributions and Gas Temperatures," Chemosphere, **51**(10), pp. 1055–1061.

[48] Sipkens, T. A., Mansmann, R., Daun, K. J., Petermann, N., Titantah, J. T., Karttunen, M., Wiggers, H., Dreier, T., and Schulz, C., 2014, "In Situ Nanoparticle Size Measurements of Gas-Borne Silicon Nanoparticles by Time-Resolved Laser-Induced Incandescence," Appl. Phys. B, **116**(3), pp. 623–636.

[49] Menser, J., Daun, K., Dreier, T., and Schulz, C., 2016, "Laser-Induced Incandescence from Laser-Heated Silicon Nanoparticles," Appl. Phys. B, **122**(11), pp. 1–15.

[50] Ni, T., Pinson, J. A., Gupta, S., and Santoro, R. J., 1995, "Two-Dimensional Imaging of Soot Volume Fraction by the Use of Laser-Induced Incandescence," Appl. Opt., **34**(30), p. 7083.

[51] Vander Wal, R. L., and Weiland, K. J., 1994, "Laser-Induced Incandescence: Development and Characterization towards a Measurement of Soot-Volume Fraction," Appl. Phys. B, **59**(4), pp. 445–452.

[52] De Iuliis, S., Cignoli, F., and Zizak, G., 2005, "Two-Color Laser-Induced Incandescence (2C-LII) Technique for Absolute Soot Volume Fraction Measurements in Flames," Appl. Opt., **44**(34), pp. 7414–7423.

[53] Hult, J., Omrane, A., Nygren, J., Kaminski, C., Axelsson, B., Collin, R., Bengtsson, P. E., and Aldén, M., 2002, "Quantitative Three-Dimensional Imaging of Soot Volume Fraction in Turbulent Non-Premixed Flames," Exp. Fluids, **33**(2), pp. 265–269.

[54] Geigle, K.-P., Hadef, R., and Meier, W., 2013, "Soot Formation and Flame Characterization of an Aero-Engine Model Combustor Burning Ethylene at Elevated Pressure," J. Eng. Gas Turbines Power, **136**(2), p. 021505.

[55] Boiarciuc, A., Foucher, F., and Mounaïm-Rousselle, C., 2006, "Soot Volume Fractions and Primary Particle Size Estimate by Means of the Simultaneous Two-Color-Time-Resolved and 2D Laser-Induced Incandescence," Appl. Phys. B, **83**(3), pp. 413–421.

[56] Snelling, D. R., Thomson, K. A., Smallwood, G. J., and Gülder, Ö. L., 1999, "Two-Dimensional Imaging of Soot Volume Fraction in Laminar Diffusion Flames," Appl. Opt., **38**(12), pp. 2478–2485.

[57] Weeks, R. W., and Duley, W. W., 1974, "Aerosol-particle Sizes from Light Emission during Excitation by TEA CO2 Laser Pulses," J. Appl. Phys., **45**(10), pp. 4661–4662.

[58] Eckbreth, A. C., 1977, "Effects of Laser-Modulated Particulate Incandescence on Raman Scattering Diagnostics," J. Appl. Phys., **48**(11), pp. 4473–4479.

[59] Melton, L. A., 1984, "Soot Diagnostics Based on Laser Heating," Appl. Opt., **23**(13), pp. 2201–2208.

[60] Dasch, C. J., 1984, "Continuous-Wave Probe Laser Investigation of Laser Vaporization of Small Soot Particles in a Flame," Appl. Opt., **23**(13), pp. 2209–2215.

[61] Rohlfing, E. A., 1988, "Optical Emission Studies of Atomic, Molecular, and Particulate Carbon Produced from a Laser Vaporization Cluster Source," J. Chem. Phys., **89**(10), pp. 6103–6112.

[62] zur Loye, A. O., Siebers, D. l., and Dec, J. E., 1990, "2-D Soot Imaging in a Direct-Injection Diesel Engine Using Laser-Induced Incandescence," *Proceedings of the International Symposium COMODIA*, pp. 523–528.

[63] Dec, J. E., zur Loye, A. O., and Siebers, D. L., 1991, "Soot Distribution in a DI Diesel Engine Using 2-D Laser-Induced Incandescence Imaging," SAE Int. J. Engines, **100**(3), pp. 277–288.

[64] Pinson, J. A., Mitchell, D. L., Santoro, R. J., and Litzinger, T. A., 1993, "Quantitative, Planar Soot Measurements in a DI Diesel Engine Using Laser-Induced Incandescence and Light Scattering," SAE Tech. Pap., (932650).

[65] Quay, B., Lee, T. W., Ni, T., and Santoro, R. J., 1994, "Spatially Resolved Measurements of Soot Volume Fraction Using Laser-Induced Incandescence," Combust. Flame, **97**(3–4), pp. 384–392.

[66] Cignoli, F., Benecchi, S., and Zizak, G., 1994, "Time-Delayed Detection of Laser-Induced Incandescence for the Two-Dimensional Visualization of Soot in Flames," Appl. Opt., **33**(24), pp. 5778–5782.

[67] Tait, N. P., and Greenhalgh, D. A., 1993, "PLIF Imaging of Fuel Fraction in Practical Devices And LII Imaging of Soot," Berichte der Bunsengesellschaft fuer Phys. Chemie, **97**(12), pp. 1619–1625.

[68] Vander Wal, R. L., 1997, "LIF-LII Measurements in a Turbulent Gas-Jet Flame," Exp. Fluids, **23**(4), pp. 281–287.

[69] Appel, J., Jungfleisch, B., Marquardt, M., Suntz, R., and Bockhorn, H., 1996, "Assessment of Soot Volume Fractions from Laser-Induced Incancescence by Comparison with Extinction Measurements in Laminar, Premixed, Flat Flames," Symp. Combust., **26**(2), pp. 2387–2395.

[70] Cignoli, F., Bellomunno, C., Maffi, S., and Zizak, G., 2009, "Laser-Induced Incandescence of Titania Nanoparticles Synthesized in a Flame," Appl. Phys. B, **96**(4), pp. 593–599.

[71] Shaddix, C. R., Harrington, J. E., and Smyth, K. C., 1994, "Quantitative Measurements of Enhanced Soot Production in a Flickering Methane/Air Diffusion Flame," Combust. Flame, **99**(3–4), pp. 723–732.

[72] Shaddix, C. R., and Smyth, K. C., 1996, "Laser-Induced Incandescence Measurements of Soot Production in Steady and Flickering Methane, Propane, and Ethylene Diffusion Flames," Combust. Flame, **107**(4), pp. 418–452.

[73] Bengtsson, P. E., and Aldén, M., 1995, "Soot-Visualization Strategies Using Laser Techniques - Laser-Induced Fluorescence in C2 from Laser-Vaporized Soot and Laser-Induced Soot Incandescence," Appl. Phys. B, **60**(1), pp. 51–59.

[74] Vander Wal, R. L., and Dietrich, D. L., 1995, "Laser-Induced Incandescence Applied to Droplet Combustion," Appl. Opt., **34**(6), pp. 1103–1107.

[75] Vander Wal, R. L., Zhou, Z., and Choi, M. Y., 1996, "Laser-Induced Incandescence Calibration via Gravimetric Sampling," Combust. Flame, **105**(4), pp. 462–470.

[76] Case, M. K., and Hofeldt, D. L., 1996, "Soot Mass Concentration Measurements in Diesel Engine Exhaust Using Laser-Induced Incandescence," Aerosol Sci. Technol., **25**(1), pp. 46–60.

[77] Vander Wal, R. L., 1998, "Soot Precursor Carbonization: Visualization Using LIF and LII and Comparison Using Bright and Dark Field TEM," Combust. Flame, **112**(4), pp. 607–616.

[78] Vander Wal, R. L., 2018, "Soot Precursor Material: Visualization via Simultaneous LIF-LII and Characterization via TEM," Symp. Combust., **26**(2), pp. 2269–2275.

[79] Vander Wal, R. L., Jensen, K. A., and Choi, M. Y., 1997, "Simultaneous Laser-Induced Emission of Soot and Polycyclic Aromatic Hydrocarbons within a Gas-Jet Diffusion Flame," Combust. Flame, **109**(3), pp. 399–414.

[80] Mewes, B., and Seitzman, J. M., 1997, "Soot Volume Fraction and Particle Size Measurements with Laser-Induced Incandescence.," Appl. Opt., **36**(3), pp. 709–717.

[81] Snelling, D. R., Gareau, D. R., Fetter, D., Medlock, J. E., Campbell, I. G., and Gülder, O. L., 1997, "Development and Application of Laser Induced Incadescence (LII) as a Diagnostic for Soot Particulate Measurements," *The Combustion Institute Canadian Section*, pp. 11–16.

[82] Choi, M. Y., and Jensen, K. A., 1998, "Calibration and Correction of Laser-Induced Incandescence for Soot

Volume Fraction Measurements," Combust. Flame, **112**(4), pp. 485–491.

[83] McManus, K. R., Frank, J. H., Allen, M. G., and Rawlins, W. T., 1998, "Characterization of Laser-Heated Soot Particles Using Optical Pyrometry," 36th Aerosp. Sci. Meet. Exhib., pp. 1–9.

[84] Vander Wal, R. L., Ticich, T. M., and Stephens, A. B., 1998, "Optical and Microscopy Investigations of Soot Structure Alterations by Laser-Induced Incandescence," Appl. Phys. B, **67**(1), pp. 115–123.

[85] Vander Wal, R. L., and Choi, M. Y., 1999, "Pulsed Laser Heating of Soot: Morphological Changes," Carbon, **37**(2), pp. 231–239.

[86] Snelling, D. R., Smallwood, G. J., Sawchuk, R. A. A., Neill, W. S. S., Gareau, D., Chippior, W. L. L., Liu, F., Gülder, O. L. L., and Bachalo, W. D. D., 1999, "Particulate Matter Measurements in a Diesel Engine Exhaust by Laser-Induced Incandescence and the Standard Gravimetric Procedure," SAE Tech. Pap., (1999-01-3653).

[87] Will, S., Schraml, S., and Leipertz, A., 1995, "Two-Dimensional Soot-Particle Sizing by Time-Resolved Laser-Induced Incandescence," Opt. Lett., **20**(22), pp. 2342–2344.

[88] Will, S., Schraml, S., and Leipert, A., 1996, "Comprehensive Two-Dimensional Soot Diagnostics Based on Laser-Induced Incandescence (LII)," Symp. Combust., **26**(2), pp. 2277–2284.

[89] Will, S., Schraml, S., Bader, K., and Leipertz, A., 1998, "Performance Characteristics of Soot Primary Particle Size Measurements by Time-Resolved Laser-Induced Incandescence," Appl. Opt., **37**(24), pp. 5647–5658.

[90] Schraml, S., Will, S., and Leipertz, A., 1999, "Simultaneous Measurement of Soot Mass Concentration and Primary Particle Size in the Exhaust of a Di Diesel Engine by Time-Resolved Laser-Induced Incandescence (TIRE-LII)," SAE Tech. Pap., (1999-1–146).

[91] Roth, P., and Filippov, A. V, 1996, "In Situ Ultrafine Particle Sizing by a Combination of Pulsed Laser Heatup and Particle Thermal Emission," J. Aerosol Sci., **27**(1), pp. 95–104.

[92] Geitlinger, H., Streibel, T., Suntz, R., and Bockhorn, H., 1998, "Two-Dimensional Imaging of Soot Volume Fractions, Particle Number Densities, and Particle Radii in Laminar and Turbulent Diffusion Flames," Proc. Combust. Inst., **27**(1), pp. 1613–1621.

[93] Geitlinger, H., Streibel, T., Suntz, R., and Bockhorn, H., 1999, "Statistical Analysis of Soot Volume Fractions, Particle Number Densities and Particle Radii in a Turbulent Diffusion Flame," Combust. Sci. Technol., **149**(1), pp. 115–134.

[94] Vander Wal, R. L., Ticich, T. M., and West, J. R., 1999, "Laser-Induced Incandescence Applied to Metal Nanostructures," Appl. Opt., **38**(27), pp. 5867–5879.

[95] Hofeldt, D. L., 1993, "Real-Time Soot Concentration Measurement Technique for Engine Exhaust Streams," SAE Tech. Pap., (930079).

[96] Schulz, C., Kock, B. F., Hofmann, M., Michelsen, H., Will, S., Bougie, B., Suntz, R., and Smallwood, G., 2006, "Laser-Induced Incandescence: Recent Trends and Current Questions," Appl. Phys. B, **83**(3), pp. 333–354.

[97] Michelsen, H. A., Schulz, C., Smallwood, G. J., and Will, S., 2015, "Laser-Induced Incandescence: Particulate Diagnostics for Combustion, Atmospheric, and Industrial Applications," Prog. Energy Combust. Sci., **51**, pp. 2–48.

[98] Michelsen, H. A., Liu, F., Kock, B. F., Bladh, H., Boiarciuc, A., Charwath, M., Dreier, T., Hadef, R., Hofmann, M., Reimann, J., Will, S., Bengtsson, P. E., Bockhorn, H., Foucher, F., Geigle, K.-P., Mounaïm-Rousselle, C.,

Schulz, C., Stirn, R., Tribalet, B., and Suntz, R., 2007, "Modeling Laser-Induced Incandescence of Soot: A Summary and Comparison of LII Models," Appl. Phys. B, **87**(3), pp. 503–521.

[99] Bladh, H., and Bengtsson, P. E., 2004, "Characteristics of Laser-Induced Incandescence from Soot in Studies of a Time-Dependent Heat- and Mass-Transfer Model," Appl. Phys. B, **78**(2), pp. 241–248.

[100] Smallwood, G. J., Snelling, D. R., Liu, F., and Gülder, O. L., 2001, "Clouds over Soot Evaporation: Errors in Modeling Laser-Induced Incandescence of Soot," J. Heat Transfer, **123**(4), pp. 814–818.

[101] Lehre, T., Jungfleisch, B., Suntz, R., and Bockhorn, H., 2003, "Size Distributions of Nanoscaled Particles and Gas Temperatures from Time-Resolved Laser-Induced-Incandescence Measurements," Appl. Opt., **42**(12), pp. 2021–2030.

[102] Schittkowski, T., Mewes, B., and Brüggemann, D., 2002, "Laser-Induced Incandescence and Raman Measurements in Sooting Methane and Ethylene Flames," Phys. Chem. Chem. Phys., **4**(11), pp. 2063–2071.

[103] Kock, B. F., Eckhardt, T., and Roth, P., 2002, "In-Cylinder Sizing of Diesel Particles by Time-Resolved Laser-Induced Incandescence (TR-LII)," Proc. Combust. Inst., **29**(2), pp. 2775–2782.

[104] Michelsen, H. A., 2003, "Understanding and Predicting the Temporal Response of Laser-Induced Incandescence from Carbonaceous Particles," J. Chem. Phys., **118**(15), pp. 7012–7045.

[105] Michelsen, H. A., Witze, P. O., Kayes, D., and Hochgreb, S., 2003, "Time-Resolved Laser-Induced Incandescence of Soot: The Influence of Experimental Factors and Microphysical Mechanisms," Appl. Opt., **42**(27), pp. 5577–5590.

[106] Daun, K. J., Smallwood, G. J., and Liu, F., 2008, "Investigation of Thermal Accommodation Coefficients in Time-Resolved Laser-Induced Incandescence," J. Heat Transfer, **130**(12), p. 121201.

[107] Daun, K. J., Smallwood, G. J., and Liu, F., 2009, "Molecular Dynamics Simulations of Translational Thermal Accommodation Coefficients for Time-Resolved LII," Appl. Phys. B, **94**(1), pp. 39–49.

[108] Daun, K. J., Sipkens, T. A., Titantah, J. T., and Karttunen, M., 2013, "Thermal Accommodation Coefficients for Laser-Induced Incandescence Sizing of Metal Nanoparticles in Monatomic Gases," Appl. Phys. B, **112**(3), pp. 409–420.

[109] Michelsen, H. A., 2009, "Derivation of a Temperature-Dependent Accommodation Coefficient for Use in Modeling Laser-Induced Incandescence of Soot," Appl. Phys. B, **94**(1), pp. 103–117.

[110] Maffi, S., De Iuliis, S., Cignoli, F., and Zizak, G., 2011, "Investigation on Thermal Accommodation Coefficient and Soot Absorption Function with Two-Color Tire-LII Technique in Rich Premixed Flames," Appl. Phys. B, **104**(2), pp. 357–366.

[111] Snelling, D. R., Liu, F., Smallwood, G. J., and Gülder, Ö. L., 2004, "Determination of the Soot Absorption Function and Thermal Accommodation Coefficient Using Low-Fluence LII in a Laminar Coflow Ethylene Diffusion Flame," Combust. Flame, **136**(1–2), pp. 180–190.

[112] Sipkens, T. A., Singh, N. R., Daun, K. J., Bizmark, N., and Ioannidis, M., 2015, "Examination of the Thermal Accommodation Coefficient Used in the Sizing of Iron Nanoparticles by Time-Resolved Laser-Induced Incandescence," Appl. Phys. B, **119**(4), pp. 561–575.

[113] Liu, F., Yang, M., Hill, F. A., Smallwood, G. J., and Snelling, D. R., 2006, "Influence of Polydisperse Distributions of Both Primary Particle and Aggregate Sizes on Soot Temperature in Low-Fluence Laser-

Induced Incandescence," Appl. Phys. B, **83**(3), pp. 383–395.

[114] Filippov, A. V, Zurita, M., and Rosner, D. E., 2000, "Fractal-like Aggregates: Relation between Morphology and Physical Properties," J. Colloid Interface Sci., **229**(1), pp. 261–273.

[115] Snelling, D., Liu, F., Smallwood, G., and Gülder, Ö. L., 2000, "Evaluation of the Nanoscale Heat and Mass Transfer Model of LII: Prediction of the Excitation Intensity," *Proceedings of 34th National Heat Transfer Conference*, Pittsburg, Pennsylvania, p. 12132.

[116] Liu, F., and Smallwood, G. J., 2010, "Effect of Aggregation on the Absorption Cross-Section of Fractal Soot Aggregates and Its Impact on LII Modelling," J. Quant. Spectrosc. Radiat. Transf., **111**(2), pp. 302–308.

[117] Kuhlmann, S. A., Reimann, J., and Will, S., 2006, "On Heat Conduction between Laser-Heated Nanoparticles and a Surrounding Gas," J. Aerosol Sci., **37**(12), pp. 1696–1716.

[118] Daun, K. J., 2010, "Effect of Selective Accommodation on Soot Aggregate Shielding in Time-Resolved Laser-Induced Incandescence Experiments," J. Heat Transfer, **132**(September 2010), p. 091202.

[119] Bladh, H., Johnsson, J., Rissler, J., Abdulhamid, H., Olofsson, N. E., Sanati, M., Pagels, J., and Bengtsson, P. E., 2011, "Influence of Soot Particle Aggregation on Time-Resolved Laser-Induced Incandescence Signals," Appl. Phys. B, **104**(2), pp. 331–341.

[120] Johnsson, J., Bladh, H., Olofsson, N.-E., and Bengtsson, P.-E., 2013, "Influence of Soot Aggregate Structure on Particle Sizing Using Laser-Induced Incandescence: Importance of Bridging between Primary Particles," Appl. Phys. B, **112**(3), pp. 321–332.

[121] Therssen, E., Bouvier, Y., Schoemaecker-Moreau, C., Mercier, X., Desgroux, P., Ziskind, M., and Focsa, C., 2007, "Determination of the Ratio of Soot Refractive Index Function E(m) at the Two Wavelengths 532 and 1064 Nm by Laser Induced Incandescence," Appl. Phys. B, **89**(2–3), pp. 417–427.

[122] Goulay, F., Schrader, P. E., and Michelsen, H. A., 2010, "Effect of the Wavelength Dependence of the Emissivity on Inferred Soot Temperatures Measured by Spectrally Resolved Laser-Induced Incandescence," Appl. Phys. B, **100**(3), pp. 655–663.

[123] Schraml, S., Dankers, S., Bader, K., Will, S., and Leipertz, A., 2000, "Soot Temperature Measurements and Implications for Time-Resolved Laser-Induced Incandescence (TIRE-LII)," Combust. Flame, **120**(4), pp. 439–450.

[124] Murakami, Y., Sugatani, T., and Nosaka, Y., 2005, "Laser-Induced Incandescence Study on the Metal Aerosol Particles as the Effect of the Surrounding Gas Medium," J. Phys. Chem. A, **109**(40), pp. 8994–9000.

[125] Eom, G. S., Park, C. W., Shin, Y. H., Chung, K. H., Park, S., Choe, W., and Hahn, J. W., 2003, "Size Determination of Nanoparticles in Low-Pressure Plasma with Laser-Induced Incandescence Technique," Appl. Phys. Lett., **83**(6), pp. 1261–1263.

[126] Eom, G. S., Park, S., Park, C. W., Choe, W., Shin, Y. H., Chung, K. H., and Hahn, J. W., 2004, "Size Monitoring of Nanoparticles Growing in Low-Pressure Plasma Using Laser-Induced Incandescence Technique," Japanese J. Appl. Physics, Part 1 Regul. Pap. Short Notes Rev. Pap., **43**(9R), pp. 6494–6498.

[127] Lehre, T., Suntz, R., and Bockhorn, H., 2005, "Time-Resolved Two-Color LII: Size Distributions of Nano-Particles from Gas-to-Particle Synthesis," Proc. Combust. Inst., **30**(2), pp. 2585–2593.

[128] Maffi, S., Cignoli, F., Bellomunno, C., De Iuliis, S., and Zizak, G., 2008, "Spectral Effects in Laser Induced

Incandescence Application to Flame-Made Titania Nanoparticles," Spectrochim. Acta - Part B At. Spectrosc., **63**(2), pp. 202–209.

[129] Eremin, A., Gurentsov, E., Popova, E., and Priemchenko, K., 2011, "Size Dependence of Complex Refractive Index Function of Growing Nanoparticles," Appl. Phys. B, **104**(2), pp. 285–295.

[130] Eremin, A., Gurentsov, E., Mikheyeva, E., and Priemchenko, K., 2013, "Experimental Study of Carbon and Iron Nanoparticle Vaporization under Pulse Laser Heating," Appl. Phys. B, **112**(3), pp. 421–432.

[131] Sipkens, T., Joshi, G., Daun, K. J., and Murakami, Y., 2013, "Sizing of Molybdenum Nanoparticles Using Time-Resolved Laser-Induced Incandescence," J. Heat Transfer, **135**(5), p. 052401.

[132] Eremin, A. V, and Gurentsov, E. V, 2015, "Sizing of Mo Nanoparticles Synthesised by Kr–F Laser Pulse Photo-Dissociation of Mo(CO)6," Appl. Phys. A, **119**(2), pp. 615–622.

[133] Reimann, J., Oltmann, H., Will, S., Bassano, E., Carotenuto, L., Lösch, S., and Günther, B. H., 2010, "Laser-Induced Incandescence during Laser Modification of Nickel Nanoparticles from Inert Gas Condensation," *Proceeding of the World Congress on Particle Technology 6*, Nuremberg, Germany.

[134] Tribalet, B., Faccinetto, A., Dreier, T., and Schultz, C., 2012, "Evaluation of Particle Sizes of Iron-Oxide Nano-Particles in a Low-Pressure Flame-Synthesis Reactor by Simultaneous Application of TiRe-LII and PMS," *5th Workshop on Laser-Induced Incandescence*, Le Touquet, France.

[135] Menser, J., 2018, "Personal Communication Regarding Germanium Laser-Induced Incandescence."

[136] Daun, K., Menser, J., Mansmann, R., Moghaddam, S. T., Dreier, T., and Schulz, C., 2017, "Spectroscopic Models for Laser-Heated Silicon and Copper Nanoparticles," J. Quant. Spectrosc. Radiat. Transf., **197**, pp. 3–11.

[137] Krüger, V., Wahl, C., Hadef, R., Geigle, K.-P., Stricker, W., and Aigner, M., 2005, "Comparison of Laser-Induced Incandescence Method with Scanning Mobility Particle Sizer Technique: The Influence of Probe Sampling and Laser Heating on Soot Particle Size Distribution," Meas. Sci. Technol., **16**(7), pp. 1477–1486.

[138] Smallwood, G. J., Clavel, D., Gareau, D., Sawchuk, R. A., Snelling, D. R., Witze, P. O., Axelsson, B., Bachalo, W. D., and Gülder, Ö. L., 2002, "Concurrent Quantitative Laser-Induced Incandescence and SMPS Measurements of EGR Effects on Particulate Emissions from a TDI Diesel Engine," SAE Tech. Pap., (2002-01-2715).

[139] Stirn, R., Baquet, T. G., Kanjarkar, S., Meier, W., Geigle, K.-P., Grotheer, H. H., Wahl, C., and Aigner, M., 2009, "Comparison of Particle Size Measurements with Laser-Induced Incandescence, Mass Spectroscopy, and Scanning Mobility Particle Sizing in a Laminar Premixed Ethylene-Air Flame," Combust. Sci. Technol., **181**(2), pp. 329–349.

[140] Hofmann, M., Bessler, W. G., Schulz, C., and Jander, H., 2003, "Laser-Induced Incandescence for Soot Diagnostics at High Pressures," Appl. Opt., **42**(12), pp. 2052–2062.

[141] Tsurikov, M. S., Geigle, K.-P., Krüger, V., Schneider-Kühnle, Y., Stricker, W., Lückerath, R., Hadef, R., and Aigner, M., 2005, "Laser-Based Investigation of Soot Formation in Laminar Premixed Flames at Atmospheric and Elevated Pressures," Combust. Sci. Technol., **177**(10), pp. 1835–1862.

[142] Zerbs, J., Geigle, K.-P., Lammel, O., Hader, J., Stirn, R., Hadef, R., and Meier, W., 2009, "The Influence of Wavelength in Extinction Measurements and Beam Steering in Laser-Induced Incandescence Measurements in Sooting Flames," Appl. Phys. B, **96**(4), pp. 683–694.

[143] Geigle, K.-P., Schneider-Kühnle, Y., Tsurikov, M. S., Hadef, R., Lückerath, R., Krüger, V., Stricker, W., and Aigner, M., 2005, "Investigation of Laminar Pressurized Flames for Soot Model Validation Using SV-CARS and LII," Proc. Combust. Inst., **30**(1), pp. 1645–1653.

[144] Beyer, V., and Greenhalgh, D. A., 2006, "Laser Induced Incandescence under High Vacuum Conditions," Appl. Phys. B, **83**(3), pp. 455–467.

[145] Snelling, D. R., Smallwood, G. J., Liu, F., Gülder, Ö. L., and Bachalo, W. D., 2005, "A Calibration-Independent Laser-Induced Incandescence Technique for Soot Measurement by Detecting Absolute Light Intensity," Appl. Opt., **44**(31), pp. 6773–6785.

[146] Snelling, D. R., Smallwood, G. J., Gülder, Ö. L., Liu, F., and Bachalo, W. D., 2001, "A Calibration-Independent Technique of Measuring Soot by Laser-Induced Incandescence Using Absolute Light Intensity," *Second Joint Meeting of the US Sections of The Combustion Institute*, Oakland, USA.

[147] Michelsen, H. A., 2006, "Laser-Induced Incandescence of Flame-Generated Soot on a Picosecond Time Scale," Appl. Phys. B, **83**(3), pp. 443–448.

[148] Bohren, C. F., and Huffman, D. R., 1983, "Absorption and Scattering by a Sphere," *Absorption and Scattering of Light by Small Particles*, John Wiley & Sons, New York, pp. 82–129.

[149] Mie, G., 1908, "Beiträge Zur Optik Trüber Medien, Speziell Kolloidaler Metallösungen," Ann. Phys., **330**(3), pp. 377–445.

[150] Schäfer, J.-P., 2011, "Implementierung Und Anwendung Analytischer Und Numerischer Verfahren Zur Lösung Der Maxwellgleichungen Für Die Untersuchung Der Lichtausbreitung in Biologischem Gewebe," Univerität Ulm. Thesis.

[151] Bohren, C. F., and Huffman, D. R., 1983, *Absorption and Scattering of Light by Small Particles*, John Wiley & Sons, New York.

[152] Tropea, C., 2011, "Optical Particle Characterization in Flows," Annu. Rev. Fluid Mech., **43**(1), pp. 399–426.

[153] Sorensen, C. M., 2001, "Light Scattering by Fractal Aggregates: A Review," Aerosol Sci. Technol., **35**(2), pp. 648–687.

[154] Janzen, J., 1979, "The Refractive Index of Colloidal Carbon," J. Colloid Interface Sci., **69**(3), pp. 436–447.

[155] Krishnan, S., Yugawa, K. J., and Nordine, P. C., 1997, "Optical Properties of Liquid Nickel and Iron," Phys. Rev. B, **55**(13), pp. 8201–8206.

[156] Hadwin, P. J., Sipkens, T. A., Thomson, K. A., Liu, F., and Daun, K. J., 2016, "Quantifying Uncertainty in Soot Volume Fraction Estimates Using Bayesian Inference of Auto-Correlated Laser-Induced Incandescence Measurements," Appl. Phys. B, **122**(1), pp. 1–16.

[157] Hadwin, P. J., Sipkens, T. A., Thomson, K. A., Liu, F., and Daun, K. J., 2017, "Quantifying Uncertainty in Auto-Compensating Laser-Induced Incandescence Parameters Due to Multiple Nuisance Parameters," Appl. Phys. B, **123**(4), pp. 114–128.

[158] Saffaripour, M., Geigle, K.-P., Snelling, D. R., Smallwood, G. J., and Thomson, K. A., 2015, "Influence of Rapid Laser Heating on the Optical Properties of In-Flame Soot," Appl. Phys. B, **119**(4), pp. 621–642.

[159] Wriedt, T., 1998, "A Review of Elastic Light Scattering Theories," Part. Part. Syst. Charact., **15**(2), pp. 67–74.

[160] Moosmüller, H., Chakrabarty, R. K., and Arnott, W. P., 2009, "Aerosol Light Absorption and Its Measurement: A Review," J. Quant. Spectrosc. Radiat. Transf., **110**(11), pp. 844–878.

[161] Mishchenko, M. I., Travis, L. D., Mackowski, D. W., and Machowski, D. W., 1996, "T-Matrix Computations of Light Scattering by Nonspherical Particles: A Review," J. Quant. Spectrosc. Radiat. Transf., **55**(5), pp. 535–575.

[162] Waterman, P. C., 1965, "Matrix Formulation of Electromagnetic Scattering," Proc. IEEE, **53**(8), pp. 805–812.

[163] Yurkin, M. A., and Hoekstra, A. G., 2007, "The Discrete Dipole Approximation: An Overview and Recent Developments," J. Quant. Spectrosc. Radiat. Transf., **106**(1–3), pp. 558–589.

[164] Draine, B. T., and Flatau, P. J., 1994, "Discrete-Dipole Approximation for Scattering Calculations," J. Opt. Soc. Am. A Opt. Image Sci. Vis., **11**(4), pp. 1491–1499.

[165] Bohren, C. F., and Huffman, D. R., 1983, "Rayleigh-Gans Theory," *Absorption and Scattering of Light by Small Particles*, John Wiley & Sons, New York, pp. 158–165.

[166] Kerker, M., 1969, *The Scattering of Light and Other Electromagnetic Radiation*, Academic Press, Postdam.

[167] Barber, P. W., and Wang, D.-S., 1978, "Rayleigh-Gans-Debye Applicability to Scattering by Nonspherical Particles," Appl. Opt., **17**(5), pp. 797–803.

[168] Barber, P. W., and Wang, D., 1979, "Rayleigh-Gans-Debye Applicability to Scattering by Nonspherical Particles: Corrigenda," Appl. Opt., **18**(7), pp. 962–963.

[169] Farias, T. L., Köylü, Ü. Ö., and Carvalho, M. G., 1996, "Range of Validity of the Rayleigh–Debye–Gans Theory for Optics of Fractal Aggregates," Appl. Opt., **35**(33), pp. 6560–6567.

[170] Liu, L., and Mishchenko, M. I., 2007, "Scattering and Radiative Properties of Complex Soot and Soot-Containing Aggregate Particles," J. Quant. Spectrosc. Radiat. Transf., **106**(1–3), pp. 262–273.

[171] Liu, F., Wong, C., Snelling, D. R., and Smallwood, G. J., 2013, "Investigation of Absorption and Scattering Properties of Soot Aggregates of Different Fractal Dimension at 532 Nm Using RDG and GMM," Aerosol Sci. Technol., **47**(12), pp. 1393–1405.

[172] Zhao, Y., and Ma, L., 2009, "Applicable Range of the Rayleigh-Debye-Gans Theory for Calculating the Scattering Matrix of Soot Aggregates," Appl. Opt., **48**(3), pp. 591–597.

[173] Garcia-Lopez, A. C., and Garcia-Rubio, L. H., 2008, "Rayleigh-Debye-Gans as a Model for Continuous Monitoring of Biological Particles: Part II, Development of a Hybrid Model," Opt. Express, **16**(7), pp. 4671–4687.

[174] Garcia-Lopez, A. C., Snider, A. D., and Garcia-Rubio, L. H., 2006, "Rayleigh-Debye-Gans as a Model for Continuous Monitoring of Biological Particles: Part I, Assessment of Theoretical Limits and Approximations," Opt. Express, **14**(19), pp. 8849–8865.

[175] Liu, F., and Smallwood, G. J., 2013, "Relationship between Soot Volume Fraction and LII Signal in AC-LII: Effect of Primary Soot Particle Diameter Polydispersity," Appl. Phys. B, **112**(3), pp. 307–319.

[176] Liu, F., Rogak, S., Snelling, D. R., Saffaripour, M., Thomson, K. A., and Smallwood, G. J., 2016, "Effects of Laser Fluence Non-Uniformity on Ambient-Temperature Soot Measurements Using the Auto-Compensating Laser-Induced Incandescence Technique," Appl. Phys. B, **122**(11).

[177] Michelsen, H. A., Linne, M. A., Kock, B. F., Hofmann, M., Tribalet, B., and Schulz, C., 2008, "Modeling Laser-Induced Incandescence of Soot: Enthalpy Changes during Sublimation, Conduction, and Oxidation," Appl. Phys. B, **93**(2–3), pp. 645–656.

[178] Lemaire, R., and Mobtil, M., 2015, "Modeling Laser-Induced Incandescence of Soot: A New Approach Based on the Use of Inverse Techniques," Appl. Phys. B, **119**(4), pp. 577–606.

[179] Mitrani, J. M., Shneider, M. N., Stratton, B. C., and Raitses, Y., 2016, "Modeling Thermionic Emission from Laser-Heated Nanoparticles," Appl. Phys. Lett., **108**(5), p. 054101.

[180] Shneider, M. N., 2015, "Carbon Nanoparticles in the Radiation Field of the Stationary Arc Discharge," Phys. Plasmas, **22**(7), pp. 1–5.

[181] Liu, F., Stagg, B. J., Snelling, D. R., and Smallwood, G. J., 2006, "Effects of Primary Soot Particle Size Distribution on the Temperature of Soot Particles Heated by a Nanosecond Pulsed Laser in an Atmospheric Laminar Diffusion Flame," Int. J. Heat Mass Transf., **49**(3–4), pp. 777–788.

[182] Koechner, W., 2013, *Solid-State Laser Engineering*, Springer-Verlag, Berlin.

[183] Bladh, H., Johnsson, J., and Bengtsson, P.-E., 2009, "Influence of Spatial Laser Energy Distribution on Evaluated Soot Particle Sizes Using Two-Colour Laser-Induced Incandescence in a Flat Premixed Ethylene/Air Flame," Appl. Phys. B, **96**(4), pp. 645–656.

[184] Delhay, J., Bouvier, Y., Therssen, E., Black, J. D., and Desgroux, P., 2005, "2D Imaging of Laser Wing Effects and of Soot Sublimation in Laser-Induced Incandescence Measurements," Appl. Phys. B, **81**(2–3), pp. 181–186.

[185] Liu, F., Daun, K. J., Snelling, D. R., and Smallwood, G. J., 2006, "Heat Conduction from a Spherical Nano-Particle: Status of Modeling Heat Conduction in Laser-Induced Incandescence," Appl. Phys. B, **83**(3), pp. 355–382.

[186] Filippov, A. V., and Rosner, D. E., 2000, "Energy Transfer between an Aerosol Particle and Gas at High Temperature Ratios in the Knudsen Transition Regime," Int. J. Heat Mass Transf., **43**(1), pp. 127–138.

[187] Bird, G. A., 1994, *Molecular Gas Dynamics and the Direct Simulation of Gas Flows*, Clarendon Press, Oxford.

[188] McCoy, B. J., and Cha, C. Y., 1974, "Transport Phenomena in the Rarefied Gas Transition Regime," Chem. Eng. Sci., **29**(2), pp. 381–388.

[189] Daun, K. J., 2009, "Thermal Accommodation Coefficients between Polyatomic Gas Molecules and Soot in Laser-Induced Incandescence Experiments," Int. J. Heat Mass Transf., **52**(21–22), pp. 5081–5089.

[190] Fuchs, N. A., 1963, "On the Stationary Charge Distribution on Aerosol Particles in a Bipolar Ionic Atmosphere," Geofis. Pura e Appl., **56**(1), pp. 185–193.

[191] Fuchs, N. A., 1964, *The Mechanics of Aerosols*, Dover Publications, New York.

[192] Liu, F., and Smallwood, G., 2008, "Study of Heat Conduction between Fractal Aggregates and the Surrounding Gas in the Transition Regime Using the DSMC Method," *40th Thermophysics Conference*, pp. 1–10.

[193] Daun, K. J., and Huberman, S. C., 2012, "Influence of Particle Curvature on Transition Regime Heat Conduction from Aerosolized Nanoparticles," Int. J. Heat Mass Transf., **55**(25–26), pp. 7668–7676.

[194] Cenker, E., Bruneaux, G., Dreier, T., and Schulz, C., 2015, "Determination of Small Soot Particles in the Presence of Large Ones from Time-resolved Laser-induced Incandescence," Appl. Phys. B, **118**(2), pp. 169–183.

[195] Cenker, E., Bruneaux, G., Dreier, T., and Schulz, C., 2015, "Sensitivity Analysis for Soot Particle Size Imaging with Laser-Induced Incandescence at High Pressure," Appl. Phys. B, **119**(4), pp. 745–763.

[196] Huber, M. L., and Harvey, A. H., 2011, "Tables of Thermal Conductivity of Common Gases as a Function of Temperature," *CRC Handbook of Chemisty and Physics*, CRC-Press, Boca Rato, pp. 240–241.

[197] Liu, F., Smallwood, G. J., and Snelling, D. R., 2005, "Effects of Primary Particle Diameter and Aggregate Size Distribution on the Temperature of Soot Particles Heated by Pulsed Lasers," J. Quant. Spectrosc. Radiat. Transf., **93**(1–3), pp. 301–312.

[198] Snelling, D. R., Thomson, K. A., Liu, F., and Smallwood, G. J., 2009, "Comparison of LII Derived Soot Temperature Measurements with LII Model Predictions for Soot in a Laminar Diffusion Flame," Appl. Phys. B, **96**(4), pp. 657–669.

[199] Cenker, E., Bennett, A., and Roberts, W. L., 2017, "Investigations of the Long-Term Effects of LII on Soot and Bath Gas," Aerosol Sci. Technol., **51**(12), pp. 1354–1367.

[200] Mansmann, R., Thomson, K., Smallwood, G., Dreier, T., and Schulz, C., 2017, "Sequential Signal Detection for High Dynamic Range Time-Resolved Laser-Induced Incandescence," Opt. Express, **25**(3), pp. 2413–2421.

[201] Gurentsov, E. V, and Eremin, A. V, 2011, "Size Measurement of Carbon and Iron Nanoparticles by Laser Induced Incadescence," High Temp., **49**(5), pp. 667–673.

[202] Watson, K. M., 1943, "Thermodynamics of the Liquid State," Ind. Eng. Chem., **35**(4), pp. 398–406.

[203] Leider, H. R., Krikorian, O. H., and Young, D. A., 1973, "Thermodynamic Properties of Carbon up to the Critical Point," Carbon, **11**(5), pp. 555–563.

[204] Román, F. L., White, J. A., Velasco, S., and Mulero, A., 2005, "On the Universal Behavior of Some Thermodynamic Properties along the Whole Liquid-Vapor Coexistence Curve," J. Chem. Phys., **123**(12), p. 124512.

[205] Meyra, A. G., Kuz, V. A., and Zarragoicoechea, G. J., 2004, "Universal Behavior of the Enthalpy of Vaporization: An Empirical Equation," Fluid Phase Equilib., **218**(2), pp. 205–207.

[206] Walas, S. M., 2013, *Phase Equilibria in Chemical Engineering*, Butterworth-Heinemann, Boston.

[207] Sipkens, T. A., Hadwin, P. J., Grauer, S. J., and Daun, K. J., 2018, "Predicting the Heat of Vaporization of Iron at High Temperatures Using Time-Resolved Laser-Induced Incandescence and Bayesian Model Selection," J. Appl. Phys., **123**(9), p. 95103.

[208] Nanda, K. K., Maisels, A., Kruis, F. E., Fissan, H., and Stappert, S., 2003, "Higher Surface Energy of Free Nanoparticles," Phys. Rev. Lett., **91**(10), pp. 1–4.

[209] Lei, Y. A., Bykov, T., Yoo, S., and Zeng, X. C., 2005, "The Tolman Length: Is It Positive or Negative?," J. Am. Chem. Soc., **127**(44), pp. 15346–15347.

[210] Kago, K., Zeng, X. C., and Shchekin, A. K., 1998, "Validity of Tolman's Equation : How Large Should a Droplet Be?," Chem. Phys., **109**(10), pp. 4063–4070.

[211] Mohri, T., Horiuchi, T., Uzawa, H., Ibaragi, M., Igarashi, M., and Abe, F., 2001, "Theoretical Investigation of L10-Disorder Phase Equilibria in Fe–Pd Alloy System," J. Alloys Compd., **317**, pp. 13–18.

[212] De Iuliis, S., Cignoli, F., Maffi, S., and Zizak, G., 2011, "Influence of the Cumulative Effects of Multiple Laser Pulses on Laser-Induced Incandescence Signals from Soot," Appl. Phys. B, **104**(2), pp. 321–330.

[213] de Heer, W. A., and Ugarte, D., 1993, "Carbon Onions Produced by Heat Treatment of Carbon Soot and Their Relation to the 217.5 Nm Interstellar Absorption Feature," Chem. Phys. Lett., **207**(4–6), pp. 480–486.

[214] Kuznetsov, V. L., and Butenko, Y. V., 2005, "Nanodiamond Graphitization and Properties of Onion-like Carbon," *Synthesis, Properties and Applications of Ultrananocrystalline Diamond*, Springer, Dordrecht, pp. 199–216.

[215] Cenker, E., and Roberts, W. L., 2017, "Quantitative Effects of Rapid Heating on Soot-Particle Sizing through Analysis of Two-Pulse LII," Appl. Phys. B, **123**(3), pp. 1–10.

[216] Bambha, R. P., and Michelsen, H. A., 2015, "Effects of Aggregate Morphology and Size on Laser-Induced Incandescence and Scattering from Black Carbon (Mature Soot)," J. Aerosol Sci., **88**, pp. 159–181.

[217] Stephens, M., Turner, N., and Sandberg, J., 2003, "Particle Identification by Laser-Induced Incandescence in a Solid-State Laser Cavity.," Appl. Opt., **42**(19), pp. 3726–3736.

[218] Nordström, E., Olofsson, N. E., Simonsson, J., Johnsson, J., Bladh, H., and Bengtsson, P. E., 2015, "Local Gas Heating in Sooting Flames by Heat Transfer from Laser-Heated Particles Investigated Using Rotational CARS and LII," Proc. Combust. Inst., **35**(3), pp. 3707–3713.

[219] Chan, T. W., Brook, J. R., Smallwood, G. J., and Lu, G., 2011, "Time-Resolved Measurements of Black Carbon Light Absorption Enhancement in Urban and near-Urban Locations of Southern Ontario, Canada," Atmos. Chem. Phys., **11**(20), pp. 10407–10432.

[220] Fuller, K. A., Malm, W. C., and Kreidenweis, S. M., 1999, "Effects of Mixing on Extinction by Carbonaceous Particles," J. Geophys. Res., **104**(D13), pp. 15941–15954.

[221] Smallwood, G. J., 2008, "A Critique of Laser-Induced Incandescence for the Measurement of Soot," Cranfield University. Thesis.

[222] Hadwin, P. J., Sipkens, T. A., Thomson, K. A., Liu, F., and Daun, K. J., 2018, "Kalman Filter Approach for Uncertainty Quantification in Time-Resolved Laser-Induced Incandescence," J. Opt. Soc. Am. A Opt. Image Sci. Vis., **35**(3), pp. 386–396.

[223] Arfken, G. B., Weber, H. J., and Harris, F. E., 2011, *Mathematical Methods for Physicists: A Comprehensive Guide*, Academic Press, Amsterdam.

[224] Kaipio, J., and Somersalo, E., 2005, *Statistical and Computational Inverse Problems*, Springer Science and Business Media, New York.

[225] Daun, K. J., Stagg, B. J., Liu, F., Smallwood, G. J., and Snelling, D. R., 2007, "Determining Aerosol Particle Size Distributions Using Time-Resolved Laser-Induced Incandescence," Appl. Phys. B, **87**(2), pp. 363–372.

[226] Kock, B. F., Tribalet, B., Schulz, C., and Roth, P., 2006, "Two-Color Time-Resolved LII Applied to Soot Particle Sizing in the Cylinder of a Diesel Engine," Combust. Flame, **147**(1–2), pp. 79–92.

[227] Liu, F., Snelling, D. R., Thomson, K. A., and Smallwood, G. J., 2009, "Sensitivity and Relative Error Analyses of Soot Temperature and Volume Fraction Determined by Two-Color LII," Appl. Phys. B Lasers Opt., **96**(4),

pp. 623–636.

[228] Crosland, B. M., Johnson, M. R., and Thomson, K. A., 2011, "Analysis of Uncertainties in Instantaneous Soot Volume Fraction Measurements Using Two-Dimensional, Auto-Compensating, Laser-Induced Incandescence (2D-AC-LII)," Appl. Phys. B, **102**(1), pp. 173–183.

[229] Laplace, P. S., 1820, *Théorie Analytique Des Probabilités*.

[230] Von Toussaint, U., 2011, "Bayesian Inference in Physics," Rev. Mod. Phys., **83**(3), pp. 943–999.

[231] Adrian E. Raftery, and Robert E. Kass, 1995, "Bayes Factors," **90**(430), pp. 773–795.

[232] Jaynes, E. T., 1968, "Prior Probabilities," IEEE Trans. Syst. Sci. Cybern., **4**(3), pp. 227–241.

[233] O'Hagan, A., 1994, *The Advanced Theory of Statistics*, University Press, Cambridge.

[234] Greenberg, P. S., and Ku, J. C., 1997, "Soot Volume Fraction Imaging," Appl. Opt., **36**(22), pp. 5514–5522.

[235] Köhler, M., Geigle, K.-P., Meier, W., Crosland, B. M., Thomson, K. A., and Smallwood, G. J., 2011, "Sooting Turbulent Jet Flame: Characterization and Quantitative Soot Measurements," Appl. Phys. B, **104**(2), pp. 409–425.

[236] Foi, A., Trimeche, M., Katkovnik, V., and Egiazarian, K., 2008, "Practical Poissonian-Gaussian Noise Modeling and Fitting for Single-Image Raw-Data," IEEE Trans. Image Process., **17**(10), pp. 1737–1754.

[237] Sipkens, T. A., Hadwin, P. J., Grauer, S. J., and Daun, K. J., 2017, "General Error Model for Analysis of Laser-Induced Incandescence Signals," Appl. Opt., **56**(30), pp. 8436–8445.

[238] Horowitz, P., and Hill, W., 1980, *The Art of Electronics*, Cambridge University Press, Cambridge.

[239] Nyquist, H., 1928, "Thermal Agitation of Electric Charge in Conductors," Phys. Rev., **32**(1), pp. 110–113.

[240] Gurvich, A. S., and Yaglom, A. M., 1967, "Breakdown of Eddies and Probability Distributions for Small-scale Turbulence," Phys. Fluids, **10**(9), pp. S59–S65.

[241] Kim, J., Moin, P., and Moser, R., 1987, "Turbulence Statistics in Fully Developed Channel Flow at Low Reynolds Number," J. Fluid Mech., **177**, pp. 133–166.

[242] Sipkens, T., Hadwin, P., Grauer, S., and Daun, K., 2017, "MATLAB Tools for a General TiRe-LII Error Model."

[243] Webster, D. R., Rahman, S., and Dasi, L. P., 2003, "Laser-Induced Fluorescence Measurements of a Turbulent Plume," J. Eng. Mech., **129**(10), pp. 1130–1137.

[244] Kiefer, J., Li, Z. S., Zetterberg, J., Bai, X. S., and Aldén, M., 2008, "Investigation of Local Flame Structures and Statistics in Partially Premixed Turbulent Jet Flames Using Simultaneous Single-Shot CH and OH Planar Laser-Induced Fluorescence Imaging," Combust. Flame, **154**(4), pp. 802–818.

[245] Schroeder, D. J., 1999, *Astronomical Optics*, Academic Press, San Diego.

[246] Mansmann, R., Dreier, T., and Schulz, C., 2017, "Performance of Photomultipliers in the Context of Laser-Induced Incandescence," Appl. Opt., **56**(28), p. 7849.

[247] Wainner, R., and Seitzman, J., 1999, "Soot Diagnostics Using Laser-Induced Incandescence in Flames and Exhaust Flows," *37th Aerospace Sciences Meeting and Exhibit*.

[248] Lemaire, R., Faccinetto, A., Therssen, E., Ziskind, M., Focsa, C., and Desgroux, P., 2009, "Experimental

Comparison of Soot Formation in Turbulent Flames of Diesel and Surrogate Diesel Fuels," Proc. Combust. Inst., **32**(1), pp. 737–744.

[249] Delhay, J., Desgroux, P., Therssen, E., Bladh, H., Bengtsson, P. E., Hönen, H., Black, J. D., and Vallet, I., 2009, "Soot Volume Fraction Measurements in Aero-Engine Exhausts Using Extinction-Calibrated Backward Laser-Induced Incandescence," Appl. Phys. B, **95**(4), pp. 825–838.

[250] Kaldvee, B., Brackmann, C., Aldén, M., and Bood, J., 2014, "LII-Lidar: Range-Resolved Backward Picosecond Laser-Induced Incandescence," Appl. Phys. B, **115**(1), pp. 111–121.

[251] Hebert, D., Coppalle, A., and Talbaut, M., 2013, "2D Soot Concentration and Burning Rate of a Vertical PMMA Slab Using Laser-Induced Incandescence," Proc. Combust. Inst., **34**(2), pp. 2575–2582.

[252] Qamar, N. H., Alwahabi, Z. T., Chan, Q. N., Nathan, G. J., Roekaerts, D., and King, K. D., 2009, "Soot Volume Fraction in a Piloted Turbulent Jet Non-Premixed Flame of Natural Gas," Combust. Flame, **156**(7), pp. 1339–1347.

[253] Bladh, H., Olofsson, N. E., Mouton, T., Simonsson, J., Mercier, X., Faccinetto, A., Bengtsson, P. E., and Desgroux, P., 2015, "Probing the Smallest Soot Particles in Low-Sooting Premixed Flames Using Laser-Induced Incandescence," Proc. Combust. Inst., **35**(2), pp. 1843–1850.

[254] Witze, P. O., Hochgreb, S., Kayes, D., Michelsen, H. a, and Shaddix, C. R., 2001, "Time-Resolved Laser-Induced Incandescence and Laser Elastic-Scattering Measurements in a Propane Diffusion Flame.," Appl. Opt., **40**(15), pp. 2443–2452.

[255] Cléon, G., Amodeo, T., Faccinetto, A., and Desgroux, P., 2011, "Laser Induced Incandescence Determination of the Ratio of the Soot Absorption Functions at 532 Nm and 1064 Nm in the Nucleation Zone of a Low Pressure Premixed Sooting Flame," Appl. Phys. B, **104**(2), pp. 297–305.

[256] Bejaoui, S., Lemaire, R., Desgroux, P., and Therssen, E., 2014, "Experimental Study of the E(m,l)/E(m,1064) Ratio as a Function of Wavelength, Fuel Type, Height above the Burner and Temperature," Appl. Phys. B, **116**(2), pp. 313–323.

[257] Bengtsson, P.-E., and Alden, M., 1995, "Soot-Visualization Strategies Using Laser Techniques," Appl. Phys. B, **60**(1), pp. 51–59.

[258] De Iuliis, S., Cignoli, F., and Zizak, G., 2006, "Peak Soot Temperature in Laser-Induced Incandescence Measurements," Appl. Phys. B, **83**(3), pp. 397–204.

[259] Bladh, H., Bengtsson, P. E., Delhay, J., Bouvier, Y., Therssen, E., and Desgroux, P., 2006, "Experimental and Theoretical Comparison of Spatially Resolved Laser-Induced Incandescence (LII) Signals of Soot in Backward and Right-Angle Configuration," Appl. Phys. B, **83**(3), pp. 423–433.

[260] Olofsson, N. E., Simonsson, J., Török, S., Bladh, H., and Bengtsson, P. E., 2015, "Evolution of Properties for Aging Soot in Premixed Flat Flames Studied by Laser-Induced Incandescence and Elastic Light Scattering," Appl. Phys. B, **119**(4), pp. 669–683.

[261] Michelsen, H. A., Schrader, P. E., and Goulay, F., 2010, "Wavelength and Temperature Dependences of the Absorption and Scattering Cross Sections of Soot," Carbon, **48**(8), pp. 2175–2191.

[262] López-Yglesias, X., Schrader, P. E., and Michelsen, H. A., 2014, "Soot Maturity and Absorption Cross Sections," J. Aerosol Sci., **75**, pp. 43–64.

[263] Desgroux, P., Betrancourt, C., Mercier, X., and Liu, F., 2018, "Coupling of Cavity-Ring-down Extinction and Laser Induced Incandescence to Determine Soot Volume Fractions in a Nucleation and Sooting Premixed Flames," *8th International Workshop on Laser-Induced Incandescence*, Tutzing, p. 24.

[264] Fan, L., McGrath, D., Zhong, H., and Hochgreb, S., 2018, "Thermographic and Two-Phase PIV Based on LII Signal from Submicron Black Particle Tracers," *8th International Workshop on Laser-Induced Incandescence*, p. 25.

[265] Alm, O., Landström, L., Boman, M., Granqvist, C. G., and Heszler, P., 2005, "Tungsten Oxide Nanoparticles Synthesised by Laser Assisted Homogeneous Gas-Phase Nucleation," Appl. Surf. Sci., **247**(1–4), pp. 262–267.

[266] Landström, L., and Heszler, P., 2004, "Analysis of Blackbody-like Radiation from Laser-Heated Gas-Phase Tungsten Nanoparticles," J. Phys. Chem. B, **108**(20), pp. 6216–6221.

[267] Landström, L., Kokavecz, J., Lu, J., and Heszler, P., 2004, "Characterization and Modeling of Tungsten Nanoparticles Generated by Laser-Assisted Chemical Vapor Deposition," J. Appl. Phys., **95**(8), pp. 4408–4414.

[268] Pustovalov, V. K., and Romanov, G. S., 1985, "The Theory of Heating and Evaporation of a Spherical Particle Exposed to Optical Radiation," Int. J. Heat Mass Transf., **28**(1), pp. 277–289.

[269] Menser, J., Daun, K., Dreier, T., and Schulz, C., 2017, "Laser-Induced Atomic Emission of Silicon Nanoparticles during Laser-Induced Heating," Appl. Opt., **56**(11), pp. 50–57.

[270] Talebi Moghaddam, S., and Daun, K. J., 2018, "Plasma Emission during Time-Resolved Laser-Induced Incandescence Measurements of Aerosolized Metal Nanoparticles," Appl. Phys. B, **124**(8), pp. 159–172.

[271] Churchill, S. W., and Usagi, R., 1972, "A General Expression for the Correlation of Rates Od Transfer and Other Phenomena," AIChE J., **18**(6), pp. 1121–1129.

[272] Habib, Z. G., and Vervisch, P., 1988, "On the Refractive Index of Soot at Flame Temperature," Combust. Sci. Technol., **59**(4–6), pp. 261–274.

[273] Charalampopoulos, T. T., and Chang, H., 1988, "In Situ Optical Properties of Soot Particles in the Wavelength Range from 340 Nm to 600 Nm," Combust. Sci. Technol., **59**(4–6), pp. 401–421.

[274] Migliorini, F., De Iuliis, S., Cignoli, F., and Zizak, G., 2006, "Absorption Correction of Two-Color Laser-Induced Incandescence Signals for Soot Volume Fraction Measurements.," Appl. Opt., **45**(29), pp. 7706–7711.

[275] Sun, Z. W., Gu, D. H., Nathan, G. J., Alwahabi, Z. T., and Dally, B. B., 2015, "Single-Shot, Time-Resolved Planar Laser-Induced Incandescence (TiRe-LII) for Soot Primary Particle Sizing in Flames," Proc. Combust. Inst., **35**(3), pp. 3673–3680.

[276] Gülder, Ö. L., Snelling, D. R., and Sawchuk, R. A., 1996, "Influence of Hydrogen Addition to Fuel on Temperature Field and Soot Formation in Diffusion Flames," Symp. Combust., **26**(2), pp. 2351–2358.

[277] Shih, C. J., Strano, M. S., and Blankschtein, D., 2013, "Wetting Translucency of Graphene," Nat. Mater., **12**(10), pp. 866–869.

[278] Michelsen, H. A., Tivanski, A. V, Gilles, M. K., van Poppel, L. H., Dansson, M. A., and Buseck, P. R., 2007, "Particle Formation from Pulsed Laser Irradiation of Soot Aggregates Studied with a Scanning Mobility Particle Sizer, a Transmission Electron Microscope, and a Scanning Transmission x-Ray Microscope,"

Appl. Opt., **46**(6), p. 959.

[279] Migliorini, F., De Iuliis, S., Maffi, S., and Zizak, G., 2015, "Saturation Curves of Two-Color Laser-Induced Incandescence Measurements for the Investigation of Soot Optical Properties," Appl. Phys. B, **120**(3), pp. 417–427.

[280] vander Wal, R. L., and Jensen, K. A., 1998, "Laser-Induced Incandescence: Excitation Intensity," Appl. Opt., **37**(9), pp. 1607–1616.

[281] Abrahamson, J. P., Singh, M., Mathews, J. P., and Vander Wal, R. L., 2017, "Pulsed Laser Annealing of Carbon Black," Carbon, **124**, pp. 380–390.

[282] Butenko, Y. V., Kuznetsov, V. L., Chuvilin, A. L., Kolomiichuk, V. N., Stankus, S. V., Khairulin, R. A., and Segall, B., 2000, "Kinetics of the Graphitization of Dispersed Diamonds at 'Low' Temperatures," J. Appl. Phys., **88**(7), pp. 4380–4388.

[283] Friedlander, S. K., and Wang, C. S., 1966, "The Self-Preserving Particle Size Distribution for Coagulation by Brownian Motion," J. Colloid Interface Sci., **22**(2), pp. 126–132.

[284] Brown, W. K., and Wohletz, K. H., 1995, "Derivation of the Weibull Distribution Based on Physical Principles and Its Connection to the Rosin–Rammler and Lognormal Distributions," J. Appl. Phys., **78**(4), pp. 2758–2763.

[285] Saxena, S. C., and Joshi, R. K., 1981, *Thermal Accommodation and Adsorption Coefficients of Gases*, McGraw-Hill Book Company, New York.

[286] Goodman, F. O., and Wachman, H. Y., 1976, *Dynamics of Gas-Surface Scattering*, Academic Press, New York.

[287] Baule, B., 1914, "Phenomena in Rarefied Gases," Ann. Phys., **44**, pp. 145–176.

[288] Logan, R. M., and Stickney, R. E., 1966, "Simple Classical Model for the Scattering of Gas Atoms from a Solid Surface," J. Chem. Phys., **44**(1), pp. 195–201.

[289] Logan, R. M., and Keck, J. C., 1968, "Classical Theory for the Interaction of Gas Atoms with Solid Surfaces," J. Chem. Phys., **49**(2), pp. 860–876.

[290] Physics, E., and Goodman, F. O., 1971, "Review of the Theory of the Scattering of Gas Atoms by Solid Surfaces," Surf. Sci., **26**(1), pp. 327–362.

[291] Goodman, F. O., 1965, "On the Theory of Accommodation Coefficients-IV. Simple Distribution Function Theory of Gas-Solid Interaction Systems," J. Phys. Chem. Solids, **26**(1), pp. 85–105.

[292] Song, S., and Yovanovich, M. M., 1987, "Correlation of Thermal Accomodation Coefficient for Engineering Surfaces," Proc. Twenty-fourth Natl. Heat Transf. Conf. Exhib., pp. 107–116.

[293] Oman, R. A., 1968, "Numerical Experiments on Scattering of Noble Gases from Single-Crystal Silver," J. Chem. Phys., **48**(9), pp. 3919–3929.

[294] Sipkens, T. A., and Daun, K. J., 2017, "Using Cube Models to Understand Trends in Thermal Accommodation Coefficients at High Surface Temperatures," Int. J. Heat Mass Transf., **111**, pp. 54–64.

[295] Wachman, H. Y., Greber, I., and Kass, G., 1992, "Molecular Dynamics Computations of Scattering from a Surface Using a Lennard-Jones Model of a Solid," *Progress in Astronautics and Aeronautics*, Vancouver,

pp. 479–493.

[296] Charita, V., Pailthorpe, B. A., and R. E. Collins, 1993, "Molecular Dynamics Study of Low-Energy Ar Scattering by the Ni(001) Surface," J. Phys. D. Appl. Phys., **26**(1), pp. 133–142.

[297] Sun, J., and Li, Z. X., 2009, "Molecular Dynamics Simulations of Energy Accommodation Coefficients for Gas Flows in Nano-Channels," Mol. Simul., **35**(3), pp. 228–233.

[298] Prabha, S. K., and Sathian, S. P., 2012, "Molecular-Dynamics Study of Poiseuille Flow in a Nanochannel and Calculation of Energy and Momentum Accommodation Coefficients," Phys. Rev. E, **85**(4), pp. 1–10.

[299] Spijker, P., Markvoort, A. J., Nedea, S. V, and Hilbers, P. A. J., 2010, "Computation of Accommodation Coefficients and the Use of Velocity Correlation Profiles in Molecular Dynamics Simulations," Phys. Rev. E, **81**(1), pp. 1–15.

[300] Hu, L., and McGaughey, A. J. H., 2013, "Energy Accommodation between Noble Gases and Carbon Nanotubes," J. Phys. Chem. C, **117**(37), pp. 18804–18808.

[301] Schiffres, S. N., Kim, K. H., Hu, L., McGaughey, A. J., Islam, M. F., and Malen, J. A., 2012, "Gas Diffusion, Energy Transport, and Thermal Accommodation in Single-walled Carbon Nanotube Aerogels," Adv. Funct. Mater., **22**(24), pp. 5251–5258.

[302] Liang, Z., and Keblinski, P., 2014, "Parametric Studies of the Thermal and Momentum Accommodation of Monoatomic and Diatomic Gases on Solid Surfaces," Int. J. Heat Mass Transf., **78**, pp. 161–169.

[303] Giri, A., and Hopkins, P. E., 2016, "Analytical Model for Thermal Boundary Conductance and Equilibrium Thermal Accommodation Coefficient at Solid/Gas Interfaces," J. Chem. Phys., **144**(8), p. 084705.

[304] Yamaguchi, H., Matsuda, Y., and Niimi, T., 2017, "Molecular-Dynamics Study on Characteristics of Energy and Tangential Momentum Accommodation Coefficients," Phys. Rev. E, **96**(1), pp. 1–8.

[305] Sha, H., Faller, R., Tetiker, G., and Woytowitz, P., 2018, "Molecular Simulation Study of Aluminum–noble Gas Interfacial Thermal Accommodation Coefficients," AIChE J., **64**(1), pp. 338–345.

[306] Daun, K. J., Titantah, J. T., and Karttunen, M., 2012, "Molecular Dynamics Simulation of Thermal Accommodation Coefficients for Laser-Induced Incandescence Sizing of Nickel Particles," Appl. Phys. B, **107**(1), pp. 221–228.

[307] Daun, K. J., Karttunen, J. T., and Titantah, M., 2013, "Erratum to: Molecular Dynamics Simulation of Thermal Accommodation Coefficients for Laser-Induced Incandescence Sizing of Nickel Particles," Appl. Phys. B, pp. 599–600.

[308] Borisov, S. F., Litvinenko, S. A., Semenov, Y. G., and Suetin, P. E., 1978, "Experimental Investigation of the Temperature Dependence of the Accommodation Coefficients for the Gases He, Ne, Ar, and Xe on a Pt Surface," J. Eng. Phys., **34**(5), pp. 603–606.

[309] Mann, W. B., 1934, "The Exchange of Energy between a Platinum Surface and Gas Molecules," Proc. R. Soc. A Math. Phys. Eng. Sci., **146**(859), pp. 776–791.

[310] Graf, U., and Nikuradse, A., 1967, "Experimental Studies on Distribution of Intensity of Reflected Molecular Beams as Functions of Adsorption and the Texture of Metals," Entropie, **115**(18).

[311] Liang, Z., Evans, W., and Keblinski, P., 2013, "Equilibrium and Nonequilibrium Molecular Dynamics Simulations of Thermal Conductance at Solid-Gas Interfaces," Phys. Rev. E, **87**(2), pp. 3–9.

[312] Hwang, G. S., and Kaviany, M., 2009, "Molecular Dynamics Simulation of Effective Thermal Conductivity of Vapor-Filled Nanogap and Nanocavity," J. Appl. Phys., **106**(2), pp. 1–6.

[313] Kamat, A. M., van Duin, A. C. T., and Yakovlev, A., 2010, "Molecular Dynamics Simulations of Laser-Induced Incandescence of Soot Using an Extended ReaxFF Reactive Force Field," J. Phys. Chem. A, **114**(48), pp. 12561–12572.

[314] Nolan, P. D., Lutz, B. R., Tanaka, P. L., Davis, J. E., and Mullins, C. B., 1999, "Molecularly Chemisorbed Intermediates to Oxygen Adsorption on Pt(111): A Molecular Beam and Electron Energy-Loss Spectroscopy Study," J. Chem. Phys., **111**(8), pp. 3696–3704.

[315] Daw, M. S., and Baskes, M. I., 1984, "Embedded-Atom Method: Derivation and Application to Impurities, Surfaces, and Other Defects in Metals," Phys. Rev. B, **29**(12), pp. 6443–6453.

[316] Sutton, A. P., and Chen, J., 1990, "Long-Range Finnis-Sinclair Potentials," Philos. Mag. Lett., **61**(3), pp. 139–146.

[317] Mishin, Y., 2005, "Interatomic Potentials for Metals," *Handbook of Materials Modeling*, Springer, Dordrecht, pp. 459–478.

[318] Gades, H., and Urbassek, H. M., 1992, "Pair versus Many-Body Potentials in Atomic Emission Processes from a Cu Surface," Nucl. Inst. Methods Phys. Res. B, **69**(2–3), pp. 232–241.

[319] Stillinger, F. H., and Weber, T. A., 1985, "Computer Simulation of Local Order in Condensed Phases of Silicon," Phys. Rev. B, **31**(8), pp. 5262–5271.

[320] Tersoff, J., 1988, "New Empirical Approach for the Structure and Energy of Covalent Systems," Phys. Rev. B, **37**(12), pp. 6991–7000.

[321] Bazant, M. Z., Kaxiras, E., and Justo, J., 1997, "Environment-Dependent Interatomic Potential for Bulk Silicon," Phys. Rev. B, **56**(14), pp. 8542–8552.

[322] Brenner, D. W., 1989, "Relationship between the Embedded-Atom Method and Tersoff Potentials," Phys. Rev. Lett., **63**(9), p. 1022.

[323] Plimpton, S., 1995, "Fast Parallel Algorithms for Short-Range Molecular Dynamics," J. Comput. Phys., **117**(1), pp. 1–19.

[324] Zhou, X. W., Johnson, R. A., and Wadley, H. N. G., 2004, "Misfit-Energy-Increasing Dislocations in Vapor-Deposited CoFe/NiFe Multilayers," Phys. Rev. B, **69**(14), pp. 1–10.

[325] Stukowski, A., 2009, "Visualization and Analysis of Atomistic Simulation Data with OVITO–the Open Visualization Tool," Model. Simul. Mater. Sci. Eng., **18**(1), p. 2010.

[326] Filippova, V. P., Kunavin, S. A., and Pugachev, M. S., 2015, "Calculation of the Parameters of the Lennard-Jones Potential for Pairs of Identical Atoms Based on the Properties of Solid Substances," Inorg. Mater. Appl. Res., **6**(1), pp. 1–4.

[327] Mendelev, M. I., Han, S., Srolovitz, D. J., Ackland, G. J., Sun, D. Y., and Asta, M., 2003, "Development of New Interatomic Potentials Appropriate for Crystalline and Liquid Iron," Philos. Mag., **83**(35), pp. 3977–3994.

[328] Müller, M., Erhart, P., and Albe, K., 2007, "Analytic Bond-Order Potential for Bcc and Fcc Iron—comparison with Established Embedded-Atom Method Potentials," J. Phys. Condens. Matter, **19**(32), p. 326220.

[329] Finnis, M. W., and Sinclair, J. E., 1984, "A Simple Empirical N-Body Potential for Transition Metals," Philos. Mag. A, **50**(1), pp. 45–55.

[330] Finnis, M. W., and Sinclair, J. E., 1986, "Erratum," Philos. Mag. A, **53**(1), p. 161.

[331] Pasianot, R., Farkas, D., and Savino, E. J., 1991, "Empirical Many-Body Interatomic Potential for Bcc Transition Metals," Phys. Rev. B, **43**(9), pp. 6952–6961.

[332] Ackland, G. J., Bacon, D. J., Calder, A. F., and Harry, T., 1997, "Computer Simulation of Point Defect Properties in Dilute Fe—Cu Alloy Using a Many-Body Interatomic Potential," Philos. Mag. A, **75**(3), pp. 713–732.

[333] Girifalco, L. A., and Weizer, V. G., 1959, "Application of the Morse Potential Function to Cubic Metals," Phys. Rev., **114**(3), pp. 687–690.

[334] Mills, K. C., 2002, *Recommended Values of Thermophysical Properties for Selected Commercial Alloys*, Woodhead Publishing, Cambridge.

[335] Imamova, S. E., Atanasov, P. A., Nedialkov, N. N., Dausinger, F., and Berger, P., 2005, "Molecular Dynamics Simulation Using Pair and Many Body Interatomic Potentials: Ultrashort Laser Ablation of Fe," Nucl. Instruments Methods Phys. Res. Sect. B, **227**(4), pp. 490–498.

[336] Basinski, Z. S., Hume-Rothery, W., and Sutton, A. L., 1955, "The Lattice Expansion of Iron," Proc. R. Soc. A Math. Phys. Eng. Sci., **229**(1179), pp. 459–467.

[337] Hixson, R. S., Winkler, M. A., and Hodgdon, M. L., 1990, "Sound Speed and Thermophysical Properties of Liquid Iron and Nickel," Phys. Rev. B, **42**(10), pp. 6485–6491.

[338] Malerba, L., Marinica, M. C., Anento, N., Björkas, C., Nguyen, H., Domain, C., Djurabekova, F., Olsson, P., Nordlund, K., Serra, A., and Terentyev, D., 2010, "Comparison of Empirical Interatomic Potentials for Iron Applied to Radiation Damage Studies," J. Nucl. Mater., **406**(1), pp. 19–38.

[339] Shibuta, Y., and Suzuki, T., 2008, "A Molecular Dynamics Study of the Phase Transition in Bcc Metal Nanoparticles," J. Chem. Phys., **129**(14), p. 144102.

[340] Sipkens, T. A., Daun, K. J., Titantah, J. T., and Karttunen, M., 2015, "Quantifying the Thermal Accommodation Coefficient for Iron Surfaces Using Molecular Dynamics Simulations," *ASME International Mechanical Engineering Congress and Exposition, Proceedings (IMECE)*.

[341] Zhou, X. W., Wadley, H. N. G., Johnson, R. A., Larson, D. J., Tabat, N., Cerezo, A., Petford-Long, A. K., Smith, G. D. W., Clifton, P. H., Martens, R. L., and Kelly, T. F., 2001, "Atomic Scale Structure of Sputtered Metal Multilayers," Acta Mater., **49**(19), pp. 4005–4015.

[342] Foiles, S. M., 1985, "Calculation of the Surface Segregation of Ni-Cu Alloys with the Use of the Embedded-Atom Method," Phys. Rev. B, **32**(12), pp. 7685–7693.

[343] Justo, J. F., Bazant, M. Z., Kaxiras, E., Bulatov, V. V., and Yip, S., 1998, "Interatomic Potential for Silicon Defects and Disordered Phases," Phys. Rev. B, **58**(5), pp. 2539–2550.

[344] Jelinek, B., Groh, S., Horstemeyer, M. F., Houze, J., Kim, S. G., Wagner, G. J., Moitra, A., and Baskes, M. I., 2012, "Modified Embedded Atom Method Potential for Al, Si, Mg, Cu, and Fe Alloys," Phys. Rev. B, **85**(24), p. 245102.

[345] Adams, J. B., Foiles, S. M., and Wolfer, W. G., 1989, "Self-Diffusion and Impurity Diffusion of Fee Metals

Using the Five-Frequency Model and the Embedded Atom Method," J. Mater. Res., **4**(1), pp. 102–112.

[346] Foiles, S. M., Baskes, M. I., and Daw, M. S., 1986, "Embedded-Atom-Method Functions for the Fcc Metals Cu, Ag, Au, Ni, Pd, Pt, and Their Alloys," Phys. Rev. B, **33**(12), pp. 7983–7991.

[347] Mishin, Y., Mehl, M. J., Papaconstantopoulos, D. A., Voter, A. F., and Kress, J. D., 2001, "Structural Stability and Lattice Defects in Copper: Ab Initio, Tight-Binding, and Embedded-Atom Calculations," Phys. Rev. B, **63**(22), p. 224106.

[348] Ryu, S., and Cai, W., 2008, "Comparison of Thermal Properties Predicted by Interatomic Potential Models," Model. Simul. Mater. Sci. Eng., **16**(8), p. 085005.

[349] Chizmeshya, A., and Zaremba, E., 1989, "Interaction of Rare Gas Atoms with Metal Surfaces: A Pseudopotential Approach," Surf. Sci., **220**(2–3), pp. 443–470.

[350] Vorontsov, A. G., Gel'chinskii, B. R., and Korenchenko, A. E., 2012, "Kinetics and Energy States of Nanoclusters in the Initial Stage of Homogeneous Condensation at High Supersaturation Degrees," J. Exp. Theor. Phys., **115**(5), pp. 789–797.

[351] Kurochkin, A. R., Yagodin, D. A., Borisenko, A. V., and Okhapkin, A. V., 2013, "Density of Copper-Aluminum Alloys at Temperatures up to 1400° c Determined by the Gamma-Ray Technique," High Temp., **51**(2), pp. 197–205.

[352] Brillo, J., and Egry, I., 2003, "Density Determination of Liquid Copper, Nickel, and Their Alloys," Int. J. Thermophys., **24**(4), pp. 1155–1170.

[353] Zaremba, E., and Kohn, W., 1977, "Theory of Helium Adsorption on Simple and Noble-Metal Surfaces," Phys. Rev. B, **15**(4), pp. 1769–1781.

[354] Bolding, B. C., and Andersen, H. C., 1990, "Interatomic Potential for Silicon Clusters, Crystals, and Surfaces," Phys. Rev. B, **41**(15), pp. 10568–10585.

[355] Cook, S. J., and Clancy, P., 1993, "Comparison of Semi-Empirical Potential Functions for Silicon and Germanium," Phys. Rev. B, **47**(13), pp. 7686–7699.

[356] Keblinski, P., Bazant, M. Z., Dash, R. K., and Treacy, M. M., 2002, "Thermodynamic Behavior of a Model Covalent Material Described by the Environment-Dependent Interatomic Potential," Phys. Rev. B, **66**(6), pp. 641041–6410414.

[357] Samela, J., Nordlund, K., Keinonen, J., and Popok, V. N., 2007, "Comparison of Silicon Potentials for Cluster Bombardment Simulations," Nucl. Instruments Methods Phys. Res. Sect. B Beam Interact. with Mater. Atoms, **255**(1 SPEC. ISS.), pp. 253–258.

[358] Nurminen, L., Tavazza, F., Landau, D. P., Kuronen, A., and Kaski, K., 2003, "Comparative Study of Si (001) Surface Structure and Interatomic Potentials in Finite-Temperature Simulations," Phys. Rev. B, **67**(3), p. 035405.

[359] Godet, J., Pizzagalli, L., Brochard, S., and Beauchamp, P., 2003, "Comparison between Classical Potentials and Ab Initio Methods for Silicon under Large Shear," J. Phys. Condens. Matter, **15**(41), pp. 6943–6953.

[360] Zhao, J., Singh, V., Grammatikopoulos, P., Cassidy, C., Aranishi, K., Sowwan, M., Nordlund, K., and Djurabekova, F., 2015, "Crystallization of Silicon Nanoclusters with Inert Gas Temperature Control," Phys. Rev. B, **91**(3), pp. 1–12.

[361] Tersoff, J., 1988, "Empirical Interatomic Potential for Silicon with Improved Elastic Properties," Phys. Rev. B, **38**(14), pp. 9902–9905.

[362] Erhart, P., and Albe, K., 2005, "Analytical Potential for Atomistic Simulations of Silicon, Carbon, and Silicon Carbide," Phys. Rev. B, **71**(3), pp. 1–14.

[363] Assael, M. J., Armyra, I. J., Brillo, J., Stankus, S. V, Wu, J., and Wakeham, W. A., 2012, "Reference Data for the Density and Viscosity of Liquid Cadmium, Cobalt, Gallium, Indium, Mercury, Silicon, Thallium, and Zinc," J. Phys. Chem. Ref. Data, **41**(3), p. 033101.

[364] Dozhdikov, V. S., Basharin, A. Y., and Levashov, P. R., 2012, "Two-Phase Simulation of the Crystalline Silicon Melting Line at Pressures from -1 to 3 GPa," J. Chem. Phys., **137**(5), p. 054502.

[365] Hara, S., Izumi, S., Kumagai, T., and Sakai, S., 2005, "Surface Energy, Stress and Structure of Well-Relaxed Amorphous Silicon: A Combination Approach of Ab Initio and Classical Molecular Dynamics," Surf. Sci., **585**(1–2), pp. 17–24.

[366] Dalton, A. S., and Seebauer, E. G., 2004, "Structure and Mobility on Amorphous Silicon Surfaces," Surf. Sci., **550**(1–3), pp. 140–148.

[367] Rhim, W. K., and Ohsaka, K., 2000, "Thermophysical Properties Measurement of Molten Silicon by High-Temperature Electrostatic Levitator: Density, Volume Expansion, Specific Heat Capacity, Emissivity, Surface Tension and Viscosity," J. Cryst. Growth, **208**(1), pp. 313–321.

[368] Ohsaka, K., Chung, S. K., Rhim, W. K., and Holzer, J. C., 1997, "Densities of Si Determined by an Image Digitizing Technique in Combination with an Electrostatic Levitator," Appl. Phys. Lett., **70**(4), pp. 423–425.

[369] Rumble, J. R., ed., 2018, *CRC Handbook of Chemistry and Physics*, CRC Press/Taylor & Francis, Boca Raton.

[370] Baskes, M. I., Nelson, J. S., and Wright, A. F., 1989, "Semiempirical Modified Embedded-Atom Potentials for Silicon and Germanium," Phys. Rev. B, **40**(9), pp. 6085–6100.

[371] Talebi Maghaddam, S., Bauer, F. J., Sipkens, T. A., Huber, F. J. T., Will, S., and Daun, K. J., 2018, "Neatural Bremsstrahlung Emission in Laser-Induced Incandescence Experiments on Soot and Silver Nanoparticles," *8th International Workshop on Laser-Induced Incandescence*, p. 47.

[372] Feldheim, D. L., and Foss, C. A., 2002, *Metal Nanoparticles: Synthesis, Characterization, and Applications*, Macrel Dekker, Inc., Basel.

[373] Quinten, M., 2011, *Optical Properties of Nanoparticle Systems: Mie and Beyond*, Wiley-VCH, Weinheim.

[374] Miller, J. C., 1969, "Optical Properties of Liquid Metals At High Temperatures," Philos. Mag., **20**(168), pp. 1115–1132.

[375] Bohren, C. F., and Huffman, D. R., 1983, "Classical Theories of Optical Constants," *Absorption and Scattering of Light by Small Particles*, John Wiley & Sons, New York, pp. 227–267.

[376] Krishnan, S., Hansen, G. P., Hauge, R. H., and Margrave, J. L., 1990, "Emissivities and Optical Constants of Electromagnetically Levitated Liquid Metals as Functions of Temperature and Wavelength," *Materials Chemistry at High Temperatures*, Humana Press, Totowa, pp. 143–164.

[377] Kobatake, H., Khosroabadi, H., and Fukuyama, H., 2012, "Normal Spectral Emissivity Measurement of

Liquid Iron and Nickel Using Electromagnetic Levitation in Direct Current Magnetic Field," Metall. Mater. Trans. A, **43**(7), pp. 2466–2472.

[378] Daun, K. J., 2016, "Discussion of "Normal Spectral Emissivity Measurement of Qiquid Iron and Nickel Using Electromagnetic Levitation in Direct Current Magnetic Field"," Metall. Mater. Trans. A, **47**(7), pp. 3300–3302.

[379] Shvarev, K. M., Gushchin, V. S., and Baum, B. A., 1978, "Effect of Temperature on the Optical Properties of Iron," High Temp., **16**, pp. 441–446.

[380] Paradis, P.-F. P.-F., Ishikawa, T., and Yoda, S., 2002, "Noncontact Measurements of Thermophysical Properties of Molybdenum at High Temperatures," Int. J. Thermophys., **23**(2), pp. 555–569.

[381] Modest, M. F., 2003, *Radiative Heat Transfer*, Academic Press, New York.

[382] Barnes, B. T., 1966, "Optical Constants of Incandescent Refractory Metals," J. Opt. Soc. Am. A Opt. Image Sci. Vis., **56**(11), pp. 1546–1550.

[383] Juenker, D. W., LeBlanc, L. J., and Martin, C. R., 1968, "Optical Properties of Some Transition Metals," J. Opt. Soc. Am., **58**(2), pp. 164–171.

[384] Palik, E. D., 2012, *Handbook of Optical Constants of Solids*, Elsevier, London.

[385] TSI, 2005, *Model 3076 Constant Output Atomizer Instruction Manual*.

[386] Grosse, A. V., and Kirshenbaum, A. D., 1962, "The Temperature Range of Liquid Lead and Silver and an Estimate of Their Critical Constants," J. Inorg. Nucl. Chem., **24**(6), pp. 739–748.

[387] Desai, P. D., 1986, "Thermodynamic Properties of Iron and Silicon," J. Phys. Chem. Ref. Data, **15**(3), pp. 967–983.

[388] Cagran, C., Wilthan, B., and Pottlacher, G., 2006, "Enthalpy, Heat of Fusion and Specific Electrical Resistivity of Pure Silver, Pure Copper and the Binary Ag-28Cu Alloy," Thermochim. Acta, **445**(2), pp. 104–110.

[389] Speight, J. G., 2005, *Lange's Handbook of Chemistry*, McGraw-Hill, New York.

[390] Mafune, F., Kohno, J. Y., Takeda, Y., and Kondow, T., 2003, "Formation of Stable Platinum Nanoparticles by Laser Ablation in Water," J. Phys. Chem. B, **107**(18), pp. 4218–4223.

[391] Rumble, J. R., 2017, *CRC Handbook of Chemisty and Physics*, Taylor & Francis.

[392] Desai, P. D., 1987, "Thermodynamic Properties of Manganese and Molybdenum," J. Phys. Chem. Ref. Data, **16**(1), pp. 91–108.

[393] Young, D. A., and Alder, B. J., 1971, "Critical Point of Metals from the van Der Waals Model," Phys. Rev. A, **3**(1), pp. 364–371.

[394] Keene, B. J., 1988, "Review of Data for the Surface Tension of Iron and Its Binary Alloys," Int. Mater. Rev., **33**(1), pp. 1–37.

[395] Novakovic, R., Ricci, E., Giuranno, D., and Passerone, A., 2005, "Surface and Transport Properties of Ag–Cu Liquid Alloys," Surf. Sci., **576**(1–3), pp. 175–187.

[396] Lu, H. M., and Jiang, Q., 2005, "Surface Tension and Its Temperature Coefficient for Liquid Metals," J. Phys. Chem. B, **109**(32), pp. 15463–15468.

[397] Liu, Y., Majetich, S. A., and Sholl, D. S., 2005, "TCE Dechlorination Rates , Pathways , and Efficiency of Nanoscale Iron Particles with Different Properties," Environ. Sci. Technol., **39**(5), pp. 1338–1345.

[398] He, F., and Zhao, D., 2007, "Manipulating the Size and Dispersibility of Zerovalent Iron Nanoparticles by Use of Carboxymethyl Cellulose Stabilizers Manipulating the Size and Dispersibility of Zerovalent Iron Nanoparticles by Use of Carboxymethyl Cellulose Stabilizers," Environ. Sci. Technol., **41**(17), pp. 6216–6221.

[399] Lee, P. C., and Meisel, D., 1982, "Adsorption and Surface-Enhanced Raman of Dyes on Silver and Gold Sols," J. Phys. Chem., **86**(17), pp. 3391–3395.

[400] Rakić, A. D., Djurišić, A. B., Elazar, J. M., and Majewski, M. L., 1998, "Optical Properties of Metallic Films for Vertical-Cavity Optoelectronic Devices," Appl. Opt., **37**(22), pp. 5271–5283.

[401] Ordal, M. A., Bell, R. J., Alexander, R. W., Long, L. L., and Querry, M. R., 1985, "Optical Properties of Fourteen Metals in the Infrared and Far Infrared: Al, Co, Cu, Au, Fe, Pb, Mo, Ni, Pd, Pt, Ag, Ti, V, and W," Appl. Opt., **24**(24), p. 4493.

[402] Phenrat, T., Kim, H. J., Fagerlund, F., Illangasekare, T., Tilton, R. D., and Lowry, G. V., 2009, "Particle Size Distribution, Concentration, and Magnetic Attraction Affect Transport of Polymer-Modified Fe0 Nanoparticles in Sand Columns," Environ. Sci. Technol., **43**(13), pp. 5079–5085.

[403] Thompson, R., 1985, "A Note on Restricted Maximum Likelihood Estimation with an Alternative Outlier Model," J. R. Stat. Soc. Ser. B, **47**(1), pp. 53–55.

[404] Schierning, G., Theissmann, R., Wiggers, H., Sudfeld, D., Ebbers, A., Franke, D., Witusiewicz, V. T., and Apel, M., 2008, "Microcrystalline Silicon Formation by Silicon Nanoparticles," J. Appl. Phys., **103**(8), p. 084305.

[405] Couchman, P. R., and Jesser, W. A., 1977, "Thermodynamic Theory of Size Dependence of Melting Temperature in Metals," Nature, **269**(5628), pp. 481–483.

[406] Beutl, M., Pottlacher, G., and Jager, H., 1994, "Thermophysical Properties of Liquid Iron," Int. J. Thermophys., **15**(6), pp. 1323–1331.

[407] Wille, G., Millot, F., and Rifflet, J. C., 2002, "Thermophysical Properties of Containerless Liquid Iron up to 2500 K," Int. J. Thermophys., **23**(5), pp. 1197–1206.

[408] Velasco, S., Román, F. L., White, J. A., and Mulero, A., 2006, "Prediction of the Enthalpy of Vaporization of Metals and Metalloids," Fluid Phase Equilib., **244**(1), pp. 11–15.

[409] Svoboda, V., and Smolová, H., 1994, "Correlation of Enthalpies of Vaporization of Pure Substances. Part I," Fluid Phase Equilib., **93**, pp. 167–175.

[410] Trotta, R., 2008, "Bayes in the Sky: Bayesian Inference and Model Selection in Cosmology," Contemp. Phys., **49**(2), pp. 71–104.

[411] Liddle, A. R., 2007, "Information Criteria for Astrophysical Model Selection," Mon. Not. R. Astron. Soc. Lett., **377**(1), pp. L74–L78.

[412] Dose, V., 2003, "Bayesian Inference in Physics: Case Studies," Reports Prog. Phys., **66**(9), pp. 1421–1461.

[413] Raftery, A. E., 1995, "Bayesian Model Selection in Social Research," Sociol. Methodol., **25**, pp. 111–163.

[414] An, S., and Schorfheide, F., 2007, "Bayesian Analysis of DSGE Models," Econom. Rev., **26**(2–4), pp. 113–172.

[415] Symonds, M. R. E., and Moussalli, A., 2011, "A Brief Guide to Model Selection, Multimodel Inference and Model Averaging in Behavioural Ecology Using Akaike's Information Criterion," Behav. Ecol. Sociobiol., **65**(1), pp. 13–21.

[416] Hooten, M. B., and Hobbs, N. T., 2015, "A Guide to Bayesian Model Selection for Ecologists," Ecol. Monogr., **85**(1), pp. 3–28.

[417] Sullivan, J., and Joyce, P., 2005, "Model Selection in Phylogenetics," Annu. Rev. Ecol. Evol. Syst., **36**(1), pp. 445–466.

[418] Sunnåker, M., and Stelling, J., 2016, "Model Extension and Model Selection," *Uncertainty in Biology*, Springer, Berlin.

[419] Thiesen, M., 1897, "Bemerkung Über Die Verdampfungswärme," Verhandlungen der Dtsch. Phys. Gesellschaft, **16**(6), pp. 80–82.

[420] Fisher, M. E., 1982, "Scaling, Universality and Renormalization Group Theory," *Lecture Notes in Physics*, Springer-Verlag Berlin Heidelberg, New York.

[421] Kendall, J., 1914, "The Heat of Vaporization of Normal Liquids," J. Am. Chem. Soc., **36**(8), pp. 1620–1630.

[422] Jones, W. J., and Bowden, S. T., 2017, "XLVII . Power Laws of Latent Heat, Orthobaric Density, Surface Tension and Viscosity of Liquids," London, Edinburgh, Dublin Philos. Mag. J. Sci., **37**(270), pp. 480–489.

[423] Bowden, S. T., 1955, "Variation of Surface Tension and Heat of Vaporization with Temperature," J. Chem. Phys., **23**(12), pp. 2454–2455.

[424] Winter, R. M., 1928, "Latent Heat of Vaporization as a Function of Temperature," J. Phys. Chem., **32**(4), pp. 576–582.

[425] Silverberg, P. M., and Wenzel, L. A., 1965, "Variation of Latent Heat with Temperature," J. Chem. Eng. Data, **10**(4), pp. 363–366.

[426] Marla, D., Bhandarkar, U. V., and Joshi, S. S., 2013, "Modeling Nanosecond Pulsed Laser Ablation: A Focus on Temperature Dependence of Material Properties," Manuf. Lett., **2**(1), pp. 13–16.

[427] Kitano, T., Nishio, J., Kurose, R., and Komori, S., 2014, "Effects of Ambient Pressure, Gas Temperature and Combustion Reaction on Droplet Evaporation," Combust. Flame, **161**(2), pp. 551–564.

[428] Zhong, X., 1984, "An Improved Generalized Watson Equation for Prediction of Latent Heat of Vaporization," Chem. Eng. Commun., **29**(1–6), pp. 257–269.

[429] Svoboda, V., Charvátová, V., Majer, V., and Pick, J., 1981, "Determination of Heats of Vaporization and Some Other Thermodynamic Quantities for Four Alkylcycloparaffins," Collect. Czechoslov. Chem. Commun., **46**(12), pp. 2983–2988.

[430] Fish, L. W., and Lielmezs, J., 1975, "General Method for Predicting the Latent Heat of Vaporization," Ind. Eng. Chem. Fundam., **14**(3), pp. 248–256.

[431] Velasco, S., Santos, M. J., and White, J. A., 2015, "Consistency of Vapor Pressure Equations at the Critical Point," Ind. Eng. Chem. Res., **54**(51), pp. 12993–12998.

[432] Forsythe, W. E., 2003, *Smithsonian Physical Tables*, Knovel.

[433] Kaye, G. W. C., and Laby, T. H., 1928, *Tables of Physical and Chemical Constants and Some Mathematical Functions*, Longmans, Green and Co., London.

[434] The National Physical Laboratory, 2005, *Tables of Physical & Chemical Constants*, Kaye & Laby Online.

[435] Earnshaw, A., and Greenwood, N., 1997, *Chemistry of the Elements*, Elsevier.

[436] Fortov, V. E., Dremin, A. N., and Leontev, A., 1975, "Estimation of Critical-Point Parameters," Teplofiz. Vys. Temp., **13**(3), pp. 1072–1080.

[437] Kopp, I. Z., 1967, "-," Zh. Fiz. Khim., **41**(5), p. 1474.

[438] Guggenheim, E. A., 1945, "The Principle of Corresponding States," J. Chem. Phys., **13**(7), pp. 253–261.

[439] Cheung, S. H., and Beck, J. L., 2009, "Bayesian Model Updating Using Hybrid Monte Carlo Simulation with Application to Structural Dynamic Models with Many Uncertain Parameters," J. Eng. Mech., **135**(4), pp. 243–255.

[440] Grauer, S. J., Hadwin, P. J., Sipkens, T. A., and Daun, K. J., 2017, "Measurement-Based Meshing, Basis Selection, and Prior Assignment in Chemical Species Tomography," Opt. Express, **25**(21), p. 25135.

[441] Posada, D., and Buckley, T. R., 2004, "Model Selection and Model Averaging in Phylogenetics: Advantages of Akaike Information Criterion and Bayesian Approaches over Likelihood Ratio Tests," Syst. Biol., **53**(5), pp. 793–808.

[442] Menser, J., Daun, K. J., Dreier, T., and Schulz, C., 2018, "Transition from Laser-Induced Incandescence (LII) to Laser-Induced Breakdown Spectroscopy (LIBS) on Elemental Nanoparticles," *8th International Workshop on Laser-Induced Incandescence*, p. 34.

[443] Daun, K. J., Menser, J., Mansmann, R., Dreier, T., and Schulz, C., 2016, "Laser-Induced Incandescence Measurements of Silicon and Copper Nanoparticles: Spectroscopic Model," *Proceedings of the 8th International Symposium on Radiative Transfer, RAD-16*, Cappadocia.

[444] Chen, Y., Richardson, D. R., Cenker, E., Halls, B. R., Skeen, S., Shaddix, C., and Guildenbecher, D. R., 2018, "Turbulent Flame LII Particle Sizing Vie Ultra-High-Speed Imaging," *8th International Workshop on Laser-Induced Incandescence*, p. 22.

[445] Liu, F., and Smallwood, G. J., 2018, "Effect of Detection Wavelengths on Soot Volume Fraction Measurements Using Auto-Compensating (Two-Color) LII," *8th International Workshop on Laser-Induced Incandescence*, p. 32.

[446] Sipkens, T. A., Singh, N. R., Daun, K. J., Bizmark, N., Ioannidis, M., Titantah, J. T., and Karttunen, M., 2014, "Time Resolved Laser Induced Incandescence for Sizing Aerosolized Iron Nanoparticles," *ASME 2014 International Mechanical Engineering Congress and Exposition*, Montreal.

[447] Tersoff, J., 1989, "Modeling Solid-State Chemistry: Interatomic Potentials for Multicomponent Systems," Phys. Rev. B, **39**(8), pp. 5566–5568.

[448] Los, H., and Fasolino, A., 2003, "Intrinsic Long-Range Bond-Order Potential for Carbon: Performance in Monte Carlo Simulations of Graphitization," Phys. Rev. B, **68**(2), pp. 1–14.

[449] Lucas, G., Bertolus, M., and Pizzagalli, L., 2010, "An Environment-Dependent Interatomic Potential for Silicon Carbide: Calculation of Bulk Properties, High-Pressure Phases, Point and Extended Defects, and Amorphous Structures," J. Phys. Condens. Matter, **22**(3), p. 035802.

[450] Bauer, F. J., Daun, K. J., Huber, F. J. T., and Will, S., 2018, "Can Soot Primary Particle Size Distribution Be Determined Using Laser-Induced Incandescence?," *8th International Workshop on Laser-Induced Incandescence*, p. 18.

[451] Maricq, M. M., 2007, "Chemical Characterization of Particulate Emissions from Diesel Engines: A Review," J. Aerosol Sci., **38**(11), pp. 1079–1118.

[452] Elmes, M., and Gasparon, M., 2017, "Sampling and Single Particle Analysis for the Chemical Characterisation of Fine Atmospheric Particulates: A Review," J. Environ. Manage., **202**, pp. 137–150.

[453] Burtscher, H., 2005, "Physical Characterization of Particulate Emissions from Diesel Engines: A Review," J. Aerosol Sci., **36**(7), pp. 896–932.

[454] Giechaskiel, B., Maricq, M., Ntziachristos, L., Dardiotis, C., Wang, X., Axmann, H., Bergmann, A., and Schindler, W., 2014, "Review of Motor Vehicle Particulate Emissions Sampling and Measurement: From Smoke and Filter Mass to Particle Number," J. Aerosol Sci., **67**, pp. 48–86.

[455] Kulmala, M., Vehkamäki, H., Petäjä, T., Dal Maso, M., Lauri, A., Kerminen, V. M., Birmili, W., and McMurry, P. H., 2004, "Formation and Growth Rates of Ultrafine Atmospheric Particles: A Review of Observations," J. Aerosol Sci., **35**(2), pp. 143–176.

[456] Jones, A. M., and Harrison, R. M., 2016, "Emission of Ultrafine Particles from the Incineration of Municipal Solid Waste: A Review," Atmos. Environ., **140**, pp. 519–528.

[457] Price, P., Stone, R., Collier, T., Davies, M., and Scheer, V., 2006, "Dynamic Particulate Measurements from a DISI Vehicle: A Comparison of DMS500, ELPI, CPC and PASS," SAE Tech. Pap., (2006-01-1077).

[458] Petzold, A., Marsh, R., Johnson, M., Miller, M., Sevcenco, Y., Delhaye, D., Ibrahim, A., Williams, P., Bauer, H., Crayford, A., Bachalo, W. D., and Raper, D., 2011, "Evaluation of Methods for Measuring Particulate Matter Emissions from Gas Turbines," Environ. Sci. Technol., **45**(8), pp. 3562–3568.

[459] Viskup, R., Alberer, D., Oppenauer, K., and del Re, L., 2011, "Measurement of Transient PM Emissions in Diesel Engine," SAE Tech. Pap., (2011-24-00197).

[460] Axelsson, B., and Witze, P. O., 2001, "Qualitative Laser-Induced Incandescence Measurements of Particulate Emissions during Transient Operation of a TDI Diesel Engine," SAE Tech. Pap., (2001-01-3574).

[461] Kawano, D., Kawai, T., Naito, H., Goto, Y., Odaka, M., and Bachalo, W. D., 2004, "Comparative Measurement of Nano-Particulates in Diesel Engine Exhaust Gas by Laser-Induced Incandescence (LII) and Scanning Mobility Particle Sizer (SMPS)," SAE Tech. Pap., (2004-01-1982).

[462] Kulkarni, P., and Wang, J., 6AD, "New Fast Integrated Mobility Spectrometer for Real-Time Measurement of Aerosol Size Distribution—I: Concept and Theory," J. Aerosol Sci., **37**(10), pp. 1303–1325.

[463] Di Iorio, S., Merola, S. S., Vaglieco, B. M., and Tornatore, C., 2005, "Diesel Exhaust Nanoparticles Characterization by Multiwavelength Techniques , Laser Induced Incandescence and ELPI," SAE Tech. Pap., (2005-24-021).

[464] Merola, S. S., Vaglieco, B. M., and Tornatore, C., 2005, "Characterization of Nanoparticles at the Exhaust of a Common Rail Diesel Engine by Optical Techniques and Conventional Method," SAE Tech. Pap., (2005-01-2155).

[465] Witze, P. O., Chase, R. E., Maricq, M. M., Podsiadlik, D. H., and Xu, N., 2004, "Time-Resolved Measurements

of Exhaust PM for FTP-75: Comparison of LII, ELPI, and TEOM Techniques," SAE Tech. Pap., (2004-1-964).

[466] Mohr, M., Lehmann, U., and Rutter, J., 2005, "Comparison of Mass-Based and Non-Mass-Based Particle Measurement Systems for Ultra-Low Emissions from Automotive Sources," Environ. Sci. Technol., **39**(7), pp. 2229–2238.

[467] Kotrappa, P., and Light, M. E., 1972, "Design and Performance of the Lovelace Aerosol Particle Separator," Rev. Sci. Instrum., **43**(8), pp. 1106–1112.

[468] Liao, B. X., Tseng, N. C., and Tsai, C. J., 2018, "The Accuracy of the Aerosol Particle Mass Analyzer for Nanoparticle Classification," Aerosol Sci. Technol., **52**(1), pp. 19–29.

[469] Ning, Z., Chan, K. L., Wong, K. C., Westerdahl, D., Močnik, G., Zhou, J. H., and Cheung, C. S., 2013, "Black Carbon Mass Size Distributions of Diesel Exhaust and Urban Aerosols Measured Using Differential Mobility Analyzer in Tandem with Aethalometer," Atmos. Environ., **80**, pp. 31–40.

[470] Dankers, S., Will, S., Reimann, J., Leipertz, A., Arndt, J., Vogel, K., Schraml, S., and Hemm, A., 2002, "Time-Resolved Laser-Induced Incandescence for in Situ Nanoparticle Characterisation in Different Reactors," *11th International Symposium on Application of Laser Techniques to Fluid Mechanics*, Lisbon.

[471] Cheng, Y. S., 2001, "Condensation Detection and Diffusion Size Separation Techniques," *Aerosol Measurement: Principles, Techniques, and Applications*, John Wiley & Sons, New York, pp. 569–601.

[472] Hinds, W. C., 1982, *Aerosol Technology: Properties, Behaviour, and Measruement of Airborne Particles*, John Wiley & Sons, New York.

[473] Knoll, M., and Ruska, E., 1932, "Das Elektronenmikroskop," Zeitschrift für Phys., **78**(5–6), pp. 318–339.

[474] China, S., Mazzoleni, C., Gorkowski, K., Aiken, A. C., and Dubey, M. K., 2013, "Morphology and Mixing State of Individual Freshly Emitted Wildfire Carbonaceous Particles," Nat. Commun., **4**(2122), pp. 1–7.

[475] Puntes, V. F., Gorostiza, P., Aruguete, D. M., Bastus, N. G., and Alivisatos, A. P., 2004, "Collective Behaviour in Two-Dimensional Cobalt Nanoparticle Assemblies Observed by Magnetic Force Microscopy," Nat. Mater., **3**(4), pp. 263–268.

[476] Williams, D. B., and Carter, C. B. B., 2009, *Transmission Electron Microscopy*, Springer Science and Business Media, New York.

[477] Pyrz, W. D., and Buttrey, D. J., 2008, "Particle Size Determination Using TEM: A Discussion of Image Acquisition and Analysis for the Novice Microscopist," Langmuir, **24**(20), pp. 11350–11360.

[478] Brasil, A. M., Farias, T. L., and Carvalho, M. G., 1999, "A Recipe for Image Characterization of Fractal-like Aggregates," J. Aerosol Sci., **30**(10), pp. 1379–1389.

[479] Spence, J. C. H., 2013, *High-Resolution Electron Microscopy*, Oxford University Press, New York.

[480] Knauer, M., Schuster, M. E., Su, D., Schlögl, R., Niessner, R., and Ivleva, N. P., 2009, "Soot Structure and Reactivity Analysis by Raman Microspectroscopy, Temperature-Programmed Oxidation, and High-Resolution Transmission Electron Microscopy," J. Phys. Chem. A, **113**(50), pp. 13871–13880.

[481] Salapaka, S., and Salapaka, M., 2008, "Scanning Probe Microscopy," IEEE Control Syst. Mag., **28**(2), pp. 65–83.

[482] Fletcher, R. A., Small, J. A., and Scott, J. H. J., 2001, "Analysis of Individual Collected Particles," *Aerosol Measurement: Principles, Techniques, and Applications*, John Wiler & Sons, New York, pp. 295–363.

[483] Aitken, J., 1888, "On the Number of Dust Particles in the Atmosphere," Nature, **37**, pp. 428–430.

[484] Okuyama, K., Kousaka, Y., and Motouchi, T., 1984, "Condensational Growth of Ultrafine Aerosol Particles in a New Particle Size Magnifier," Aerosol Sci. Technol., **3**(4), pp. 353–366.

[485] Kousaka, Y., Endo, Y., Muroya, Y., and Fukushima, N., 1992, "Development of a High Flow Rate Mixing Type CNC and Its Application to Cumulative Type Electrostatic Particle Size Analysis," Aerosol Res., **7**(3), pp. 219–229.

[486] Wainner, R. T., Seitzman, J. M., and Martin, S. R., 1999, "Soot Measurements in a Simulated Engine Exhaust Using Laser-Induced Incandescence," AIAA J., **37**(6), pp. 738–743.

[487] Santoro, R. J., and Shaddix, C. R., 2002, "Laser-Induced Incandescence," *Applied Combustion Diagnostics*, Taylor & Francis, New York, pp. 252–286.

[488] Knutson, E. O., and Whitby, K. T., 1975, "Aerosol Classification by Electric Mobility: Apparatus, Theory, and Applications," J. Aerosol Sci., **6**(6), pp. 443–451.

[489] Wang, S. C., and Flagan, R. C., 1990, "Scanning Electrical Mobility Spectrometer," Aerosol Sci. Technol., **13**(2), pp. 230–240.

[490] Levin, M., Gudmundsson, A., Pagels, J. H., Fierz, M., Mølhave, K., Löndahl, J., Jensen, K. A., and Koponen, I. K., 2015, "Limitations in the Use of Unipolar Charging for Electrical Mobility Sizing Instruments: A Study of the Fast Mobility Particle Sizer," Aerosol Sci. Technol., **49**(8), pp. 556–565.

[491] Russell, L. M., Flagan, R. C., and Seinfeld, J. H., 1995, "Asymmetric Instrument Response Resulting from Mixing Effects in Accelerated DMA-CPC Measurements," Aerosol Sci. Technol., **23**(4), pp. 491–509.

[492] Asbach, C., Kaminski, H., Fissan, H., Monz, C., Dahmann, D., Mülhopt, S., Paur, H. R., Kiesling, H. J., Herrmann, F., Voetz, M., and Kuhlbusch, T. A. J., 2009, "Comparison of Four Mobility Particle Sizers with Different Time Resolution for Stationary Exposure Measurements," J. Nanoparticle Res., **11**(7), pp. 1593–1609.

[493] Ham, S., Lee, N., Eom, I., Lee, B., Tsai, P. J., Lee, K., and Yoon, C., 2016, "Comparison of Real Time Nanoparticle Monitoring Instruments in the Workplaces," Saf. Health Work, **7**(4), pp. 381–388.

[494] Leskinen, J., Joutsensaari, J., Lyyränen, J., Koivisto, J., Ruusunen, J., Järvelä, M., Tuomi, T., Hämeri, K., Auvinen, A., and Jokiniemi, J., 2012, "Comparison of Nanoparticle Measurement Instruments for Occupational Health Applications," J. Nanoparticle Res., **14**(718), pp. 1–16.

[495] Kaminski, H., Kuhlbusch, T. A. J., Rath, S., Götz, U., Sprenger, M., Wels, D., Polloczek, J., Bachmann, V., Dziurowitz, N., Kiesling, H. J., Schwiegelshohn, A., Monz, C., Dahmann, D., and Asbach, C., 2013, "Comparability of Mobility Particle Sizers and Diffusion Chargers," J. Aerosol Sci., **57**, pp. 156–178.

[496] Reavell, K., Hands, T., and Collings, N., 2002, "A Fast Response Particulate Spectrometer for Combustion Aerosols," SAE Tech. Pap., (2002-01-2714).

[497] Mirme, A., Noppel, M., Peil, I., Salm, J., Tamm, E., and Tammet, H., 1984, "Multi-Channel Electric Aerosol Spectrometer," *11th International Conference on Atmospheric Aerosols*, Budapest.

[498] Jeong, C. H., and Evans, G. J., 2009, "Inter-Comparison of a Fast Mobility Particle Sizer and a Scanning

Mobility Particle Sizer Incorporating an Ultrafine Water-Based Condensation Particle Counter," Aerosol Sci. Technol., **43**(4), pp. 364–373.

[499] Ranjan, M., and Dhaniyala, S., 2007, "Theory and Design of a New Miniature Electrical-Mobility Aerosol Spectrometer," J. Aerosol Sci., **38**(9), pp. 950–963.

[500] Kulkarni, P., and Wang, J., 2006, "New Fast Integrated Mobility Spectrometer for Real-Time Measurement of Aerosol Size Distribution: II. Design, Calibration, and Performance Characterization," J. Aerosol Sci., **37**(10), pp. 1326–1339.

[501] Ahn, K. H., and Chung, H., 2010, "Aerosol Electrical Mobility Spectrum Analyzer," J. Aerosol Sci., **41**(4), pp. 344–351.

[502] Keskinen, J., Pietarinen, K., and Lehtimäki, M., 1992, "Electrical Low Pressure Impactor," J. Aerosol Sci., **23**(4), pp. 353–360.

[503] Marjamäki, M., Keskinen, J., Chen, D. R., and Pui, D. Y. H., 2000, "Performance Evaluation of the Electrical Low-Pressure Impactor (ELPI)," J. Aerosol Sci., **31**(2), pp. 249–261.

[504] Marjamäki, M., Ntziachristos, L., Virtanen, A., Ristimäki, J., Keskinen, J., Moisio, M., Palonen, M., and Lappi, M., 2002, "Electrical Filter Stage for the ELPI," SAE Tech. Pap., (2002-1–55).

[505] Ahlvik, P., and Ntziachristos, L., 1998, "Real Time Measurements of Diesel Particle Size Distribution with an Electrical Low Pressure Impactor," SAE Tech. Pap., (980410).

[506] Horton, K. D., Ball, M. H. E., Mitchell, J. P., Crystal, P.-Q., Impactor, C., Horton, K. D., Ball, M. H. E., and Mitchell, J. P., 1992, "The Calibration of a California Measurements PC-2 Quartz Crystal Cascade Impactor (QCM)," J. Aerosol Sci., **23**(5), pp. 505–524.

[507] Maricq, M. M., Xu, N., and Chase, R. E., 2006, "Measuring Particulate Mass Emissions with the Electrical Low Pressure Impactor," Aerosol Sci. Technol., **40**(1), pp. 68–79.

[508] Van Gulijk, C., Schouten, J. M., Marijnissen, J. C. M., Makkee, M., and Moulijn, J. A., 2001, "Restriction for the ELPI in Diesel Particulate Measurements," J. Aerosol Sci., **32**(9), pp. 1117–1130.

[509] Maricq, M. M., Podsiadlik, D. H., and Chase, R. E., 2000, "Size Distributions of Motor Vehicle Exhaust PM: A Comparison between ELPI and SMPS Measurements," Aerosol Sci. Technol., **33**(3), pp. 239–260.

[510] Lehmann, U., Niemelä, V., and Mohr, M., 2004, "New Method for Time-Resolved Diesel Engine Exhaust Particle Mass Measurement," Environ. Sci. Technol., **38**(21), pp. 5704–5711.

[511] Baron, P. A., 2001, "Measurement of Airborne Fibers: A Review," Ind. Health, **39**(2), pp. 39–50.

[512] Ehara, K., Hagwood, C., and Coakley, K. J., 1996, "Novel Method to Classify Aerosol Particles According to Their Mass-to-Charge Ratio—aerosol Particle Mass Analyser," J. Aerosol Sci., **27**(2), pp. 217–234.

[513] Olfert, J. S., and Collings, N., 2005, "New Method for Particle Mass Classification—the Couette Centrifugal Particle Mass Analyzer," J. Aerosol Sci., **36**(11), pp. 1338–1352.

[514] Kuwata, M., 2015, "Particle Classification by the Tandem Differential Mobility Analyzer–particle Mass Analyzer System," Aerosol Sci. Technol., **49**(7), pp. 508–520.

[515] Hansen, A. D. A. D. A., Rosen, H., and Novakov, T., 1984, "The Aethalometer—an Instrument for the Real-Time Measurement of Optical Absorption by Aerosol Particles," Sci. Total Environ., **36**(C), pp. 191–196.

[516] Arnott, W. P., Hamasha, K., Moosmüller, H., Sheridan, P. J., and Ogren, J. A., 2005, "Towards Aerosol Light-Absorption Measurements with a 7-Wavelength Aethalometer: Evaluation with a Photoacoustic Instrument and 3-Wavelength Nephelometer," Aerosol Sci. Technol., **39**(1), pp. 17–29.

[517] Bond, T. C., Anderson, T. L., and Campbell, D., 1999, "Calibration and Intercomparison of Filter-Based Measurements of Visible Light Absorption by Aerosols," Aerosol Sci. Technol., **30**(6), pp. 582–600.

[518] Müller, T., Schladitz, A., Massling, A., Kaaden, N., Kandler, K., and Wiedensohler, A., 2009, "Spectral Absorption Coefficients and Imaginary Parts of Refractive Indices of Saharan Dust during SAMUM-1," Tellus, Ser. B Chem. Phys. Meteorol., **61**(1), pp. 79–95.

[519] Petzold, A., and Schönlinner, M., 2004, "Multi-Angle Absorption Photometry—a New Method for the Measurement of Aerosol Light Absorption and Atmospheric Black Carbon," J. Aerosol Sci., **35**(4), pp. 421–441.

[520] Moteki, N., and Kondo, Y., 2010, "Dependence of Laser-Induced Incandescence on Physical Properties of Black Carbon Aerosols: Measurements and Theoretical Interpretation," Aerosol Sci. Technol., **44**(8), pp. 663–675.

[521] Schwarz, J. P., Spackman, J. R., Gao, R. S., Perring, A. E., Cross, E., Onasch, T. B., Ahern, A., Wrobel, W., Davidovits, P., Olfert, J., Dubey, M. K., Mazzoleni, C., and Fahey, D. W., 2010, "The Detection Efficiency of the Single Particle Soot Photometer," Aerosol Sci. Technol., **44**(8), pp. 612–628.

[522] Baumgardner, D., Kok, G., and Raga, G., 2004, "Warming of the Arctic Lower Stratosphere by Light Absorbing Particles," Geophys. Res. Lett., **31**(6), p. L06117.

[523] Slowik, J. G., Cross, E. S., Han, J.-H., Davidovits, P., Onasch, T. B., Jayne, J. T., Williams, L. R., Canagaratna, M. R., Worsnop, D. R., Chakrabarty, R. K., Moosmüller, H., Arnott, W. P., Schwarz, J. P., Gao, R.-S., Fahey, D. W., Kok, G. L., and Petzold, A., 2007, "An Inter-Comparison of Instruments Measuring Black Carbon Content of Soot Particles," Aerosol Sci. Technol., **41**(3), pp. 295–314.

[524] Faxvog, F. R., and Roessler, D. M., 1979, "Optoacoustic Measurements of Diesel Particulate Emissions," J. Appl. Phys., **50**(12), pp. 7880–7882.

[525] Petzold, A., and Niessner, R., 1996, "Photoacoustic Soot Sensor for In-Situ Black Carbon Monitoring," Appl. Phys. B, **63**(2), pp. 191–197.

[526] Jayne, J. T., Leard, D. C., Zhang, X., Davidovits, P., Smith, K. A., Kolb, C. E., and Worsnop, D. R., 2000, "Development of an Aerosol Mass Spectrometer for Size and Composition Analysis of Submicron Particles," Aerosol Sci. Technol., **33**(1–2), pp. 49–70.

[527] DeCarlo, P. F., Kimmel, J. R., Trimborn, A., Northway, M. J., Jayne, J. T., Aiken, A. C., Gonin, M., Fuhrer, K., Horvath, T., Docherty, K. S., Worsnop, D. R., and Jimenez, J. L., 2006, "Field-Deployable, High-Resolution, Time-of-Flight Aerosol Mass Spectrometer," Anal. Chem., **78**(24), pp. 8281–8289.

[528] Onasch, T. B., Trimborn, A., Fortner, E. C., Jayne, J. T., Kok, G. L., Williams, L. R., Davidovits, P., and Worsnop, D. R., 2012, "Soot Particle Aerosol Mass Spectrometer: Development, Validation, and Initial Application," Aerosol Sci. Technol., **46**(7), pp. 804–817.

[529] Sedlacek, A. J., Lewis, E. R., Kleinman, L., Xu, J., and Zhang, Q., 2012, "Determination of and Evidence for Non-core-shell Structure of Particles Containing Black Carbon Using the Single-Particle Soot Photometer (SP2)," Geophys. Res. Lett., **39**(6), p. L06802.

[530] Lee, B. P., Li, Y. J., Flagan, R. C., Lo, C., and Chan, C. K., 2013, "Sizing Characterization of the Fast-Mobility Particle Sizer (FMPS) Against SMPS and HR-ToF-AMS," Aerosol Sci. Technol., **47**(9), pp. 1030–1037.

[531] Brunauer, S., Emmett, P. H., and Teller, E., 1938, "Adsorption of Gases in Multimolecular Layers," J. Am. Chem. Soc., **60**(2), pp. 309–319.

[532] Patashnick, H., and Rupprecht, E. G., 1991, "Continuous Pm-10 Measurements Using the Tapered Element Oscillating Microbalance," J. Air Waste Manag. Assoc., **41**(8), pp. 1079–1083.

[533] Booker, D. R., 2007, "Road Test of an On-Board Particulate Matter Mass Measurement System," SAE Tech. Pap., (2007-01-1116).

[534] Jaques, P. A., Ambs, J. L., Grant, W. L., and Sioutas, C., 2004, "Field Evaluation of the Differential TEOM Monitor for Continuous PM 2.5 Mass Concentrations Special Issue of Aerosol Science and Technology on Findings from the Fine Particulate Matter Supersites Program," Aerosol Sci. Technol., **38**, pp. 49–59.

[535] Patashnick, H., Rupprecht, G., Ambs, J. L., and Meyer, M. B., 2001, "Development of a Reference Standard for Particulate Matter Mass in Ambient Air," Aerosol Sci. Technol., **34**(1), pp. 42–45.

[536] Fierz, M., Scherrer, L., and Burtscher, H., 2002, "Real-Time Measurement of Aerosol Size Distributions with an Electrical Diffusion Battery," J. Aerosol Sci., **33**(7), pp. 1049–1060.

[537] Dreier, T., and Schulz, C., 2016, "Laser-Based Diagnostics in the Gas-Phase Synthesis of Inorganic Nanoparticles," Powder Technol., **287**, pp. 226–238.

[538] Zhao, H., and Ladommatos, N., 1998, "Optical Diagnostics for Soot and Temperature Measurement in Diesel Engines," Prog. Energy Combust. Sci., **24**(3), pp. 221–255.

[539] Desgroux, P., Mercier, X., and Thomson, K. A., 2013, "Study of the Formation of Soot and Its Precursors in Flames Using Optical Diagnostics," Proc. Combust. Inst., **34**(1), pp. 1713–1738.

[540] Hassel, E. P., and Linow, S., 2000, "Laser Diagnostics for Studies of Turbulent Combustion," Meas. Sci. Technol., **11**(2), pp. R37–R57.

[541] Thurow, B., Jiang, N., and Lempert, W., 2013, "Review of Ultra-High Repetition Rate Laser Diagnostics for Fluid Dynamic Measurements," Meas. Sci. Technol., **24**(012002), pp. 1–22.

[542] Schulz, C., Dreizler, A., Ebert, V., and Wolfrum, J., 2007, "Combustion Diagnostics," *Springer Handbook of Experimental Fluid Mechanics*, Springer, Heidelberg, pp. 1241–1315.

[543] Ma, B., and Long, M. B., 2014, "Combined Soot Optical Characterization Using 2-D Multi-Angle Light Scattering and Spectrally Resolved Line-of-Sight Attenuation and Its Implication on Soot Color-Ratio Pyrometry," Appl. Phys. B, **117**(1), pp. 287–303.

[544] Lee, K., Han, Y., Lee, W., Chung, J., and Lee, C., 2005, "Quantitative Measurements of Soot Particles in a Laminar Diffusion Flame Using a LII/LIS Technique," Meas. Sci. Technol., **16**(2), pp. 519–528.

[545] Axelsson, B., Collin, R., and Bengtsson, P. E., 2001, "Laser-Induced Incandescence for Soot Particle Size and Volume Fraction Measurements Using on-Line Extinction Calibration," Appl. Phys. B, **72**(3), pp. 367–372.

[546] Vander Wal, R. L., and Ticich, T. M., 1999, "Cavity Ringdown and Laser-Induced Incandescence Measurements of Soot," Appl. Opt., **38**(9), pp. 1444–1451.

[547] Vander Wal, R. L., 1998, "Calibration and Comparison of Laser-Induced Incandescence with Cavity Ring-

Down," Proc. Combust. Inst., **27**(1), pp. 59–67.

[548] Bockhorn, H., Geitlinger, H., Jungfleisch, B., Lehre, T., Schön, A., Streibel, T., and Suntz, R., 2002, "Progress in Characterization of Soot Formation by Optical Methods," Phys. Chem. Chem. Phys., **4**(15), pp. 3780–3793.

[549] Reimann, J., Kuhlmann, S. A., and Will, S., 2009, "2D Aggregate Sizing by Combining Laser-Induced Incandescence (LII) and Elastic Light Scattering (ELS)," Appl. Phys. B, **96**(4), pp. 583–592.

[550] Simonsson, J., Olofsson, N. E., Bladh, H., Sanati, M., and Bengtsson, P. E., 2017, "Influence of Potassium and Iron Chloride on the Early Stages of Soot Formation Studied Using Imaging LII/ELS and TEM Techniques," Proc. Combust. Inst., **36**(1), pp. 853–860.

[551] Snelling, D. R., Link, O., Thomson, K. A., and Smallwood, G. J., 2011, "Measurement of Soot Morphology by Integrated LII and Elastic Light Scattering," Appl. Phys. B, **104**(2), pp. 385–397.

[552] Olofsson, N. E., Johnsson, J., Bladh, H., and Bengtsson, P. E., 2013, "Soot Sublimation Studies in a Premixed Flat Flame Using Laser-Induced Incandescence (LII) and Elastic Light Scattering (ELS)," Appl. Phys. B, **112**(3), pp. 333–342.

[553] Yon, J., Ouf, F. X., Hebert, D., Mitchell, J. B., Teuscher, N. . L., Garrec, J. L., Bescond, A., Baumann, W., Ourdani, D., Bizien, T., and Perez, J., 2018, "Investigation of Soot Oxidation by Coupling LII, SAXS and Scattering Measurements," Combust. Flame, **190**, pp. 441–453.

[554] Herdman, J. D., Connelly, B. C., Smooke, M. D., Long, M. B., and Miller, J. H., 2011, "A Comparison of Raman Signatures and Laser-Induced Incandescence with Direct Numerical Simulation of Soot Growth in Non-Premixed Ethylene/Air Flames," Carbon, **49**(15), pp. 5298–5311.

[555] Bengtsson, P. E., Aldén, M., Kröll, S., and Nilsson, D., 1990, "Vibrational CARS Thermometry in Sooty Flames: Quantitative Evaluation of C2 Absorption Interference," Combust. Flame, **82**(2), pp. 199–210.

[556] D'alessio, A., Di Lorenzo, A., Borghese, A., Beretta, F., and Masi, S., 1977, "Study of the Soot Nucleation Zone of Rich Methane-Oxygen Flames," Proc. Combust. Inst., **16**(1), pp. 695–708.

[557] Santoro, R. J., Semerjian, H. G., and Dobbins, R. A., 1983, "Soot Particle Measurements in Diffusion Flames," Combust. Flame, **51**, pp. 203–218.

[558] Bengtsson, P. E., and Aldén, M., 1989, "Application of a Pulsed Laser for Soot Measurements in Premixed Flames," Appl. Phys. B, **48**(2), pp. 155–164.

[559] Axelsson, B., Collin, R., and Bengtsson, P.-E., 2000, "Laser-Induced Incandescence for Soot Particle Size Measurements in Premixed Flat Flames," Appl. Opt., **39**(21), p. 3683.

[560] Migliorini, F., Thomson, K. A., and Smallwood, G. J., 2011, "Investigation of Optical Properties of Aging Soot," Appl. Phys. B, **104**(2), pp. 273–283.

[561] Berden, G., and Engeln, R., 2009, *Cavity Ring-down Spectroscopy: Techniques and Applications*, John Wiley & Sons, New York.

[562] Moreau, C. S., Therssen, E., Mercier, X., Pauwels, J. F., and Desgroux, P., 2004, "Two-Color Laser-Induced Incandescence and Cavity Ring-down Spectroscopy for Sensitive and Quantitative Imaging of Soot and PAHs in Flames," Appl. Phys. B, **78**(3–4), pp. 485–492.

[563] Allen, M. G., 1998, "Diode Laser Absorption Sensors for Gas-Dynamic and Combustion Flows," Meas. Sci. Technol., **9**(4), pp. 545–562.

[564] Liu, C., and Xu, L., 2018, "Laser Absorption Spectroscopy for Combustion Diagnosis in Reactive Flows: A Review," Appl. Spectrosc. Rev., pp. 1–44.

[565] Reid, J., and Labrie, D., 1981, "Second-Harmonic Detection with Tunable Diode Lasers—comparison of Experiment and Theory," Appl. Phys. B, **26**(3), pp. 203–210.

[566] Kluczynski, P., Gustafsson, J., Lindberg, Å. M., and Axner, O., 2001, "Wavelength Modulation Absorption Spectrometry - An Extensive Scrutiny of the Generation of Signals," Spectrochim. Acta Part B At. Spectrosc., **56**(8), pp. 1277–1354.

[567] Dasch, C. J., 1992, "One-Dimensional Tomography: A Comparison of Abel, Onion-Peeling, and Filtered Backprojection Methods," Appl. Opt., **31**(8), pp. 1146–1152.

[568] Smith, L. M., Keefer, D. R., and Sudharsanan, S. I., 1988, "Abel Inversion Using Transform Techniques," J. Quant. Spectrosc. Radiat. Transf., **39**(5), pp. 367–373.

[569] Daun, K. J., Grauer, S. J., and Hadwin, P. J., 2016, "Chemical Species Tomography of Turbulent Flows: Discrete Ill-Posed and Rank Deficient Problems and the Use of Prior Information," J. Quant. Spectrosc. Radiat. Transf., **172**, pp. 58–74.

[570] Link, O., Snelling, D. R., Thomson, K. A., and Smallwood, G. J., 2011, "Development of Absolute Intensity Multi-Angle Light Scattering for the Determination of Polydisperse Soot Aggregate Properties," Proc. Combust. Inst., **33**(1), pp. 847–854.

[571] Burr, D. W., Daun, K. J., Thomson, K. A., and Smallwood, G. J., 2012, "Optimization of Measurement Angles for Soot Aggregate Sizing by Elastic Light Scattering, through Design-of-Experiment Theory," J. Quant. Spectrosc. Radiat. Transf., **113**(5), pp. 355–365.

[572] Moghaddam, S. T., Hadwin, P. J., and Daun, K. J., 2017, "Soot Aggregate Sizing through Multiangle Elastic Light Scattering: Influence of Model Error," J. Aerosol Sci., **111**, pp. 36–50.

[573] Oltmann, H., Reimann, J., and Will, S., 2010, "Wide-Angle Light Scattering (WALS) for Soot Aggregate Characterization," Combust. Flame, **157**(3), pp. 516–522.

[574] Huber, F. J. T., Will, S., and Daun, K. J., 2016, "Sizing Aerosolized Fractal Nanoparticle Aggregates through Bayesian Analysis of Wide-Angle Light Scattering (WALS) Data," J. Quant. Spectrosc. Radiat. Transf., **184**, pp. 27–39.

[575] Huber, F. J. T., and Will, S., 2018, "Characterization of a Silica-Aerosol in a Sintering Process by Wide-Angle Light Scattering and Principal Component Analysis," J. Aerosol Sci., **119**, pp. 62–76.

[576] Guiner, A., Fournet, G., and Walker, C. B., 1955, *Small-Angle Scattering of X-Rays*, John Wiley & Sons, New York.

[577] Hessler, J. P., Seifert, S., and Winans, R. E., 2002, "Spatially Resolved Small-Angle X-Ray Scattering Studies of Soot Inception and Growth," Twenty-Ninth Symp. Combust., **29**(2), pp. 395–407.

[578] Di Stasio, S., Mitchell, J. B. A., Legarrec, J. L., Biennier, L., and Wulff, M., 2006, "Synchrotron SAXS 〈in Situ〉 Identification of Three Different Size Modes for Soot Nanoparticles in a Diffusion Flame," Carbon, **44**(7), pp. 1267–1279.

[579] Braun, A., Huggins, F. E., Seifert, S., Ilavsky, J., Shah, N.; Kelly, K. E., Sarofim, A., and Huffman, G. P., 2004, "Size-Range Analysis of Diesel Soot with Ultra-Small Angle X-Ray Scattering," Combust. Flame, **137**(1–2),

pp. 63–72.

[580] Rader, D. J., and O'Hern, T. J., 1993, "Optical Direct-Reading Techniques: In Situ Sensing," *Aerosol Measurement: Principles, Techniques and Applications*, John Wiley & Sons, New York, pp. 345–380.

[581] King, G. B., Sorensen, C. M., Lester, T. W., and Merklin, J. F., 1982, "Photon Correlation Spectroscopy Used as a Particle Size Diagnostic in Sooting Flames," Appl. Opt., **21**(6), pp. 976–978.

[582] Charalampopoulos, T. T., and Felske, J. D., 1987, "Refractive Indices of Soot Particles Deduced from In-Situ Laser Light Scattering Measurements," Combust. Flame, **68**(3), pp. 283–294.

[583] Flower, W. L., and Hurd, A. J., 1987, "In Situ Measurement of Flame-Formed Silica Particles Using Dynamic Light Scattering," Appl. Opt., **26**(11), pp. 2236–2239.

[584] Sadezky, A., Muckenhuber, H., Grothe, H., Niessner, R., and Pöschl, U., 2005, "Raman Microspectroscopy of Soot and Related Carbonaceous Materials: Spectral Analysis and Structural Information," Carbon, **43**(8), pp. 1731–1742.

[585] Stiles, P. L., Dieringer, J. A., Shah, N. C., and Van Duyne, R. P., 2008, "Surface-Enhanced Raman Spectroscopy," Annu. Rev. Anal. Chem., **1**(1), pp. 601–626.

[586] Miles, R. B., Lempert, W. R., and Forkey, J. N., 2001, "Laser Rayleigh Scattering Review," Meas. Sci. Technol., **12**, pp. 33–51.

[587] Zhao, F. Q., and Hiroyasu, H., 1993, "The Applications of Laser Rayleigh Scattering to Combustion Diagnostics," Prog. Energy Combust. Sci., **19**(6), pp. 447–485.

[588] Dibble, R. W., and Hollenbach, R. E., 1981, "Laser Rayleigh Thermometry in Turbulent Flames," Symp. Combust., **18**(1), pp. 1489–1499.

[589] Martyshkin, D. V., Ahuja, R. C., Kudriavtsev, A., and Mirov, S. B., 2004, "Effective Suppression of Fluorescence Light in Raman Measurements Using Ultrafast Time Gated Charge Coupled Device Camera," Rev. Sci. Instrum., **75**(3), pp. 630–635.

[590] Clark, R. J. H., and Long, D. A., 1977, *Raman Spectroscopy*, McGraw-Hill, New York.

[591] Dibble, R. W., Stårner, S. H., Masri, A. R., and Barlow, R. S., 1990, "An Improved Method of Data Aquisition and Reduction for Laser Raman-Rayleigh and Fluorescence Scattering from Multispecies," Appl. Phys. B, **51**(1), pp. 39–43.

[592] Roy, S., Gord, J. R., and Patnaik, A. K., 2010, "Recent Advances in Coherent Anti-Stokes Raman Scattering Spectroscopy: Fundamental Developments and Applications in Reacting Flows," Prog. Energy Combust. Sci., **36**(2), pp. 280–306.

[593] Tolles, W. M., Nibler, J. W., McDonald, J. R., and Harvey, A. B., 1977, "A Review of the Theory and Application of Coherent Anti-Stokes Raman Spectroscopy (CARS)," Appl. Spectrosc., **31**(4), pp. 253–271.

[594] Bohlin, A., and Kliewer, C. J., 2013, "Communication: Two-Dimensional Gas-Phase Coherent Anti-Stokes Raman Spectroscopy (2D-CARS): Simultaneous Planar Imaging and Multiplex Spectroscopy in a Single Laser Shot," J. Chem. Phys., **138**, p. 221101.

[595] Jonuscheit, J., Thumann, A., Schenk, M., Seeger, T., and Leipertz, A., 1996, "One-Dimensional Vibrational Coherent Anti-Stokes Raman-Scattering Thermometry," Opt. Lett., **21**(19), pp. 1532–1534.

[596] Diau, E. W. G., Smith, G. P., Jeffries, J. B., and Crosley, D. R., 1998, "HCO Concentration in Flames via Quantitative Laser-Induced Fluorescence," Proc. Combust. Inst., **27**(1), pp. 453–460.

[597] Zhou, B., Brackmann, C., Li, Z., and Aldén, M., 2015, "Development and Application of CN PLIF for Single-Shot Imaging in Turbulent Flames," Combust. Flame, **165**(2), pp. 368–374.

[598] Lee, T., Jeffries, J. B., and Hanson, R. K., 2007, "Experimental Evaluation of Strategies for Quantitative Laser-Induced-Fluorescence Imaging of Nitric Oxide in High-Pressure Flames (1–60 Bar)," Proc. Combust. Inst., **31**(1), pp. 757–764.

[599] Schulz, C., and Sick, V., 2005, "Tracer-LIF Diagnostics: Quantitative Measurement of Fuel Concentration, Temperature and Fuel/Air Ratio in Practical Combustion Systems," Prog. Energy Combust. Sci., **31**(1), pp. 75–121.

[600] Lozano, A., Yip, B., and Hanson, R. K., 1992, "Acetone: A Tracer for Concentration Measurements in Gaseous Flows by Planar Laser-Induced Fluorescence," Exp. Fluids, **13**(6), pp. 369–376.

[601] Seitzman, J. M., Kychakoff, G., and Hanson, R. K., 1985, "Instantaneous Temperature Field Measurements Using Planar Laser-Induced Fluorescence," Opt. Lett., **439**–**441**(10), p. 9.

[602] Paul, P. H., and Najm, H. N., 1998, "Planar Laser-Induced Fluorescence Imaging of Flame Heat Release Rate," Proc. Combust. Inst., **27**(1), pp. 43–50.

[603] Wu, Y., Xu, W., Lei, Q., and Ma, L., 2015, "Single-Shot Volumetric Laser Induced Fluorescence (VLIF) Measurements in Turbulent Flows Seeded with Iodine," Opt. Express, **23**(26), pp. 33408–33418.

[604] Wellander, R., Richter, M., and Aldén, M., 2014, "Time-Resolved (KHz) 3D Imaging of OH PLIF in a Flame," Exp. Fluids, **55**(6), p. 1764.

[605] Li, T., Pareja, J., Becker, L., Heddrich, W., Dreizler, A., and Böhm, B., 2017, "Quasi-4D Laser Diagnostics Using an Acousto-Optic Deflector Scanning System," Appl. Phys. B, **123**(3), p. 78.

[606] Reinhard, N., 2006, *Laser-Induced Breakdown Spectroscopy: Fundamentals and Applications*, Springer-Verlag, Heidelberg.

[607] Galbács, G., 2015, "A Critical Review of Recent Progress in Analytical Laser-Induced Breakdown Spectroscopy," Anal. Bioanal. Chem., **407**(25), pp. 7537–7562.

[608] Radziemski, L. J., Loree, T. R., Cremers, D. A., and Hoffman, N. M., 1983, "Time-Resolved Laser-Induced Breakdown Spectrometry of Aerosols," Anal. Chem., **55**(8), pp. 1246–1252.

[609] Blevins, L. G., Shaddix, C. R., Sickafoose, S. M., and Walsh, P. M., 2003, "Laser-Induced Breakdown Spectroscopy at High Temperatures in Industrial Boilers and Furnaces.," Appl. Opt., **42**(30), pp. 6107–6118.

[610] Zhang, Y., Li, S., Ren, Y., Yao, Q., and Stephen, D. T., 2015, "A New Diagnostic for Volume Fraction Measurement of Metal-Oxide Nanoparticles in Flames Using Phase-Selective Laser-Induced Breakdown Spectroscopy," Proc. Combust. Inst., **35**(3), pp. 3681–3688.

[611] Xiong, G., Li, S., Zhang, Y., Buckley, S. G., and Stephen, D. T., 2016, "Phase-Selective Laser-Induced Breakdown Spectroscopy of Metal-Oxide Nanoparticle Aerosols with Secondary Resonant Excitation during Flame Synthesis," J. Anal. At. Spectrom., **31**(2), pp. 482–491.

[612] Liu, C., Li, S., Zong, Y., Yao, Q., and Stephen, D. T., 2017, "Laser-Based Investigation of the Transition from Droplets to Nanoparticles in Flame-Assisted Spray Synthesis of Functional Nanoparticles," Proc.

Combust. Inst., **36**(1), pp. 1109–1117.

[613] Payri, F., Pastor, J. M. V, García, J. M., and Pastor, J. M. V, 2007, "Contribution to the Application of Two-Colour Imaging to Diesel Combustion," Meas. Sci. Technol., **18**(8), pp. 2579–2598.

[614] Weeks, R. W., and Duley, W. W., 1974, "Aerosol-Particle Sizes from Light Emission during Excitation by TEA CO2laser Pulses," J. Appl. Phys., **45**(10), pp. 4661–4662.

[615] Tolman, R. C., 1938, *The Principles of Statistical Mechanics*, Oxford University Press, London.

[616] Sazhin, O., Kulev, A., Borisov, S., and Gimelshein, S., 2008, "Numerical Analysis of Gas – Surface Scattering Effect on Thermal Transpiration in the Free Molecular Regime," **82**, pp. 20–29.

[617] Maxwell, J. C., 1890, *The Scientific Papers of James Clerk Maxwell*, Dover Publications, New York.

[618] Cercignani, C., and Lampis, M., 1971, "Kinetic Models for Gas—surface Interactions," Transp. Theory Stat. Phys., **1**(2), pp. 101–114.

[619] Lord, R. G., 1991, "Some Extensions to the Cercignani–Lampis Gas–surface Scattering Kernel," Phys. Fluids A Fluid Dyn., **3**(4), pp. 706–710.

[620] Goodman, F. O., 1967, "Three-Dimensional Hard Spheres Theory of Scattering of Gas Atoms from a Solid Surface I. Limit of Large Incident Speed," Surf. Sci., **7**(3), pp. 391–421.

[621] Özer, A., and Manson, J. R., 2002, "Comparison of One-Dimensional and Three-Dimensional Models for the Energy Accommodation Coefficient," Surf. Sci., **502**, pp. 352–357.

[622] Goodman, F. O., 1963, "On the Theory of Accommodation Coefficients-III. Classical Perturbation Theory for the Thermal Accommodation of Light Gases," J. Phys. Chem. Solids, **24**(12), pp. 1451–1466.

[623] Zwanzig, R. W., 1960, "Collision of a Gas Atom with a Cold Surface," J. Chem. Phys., **32**(4), pp. 1173–1177.

[624] Cercignani, C., 1995, "Aerodynamical Applications of the Boltzmann Equation," La Riv. del Nuovo Cim., **18**(7), pp. 1–40.

[625] Grimmelmann, E. K., Tully, J. C., Cardillo, M. J., Grimmelmann, E. K., Tully, J. C., Cardillo, M. J., Laboratories, B., and Hill, M., 1980, "Hard-Cube Model Analysis of Gas-Surface Energy Accommodation," J. Chem. Phys., **72**(2), pp. 1039–1043.

[626] Tully, J. C., 1990, "Washboard Model of Gas-Surface Scattering," J. Chem. Phys., **92**(1), pp. 680–686.

[627] Singh, N., 2016, "Time Resolved Laser Induced Incandescence Analysis of Metal Aerosols," University of Waterloo. Thesis.